TUDelft

Delft University of Technology

On the slamming of ships
Development of an approximate slamming prediction method

Kapsenberg, Geet Kees

DOI
10.4233/uuid:14eac2bb-63ee-47e4-8218-1ba3830a97b4

Publication date
2018

Document Version
Final published version

Citation (APA)
Kapsenberg, G. K. (2018). *On the slamming of ships: Development of an approximate slamming prediction method*. [Dissertation (TU Delft), Delft University of Technology]. https://doi.org/10.4233/uuid:14eac2bb-63ee-47e4-8218-1ba3830a97b4

Important note
To cite this publication, please use the final published version (if applicable).
Please check the document version above.

On the slamming of ships

Development of an approximate slamming prediction method

Proefschrift

ter verkrijging van de graad van doctor
aan de Technische Universiteit Delft,
op gezag van de Rector Magnificus prof. dr. ir. T.H.J.J. van der Hagen,
voorzitter van het College voor Promoties,
in het openbaar te verdedigen op donderdag 14 juni 2018 om 12:30 uur

door

Geert Kees KAPSENBERG

Scheepsbouwkundig Ingenieur (Technische Hogeschool Delft, Nederland)
geboren te Sluis, Nederland

Dit proefschrift is goedgekeurd door de promotor:

Prof. dr. ir. R.H.M. Huijsmans

Samenstelling promotiecommissie bestaat uit:

Rector Magnificus,	voorzitter
Prof. dr. ir. R.H.M. Huijsmans,	promotor

onafhankelijke leden:

dr. ir. J.A. Keuning,	Technische Universiteit Delft
Prof. dr. R.R. Negenborn,	Technische Universiteit Delft
Prof. dr. ir. C.H. Venner,	Technische Universiteit Twente
dr. A. Iafrati,	CNR - INSEAN
Prof. dr. A.A. Korobkin,	University of East Anglia
Prof. dr. G.A. Thomas,	University College London
Prof. dr. ir. A.P. van 't Veer,	Technische Universiteit Delft, reservelid

Summary

On slamming of ships
by Geert Kapsenberg

Slamming of ships is a phenomenon characterized by a high wave load of short duration. Usually the ships structure responds in a vibratory manner on this load; the response can be either a local or a global vibration mode or it can be in both modes together. These short duration loads are caused by large amplitude motions, even to the point that the fore body of the ship emerges from the water and slams upon re-entry, or they are caused by very steep waves that impact against the hull.

The global elastic vibratory response of the structure is called whipping. It is characterized by a very low damping, so it takes many oscillations before it is extinguished. This dynamic response of the structure increases as well the maximum load as the number of load cycles relevant for fatigue damage due to seakeeping loads. Local and global responses can result in local high stresses such that it results in plastic deformation. Slamming loads can lead to catastrophic damage as illustrated by the accidents with the ferry *Estonia* and the container ship *Napoli*. Slamming loads are known to be a major reason for operators to change course and/or reducing speed, therefore there is a large effect on the economy of a ship. These aspects are the motivation for carrying out this study.

The objective of this thesis is to develop an approximate and fast method to calculate slamming loads. This method, called Marin Momentum Theory (MMT) can be included in a time domain simulation of ship motions in waves. It is intended for the design process of a ship to study hull form variations and it can be used to detect worst cases in long time simulations. The detected cases can then be studied in detail by either CFD methods or experiments using a model of the ship.

The approximate method is based on momentum theory; it uses the amount of fluid that moves with the ship and how this amount, the added mass, changes in time. The added mass is determined by linear potential flow calculations. Since the ship makes large motions, the added mass calculations are made for a series of drafts from the keel up to the deck. In order to determine the actual intersection of the water surface and the hull of the ship, it is necessary to include the effect of water pile-up along the hull due to the

immersing hull and the effect of the bow wave generated by the forward speed of the ship. The basics of MMT have been verified by comparing calculations to results of drop tests of a wedge and of a ship section that were available in the literature.

In order to validate the method for ships, dedicated model experiments have been carried out with the model of a ferry. In the first series of experiments the loads on a segment in the bow have been measured; in the second series the loads were determined on 10 segments in the forward L/4 part of the hull. Since it has been realized that the primary wave parameter important for the magnitude of the slamming load is the wave steepness, special wave trains have been used in the experiments. These wave trains consist of waves having roughly the same height and a continuously decreasing wave length, thus increasing the wave steepness. These wave trains appeared to generate very useful validation data, but they cannot be directly used to determine the probability of a slam of a certain magnitude in a specified seaway.

A result of the experiments also was, that short duration impulsive forces were measured in a short wave in which the vessel hardly moved other than its forward speed. The wave causing this short duration impact and causing a whipping response of the structure of the model was a very steep one on the edge of breaking. The presented calculation method was not always successful in predicting this load, most probably because the breaking wave is not properly described by the linear wave theory used in the simulation.

The results of the validation of the forces on the bow segment showed a satisfactory degree of agreement. The agreement of the forces on the hull segments in the second series of experiments was less accurate but it is assumed that the method can be useful in predicting the first vibration modes of a vessel and thereby making an estimate of the additional fatigue damage of a ship.

The MMT model has been used to explore some trends in the magnitude of slamming forces. The large effect of reducing the speed of the vessel has been illustrated and also the effect of the wave direction. It appears that a large change in course such as 60 deg is necessary to significantly reduce the excitation of the first few elastic modes of the ship.

Samenvatting

Over slamming van schepen
door Geert Kapsenberg

Onder slamming van schepen verstaan we hoge, kortdurende, golfkrachten op de romp van het schip. Gewoonlijk brengt deze belasting de scheepsconstructie in trilling; dit kan zowel een lokale als een globale trilvorm zijn; het komt ook voor dat beide trilvormen worden aangeslagen. Deze kortdurende golfkrachten worden veroorzaakt door of grote bewegingen van het schip waarbij de voorvoet uit het water komt en met een klap weer terug in het water valt, of door steile golven die tegen de romp slaan.

De globale elastische trilvorm wordt aangeduid met de term 'whipping'. De trilvorm is zeer licht gedempt zodat hij pas na veel oscillaties is uitgedempt. Deze dynamische vervorming vergroot zowel de extreme belasting, oa. midscheeps, als het aantal belasting-wisselingen wat relevant is voor o.a. de vermoeiing van de constructie. Zowel lokale als globale belastingen kunnen tot dusdanig hoge spanningen in het materiaal leiden, dat het plastisch vervormt. Slamming kan tot grote problemen leiden zoals is aangetoond door het ongeluk met de veerboot *Estonia* en het containerschip *Napoli*. Voor gezagvoerders en kapiteins is slamming een van de belangrijkste reden om koers te veranderen en/of vaart te verminderen. Hiermee heeft slamming een groot effect op de economie van het schip als gevolg van tijdverlies en een hoger brandstof verbruik. De genoemde aspecten zijn de motivatie om deze studie uit te voeren.

Het doel van dit proefschrift is om een benaderende methode te ontwikkelen die slamming krachten uitrekent. Deze methode, de Marin Momentum Theorie (MMT), kan ingebouwd worden in een programma dat scheepsbewegingen in golven berekent door middel van ti-jddomein simulaties. De methode is bedoeld om in het ontwerpproces te worden gebruikt om verschillende rompvormen te bestuderen; de methode kan ook worden gebruikt om de ergste klappen te vinden in een lange tijd simulatie. Deze ergste klappen kunnen dan in detail worden bestudeerd door òf CFD berekeningen òf proeven met een schaalmodel van het schip.

De benaderende methode is gebaseerd op impulstheorie; zij gebruikt de hoeveelheid water die met het schip meebeweegt en in welke mate deze hoeveelheid, de toegevoegde massa,

verandert in de tijd. De toegevoegde massa wordt berekend met behulp van potentiaalt-theorie. Omdat het schip grote bewegingen maakt wordt deze berekening gedaan voor een aantal diepgangen vanaf de kiel tot aan het dek. Om de hoogte van het wateroppervlak tegen de huid te bepalen, is het nodig om de opstuwing van het water langs de romp ten gevolge van de neerwaartse beweging van het schip mee te nemen. Ook de hoogte van de boeggolf die door de snelheid van schip wordt gegenereerd dient in deze berekening te worden meegenomen.

De principes van MMT zijn geverifieerd door berekeningen te vergelijken met in de lite-ratuur beschikbare resultaten van valproeven met een wig en scheepssectie.

Om de methode voor schepen te testen, zijn speciale proeven uitgevoerd met een model van een veerboot. In de eerste serie proeven zijn de belastingen op de boeg van het schip gemeten; in de tweede serie zijn de belastingen op 10 segmenten in het voorste kwart van het schip bepaald. Omdat bekend was dat de belangrijkste parameter voor de grootte van de slamming de steilheid van de golf is, zijn speciale reeksen golven gebruikt in de proeven. Deze golftreinen bestaan uit golven die ongeveer dezelfde hoogte hebben, maar een continu afnemende golflengte. Hierdoor neemt de steilheid van de golf steeds toe. Gebleken is, dat deze golftreinen een hoop nuttige informatie opleverden om de methode te testen. Een nadeel is, dat ze niet kunnen worden gebruikt om de kans op een klap van een bepaalde grootte in een specifieke zeegang te bepalen.

Een ander resultaat van de proeven was, dat het schip ook grote impulsieve krachten kreeg in hele korte golven. In deze golven beweegt het schip nauwelijks anders dan met een voorwaartse snelheid. De golf die deze kortdurende klap veroorzaakte en daarmee een trilling in het model, was een hele steile golf die op het punt van breken staat. De ontwikkelde methode was niet altijd in staat deze kracht te voorspellen, waarschijnlijk omdat de brekende golf niet wordt beschreven door de lineaire golftheorie die gebruikt is in de simulaties.

De krachten die voorspeld worden door de benaderende methode zijn vergeleken met de resultaten van de eerste serie proeven. De krachten op de boeg werden redelijk goed voorspeld. De berekende en gemeten krachten op de segmenten, gemeten in de tweede serie modelproeven, komen minder goed overeen, maar aangenomen wordt dat de methode wel bruikbaar is in het ontwerpstadium van het schip om de eerste trilvormen te voorspellen en daarmee de vermoeiingsbelasting van de constructie.

Het MMT model is ook gebruikt om enkele trends in de grootte van de slammingkrachten te onderzoeken. Hieruit bleek dat het verminderen van snelheid inderdaad een grote invloed heeft op de grootte van de krachten en ook het veranderen van de koers ten opzichte van de golven. Het blijkt wel dat een behoorlijk grote koersverandering nodig is om de belasting van de constructie significant te verminderen.

Contents

Acronyms

BEM   Boundary Element Method. 25, 52, 70
BVP   Boundary Value Problem. 28
CFD   Computational Fluid Dynamics. 2, 7, 9, 16, 17, 61, 62, 69, 161
CIP   Constrained Interpolation Profile. 19
CoG   Center of Gravity of the ship. 49
CRS   Co-operative Research Ships. 25
DTU   Technical University of Denmark. 11
ELP   Elementary Loading Processes. 65
EoM   Equations of Motion. 49, 120, 151
FFT   Fast Fourier Transform. 40, 41, 61, 95, 185
FKR   Froude-Krilov-Restoring force. 121, 122
FPP   Forward PerPendicular. 93, 106, 161, 185
FPSO   Floating Production Storage and Offloading. 29, 65, 76, 85
GWM   Generalized Wagner Model. 18, 25, 57, 58
HB   Horizontal Bending. 21, 141
IRF   Impulse Response Function. 28, 96
LDV   Laser Doppler Velocimetry. 65–67
MARIN   Maritime Research Institute Netherlands. 3, 43, 45, 179
MMT   MARIN Momentum Theory. 47, 62, 63, 70, 73, 74, 123, 145, 147
PIV   Particle Image Velocimetry. 65, 67
RAO   Response Amplitude Operator. 97
RuG   University of Groningen. 29
SMB   Seakeeping and Manoeuvring Basin. 2
SPH   Smoothed Particle Hydrodynamics. 17, 161
T   Torsion. 21
VB   Vertical Bending. 21, 140, 141
VBM   Vertical Bending Moment. 3, 5
VoF   Volume of Fluid method. 29, 61

Nomenclature

Symb	Units	Description
B	[m]	Beam of the ship
D	[m]	Depth of the ship
$\vec{F}$	[N]	Force vector
F_X	[N]	Component of force vector in X-direction
F_Y	[N]	Component of force vector in Y-direction
F_Z	[N]	Component of force vector in Z-direction
F_{2H}	[Nm]	Excitation of the 2-node horizontal bending mode
F_{2V}	[Nm]	Excitation of the 2-node vertical bending mode
H_W	[m]	Wave height, used to indicate the average height in the wave sweep
L_{OA}	[m]	Length over all of the ship
L_{PP}	[m]	Length between perpendiculars
LcG	[m]	Longitudinal position Centre of Gravity
m	[kg]	Mass of a body
$\vec{n}$	[-]	Normal on a body
p	[Pa]	Pressure
s	[m]	Relative motion
T	[m]	Draft of the ship
$\mathbf{T}^{(2)}_{(1)}$	[-]	Transformation matrix for vectors from system 1 to system 2
$x_{1...3}$	[m]	Linear ship motions, defined in the CoG of the ship
$x_{4...6}$	[rad]	Angular ship motions
u	[m/s]	Velocity in X-direction
v	[m/s]	Velocity in Y-direction
w	[m/s]	Velocity in Z-direction
$\vec{u}$	[m/s]	Velocity vector
v_S	[kt]	Ship speed
GM	[m]	Metacentric height
KM	[m]	Height metacentre above keel
KG	[m]	Height Centre of Gravity above keel
a_{33}	[kg/m]	Added mass for accelerations in vertical direction of a 2D section

Nomenclature continued

Symb	Units	Description
b_{33}	[kg s/m]	Damping for a velocity in vertical direction of a 2D section
A_{33}	[kg]	Added mass for accelerations in vertical direction of a 3D body
k_{XX}	[m]	Roll gyradius
k_{YY}	[m]	Pitch gyradius
k_{ZZ}	[m]	Yaw gyradius
β	[rad]	Deadrise angle (of a wedge)
δ	[rad]	Rotation angle
ϵ	[-]	Wave slope parameter
κ	[m^{-1}]	Wave number
ψ	[-]	Pile-up factor
ω	[rad/s]	Frequency of oscillation
ζ	[m]	Wave elevation
ζ_{BW}	[m]	Elevation of the stationary bow wave
∇	[m^3]	Displaced volume
Δ	[ton]	Displacement

Chapter 1

Introduction

1.1 Philosophical context

This study is not a study on ship slamming at sea. Ship slamming at sea is a very complex phenomenon which includes short crested - possibly breaking - waves, air bubbles in water, air pockets created during the impact, escaping air form these air pockets and a possible elastic response of the ship's structure. This study is about a simplification of this complex real world; it is about a model to predict the order of magnitude of slamming forces on the bow of ships sailing at speed in waves. The model has a physical background, the goal is to model the effect of the main parameters: speed, heading and hull shape on the magnitude of the slamming force. First of all, the model should be practical, it has to be used on a standard desktop PC and should require a computation time that is less than real time. This latter requirement is necessary to allow long simulations in order to derive extreme values which are necessary to determine design loads.

Models are often used in science; when scientists study a certain problem and when they pose a theory to solve it, they are essentially building a model. Sometimes models appear to be universally valid and they are called laws. However, nature does not obey laws and is never called to justice when a law is broken. Also Newtons 2nd law [1], the fundamental basis of this and many other theses, is just a model and has a limited range of application.

The theory used to solve the problem is invariably based on a set of assumptions, thus simplifying the problem. The task of the scientist is now to explain that this simplification still contains the essential features of the physics of the problem at hand. The result of this work is the so-called validation, the results of the model applied on the problem are compared to measured data from the real world. Unfortunately, this simple sentence introduces a new problem: measured data is obtained from sensors that produce this

---

[1]Newtons 2nd law: In an inertial reference frame, the vector sum of the forces F on an object is equal to the mass m of that object multiplied by the acceleration a of the object: $F = ma$ (Assuming that mass m is constant).

data. Most sensors have the nasty habit to create output depending on (at least) two parameters. The first parameter can be found from the brochure, the problem is to find the type of parameter that also affects the output and to find ways to compensate for it. Classical secondary parameters are temperature and electro-magnetic noise, but also some pressure sensors are known to be sensitive to UV light.

The use of a numerical rather than an analytical procedure to solve a certain problem introduces yet another hurdle. The scientist has to prove that the presented solution is indeed a solution of the model proposed and not a solution that is affected by numerical parameters like the number of elements used. The work to be done is to demonstrate that the solution presented is the converged solution for an increasing number of elements and a decreasing time step. This procedure is called verification of the solution; a formal procedure for CFD calculations has been detailed by Eça and Hoekstra [47].

To validate a model for ship slamming requires essentially measurements at sea. However, this is far from easy. The response of the ship to the impact has to be measured, this involves the spatial distribution of the pressure during the impact and stresses and deformations in the ships hull. The structural properties of the hull must be known; the actual mass distribution is very difficult to establish, determining the damping for the different modes is even more problematic. Next to this, all relevant parameters of the wave hitting the ship must be measured. This involves the geometry and velocity of the wave and also the air content in this wave and the shape and volume of air pockets that are created during the impact. This requires remote sensors that have not yet been developed. If these sensors are available, a measurement campaign at sea can be started. A practical problem then is, to find the right environmental conditions to do the measurements. Using a ship that sails on a fixed route can require a measurement campaign of several years before real heavy weather is being encountered as was experienced by Koning and Kapsenberg [100].

This study does not use full-scale measurements to validate the model developed. Instead it uses a model of the full scale environment: experiments were carried out with a scaled model of the ship in a large size wave basin, the Seakeeping and Manoeuvring Basin (SMB) of MARIN. This facility is described in detail by Dallinga (1999) [38]. This basin is a model of reality, not a scaled version of reality. Waves are generated by a large number of rotating flaps rather than by the wind; for most experiments wind is not being generated. Using a large number of narrow flaps allows making waves in quartering direction by setting a phase angle between the motions of adjacent flaps. Doing experiments with a scaled model in such a wave basin invariably include violation of scaling 'laws'. It is however generally accepted that most phenomena associated with ships moving in waves are dominated by gravity effects. Therefore model experiments in waves are always following Froude's law of similitude as discussed, amongst others, by Dallinga and Huijsmans [40]. A major advantage of a wave basin as the SMB is control over the wave conditions and the model. Special wave trains can be generated that might be unrealistic, but allow the generation of a lot of useful data in a short period of time. This aspect has been extensively used in this study.

One more aspect that is relevant for this type of research needs mentioning. The scientist is supposed to 'understand' his problem and to have built a picture of the relevant physics in his mind. This picture is leading in developing a theoretical model and in designing a series of experiments. It also determines the choice of sensors and the location where to put them to measure physical quantities during the experiments. The fundamental problem is, that there might be shortcomings in the mental model, the picture in his/her mind, which results in having not enough or the wrong type of sensors. If the measurements fit our model, suspicion is not raised and the scientist is not pushed into unknown territory to improve his mental model. We are unaware of the 'unknown unknowns' and we proceed until proven wrong.

The purpose of this chapter is to set the scene for the research presented. This thesis is on the development of a mathematical model to predict forces on a scaled model of a ship that experiences slamming in a wave basin. The choice has been made to build a model on the global effect of bow flare slamming, the impulsive loads on the forward part of the ship. The force calculation is based on the change in momentum in the fluid rather than on a pressure integration over the hull. The flexural response of the ships hull and the effect of slamming on the extreme Vertical Bending Moment (VBM) amidships is not determined; this aspect has been well covered by Tuitman in his thesis [178].

1.2   Motivation of this study

Seakeeping research is usually carried out as a validation of a certain design rather than as part of the 'design spiral' in the concept phase. This situation has developed since there are very strict and quantifiable requirements with respect to powering performance, while the seakeeping of the ship should be 'good' without defining what can be considered 'good'. An important aspect is also that the seakeeping performance of a certain ship cannot be changed easily. Exception to this is the ability to affect the roll motion; relatively small changes to appendages can have a large effect on the magnitude of the roll motion when the roll damping is low. Since the hydrodynamic damping of the other modes of motion is usually higher, more drastic hull changes are needed to change the vertical plane motions as shown by Kapsenberg and Brouwer [87]. Some effect can also be achieved by changing the mass distribution; a 4 % increase in the pitch radius of gyration k_{yy}/L can give an 8 % increase in the wave added resistance as was shown by Grin and Fernandez Ruano [60].

A lot of work has been done at MARIN to promote seakeeping as a topic in the early phase of the design spiral since the mid-eighties of last century. Key in this work were efforts to reduce all different aspects of seakeeping in many different environmental conditions to one overall figure of merit like operability or workability, Aalbers *et al.* [2]. The advantage of an operability study is, that it combines the ship with the actual sea

conditions in which it has to operate, a big improvement over the more academic motion response curves resulting from experiments or calculations.

Further attempts were made to quantify seakeeping in risk or in even more appealing units: Euros. This was done by developing voyage simulation programs, Aalbers (2001) [1]. This development was first applied to heavy transports; the program included a historical weather database, weather forecasts and a model of a captain to take decisions whether or not to change speed, course or even to go for a safe haven. The hydrodynamic problem is thus reduced to only one element in a complex system containing many more, and larger, uncertainties than just the fact that hydrodynamics are usually determined by a linear model.

The work presented in this thesis must be seen in these developments. It is a contribution to quantify voluntary speed reductions, or changes in course, that are deemed necessary to avoid heavy bow flare slamming. The perceived danger of damage due to slamming has been recognized for a long time as the main reason for voluntary speed reduction. This conclusion was drawn in the late 1960-ies by Aertssen from the analysis of long-term sea trials on various ship types, [4, 5, 6]. Voluntary speed reduction affects the arrival time of the ship and hence the economy and, if the master decides to avoid a heavy weather area, it also affects the fuel required for a certain voyage as shown by Dallinga (2006), [39]. These results illustrate that a good prediction of slamming impacts is very important to quantify the economy of a ship.

1.3   Consequences of ship slamming

Even mild slamming can introduce a dynamic response of the ship's hull. When the impulsive slamming force has a duration shorter than one-quarter of the period of the lowest bending mode, it excites a vibration that only slowly reduces in amplitude because of the low damping. This vibration, the whipping response, can result in high accelerations, especially at the forward and aft end of the ship. It also contributes to the bending moment amidships by increasing the extreme values and by increasing the load cycles and hence the fatigue damage as shown by Aalberts and Nieuwenhuijs [3].

Severe slamming can cause damage due to one single impact. Yamamoto *et al.* (1985) [204] reported damage due to bow flare slamming on a small 819 TEU container ship in cyclone conditions. He concluded that the large impact developed a pressure on the hull of about 840 kPa on a circular area with a diameter of 13.7 m. This very high force caused buckling and cracks in the structure, Figure 1.1.

An extreme event was also experienced by the *Estonia* in 1994 when she lost her bow visor and damaged her watertight front door. This damage caused the ship to capsize and founder in a relatively short time with loss of a large number of passengers and crew.
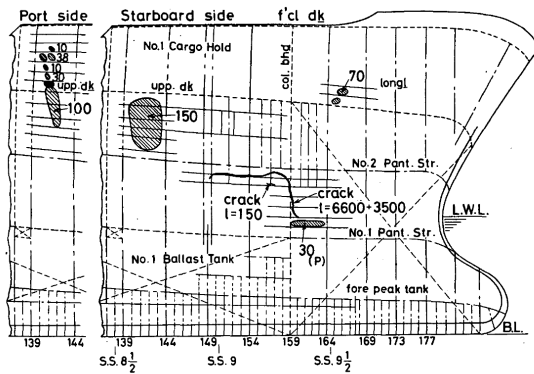
Figure 1.1: *Buckled areas (shaded) and a crack with a length of 10 m in the bow of a container ship, Yamamoto et al. (1985).*
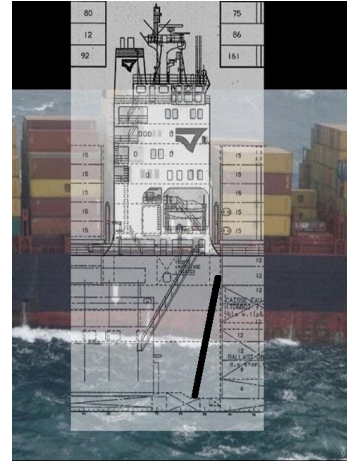
Figure 1.2: *Path of the fracture line over 80% of the depth of the container ship Napoli, MAIB report (2008).*

The official report, JAIC (1997) [107], indicates heavy slamming as the cause of losing the bow visor.

The 4400 TEU container ship *Napoli* buckled amidships in the English Channel in 2007. The report on the accident, MAIB (2008) [120], Figure 1.2, clearly revealed the state of the art in Class rules with respect to the level at which whipping stresses are incorporated: just by a safety factor on the VBM based on experience. In the investigation, Bureau Veritas used an estimation method based on a strip theory approach, (MAIB 2008, Annex E), this was later published by Tuitman (2010) [178]. This method resulted in an estimated contribution of whipping to the maximum wave bending moment of 30%. Later on, Storhaug (2009) [169] estimated that the whipping contribution could be anywhere between 20 - 60% of the wave bending moment in the sea state at the time of the accident. To complicate matters further, he raised doubts about the role of the short duration whipping stresses in the collapse mechanism of the ship's structure.

The larger 8000 TEU container ship *MOL Comfort*, broke her back in the Indian Ocean in 2013. The ship finally broke in two and although salvage attempts were undertaken, both parts ended on the bottom of the ocean. The ship was just five years old and there was no warning of problems. A detailed analysis of the accident was published [170], the main conclusions from this report are:

- The vessel was properly built according to the rules of Class NK.

- There was a large uncertainty on the sea state parameters at the time of the accident and on the actual weight of the containers. Therefore it was not considered impossible that the loads exceeded the hull girder ultimate strength.

- A detailed dynamic structural analysis of a 3-hold part of the ship revealed a weakness in the bottom panel adjacent to the keel plate. The combined lateral load and the loads due to vertical bending could cause buckling and collapse of the bottom panel. This combined load was not specified as a design case in the rules.

Although the last conclusion could well be the main cause of the accident, the second conclusion also raises a major problem. The sea state at the time of the accident was estimated to have a significant wave height $H_S = 5.5\ m$ and a mean period $T_1 = 10.3\ s$. The conditions were not considered extreme by the crew, the ship was still sailing at a speed of 17 kt speed, while the service speed was 25 kt. Even in this situation it was considered possible that the design load was exceeded. A main component of the actual load is the still water bending moment; it is worrying that this component has a large degree of uncertainty due to the fact that the weight of the containers is not really known. This large still water bending moment also played a major role in the mentioned accident with the *Napoli*.

The *MOL Comfort* belonged to a series of seven vessels. The sister ships and four similar vessels were inspected and buckling deformations were found in the bottom plating of five of the six sister ships and in one of the other vessels. These findings supported the third conclusion drawn in the investigation report.

Although the list of conclusions does not point directly into the direction of slamming, it was recommended in the report to include combined lateral and vertical load cases and to include the effects of whipping on these loads.

Figure 1.3: The container vessel MOL Comfort broke her back in 2013.

1.4   Perceived danger of slamming

The main reason why ship captains reduce speed to avoid slamming is the fact that the peaks of slamming forces have a peculiar distribution function for the probability of exceedance. The naval architect is used to a distribution function that shows only a modest increase of the design load if the probability of exceedance is reduced one order of

magnitude. Long duration measurements of peak loads are often presented in probability diagrams and a fit is being made through the data points to allow extrapolation. The fit is often based on a Weibull distribution; if we use a 3-parameter Weibull distribution, Equation 1.1, we are used to a Rayleigh distribution ($\beta = 2$) for linear processes and to an exponential distribution ($\beta = 1$) for quadratic processes.

$$Pr\{x > a\} = e^{((x-c)/\alpha)^\beta} \tag{1.1}$$

Peak values of impact loads often have a distribution with a value $\beta < 1$; this was shown for fast ships by Kim *et al.* [97] and for loads on hatch covers by Kapsenberg and the Kat [88]. A consequence is, that extreme values are really extreme: the slamming force associated with a probability of exceedance of 10^{-4} can be 3 times higher than the slamming force at a probability of exceedance of 10^{-3}. It seems plausible that this aspect of the distribution makes operators cautious. The magnitude of the next impact is quite unpredictable, so they react to incidental impacts by reducing speed.

1.5 Objective

The objective of this study is to develop a practical method that predicts the severity of ship slamming when sailing at speed in waves. Practical in this context means that including the method in a time-domain ship motion program will not cause a disproportionate increase of the processing time of the program. The severity of ship slamming is quantified in this thesis as the excitation load for the global deformation of the ship.

1.6 Possible use of the approximate method

The developed method is semi-empirical. It is expected that the method needs tuning for a particular ship through either a series of experiments in well chosen conditions or through a series of CFD calculations simulating similar conditions. The tuned method can then be used for long term simulations in a multitude of conditions in order to derive long term statistical values of global deformation and extreme values of stresses in the structure.

CFD calculations are now on the brink of solving wave impact problems. Successful calculations were already carried out in 2011 by Kapsenberg and Thornhill [85] and are now carried out by many more researchers. However, such calculations require extensive hardware and even then simulating minutes takes many hours. Building statistics and extreme values this way is very time consuming and hence totally impractical.

A possible solution is to develop screening methods, a simplified approach that is capable of detecting the main important events in a long duration simulation. These main events can then, either individually or as a compressed time series, be evaluated by CFD. The magnitude of the event is then resulting from the CFD calculation while the probability of occurrence results from the approximate method. It is expected that the
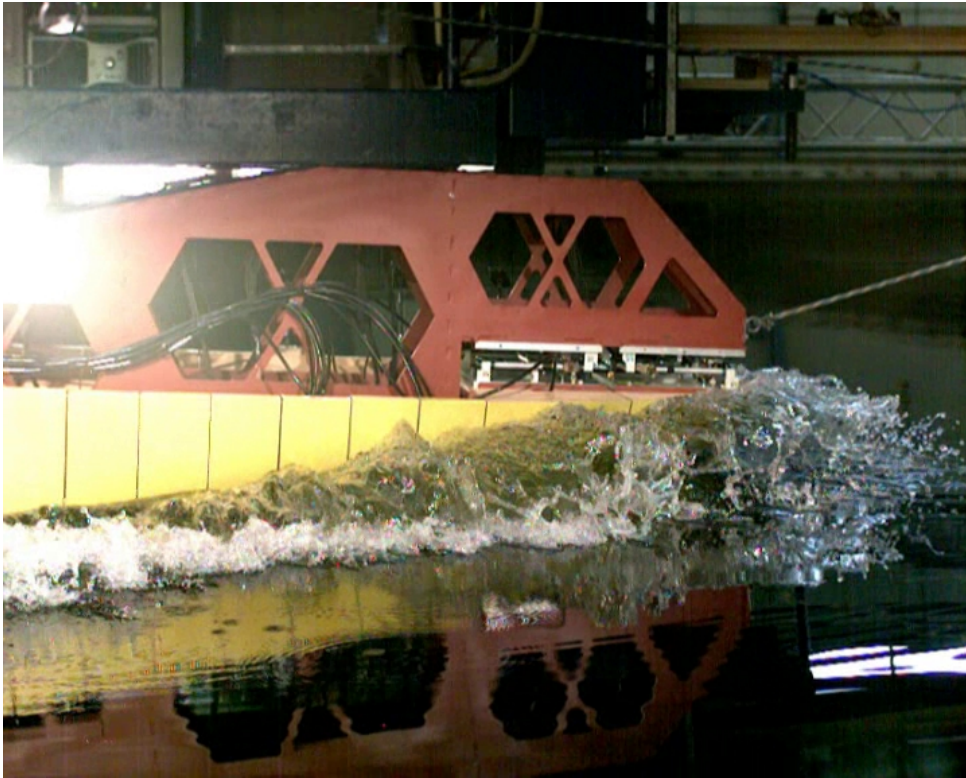
Figure 1.4: Model of a ferry in a large amplitude motion that creates an important impulsive force.

developed method can also be used as a screening method. Such an approach was also used by Moctar *et al.* [129]; he did BEM calculations for different speeds and headings to select a critical condition for a CFD calculation.

Apart from using the method as a screening tool to find critical events, it can also be used as a design tool. It gives an indication of the load level of the impacts and on the whipping response of the ships structure. Such a result can also be used to determine consequences for vibration discomfort on board and for the need to reduce speed. In this way the effect of, for instance, the amount of bow flare on the arrival time reliability and hence on the economy of a proposed design can be evaluated.

Chapter 2

Review of the literature

2.1 General

An extensive review of the literature was given by Kapsenberg in 2011 [85]. The review below is a shortened and updated version, especially in the area of Computational Fluid Dynamics (CFD). In fact, it is surprising how little new developments there are in the areas of momentum theory, analytical-, boundary element and statistical methods, or in the areas of model test techniques or full scale measurements. Most researchers want to use the latest CFD implementations and especially the newest hardware to launch large computations using a detailed model and to produce very impressive animations of their results.

It should however be realised that CFD is just another model of reality. It is more complete than potential flow theory and certainly more versatile and robust with respect to large surface deformations. However, details matter in slamming calculations, certainly if one wants to calculate local pressures. This means that small cells and small time steps are required. Long duration calculations are therefore very expensive and time consuming. Combining this with the notion that slamming should not occur too frequently, shows that CFD is not the way forward for all problems.

2.2 Literature related to Momentum Theory

The classical publication on momentum theory dates from the early years of aviation, 1929. In Germany von Kármán (1929) [91] worked on the landing of seaplanes on water and developed a theory to calculate the forces on the floaters. His calculation was based on the change in added mass of the wetted part of the floater; the added mass calculation was based on an approximate method for fully submerged 2D sections, this approach to ignore free surface effects is equivalent to using an infinite frequency added mass calculation for a body at the free surface.

Pabst (1930) [142] improved a shortcoming of von Kármán's approach, the use of only the vertical velocity component for the calculation of the momentum and thus totally

ignoring forward speed effects. Instead he used the velocity component normal to the float and derived an impact force also normal to the float; in this way he also arrived at a force component in horizontal direction.

Wagner [187] made an important step in 1932 by pointing out the importance of the pile-up effect. He used potential flow theory to calculate the impact force and the rise of water close to the impacting body. His analysis showed the analogy between an impacting wedge and a planing body having a wedge shaped cross-section.

Mayo (1945) [126] combined the impact of the float and the planing phase immediately after the impact. He added an analysis of the momentum lost in the wake of the floater, this effect is proportional to the tangential velocity component. He derived an expression for the force distribution along the length that compared much better to experimental data than previous theories.

Bisplinghoff (1952) [1] [14] presented a derivation of the added mass and the deformation of the free surface along the lines of Wagner. He also carried our impact experiments on wedges having deadrise angles of 10, 20, 30 and 40 deg. A high speed camera, 1500 frames/s, was used to quantify pile-up effects, but these results did not agree very well to the predictions by Wagner or his 'expanding prism' theory. Especially the result for the 10 deg wedge was quite different.

Leibowitz (1962, 1963) [112, 113] analysed motions in large waves of a destroyer derived from still photographs taken from full scale experiments by Bledsoe *et al.* (1961) [15]. He used a strip theory approach (he calls it cross-flow hypothesis) to determine the sectional force. He included the added mass derivative in vertical and longitudinal direction to arrive at the impulsive force. Using a beam model for the ships structure he finally arrived at stresses amidships which compared surprisingly well to the mentioned full scale measurements.

Beukelman (1991) [11] carried out experiments on vertically oscillating wedges with very low deadrise angles. The wedges were towed at various trim angles and at different values of the forward speed. Unfortunately he only focussed on the peak value of the slam pressure. There was a large effect of the forward speed, although mainly for the lower values of the deadrise angle. In the analysis of the experiments, Beukelman and Radev (1991) [12] developed a model in which they used as well the vertical as the horizontal derivative of the sectional added mass and damping, Equation 2.1.

$$FZ_{\text{IMPACT}} = -a_{33}\ddot{z} - b_{33}\dot{z} - \frac{\partial a_{33}}{\partial z}w^2 + \frac{\partial a_{33}}{\partial x}wU - \frac{\partial b_{33}}{\partial z}wz + \frac{\partial b_{33}}{\partial x}Uz \qquad (2.1)$$

Beukelman noted that the effect of the damping terms is small although he did not really proof it. Interestingly, he did not use any form of pile-up effect. Although the model given in Equation 2.1 is basically a model for the force due to a change in the momentum, he used it also for the peak slamming pressure just by dividing it by the beam. He showed a reasonable agreement with his experiments, including the effect of forward speed. There

---

[1]The derivation of the added mass by Bisplinghoff and Doherty contains errors as noted by Moran [135] and Faltinsen [50]
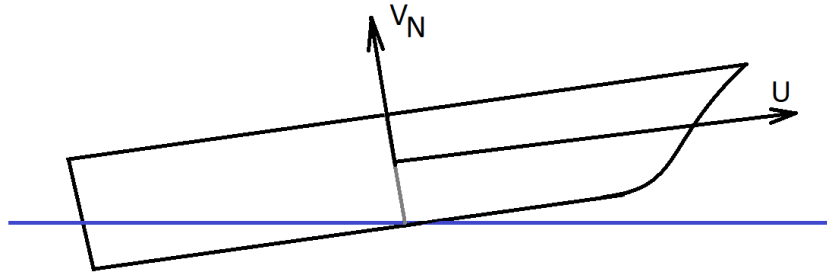
Figure 2.1: Definition of velocities by Keuning [94].

are no remarks made on air cushioning effects that surely must have played a role at the lower deadrise angles of 0, 0.5 and 1.0 deg as shown by *eg.* Chuang [27].

Keuning (1994) [94] focused on the seakeeping behaviour of fast (planing) monohulls. He used a special implementation of strip theory with non-linear components comparable to what is known in literature as '$2\frac{1}{2}$D' theory. This theory considers an earth fixed position over which the ship passes in time. Usually the method takes the solution of the 2D BVP along downstream to solve the hydrodynamic problem of the next section (as used by *i.e.* Tulin and Wu [181] and Sun and Faltinsen [172]); Keuning did not consider this type of interaction. His method is based on considering the local cross section to an impacting wedge. He used approximation formula's for the added mass of wedges similar to Taylor (1930) [115], together with a pile-up correction as proposed by Pierson (1954) [145] to calculate motions in head waves. Keuning did not use the analogy to planing ships to calculate the calm water trim and sinkage with the same theory. Instead he used the results of a systematic series of experiments for regression analysis; this limits his predictions to the hull forms of the systematic series.

The formula used by Keuning for the vertical force, Equation 2.2, is quite similar to the one used by Beukelman although the terms with the damping coefficient are not used.

$$FZ_{\text{IMPACT}} = (m + A_{33})\,\dot{V}_N + V_N \frac{\partial A_{33}}{\partial t} - u\frac{\partial}{\partial x}\left(A_{33}V_N\right) \qquad (2.2)$$

In this formula he used the velocity component V_N normal to hull; the velocity component u is defined in the ship fixed system of axes, Figure 2.1.

A time domain strip theory method was developed at DTU by Petersen (1992) [144]. This program was further developed to include non-linear forces by Xia *et al.* (1998) [199] and Wang (2000) [189]. Calculations were made for the S-175 container ship and compared to experiments in head waves carried out by Watanabe (1989) [190] and O'Dea (1992) *et al.* [140]. This theory showed decreasing first order harmonic responses of motions and internal loads in comparison to linear theory for waves of very moderate steepness, $2\zeta_A/\lambda = 60$. The lower RAOs compared better to the experimental results. Calculations were also made for a container ship and compared to experiments in multiple wave directions as carried out by Tan (1992) [175] with comparable results. Again, mainly results of the first order harmonic component of motion and internal loads were compared.

Gu, Shen and Moan (2003) [66] derived a non-linear strip theory for vertical ship motions. The non-linear terms automatically include the momentum theory terms with the vertical added mass derivatives. The ships structure was modelled as a Timoshenko beam. The program was verified by results from model experiments with a ship having an extreme bow flare; the results agreed reasonably well. Results were also shown for the S-175 container ship and comparisons were made to other non-linear codes, the one developed by Xia (1997, 1998) [198, 199] and also the one developed by Wu and Moan (1996) [196]. The performance of all codes was quite similar and compared reasonably well to the experiments (10 - 30% difference in peak values between the different calculation methods and in between calculation and experiment is considered 'reasonably well').

2.3 Literature related to the pile-up factor

The pile-up effect is the effect that, during the impact of a body in a fluid, the fluid level close to the body rises. This effect is quantified by the pile-up factor $(1 + \psi)$, this is the ratio of the vertical distance of the lowest point of the body to the intersection point of fluid surface and body (z^*) to the vertical distance of the same lowest point of the body to the undisturbed surface of the fluid (z). This is illustrated in Figure 2.2, using the parameters in this figure, the pile-up factor is:

$$(1 + \psi) = \frac{z^*}{z} \qquad [-] \tag{2.3}$$
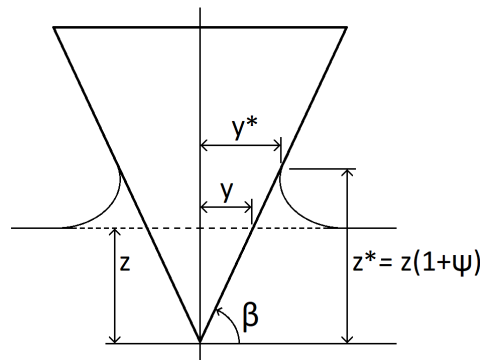
Figure 2.2: Definition of the pile up for an impacting body

Szebehely (1952) [173] studied the impact of a wedge along the same lines as Wagner. For the added mass he referred to Bisplinghoff and Doherty (1952) [14]. He acknowledged the importance of pile-up effects and found a pile-up factor of $\pi/2$, similar as Wagner, for small values of the deadrise angle β. For large values of β he derived:

$$(1 + \psi) = \frac{\pi}{2} \frac{\tan \beta}{\beta} K \tag{2.4}$$

with:

$$K = \frac{\Gamma\left(\frac{1}{2} + \frac{\beta}{\pi}\right)\Gamma\left(1 - \frac{\beta}{\pi}\right)\cos\beta}{\sqrt{\pi}} \qquad (2.5)$$

and $\Gamma(r)$ the incomplete gamma function.

Payne [143] used the flat-plate limit of Wagner and the effect of the finite deadrise angle of wedges from experiments by Pierson [145] and from calculations by Zhao and Faltinsen [205]. His analysis resulted in the approximation formula:

$$(1 + \psi) = \frac{\pi}{2} - \beta\left(1 - \frac{2}{\pi}\right) \qquad (2.6)$$

Fairlie-Clarke and Tveitnes (2008) [48] used a commercial CFD code to calculate impacts of wedges and to analyse the results in terms of added mass and pile-up parameters. Calculations were carried out for normal and zero-gravity conditions. It was concluded that the zero-gravity results for the pile-up factor were independent of the deadrise angle and very close to the Wagner factor of $\pi/2$. Interesting differences in the shape of the pile-up were found when gravity was included in the calculations, Figure 2.3. A jet is always produced in zero-gravity conditions, while in normal gravity conditions a wave is being radiated by the wedges having a higher deadrise angle.

β = 10deg. z/d=1.02   β = 15deg. z/d=1.12   β = 30deg. z/d=1.04   β = 45deg. z/d=1.0
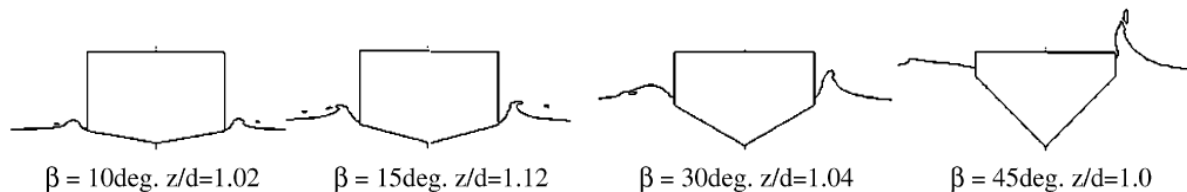
Figure 2.3: Results of CFD calculations for an impacting wedge having different deadrise angles. The left hand side of each figure shows a result in normal gravity conditions while the right hand side shows a zero-gravity result. Impact velocity is 0.5 m/s. Results by Fairlie-Clarke and Tveitnes (2008)

Tveitnes, Fairlie-Clark and Varyani (2008) [182] carried out experiments with wedges having a deadrise angle of 0, 5, 10, 15, 30 and 45 deg. They used a forcing system to ensure a constant velocity impact. The pile-up factor was analysed from high-speed video recordings of the experiments and results were compared against different theoretical values, Figure 2.4. Their results compared well to the results of the fully non-linear method by Zhao and Faltinsen (1993) [205] and the empirical formula of Payne (1994) [143]. The results of their CFD calculations were not presented in this plot, the predicted force during the impact correlated well to the result of the experiments.
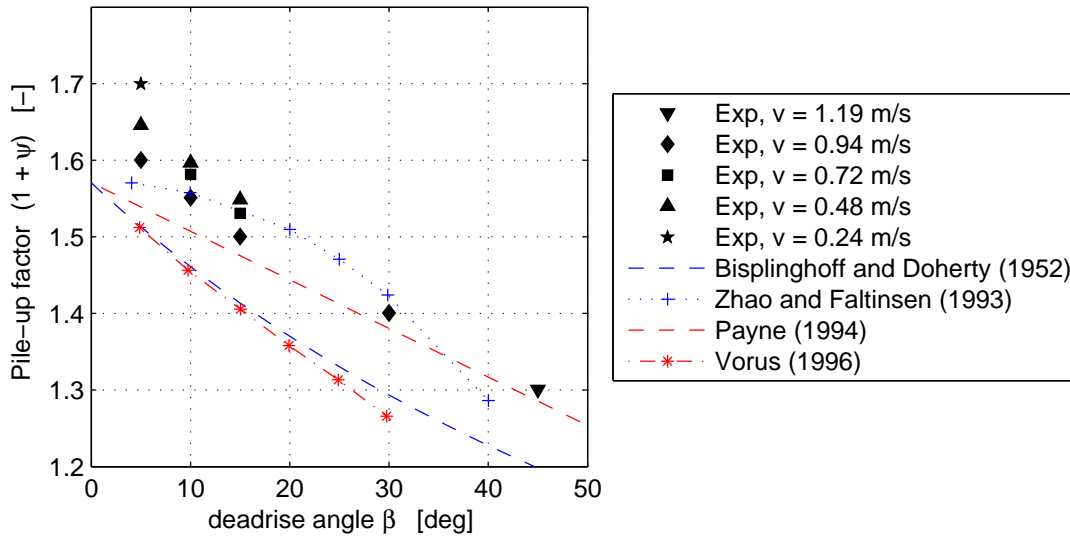
Figure 2.4: Results of the experiments by Tveitnes and Fairlie-Clarke compared to theoretical results from Bisplinghoff and Doherty [14], Zhao and Faltinsen [205], Payne [143] and Vorus [186].

2.4 Literature related to approximate methods to calculate slamming impacts

There are not many approximate methods published in the literature. The most well known methods are based on a 2D approach; the impact area is modelled by a series of 2D sections on which local pressures or the impact force are calculated by way of a drop test simulation. The forces on these sections are integrated over the third axis accounting for the appropriate shift in time. This approach was introduced by Kvålsvold *et al.* (1996) [105] in their analysis of the loads on the bow of a ferry. He used the approximate Boundary Element Method by Zhao and Faltinsen (1996) [207] for the simulation of the 2D drop test of the ship sections. The sections were tilted around the lateral axis as shown in Figure 2.5, reasoning that the plane of the section should be in line with the relative velocity. Kvålsvold *et al.* showed good agreement to experimental results.

A similar approach was used by Sames *et al.* (2001) [154]. Essentially these authors showed two methods along the same lines. The first method was identical to the one used by Kvålsvold: simulation of the 2D drop test with the approximate BEM and the use of tilted sections; the second method used a Volume of Fluid (VoF) method for the simulation of the 2D drop tests for vertical sections. The consequence of choosing vertical sections is, that forward speed is not directly included in the simulation of the drop test. The results showed quite some differences between these methods; one (the vertical sections VoF method) appeared to be a lower limit to the measured forces, the other (tilted sections - BEM) appeared to be an upper limit. Predictions were also made for bow quartering waves with the vertical sections VoF method; these calculations compared well to the experiments. These results are illustrated in Figure 2.6.
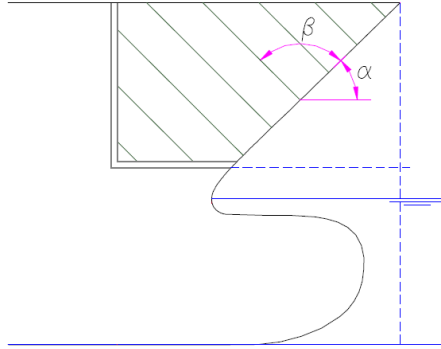
Figure 2.5: Sketch of tilted sections to calculate impulsive forces on a bow segment using a 2D method. The tilt angle relative to the stem line β can be chosen for each individual impact in the direction of the incoming flow, or it can be chosen at a fixed value like $\beta = \pi/2$ [rad].

Hermundstad and Moan worked on an identical method; they used vertical sections and the approximate BEM by Zhao and Faltinsen (1996) [207]. The quasi-static bow wave was included by using a steady linear potential flow method at different drafts. They published a series of papers starting with [71, 74]. They also chose to have vertical sections, so forward speed is not really incorporated other than adding a $U \cdot \theta$ term for the relative vertical velocity and by adding a contribution of the spatial static bow wave derivative to the relative velocity.

Gradually they improved the method by adding the effect of the roll velocity, adopting the BEM to be able to cope with bulbous bow ship sections in 2005 [72]. 3D effects were
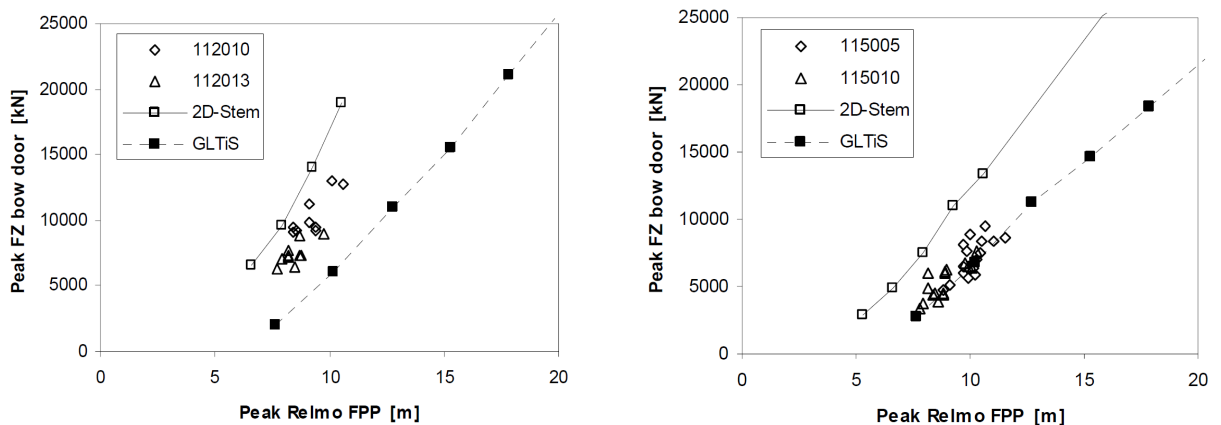
Figure 2.6: Peak loads on the bow door of a ferry sailing at 26 kt in head seas. Calculations using a 2D approximation method based on a BEM approach and tilted sections and using a 2D VoF approach and vertical sections. These results are compared to experiments in regular waves of different amplitude. Results for a wide bow (left) and a more narrow bow (right), Sames et al. [154]

added based on the paper of Scolan and Korobkin (2001) [162]. Their final result is shown in the 2009 paper [73]; rather then focussing on the overall force or whipping response, they compared the force on panels in the bow area of a ferry. The comparison of these local slamming forces to experimental results show the same order of magnitude, but individual correlation of impacts is poor; results are about equally accurate in head and bow quartering seas.

Tuitman worked on a similar method. He used the pressure calculated on the 2D sections for a pressure integration over the 3D segment of interest. In this way he achieved results that were almost independent of the choice of the tilt angle. He took great care in properly coupling the simulations of the drop tests of the sections to the structural model of the ship to determine the hydro-elastic response. The deformation modes were included in his model as generalized modes [179]. Details were published in several conference papers [123, 41]. The final result, including results of experiments with a model having very flat and shallow bow sections was published in his thesis [178].

2.5   Literature related to analytical methods to calculate slamming impacts

In general, analytical methods provide the exact solution for a simplified impact problem. As such, they are used as benchmark tools for approximate methods and also for Computational Fluid Dynamics (CFD) methods. One has to be aware, however, that the analytical solution has no problems in predicting an infinite pressure or an infinite pressure gradient; this will never be possible for a CFD solution with a grid of finite dimensions.

Analytical work on impact problems was first carried out by Wagner (1932) [187]. Potential theory was used to develop a solution for a wedge impacting on a flat water surface. The approximate solution for the free surface was improved upon by Dobrovol'skaya (1969) [44], who developed an exact method for impacting wedges, known as the similarity solution. Korobkin (2004) [102] also used Wagners analysis, he included higher order terms in the Bernoulli equation in order to improve the comparison to experiments. The method was extended to three-dimensional problems by Scolan and Korobkin [162] and Korobkin and Scolan [103]; a solution for axisymmetric bodies or bodies that resemble an axisymmetric body was found. Because the body boundary conditions were imposed on the plane of the free surface, the method can only be used for the initial impact of bodies with a small deadrise angle.

Cointe and Armand (1987) [33] studied the problem of an impacting circular cylinder. It was clearly shown that their analytical method was very good for the initial impact problem where the leading parameter $Vt \ll R$, in other words, the immersion must be very small compared with the width of the section.

Scolan (2004) [160] showed results of impact force calculations and of experiments. The calculated impact force shows the infinitely quick force build-up of the analytical

solution while the experimental force build-up is limited by the speed of sound in the fluid.

2.6 Computational Fluid Dynamics

Computational Fluid Dynamics (CFD) calculations, by which we mean volumetric methods rather than boundary element methods, have been applied to impact problems for some 25 years. Arai *et al.* (1994, 1995) [7, 8] were the first to apply this approach to slamming of ship sections; in those days this was a simulation of a drop test of a 2D section in calm water. He used an Euler solver and the Volume of Fluid (VoF) method to determine the free surface and the intersection with the body. This technique was also used by Germanischer Lloyd: Sames (1998) [155], Muzaferija *et al.* (1998) [136] and Sames *et al.* (2001) [154]; it was applied in a strip-theory manner to calculate the impact pressure on ships in waves. The basic ship motions were calculated using a classical linear 3D Boundary Element Method.

Work was first done to develop CFD codes that could predict ship motions in waves without considering steep waves and slamming. Problems were encountered with wave propagation into the computational domain, proper handling of the outgoing waves at the boundaries and, of course, the large grids required were limited by computer memory. CPU requirements were impressive; together with memory and storage limitations this was often a reason not to do grid refinement studies. Moctar *et al.* (2006) [129] presented results of CFD calculations for a large container vessel where both ship motions and impact pressures were calculated. Calculations were done for critical conditions that were identified by a ship motion program based on a BEM. He showed a good agreement for rigid body motions, internal loads and local pressure under the bow of the ship. Pressures from the CFD calculation were transferred to a Finite Element code for a whipping analysis. It is noted that the wave condition used for the CFD analysis was not a very steep one; it was a condition selected to produce a maximum vertical bending moment amidships: a head seas condition with a wave length in the order of the ship's length.

Results of calculations for the S-175 container ship were shown by Wilson *et al.* (2008) [195]. Their results showed non-linear force components but not real slamming events. Kapsenberg and Thornhill (2010) [89] showed results for a ferry; the ship was held captive in agreement with the model experiments. The calculated impact force on a bow element and local pressures agreed very well with the experimental results. On the other hand, they could not successfully calculate the impact force for the steepest waves used in the experiments, these waves were much shorter than the ship length.

More recently the particle method Smoothed Particle Hydrodynamics (SPH) has been applied to impact problems. The method is numerically very robust since it is meshless. Several overviews of the features of the method and the developments were given by Monaghan in 1988, 1992 and 2005, [131, 133, 132]. Since the method is based on compressibility of the fluid, it needs a very small time step for stable results. Persisting

problems are the interface between fluid and body, numerical damping which prohibits accurate wave propagation in large domains, and internal pressure oscillations which are apparent in local pressures. Despite this, good results have been obtained for the classical dam break problem, Molteni *et al.* (2007) [130], problems with 2-phase flows like a rising bubble in a fluid, Colagrossi and Landrini (2003) [35] and violent wave impacts, Marrone *et al.* (2010) [125].

All CFD methods are quite CPU intensive and need parallelization on a large number of processors to get reasonable performance, but SPH is worse than other methods in this respect. The solver is quite fast since no iterative solution method is used. Each particle only interacts with its close neighbours, so there are no large matrices to be inverted. However, the small time step that is required more than compensates this advantage. An important performance parameter is the choice of the required degree of compressibility: the speed of sound in the fluid. It is advised to choose it a factor 10 above the highest velocity that is expected in the flow so that the time step can be as large as possible.

The use of a particular suite of CFD programs for a very broad range of hydrodynamic problems was reviewed by Stern *et al.* (2015) [168]. Slamming and planing hulls are briefly mentioned, some results are shown that correspond well to experimental data and measurements on a small craft.

Sasson *et al.* (2016) [156] compared calculations using a commercial RANS code and a public domain SPH code to results from experiments for a free drop test of a 25 deg wedge. They found both results quite satisfying, but the RANS result was more accurate for the initial stage of the impact.

Drop tests were carried out in the Joint Industry Project WILS (Wave-Induced Loads on Ships) on a 30 deg wedge section and on a ship section having a bulbous lower part, Kim *et al.* (2014) [96]. Different partners in this project carried out calculations using different (mostly CFD) methods. Southall *et al.* (2014) [166] compared results of an open source CFD code to the results of the wedge. Good results were obtained after smoothening the input motion. A compressible fluid solver was used to improve the predictions for low deadrise impacts resulting from a drop test with a tilted section. They also used the open source code and a commercial CFD code to calculate the pressure on the ship section Southall *et al.* (2015) [165], again obtaining quite good results.

Monroy *et al.* (2016) [134] compared results of a 2D Generalized Wagner Model (GWM), an open source CFD code and an SPH code to the drop test results for the wedge and ship section. The results compared well to the result of the wedge, but the ship section created problems for the computational methods due to its convex shape just above the bulbous part. The input for the GWM needs to be adapted by changing the geometry such that there is no convex part. For a high speed impact this is comparable to the trajectory of a water particle that separates from the bulbous part of the section. The comparison to measured pressures and the force on a panel is somewhat erratic for the GWM and the CFD; results for the SPH code were not presented. Ren *et al.* (2016) [152]

used a particle method originally proposed by Koshizuka and Oka (1996) [104]. They showed very good agreement of calculated pressures for the wedge, both the symmetrical case and the tilted section and quite acceptable results for the ship section. Wen and Qiu (2016) [192] used a Constrained Interpolation Profile (CIP) method, the basics of which were developed by Takewaki *et al.* (1985) [174]. They obtained very good results for the wedge (symmetrical and tilted) and less perfect results for the ship section. The cells used in the verification study are very small and the time step was extremely low. The CPU effort required was not mentioned.

2.7   Literature related to experimental techniques

This section reviews different techniques to measure impact loads on models of ships at speed rather then techniques for drop tests. The more useful experiments use segmented models that are instrumented such that the load on an isolated part can be determined. Having only pressure sensors on the model is considered less useful; it has to be assumed that the pressure distribution during an impact is not a smooth surface over the hull. Choices that can be made are related to flexible or rigid models and in case the first option is chosen, if the flexibility should be in the hull segments or just in a flexible connection of the rigid hull segments.

Sawada *et al.* (1987) [157] built models of various ships using a flexible structure from composites and alternatively a model consisting of rigid segments connected by a flexible beam. Both methods seem to work satisfactory. Details are unknown to this author since the article is in Japanese, only the summary is in English.

Watanabe *et al.* (1989) [190] studied wave loads on a model of the S-175 container ship and on a variant of this design having more bow flare. He used a flexible model made of PU foam and resin. No details are given on either sensors to measure the strains, resonance frequencies of the model or on damping ratio's. Results are presented on the differences between the peaks in hogging and sagging in a regular head wave.

Hay *et al.* (1994) [69] reported on experiments in a wave tank (DTMB) using a flexible PVC model of a frigate. The main structural members of the ship were present in the model. Normal electrical strain gauges were used to measure strains at seven longitudinal positions. The distribution of the first order vertical bending moment over the length showed a (1-cos) curve, the distribution of the whipping component is more triangular with the maximum amidships. Short term statistics were presented of the whipping component showing a β value (of the Weibull distribution) close to 1.0 in head and bow quartering seas for as well the vertical as the horizontal bending moment. This distribution can therefore be approximated by an exponential distribution. RAOs of ship motions are surprisingly linear for sea state 5, 6 and 7.

Hermundstad (1995) [70] used a model of a catamaran consisting of 2*3 segments. The segments are connected by a frame constructed of rigid beams and flexible joints. The

joints connecting the segments (longitudinal and transverse) have elastic hinges (slender steel beams) and force/moment transducers. The hulls are made from sandwich FRP and are intended as rigid elements. The wet deck consists of three separate panels, connected with pins to the hulls on both sides in order to minimize the effect on measurements. Tests were carried out in irregular seas and in focused waves; wave directions were head, beam and quartering directions at high speed. Hermundstad found structural damping ratios in the range of 2 - 3% for the typical catamaran deformation modes longitudinal bending, prying and wetdeck torsion.

McTaggart *et al.* (1997) [127] built a model of a frigate consisting of six fibreglass segments held together by a flexible beam. The spacing between the hull segments was 10 mm to allow relative motions of the segments. The beam was constructed of Lexan, a polycarbonate plastic, with carbon/epoxy stiffeners in the corners. The carbon/epoxy elements determine the stiffness of the beam. The width of these stiffeners and the horizontal separation varied over the length to properly model the structural properties at each cut. The thickness of the vertical and horizontal members of the web vary to properly represent the shear stiffness. The beam was connected to the hull segments through aluminum mounting platforms on a hardwood surface. The hardwood was machined to have a perfect horizontal plane to mount the beam on. Strain on the beam was measured using strain gauges. McTaggart achieved to model the resonance frequencies of the first 3 modes for vertical bending; there was no full scale data to compare horizontal bending. The damping ratio for the vertical plane deformation varied from 2.3 - 3.1%, there was hardly any difference in damping between the dry and the wet tests.

Kapsenberg *et al.* (1999) [86] built a model of a fast ferry consisting of two segments. The segments were connected with a spring with adjustable stiffness. Loads were measured in a section just next to the spring. The construction allowed a reduction of the resonance frequency by a factor two. Reducing the stiffness showed a very strong increase of higher harmonics in the vertical bending moment.

Dessi (2003, 2006) [43, 42] and Ciappi (2003) [28] carried out model tests on a (very) fast ferry. The model consisted of 6 segments, connected with an elastic beam. The beam consisted of 20 elements of aluminum extrusions with varying dimensions to properly model the vertical mode shapes. The hull segments were made from fiberglass and are considered rigid. The choice of the number of segments was based on weight considerations for the model rather than on an ambition to model a certain number of flexural modes.

Lavroff *et al.* (2007) [110] carried out model tests on a segmented catamaran. The hulls were segmented in 3 parts lengthwise, while the bow centrepiece (it was a model of an Incat type catamaran) formed the 7th segment. The segments are constructed from carbon fiber and foam sandwich and are considered rigid. Aluminium square backbone beams were glued in the model, special exchangeable hinges with torsion springs were developed to couple the segments. The lay-out of the structure was essentially similar as the one used by Hermundstad (1995) [70]. Damping of the dry 2-node mode was about 0.6%, of the wet mode abt. 1% - both results independent of the stiffness of the springs, so the resonance frequency. The full scale catamaran was measured to have a

3% damping of the 2-node vibration as reported by Thomas *et al.* (2003) [177]). Closing or not the gaps between the segments with latex seals affects the resonance frequency some 10% (lower value with latex seals); the damping is also 10% different, an open gap showed lower damping. The resonance frequency appeared to be speed independent, the damping slowly increased from 2% at zero speed to 3% at Fn = 0.6.

Drummen (2008) [45] carried out model tests on a segmented model of a container ship. The model consisted of 4 segments. The backbone was not a flexible beam, but consisted of a rigid structure and of flexible parts in between the segments. These flexural parts consisted of one part with the strain gauges and a second part with an adjustable spring. The system was designed to measure flexural modes in the vertical plane only; the experiments were limited to head waves.

Iijima *et al.* (2009) [81] balances pro's and con's of a fully elastic model versus a segmented model. He concludes that a fully elastic model, made from some plastic, suffers from too much internal damping for a proper evaluation of the vibration modes. Instead he opts for a segmented model with a flexural beam consisting of a rectangular aluminium extrusion with 5, relatively small, cut-outs in the upper face. He ends up with a model with a very long parallel mid body and ship-like fore and aft ends; in total 15 segments. In a dry tests he measured damping ratio's ranging from 0.1% for the 1st Vertical Bending VB mode to 0.5% for the 2nd VB mode. Damping in the 1st and 2nd Torsion T mode was both 0.4%. The wet tests showed a twice as high damping for the VB and Horizontal Bending HB modes, but similar damping for the T modes was found as for the dry tests.

Malenica *et al.* (2003) [121] presented the results of motions of a very flexible barge consisting of 10 elements. Because of the extremely flexible model, the gaps between the elements were large and not closed by any seal. The experiments were carried out at zero speed. No analysis of the pro's and con's of this set-up was presented.

The mentioned WILS project focussed on the loads on large size container ships. The model of the ship consisted of six rigid segments that were connected to a flexible steel beam. Two beams were used, one H-section and a second U-section; the latter to represent the low shear centre of a real container ship. Results of the experiments were presented by Hong *et al.* (2014) [76] and Kim *et al.* (2014) [95]; comparisons to calculations were presented by Bigot *et al.* (2011) [13].

In parallel with the WILS project, the TULCS (Tools for Ultra Large Container Ships) project was carried out. In the course of this project new experiments were carried out with a variation on the very flexible barge, Malenica *et al.* (2003) [121], but now with an external connection rod well below the keel to represent the low shear centre of a container ship. A second series of experiments was carried out on a model of a large container ship. The model consisted of six rigid segments connected via a flexible aluminium beam. The beam was box shaped and had various cut-outs to properly model the first vertical, horizontal and torsional modes. Stresses were measured on the beam to arrive at sectional loads. Care was taken how to connect the beam to the segments in order not to change the resonance frequencies. The model was described by Maron and

Kapsenberg (2014) [124].

2.8   Conclusions from the review

Present approximate methods for ship slamming are using 2D simulations of drop tests. Such methods have been and are being developed by MARINTEK [73] and by Germanischer Lloyd, Bureau Veritas [108] and Lloyds Register [111]. MARINTEK uses the approximate method by Zhao and Faltinsen while BV uses a GWM which is quite similar to the approximate method. LR uses the open source code OpenFOAM for the 2D calculations, thus avoiding the need to adapt concave sections. A major problem is the orientation of the sections for the 2D calculation. For head seas tilting the sections can be motivated since then the plane of the section is in the direction of the incoming flow. If this reasoning is strictly used, the sections should rotate during the impact until they are horizontal at maximum immersion. Having vertical sections has the important disadvantage that forward speed is not included other than the component in the ship-fixed reference frame when there is a non-zero pitch angle. It has been suggested to rotate the sections around a vertical axis for calculations in oblique waves. This means that simulations of drop tests are needed with sections that are rotated over a large angle to be in line with the relative velocity. This approach is also different to the method of using tilted sections for the simulation of impact forces in head seas. Taking this approach would result in sections having a beam of the length of the ship for simulations in beam seas. Another problem can develop when simulating impacts in quartering waves. If there is a significant roll velocity, the impact velocity on one side of the section can be negative indicating water exit. Such a condition gives large problems in most methods.

Model experiments with segmented models to measure the internal loads have been done for decades. Usually the interest was in rigid body loads so that comparisons to computer codes could be made. More recently interest changed and researchers now want to include the dynamic response of the ships structure. The approach to cut a model in segments is also spread to the world of arts as demonstrated in Figure 2.7.

Figure 2.7: Xavier Mascaró, 'Departure' (1980). Sculpture in front of the Prado Museum, Madrid.

There are two approaches to construct a flexible model:

1. Build a model of some flexible material so that directly the flexural modes are present in the model.

2. Build a segmented model and connect the segments or via a flexible beam or via elastic hinges.

The first approach is the more complicated one. It is impossible to build a model exactly as the ship with all structural members scaled to the model and constructed from a material with a scaled Young's modulus. A scaled Young's modulus normally requires the use of some plastic material and to ensure through FE analysis of this structure that the main deformation modes are properly modelled. This approach results in a model which must be very carefully designed and constructed, no doubt at high cost. Examples of this are models built in Japan, as reported by Watanabe *et al.* (1989) [190] and in the US, reported by Hay *et al.* (1994) [69].

Apart from the cost and effort involved in designing and constructing such models, it appears to be a problem to accurately measure the loads in such a model. The experience of the author to measure loads in a composite structure is, that conventional electrical strain gauges often cause problems. The material is locally heated due to the electrical current running through the strain gauge. Due to low heat conductivity of composites, there is a strong temperature gradient and hence local stresses. A solution to this might be in using fibre-optics to measure the loads. This is nowadays of-the-shelf technology although not very cheap and not yet standard practice at the experimental facilities.

A relatively recent technique is Digital Image Correlation (DIC), a method were contrasting spots are applied to the surface of the object and the change in distance between the spots in the loaded versus the unloaded condition is a measure for the strain. This technique has been used by van de Bunt and Lafeber [26] to measure the deformation of a panel used for a LNG containment system due to wave impact loads. Noted is, that problems in measuring strain in the composite models are not mentioned in the papers. A real problem is the high structural damping of composites. This will result in different answers for a fatigue analysis when compared to a real ship; also it will affect the reponse of the structure on repeated slams as shown by Kapsenberg *et al.* (2002) [90].

Seven out of nine researchers covered in this review opted for an approach using a segmented model and some flexible connection in between the different segments. It is realized that only the lowest flexural modes are modelled and they are represented in a schematic way depending on the number of segments. Unfortunately there is no study known that looks into the effect of the finite number of segments on the springing and whipping response of the model and on the measured loads.

The relative ease of design and the control over the deformation modes is the main advantage of the segmented model approach. Usually there is a flexible beam out of some metal which allows an easy and reliable way of measuring the stresses. One example is

known, McTaggart (1997) [127], of a researcher building a flexible beam out of composites. There are two 'schools' of constructing the beam. MARINTEK uses rigid beams in the segments and an elastic hinge at the connection of the segments; occasionally this system has also been used at MARIN. McTaggart, Dessi, Ijima and Maron use a beam that continuously flexes over the full length. A point of concern is the connection of the beam to the segments; this connection must not change the flexural properties of the beam other than the increase in mass and inertia. At MARIN a method has been adopted to connect the segments to the beam via two very thin bulkheads. The idea is, that the bulkheads only transfer forces to the beam and no moments. This has proven to work very well and it resulted in models with a dynamic behaviour close to the predictions made in the design phase.

A point of concern is the damping of the model, this is especially important for repeated slamming and it is quite critical for springing studies. Controlling the damping of a model is quite complicated but it is even more difficult to obtain reliable data from full scale. Betts *et al.* (1977) [10] made a review of damping values of different ships, in which they suggest that stress concentrations, welding details and small cracks are major sources of damping. This review is now quite old, a new state-of-the-art would be welcomed. Thomas *et al.* (2008) [176] measured stresses on two different large size aluminium wave piercing catamarans. They measured the damping from the decay of the stress after an impact when the vessel was at speed. The damping was also measured at zero speed by a dropping the anchor. The results were quite scattered: on average the damping from the exciter test was about half the value (2.3% of critical damping) of the one resulting from the impact at speed. Koning and Schiere (2014) [101] found a much higher damping for horizontal plane and torsion bending than for vertical plane bending on a container ship. An explanation for this could be friction of adjacent stacks of containers. Anyway, if the objective of the experiments is to generate data for validation of calculation methods, a low damping is not strictly necessary. To compare results, it is necessary to know the amount of damping, it is not required that is comparable to a full scale value. In fact, a low damping creates problems since it will take a very long time before transient effects in the vibrations are gone, it is quite possible that this takes more time than a single run in the wave basin!

Chapter 3

Computational Methods used

The method that is presented in this thesis is a component in a non-linear seakeeping calculation. It needs to be integrated in a time-domain program because it includes non-linear effects more than second and third order components. The time-domain program that is used for this purpose has been developed by the CRS consortium[1]. The program makes use of a linear frequency domain pre-processor; initially a program that also was developed by the CRS, later on also a program with an improved description of forward speed in the governing equations. Since these programs play a role in the validation part of this thesis and since the CRS hardly ever publishes results of their developments, they are briefly described here.

Several other programs have also been used in the development of the slamming program, notably a 2D non-linear Boundary Element Method (2D-BEM), a non-linear panel program for steady flows (RAPID) and a 3D CFD method (COMFLOW). The theoretical background of these programs is briefly presented in this chapter.

3.1 2D Boundary Element Method

The theory for the program 2D-BEM was developed by Zhao, Faltinsen and Aarsnes, [207]. The program solves the problem of a 2D body entering into a fluid through a Boundary Element Method (BEM). The program uses the exact body boundary conditions, but the dynamic free surface condition, $\Phi = 0$, is approximated by imposing it on a horizontal surface at the height of the intersection of the free surface and the body; this approach is referred to as the Generalized Wagner Model (GWM). The solution method ignores gravity effects. This so-called simplified solution is compared by Faltinsen [50] to the fully non-linear solution and appears to give very comparable results, Figure 3.1. Also for ship-like sections the results appear to be quite good as will be shown in Section 5.12.

---

[1]The Co-operative Research Ships community consists of a group of ship yards, ship owners, classification societies, navies and research institutes that together carry out research on ships. The focus areas are hydrodynamics, hydro-structure coupling and performance predictions. The reports of the community are restricted to its members.
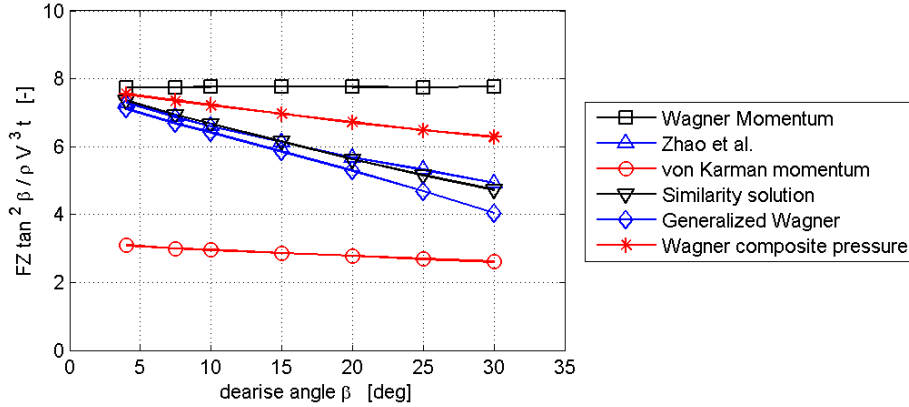
Figure 3.1: Impact force coefficients for wedges with varying deadrise angle according to different theories, Faltinsen (2002) [50]. The approximate solution 2D-BEM is indicated as "Zhao et al."
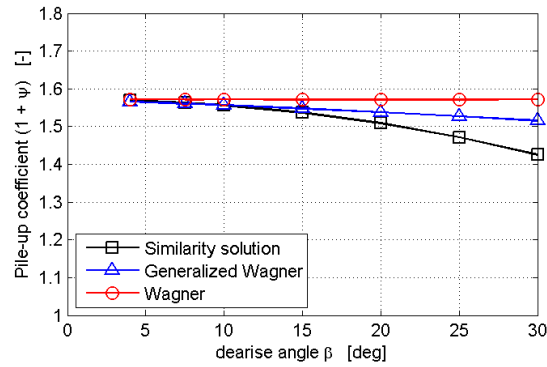
Figure 3.2: Pile-up factor according to Wagner [188], the similarity solution from Dobrovol'skaya [44] and the Generalized Wagner solution. Figure reproduced from Faltinsen (2002) [50].

A recent development in this field has been published by de Lauzon *et al.* [109]. Their method is based on the same principles, but it uses a conformal mapping approach to handle the difference in pile-up for both faces of an asymmetric wedge. They also used an analytical method to solve the singularity at the intersection of the body and the fluid surface saving many panels in this area making the program more efficient and robust.

The 2D-BEM program can be used either in the von Kármán or the Wagner mode; in the first case the free surface remains undisturbed, while in the second case the free surface deforms due to the pile-up, the effect of the displaced water and the high pressure at the interface of the body and the free surface. The pile-up effect has large consequences: it increases the velocity of the intersection point of fluid and body and hence the wetted part of the body. Considering the magnitude of this effect, it implies that the impulsive force using the Wagner method is more than a factor 2 higher than the force estimated using the von Kármán approximation. These different approximation methods have been used in Subsection 5.5.3 to derive a new formula for the pile-up factor.

Flow separation is not included in the approximate method, so one has to be careful when considering sections with a convex lower half. A practical solution for such sections is to adapt the shape of the section to a vertical line in the convex region. Such an approach has been been shown by de Lauzon [108].

3.2   2D Diffraction

The program SHIPMO is a strip theory program that solves the problem of ship motions in waves. It contains a linear 2D BEM to solve the radiation and diffraction problem of the 2D sections. Due to the fact that it is a 2D approach, it is essentially a zero speed method. This program has only been used in some basic studies in Subsection 5.7.

3.3   3D Diffraction using zero speed Green functions

A BEM to solve the problem of ship motions in waves has been developed by the CRS. This program, PRECAL, is a linear potential flow method that solves the 3D diffraction/radiation problem. The solution method is based on the use of a Green function that represents the radiated waves on the surface. As a consequence the boundary conditions need only to be imposed on the body, so a panelization of the body is required. The Green function is valid for zero speed, a simplified method of adding an uniform flow to the velocity potential on the body has been included. This method is just an approximation for non-zero speeds; details of the physics, like local relative motions along the hull, might be quite different in comparison to reality. Especially this aspect makes the program less useful for the calculation of impulsive forces, although the relative motions at the bow are correctly predicted since they are dominated by the undisturbed incoming wave and the ship motions.

The program uses generalized modes as described by Farstad [51] and by Tuitman and Aanhold [179]. Generalized modes describe the displacement of each panel centroid for each mode of motion. This approach allows a uniform treatment of rigid and flexible body modes; it is also possible to treat multi-body problems with this method as shown by Malenica *et al.* [122].

3.4   3D Diffraction with exact forward speed

The program FATIMA has been developed by Bunnik [23]. The program includes forward speed in a different way than PRECAL; the basis flow is calculated using the steady non-linear potential flow program RAPID. RAPID also calculates the deformation of the free surface due the forward speed of the ship in an iterative manner. This solution is used in FATIMA, not just the steady flow potential on the hull, but the method also uses the actual free surface to impose the linear free surface boundary conditions. Since the free surface deformation is not an analytical function, the boundary conditions need to be

imposed on a discretization of the surface. The additional number of panels required on the free surface makes the program more CPU intensive than PRECAL. The results in the sense of calculated motions and added resistance appear to be quite accurate for ships at speed as has been demonstrated in a benchmark study [24]. The program uses generalized modes similar as PRECAL.

3.5   Non-linear time domain program

The CRS program PRETTI has been used as basis for the time domain program that calculates the slamming excitation and the whipping response of the vessel. PRETTI is the weakly non-linear extension of PRECAL. The program calculates the hydrostatic forces and the forces due to the undisturbed incoming wave directly in the time domain, thus the actual geometry up to the instantaneous intersection of the hull and the water surface is taken into account.

The hydrodynamic forces are essentially just the forces calculated by the frequency domain program transferred to the time domain and made dimensional by using the actual incoming wave amplitudes (for the diffraction forces) and actual motion amplitudes (for the radiation forces). The incoming wave is usually defined by its frequency components, so the diffraction forces can be pre-calculated since speed and heading are considered constant. This is not the case for the radiation forces since the motions are unknown a-priori. Therefore Impulse Response Function (IRFs) as introduced in hydrodynamics by Cummins [36] are used. The theoretical background of this method is called Linear Time-Invariant system theory. This theory considers the output of a system as the integral of the response of the system on a series of Dirac delta functions that represent the input. This integral is called the Impulse Response Function (IRF) and is calculated by multiplying the complex motion response in the frequency domain (RAO) with the Dirac delta function. These IRFs are pre-calculated and used in the time domain as an integral over a finite time span using the history of the motions. The proper time span for this integral can be verified by re-calculating the frequency domain input from the IRF and comparing this to the original input. Usually an integration over a period of 30 s is sufficient for full-scale seakeeping problems.

3.6   Non-linear stationary flow

The program RAPID has been developed by Raven, [149]. The program solves the stationary potential flow problem of a ship sailing at speed in calm water. The Boundary Value Problem is solved using a BEM approach, the type of singularity used to force a Neumann condition on the hull also requires a panelization on the free surface. By using an iterative approach, the free surface boundary conditions are imposed on the actual distorted free surface. The pressure on the hull is integrated and balanced against the gravitational force resulting in a speed dependent trim and sinkage of the vessel.

The program has proven to give accurate results for the bow wave system, but especially at the stern there are effects of the boundary layer on the wave system; the potential flow method exaggerates the height of the stern wave, as shown by Raven [149] and Starke [167].

The wave elevation in the forebody is needed to calculate bow flare slamming; in general these results are accurate. Problems occur for blunt bows where the bow wave can be expected to break. This breaking phenomenon is not included in RAPID, so also the associated energy dissipation is not included. Despite these limitations, the program has also shown to give reasonable results for tanker-like bow forms, as shown in Raven *et al.* [151].

3.7 Non-linear instationary flow

Some basic studies on oscillating wedges were carried out using the program COMFLOW. This program has been developed at University of Groningen by Veldman and several PhD students. The work of Loots [116], Fekken [52] and Kleefsman [98] is especially relevant for this study. The program COMFLOW uses the Volume of Fluid method (VoF) method as introduced by Hirt and Nichols [75]. This method solves hydrodynamic problems by considering global fluid parameters in relatively large size elements. The implementation of COMFLOW is based on a Cartesian grid. This approach makes the code very efficient, but solid boundaries crossing the cells at some angle posed problems for quite some time. A problem of the VoF method is, that the free surface is not exactly known. Elements that contain the free surface have a volume fraction in between 0 and 1; the free surface is reconstructed from these elements. An advantage of this approach is, that re-entry of blobs of fluid back into the main fluid domain pose no problems. This makes the method very attractive for violent fluid dynamics.

The method has been used for sloshing problems in a micro-gravity environment by Gerrits *et al.* [54, 55] and in normal gravity conditions for an Anti-Roll Tank by van Daalen *et al.* [37]. Wave impacts were investigated by Veldman *et al.* [184]. Results of an impact on an object on deck of a Floating Production Storage and Offloading FPSO due to green water were shown by Kleefsman *et al.* [99, 98]. 2D simulations of drop tests were carried out by Gourmel [57], Luppes *et al.* [119], Wemmenhove *et al.* [191], van der Plas and Veldman [147]. In all cases a good correlation between predictions and experiments were obtained; this shows the versatility of the program for this type of problems.

Chapter 4

Model experiments

4.1 Introduction

The model experiments started with a very ambitious test campaign using a segmented model for which the segments were connected by a flexible beam. The model was free running and the loads on a bow segment were measured. Although this campaign was quite successful, it appeared to have too many degrees of freedom for validation purposes. In other words, the slamming phenomenon was too complicated to solve everything in one go. Therefore it was accepted to go several steps backwards and to design a much more basic set of experiments. The 'first phase' tests were done with a rigid model, rigidly connected to the carriage. The forces on the bow segment were still the main focus for slamming; tests were done with a captive model and also with a model in a forced (pitch) motion using an oscillator mechanism. Much attention was paid to measuring the shape of the wave just before the impact by a specially designed array of wave probes. The results of these tests compared quite well to the version of the slamming model at that time. Considering this, it was decided that it would be very valuable to extend the measurements over a larger part of the hull. The hull form used had a relatively large deadrise angle at the level of the waterline in the range St 15 - St 18, therefore it was expected that important slamming forces would also be generated by this part of the hull. In quartering waves it was expected that the main forces would be in this forward area of the hull and it was realized that quartering conditions might very well be the more demanding ones.

4.2 Hull form and main dimensions

Essentially only one hull form has been used for the experiments carried out in the course of this investigation. The hull form is that of a ferry that was especially designed for the EU-project Dextremel by the Spanish shipyard IZAR and published by Sames *et al.* [154]. It was a contemporary hull form at that time (2001), but it was not actually built. This hull form is very convenient for this type of experiments because of the sections in

the bow are V-shaped at the height of the design waterline, Figure 4.1. This shape allows a variation of the flare angle in the bow area by a re-design of the upper hull without changing the part of the hull below the design water line. The actual hull form has been re-designed to remove the bulbous bow; this change was made to reduce the complexity of the impact problem. The experience from the referenced project was, that the bulbous bow disturbs the flow enormously by creating a cavity upon re-entry. This cavity collapses as the wave hits the upper part of the bow thereby creating ill-defined inflow conditions for the impact. The re-designed hull, without the bulbous bow, was considered to produce better data for validation of impact calculation methods. The original hull form and the re-designed one are shown in Figure 4.1.
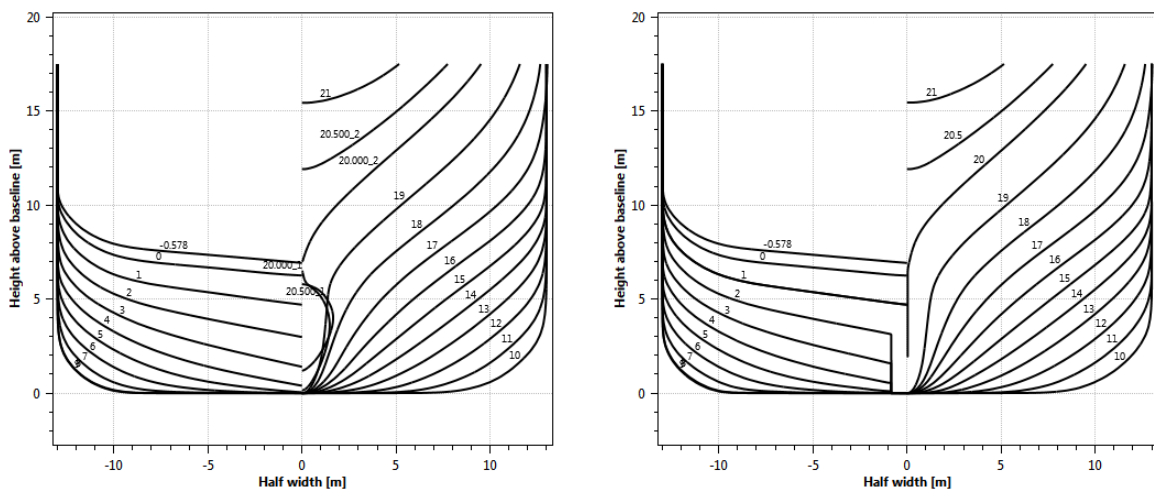
Figure 4.1: Body plan of the ferry as designed (left) and the hull form with the removed bulbous bow that has been used for the first series of experiments (right).
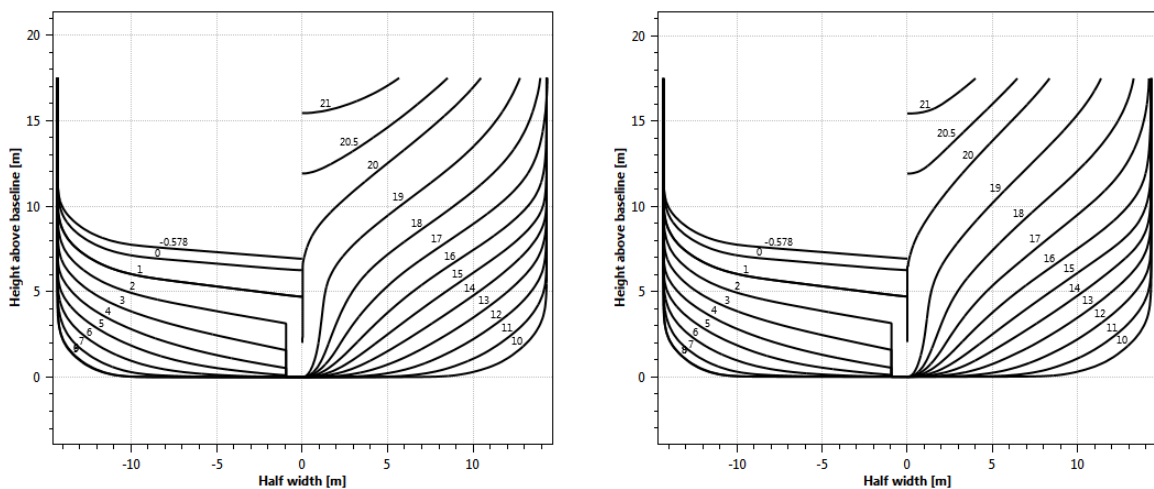
Figure 4.2: Body plan of the hull forms used for the second series of experiments. Hull forms with all lateral dimensions increased by 10% (left) and the hull form with the reduced bow flare (right).

Table 4.1: Main dimensions of the ferry model, original beam, no bulbous bow

Name	Abbr.	Value	Units
Length over all	L_{OA}	189.51	$[m]$
Length between perpendiculars	L_{PP}	173.00	$[m]$
Beam	B	26.00	$[m]$
Draft	T	6.30	$[m]$
Depth	D	17.50	$[m]$
Displaced volume	∇	15520	$[m^3]$
Displacement	Δ	15908	$[ton]$
Height metacentre above keel	KM	14.295	$[m]$
Height Centre of Gravity	KG	12.295	$[m]$
Metacentric height	GM	2.00	$[m]$
Long. position Centre of Gravity	LcG	78.289	$[m]$

Table 4.2: Main dimensions of the widened ferry model, no bulbous bow

Name	Abbr.	Value	Units
Length over all	L_{OA}	189.51	$[m]$
Length between perpendiculars	L_{PP}	173.00	$[m]$
Beam	B	28.60	$[m]$
Draft	T	6.30	$[m]$
Displaced volume	∇	17070	$[m^3]$
Displacement	Δ	17496	$[ton]$
Height metacentre above keel	KM	16.537	$[m]$
Height Centre of Gravity	KG	12.087	$[m]$
Metacentric height	GM	4.45	$[m]$
Long. position Centre of Gravity	LcG	78.308	$[m]$
Roll gyradius	k_{XX}	12.046	$[m]$
Pitch gyradius	k_{YY}	61.386	$[m]$
Yaw gyradius	k_{ZZ}	61.265	$[m]$

The re-designed hull form has been used in the first series of experiments. A variation of the shape was deemed necessary for the second series of experiments, it was decided to increase all lateral dimensions by 10% thus decreasing the flare angle in the bow. A variation of this hull form was made by increasing the flare angle in the upper part of the bow. These two hull forms are shown in Figure 4.2.

The main dimensions of the models used are given in Table 4.1 and in Table 4.2.

4.3   First series of experiments

The first series of model experiments were carried out to measure loads on the bow door area only. The experiments were designed with the accident with the ferry *Estonia* in mind, therefore the focus was on the bow door loads.
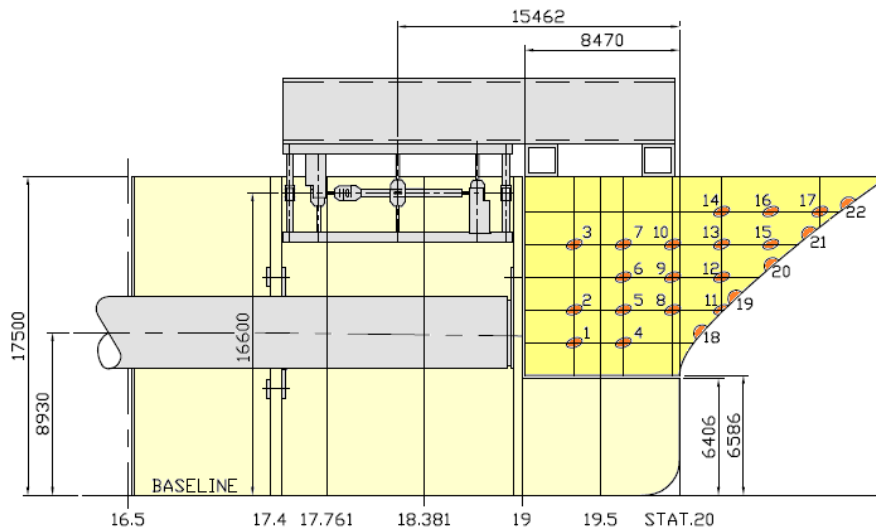
Figure 4.3: Bow of the ferry used for the first series of experiments. The measurement segment is indicated in bright yellow, the pressure sensors in orange. The lower end of the segment is just above the calm water line.

A model was built from wood at scale 36 with a length $L_{PP} = 4.8\ m$. The bow door was constructed as a separate segment connected to the main hull through a large size six-component force balance resulting in a relatively stiff connection between bow segment and hull. The set-up is illustrated in Figure 4.3, a picture of the bow piece of the model is shown in Figure 4.4 and in Figure 4.5.

4.3.1 Instrumentation

Six component strain gauge system

A six component strain gauge system consists of two frames that are connected by three one-axis strain gauges in a first direction, two in a second direction and one strain gauge in the third direction. This set-up allows a selection of different capacity strain gauges for different directions and an optimization of the orientation of the frame relative to the primary load. The linear stiffness of the assembled strain gauge system is determined by the deformation of the individual strain gauges at the maximum design load. The rotational stiffness is also determined by the relative distance between the strain gauges; this allows a control over the stiffness of the connection between the primary object and the object to measure the loads on.

Pressures

Local pressures were measured using 23 pressure sensors in the bow segment; the number of pressure sensors was limited by the available space on the inside of the segment.

Accelerometers

Accelerometers were fitted in the segment to be able to correct the measured forces for

Figure 4.4: Force balance to measure the forces on the bow segment. The force is transferred from the bow segment to the 6-component frame through the large size aluminium beams fitted in longitudinal direction. The 6-component frame is fitted underneath these beams on the left hand side. The force sensors are protected during handling by vertical plates - these are still fitted in the picture.
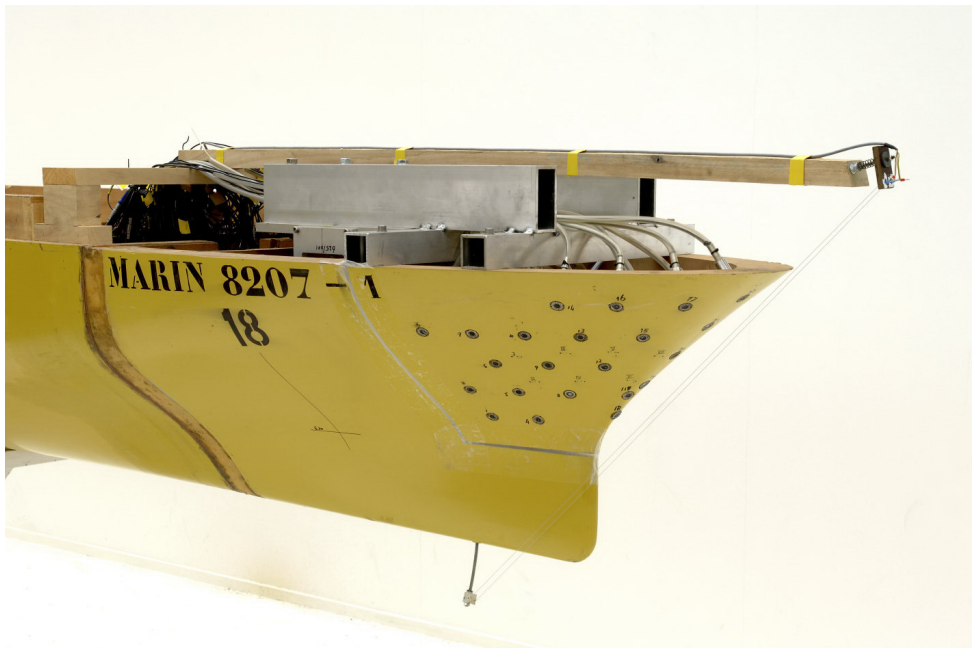
Figure 4.5: View on the bow of the model used for the first series of experiments. The picture shows the bow segment with pressure gauges and the wire sensor to measure the relative motion on the CL.

Figure 4.6: The ferry model in the wave basin for the first series of experiments. The structure on the right is a part of the system to measure the wave profile by an array of wave sensors.

inertia effects.

Relative motions measurement

Measuring the relative motions at some location during impact conditions is of paramount importance when results of experiments are to be used for validation. The relative velocity derived from this measurement is a primary parameter to calculate the impact pressure and force. There are different techniques available to measure the relative motions:

- Two conductive inlays in the hull,

- Two conductive wires at some distance from the hull,

- A vertical row of pressure sensors flush with the hull.

The first technique is in fact never recommended. Models of slender vessels at speed have, even in calm water, a thin sheet of water over to the hull in the bow region. This sheet of water has no practical consequences for the loads; the pressure inside is atmospheric and at full scale it is broken up in droplets due to the much higher Weber number [1] and hull-surface irregularities. The thin sheet wets the inlays and thus corrupts the measurement. The jet along the hull developed during the impact has an identical effect on the measurement; also the pressure in the jet is atmospheric, so it is irrelevant for the loads.

The second technique is useful for non-impact conditions because then there is an unique interface of water and air. The technique can be applied by using rods or pre-tensioned wires; the latter is preferred because of the smaller diameter and hence the

---

[1]The Weber number describes the relative magnitude of the surface tension and inertia forces. For a model at scale 10 the Weber number is a factor 100 lower than for the full scale ship.

smaller disturbance of the flow. The amount of pre-tensioning is important to avoid large deflections at speed that corrupt the calibration. The use of these sensors for a model test at speed is still a matter of debate; there is a rise of the water level at the front and ventilation at the back of the wire. The nett effect is however small, see also section 10.1.

The third method involves more effort, because it requires more sensors that also need to be sampled at high frequency. Nevertheless, it is considered ideal to measure some flow parameters in impact conditions. The parameter measured, the pressure, is in fact the only relevant quantity for the loads. It also solves the problems of conductive wires in overturning waves when there can be multiple water/air interfaces along the wires or when there is white capping of the crests. The relative velocity can be extracted from the pressure signals by comparing the time instant of the rise of the pressure pulse at different vertical and horizontal locations. The disadvantage of this method is the low density of sensors, so the low resolution of the relative motion and velocity.

4.4   Second series of experiments

The second series of experiments was designed to measure impulsive forces on a larger area of the bow than the first series. The area of interest was the forward 25 % of the length of the model, so forward of St 15. This part of the model was subdivided in 10 segments. The segments were not equally long: the aft segment is twice the normal length because no significant impulsive forces were expected in this area. The segment just aft of the forward perpendicular was also twice the normal length. This segment could be outfitted in different configurations: with or without a bulbous bow. Since significant impacts were expected at the bottom of the bulbous bow, the segment to which the bulb was connected needed to be stiff with respect to rotations around the lateral axis. Therefore it was designed as a longer segment, thus allowing a larger size six component strain gauge system.

The large aft part of the hull houses the propulsion system for the model; this system consists of one steerable podded propulsion unit. This lay-out allows a completely free sailing model although ropes were used to keep the speed constant when the model sailed in large waves.

The segments were all connected to a large size steel beam through individual 6-component strain gauge systems. The beam in its turn was connected to the aft segment consisting of 75 % of the length of the model. An on-shore picture of the model is shown in Figure 4.7, the model is shown during one of the experiments in the seakeeping basin in Figure 4.8.

The gaps between the segments were designed to be narrow at 5 mm. The gap was covered with thin rubber sheet, glued to the segments in recesses. The main argument for the choice of the width of the gaps was to minimize the loss of the pressure pulse on the hull. The opposite side of this choice is the interaction between the segments due to forces transferred by the rubber seals. The strain gauge system introduces some flexibility

Figure 4.7: Model of the ferry with 10 segments in the forward part of the hull

Figure 4.8: Model of the ferry in the Seakeeping and Manoeuvring Basin. Captive set-up.

in the connection of the segment to the beam by nature. As a consequence the segment rotates slightly due to a lateral load, thus introducing shear stresses in the rubber seal at the bottom of the segment. This small shear stress over the full beam of the segment can introduce an interaction force. The magnitude of the shear stress is affected by the width of the gap between the segments.

4.4.1   Instrumentation

The ship motions amidships were measured with an optical 6DoF system. The forces between the 10 segments and the steel beam were recorded by 10 6-component force balance. Several accelerometers were used in the hull and segments for verification purposes. Relative motions were measured by traditional wire sensors on the leeward side of the model. Vertical rows of pressure sensors were fitted on the windward side Figure 4.9 to measure the rise of water along the hull and if a jet should be present, to find the location of the jet root. The traditional wire sensors and the rows of pressure sensors were fitted on the same longitudinal position to allow comparison in head seas.

Figure 4.9: Pressure sensors on the windward side of the segmented model. The rows are vertical and located on St 17.89, St 18.77 and on St 19.50. The horizontal levels are -1.472, 0.039, 1.547, 3.051, 5.055 and 7.050 m relative to the undisturbed water surface. The row at St 19.50 has the sensors only at the top 3 positions.

4.5 Wave conditions for the experiments

4.5.1 Wave sweeps

Normally slamming is considered as an extreme event and it should not occur very often. This means that if experiments in a normal irregular sea state would be carried out, the probability of a slam in a realistic condition (combination of speed heading and sea state) should be low; a much used criterion is the one resulting from a study carried out by the Nordic Co-operative Organization for Applied Research (Nordforsk) [92] shown in Figure 4.10. This means that for the subject ferry, with a length $L_{PP} = 173\ m$, the acceptable number of slams would only be twice every 100 wave encounters. This results
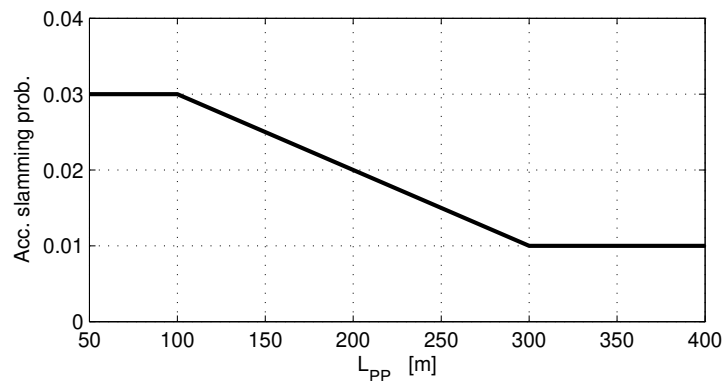
Figure 4.10: Acceptable probability of slamming for merchant ships according to the Nordforsk study 'Assessment of ship performance in a seaway' (1987), [92].
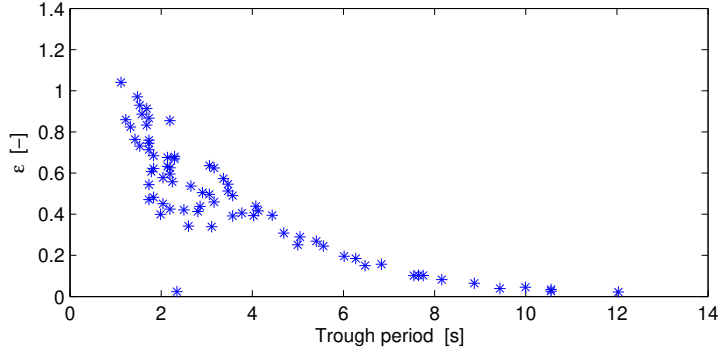
Figure 4.11: Steepness parameter ϵ in the wave train as a function of the trough-to-trough period.

in a rather inefficient testing campaign, so the choice was made to construct artificial wave trains. The aim of this wave train is to have a series of wave encounters in a wave height that is as constant as possible, but a wave steepness that increases at successive encounters. A plot of the wave steepness parameter ϵ as defined by Grue et al. [64], see also section 5.8, is shown in Figure 4.11. This parameter ϵ is plotted against the trough period of the wave and is equivalent to $2\pi\zeta_{\mathrm{MAX}}/\lambda$ in the linear context. The figure shows that very steep waves can be generated in this way. The waves are much steeper than the steepness based on global parameters that are known for the open ocean, $2\pi H_S/(gT_P^2) < 0.05$ (roughly equivalent to $2\zeta_A/\lambda$ for a regular wave) as quoted by de Kat [93] from the book *'The Sea, Ocean Engineering Science'* by le Méhauté and Hanes (1990).

An example of such a wave train, identified as a wave sweep, is shown in Figure 4.12. The waves in the early part of the wave train are sufficiently long to induce significant ship motions; in the latter part of the experiments the waves are very short, so the vessel hardly moves as shown in Figure 4.13. The results have shown that the steep waves in this last part of the run are the ones that cause very large impacts on the bow of the model. The choice of having the long waves first was made to avoid overtaking waves that might result in wave breaking, a loss of wave energy and less control over the wave train encountered.

The measured wave train is used as input for the simulations. A Fast Fourier Transform (FFT) of the wave is made using 500 - 600 frequency components in the range $0 < \omega < 3.0 \ rad/s$ to have an accurate description of the wave profile. An example of an amplitude spectrum of such a wave train is given in Figure 4.14.

The frequencies of the FFT are transformed to the earth fixed reference frame and the phase of each component is adapted to represent the wave at the CoG of the ship (at $t = 0$) as required by the time domain program. The wave encountered in the simulations resembles the measured one very closely as is also indicated in Figure 4.12.

Using a FFT in the analysis of the wave, and an inverse FFT in the simulations, is not a restriction in representing a steep wave. A FFT is just a mathematical operation that transforms a signal form one domain, time in this case, to the frequency domain. Using
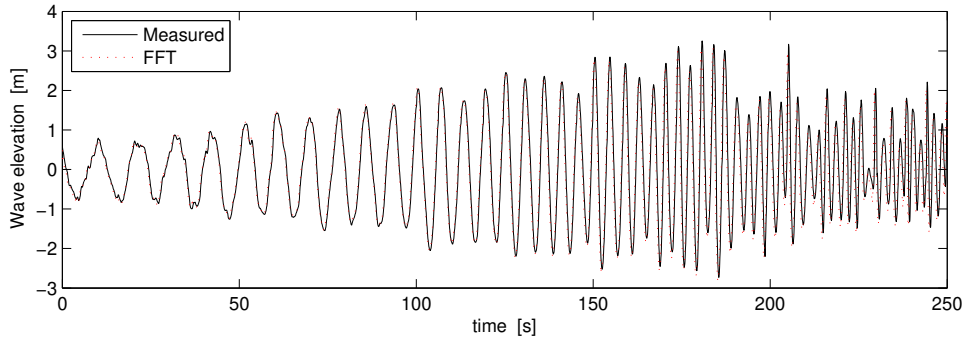
Figure 4.12: Example of a wave train used in the experiments. The waves in the early part of the run are long and they are getting steeper as the run progresses; in the last part of the run they are breaking. The line indicated 'FFT' shows the encountered wave as used in the simulations.
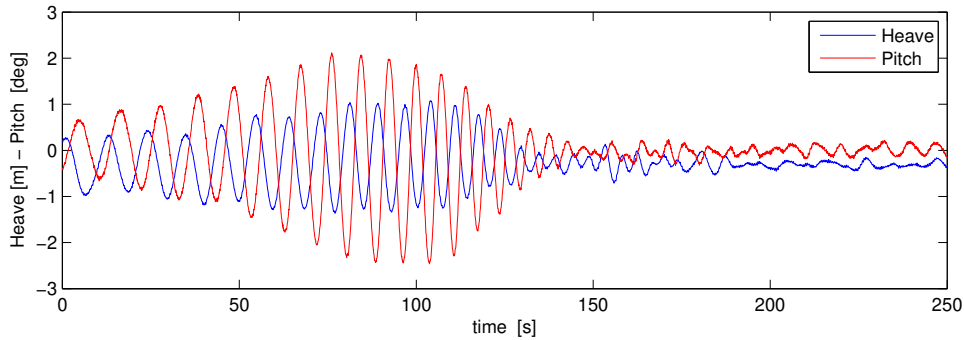
Figure 4.13: Measured motions of the ship model in the wave train shown in Figure 4.12. The waves in the second part of the run are too short to induce significant motions.

the frequency domain result of the FFT to determine the wave in the earth reference system and to transpose it to the CoG of the ship is done using linear wave theory. The validity of linear theory is questionable for the steep and breaking waves as used in the experiments. However, by measuring the wave as close as possible to the model, these errors are quite small; details are given in Appendix A.

4.5.2   Extreme Waves

A second specially constructed wave train that was used in the experiments is a so-called focussed wave, a wave train in which different frequency components are generated starting with the highest frequency and ending with the lowest. By properly choosing the $d\omega/dt$ ratio of the wave train, the wave crests of all generated waves can arrive at the same time, on the same location, in the wave basin. This technique was proposed by Clauss and Kühnlein [30] to determine response functions of ship motions in waves by a single experiment that was sufficiently short not to be bothered by basin effects like wave reflections from the walls. Later on, they used the technique to generate (nonlinear) extreme waves [31, 29]; a famous example was the re-creation of the 18.50 m high 1995
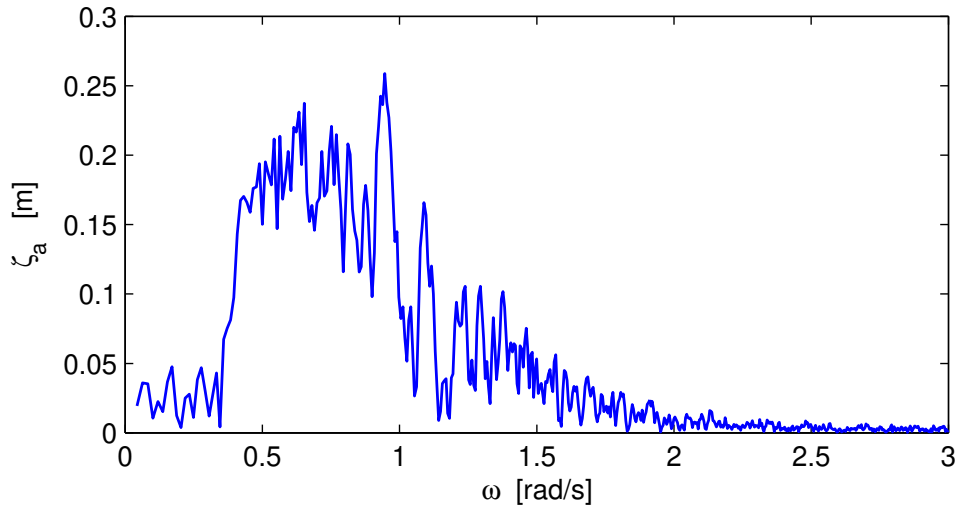
Figure 4.14: Example of a wave amplitude spectrum of the wave sweep shown in Figure 4.12.

New Year wave [32]. A further development in creating extreme waves was made by One-rato *et al.* [141]. He used a solution of the non-linear Schrödinger equation known as the Peregrine breather solution to create an extreme wave in a basin. The advantage of this method is, that it uses only a single carrier wave rather than a range of frequencies as used in the focussed wave technique. The method makes use of a modulation instability that can result in a wave height three times the height of the original wave.

The focused wave technique has been used in this project to generate steep waves with a prescribed wave height; an example is given in Figure 4.15. The amplitude spectrum of this wave is given in Figure 4.16. The challenge while carrying out the experiments was to start the carriage in time to be at speed with the bow of the model at the right place, right time - similar as the focused wave. Repeat tests showed that this could be done with an accuracy of $0.20\ m$ (value from the basin) due to the accuracy of the manual start of the carriage after starting the wave generator. This manual procedure had an error of about $0.1\ s$; together with a speed of the model of $1.7\ m/s$ this resulted in the quoted accuracy.

It appeared that the experiments using the wave sweep were more useful and efficient for the purpose of validating a numerical technique. One run results in a large number (abt. 40) wave encounters in which the most important parameter, the wave steepness is varied. In contrast to this, the extreme wave consist of only one major event. Next to this, some fine tuning is always necessary to properly generate an extreme wave. The propagation speed of steeper waves differs more and more from linear theory causing phase differences between the different frequency components at the focusing point.
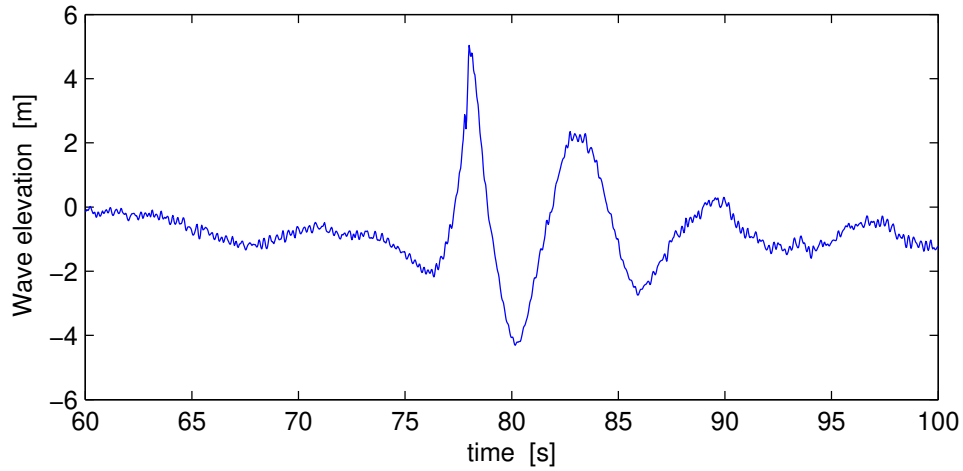
Figure 4.15: Example of an extreme wave used in the experiments.
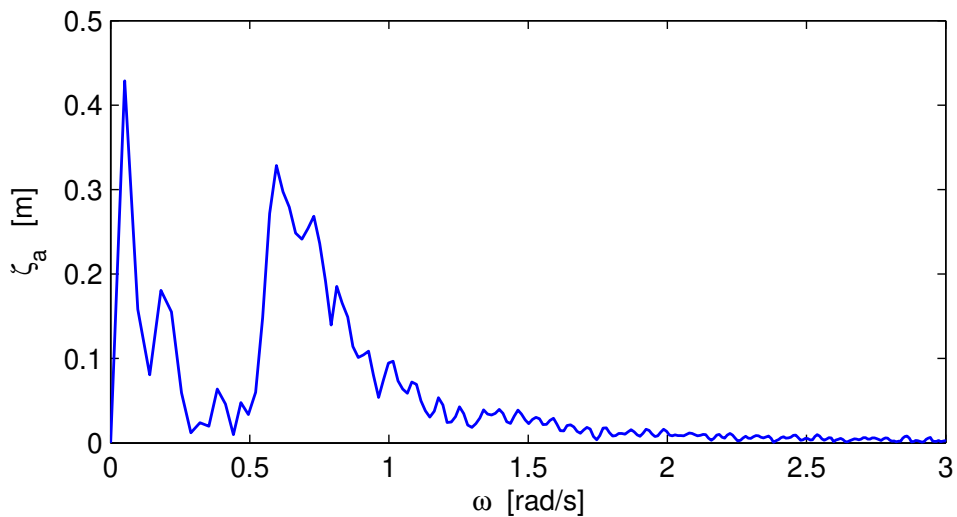
Figure 4.16: Example of a wave amplitude spectrum of an extreme wave.

4.6   Measurement accuracy

An elaborate study to determine the measurement accuracy has not been carried out. The list in this chapter is based on the standard procedures for calibrating sensors at MARIN.

Individual strain gauge

Individual strain gauges are very accurate sensors. The accuracy as determined in the calibration procedure is in the range 0.15 - 0.20 % of the load. The calibration procedure consists of a stepwise increase of the load, about 5 levels, and then a stepwise decrease to zero. This procedure is repeated a few times. All load cases are static loads; the loading and unloading sequence is done to detect hysteresis in the sensor.
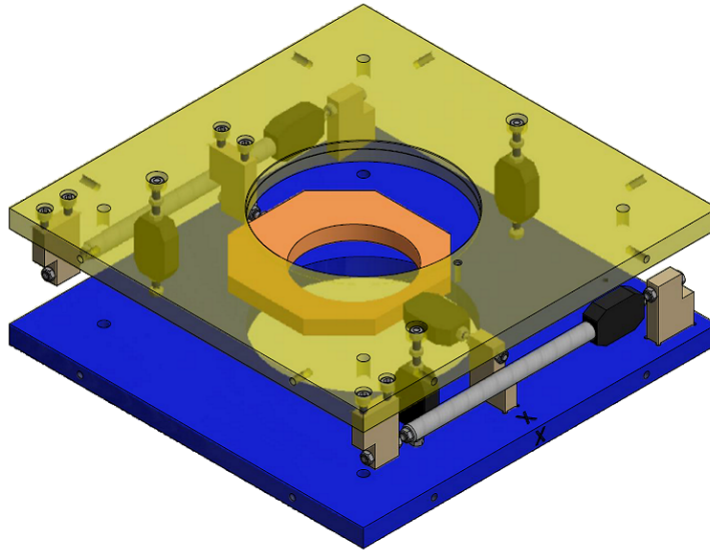
Figure 4.17: Example of 6-component frame. The blue and yellow plates connect to the bodies in between which the forces need to be measured. The actual strain sensors are shown in black, they are connected to supports on the plate through steel bars. There is a very thin section at the outer ends of these bars just before the support. These thin parts avoid important losses in the sensor due to shear forces in the bars. In this example there are three strain sensors in vertical direction, two in transverse direction and one in longitudinal direction.

Six component strain gauge system

A six component strain gauge system consists of 6 individual strain gauges built together in two special frames, an example is shown in Figure 4.17. An important component of the accuracy of such a system are the thin parts in the connecting rods between the frame and the sensor. These thin parts reduce the shear force produced by the connecting rod when one frame is translated with respect to the second frame. This shear force is a 'loss' of force for the sensor that was intended to measure it as an in-line load, but since this effect is elastic, so linear, it is taken into account when calibrating the six component system as one unit. Nevertheless, effort is spent minimizing it. The accuracy for measuring forces is about 0.30 % of the load.

The accuracy for moments depends to some extent on the dimensions of the frame. Large dimensions of the frame result in low forces in the sensors, in a low rotation of one frame relative to the second one as a result of a moment, so in a stiff connection. The frame needs to be properly designed for a specific purpose and in order to do so, the magnitude of the loads should be known. If this is however the case, a very clean and accurate measurement can be made, a typical accuracy for moments is about 1 % of the load.

Force on segments

The segments in the second series of tests are connected to a very stiff steel frame via a six-component strain gauge system. In principle the steel frame adds a little to measurement

inaccuracy since it deforms under load and hence the orientation of the frame changes slightly. This effect is however very low and is ignored.

More serious is the consequence of sealing the gaps between segments with a thin rubber sheet. In principle the six component frames were mounted as low as possible in the segments, but due to the narrow shape this was not possible for the three foremost segments. Having the measurement frame at the top means that there is some flexibility for rotations around the longitudinal axis and this causes shear forces in the rubber sheet at the bottom of the segment. This shear force transfers part of the load to neighbouring segments. The effect can be minimized by making the rubber sheet wide, so it should not be glued to the segment over the full width of the overlap, but only at the outer ends. If sufficient care is taken, the 'crosstalk' between the segments can be limited to 5 % of the load, but if neighbouring segments deform in a similar manner, the crosstalk is less of course.

Pressure sensor

The sensors to measure the pressure during a slamming event consist of a silicon membrane on which a piezo-resistive chip is mounted. These sensors have an advertised very high resonance frequency, but this value is measured in air. The resonance frequency is substantially lower when the sensor is submerged, due to the added mass effect. The added mass of the membrane is several orders of magnitude larger than the physical mass.

In order to calibrate a pressure sensor in real impact conditions, a special apparatus was designed and built at MARIN. The apparatus consisted of a cone that could be launched into the water by a series of loaded springs. Eight pressure sensors could be fitted at the same distance from the tip of the cone. The idea was to use the analytical solution of the potential flow problem as found by Korobkin and Scolan [103] as the reference signal for the pressure sensors being tested. The procedure proved to work, but it took quite some effort to have good results. Especially the inclination of the cone when hitting the water was a point of concern. The results were not very encouraging; especially the peak pressure did not match very well to the result of the analytical solution, even when the diameter of the sensor was taken into account. This work has been published by van de Bunt and Bouvy [25].

A second method was developed using a special pressure vessel fitted with an oscillating exciter and a reference pressure sensor. The idea is simply to compare the measurement of the sensor being tested to the result for the reference sensor. This system is still under development, at present it can only be used for a maximum frequency of 500 Hz. Some results of the calibration procedure are shown by Bouvy [18].

In conclusion: a lot of work to actually do a dynamic calibration of pressure sensors is in progress, but at the time of the experiments reported in this thesis the accuracy of the pressure sensors was unknown.

Ship motions

The normal procedure for a seakeeping test is based on the use of a free running model. The model is propelled by an electric motor and the rudder is controlled by an auto-pilot.

The carriage is normally in the 'following' mode, meaning that it follows the model in both X and Y directions. The position and speed of the model is measured in two steps: the position and speed of the carriage is determined by a position measuring system fitted along the rail on both sides of the basin and secondly, the position and speed of the model is measured by an optical system that measures the position of the model relative to the carriage (on which the cameras of the optical system are mounted).

The position of the carriage is measured by rulers fitted along the rail on both sides of the basin. The accuracy of this measurement is 0.1 mm, but errors are introduced in the measurement system that result in a delay of the measured velocity of 0.02 s (the sampling rate of the position signal is 100 Hz). This system creates high frequent noise on the velocity signal with an amplitude of 0.01 m/s, this noise can be removed by a low-pass filter. The error on the velocity due to the time delay depends on the acceleration; for a velocity of 1 m/s and an acceleration of 1 m/s^2 it is 2%.

The motions of the model relative to the carriage have been measured by an optical system consisting of a 'target' of three LED's of different colour. The position of these LED's is being measured by three camera's. The accuracy of the system is very high. In the 'measurement cube' of 1*1*2 m the position of the target is measured with a 1 mm accuracy for translations and a 0.3 deg accuracy for rotations. These motions are the motions of the model relative to the carriage following the model.

Chapter 5

The Approximate method

5.1 Approach

Short description of the approach

The semi-empirical tool is based on momentum theory, similar to von Kármán's original idea published in 1929 [91]. Therefore the method has been given the name MARIN Momentum Theory (MMT). Momentum theory relates the impulsive force to the rate of change of the momentum in the fluid. The rise of water along the body (or pile-up) is an important factor for the magnitude of the impulsive force as pointed out in 1932 by Wagner [187]. This effect is incorporated in the present method and, since this method aims at predicting impact forces on ships at speed, it is augmented by the effect of the draft dependent stationary bow wave. Especially when the blunt part of the bow immerses, this adds considerably to the relative motions.

The momentum in the fluid is calculated using spatial added mass derivatives. Since slamming is a phenomenon of short duration, it is assumed that free surface effects other than the pile-up, like the generation of radiating waves, do not play an important role during the impact. Therefore the so-called infinite frequency added mass is used, in this case the Green's function on the panels of the body just contain the frequency independent part $\frac{1}{r}$ of the source strength - and the source strength of the mirror image of the panel.

Added mass derivatives are pre-calculated using 3D potential flow theory. The calculation is basically done for a range of drafts from keel to deck in order to derive the vertical added mass derivatives. A key aspect of the implementation is, that not the actual added

Figure 5.1: Sketch of calculation grid on the body of a ship and the row of waterline panels indicated in blue.

mass on each panel for each draft is stored, but instead the change in the total added mass due to an increase of the draft is attributed to the row of panels just below the new waterline. This top row is identified as the water line panels, Figure 5.1.

The stationary bow wave is also calculated for the same range of drafts. Also the change in local bow wave height is stored at each row of water line panels.

The time domain simulation calculates the impulsive force as a line integral along the actual water line panels, Figure 5.2. In general the actual waterline will cover several horizontal layers, so added mass coefficients are used in one particular time step that do not result from the same solution of the BVP. It is assumed that this is an acceptable approximation.

If forces are calculated on ship segments that continue below the design water line, additional forces due to the hydrodynamics (radiation and diffraction) are taken into account. For all segments the hydrostatics are added up to the actual water line.
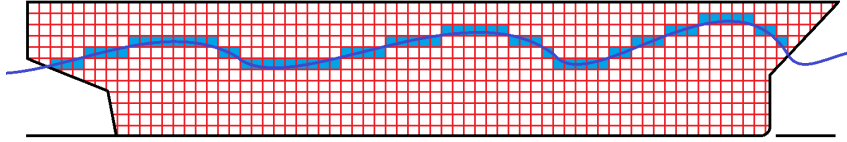
Figure 5.2: Sketch of calculation grid on the body of a ship, the intersection with the surface and the panels used for the calculation of the impulsive forces.

5.2   System of axes

It is convenient to have different reference frames to describe simulations of ship motions in waves; especially if large motions - either in the horizontal or vertical plane - are allowed. The systems used are defined in Table 5.1. The reference frame in which variables are defined are indicated by a super script: $v^{(b)}$ is a velocity defined in the body fixed reference frame. Transformation matrices are used to transfer variables from one reference frame to the other; these matrices are identified by two indices. The principle is illustrated by Equation 5.1 that calculates a translational velocity vector in the ship system by multiplying the velocity in the earth system with the appropriate transformation matrix. The same principle, but a different transformation matrix, is used for rotational velocities. Apart from the different orientation, also a different location of the origin of the reference frame can be used, this requires a translation next to the rotation defined in Equation 5.1.

$$\vec{u}^{(b)} = \mathbf{T}^{(b)}_{(e)} \cdot \vec{u}^{(e)} \tag{5.1}$$

The waves are defined in the XYZw system; the wave always travels in the negative $X^{(w)}$ direction. The heading of the ship is β in this system; this angle is measured from the negative $X^{(w)}$-axis, consequently $\beta = 180 \ deg$ indicates head waves.

The earth system is rotated with angle $\beta - 180 \ deg$ with respect to the XYZw system. The $X^{(e)}$ axis is on the CL of the ship at t=0 and pointing towards the bow.

Table 5.1: Definition of different reference frames

Id	Name	Moves	Origin	Used for
XYZw	Wave system	Not	At the position of CoG ship for t=0 except that the vertical coordinate z is defined zero on the fluid surface at rest.	Definition of the waves
XYZe	Earth fixed system	Not	At the position of CoG ship for t=0 except that the vertical coordinate z is defined zero on the fluid surface at rest.	Definition of the average position of the ship. The heading of the ship is in the positive $X^{(e)}$ direction
XYZh	Hydro-dynamic system	With the initial velocity and course of the ship	At the average position of CoG ship	System in which the EoM are solved; also in which the first order ship motions are defined.
XYZb	Ship (rigid body) system	With the actual motions (6DoF) of the ship	Can be chosen freely, usually at St 10, centre-line, still water level	Definition of the geometry of the ship, local quantities, forces on the ship. The flexural modes are defined in this system.

The XYZh system moves along with the average position of the CoG of the ship. The first order ship motions are defined and calculated in this system. The definition of the average position of the ship is dependent on how low frequency speed and course variations are taken into account; this is a subjective choice. For this project the speed U and course are constant, therefore the origin of the XYZh system has coordinates $(Ut, 0, 0)$ in the XYZe system.

The XYZb system is shifted and rotated from the XYZh system with the oscillating motions of the body and also due to the change of the origin: from the average position of the CoG to St 10, centreline and still water level.

5.3   Basic equations for the impulsive force

The approximate method is based on momentum theory which essentially starts with Newton's second law. This law, Equation 5.2, describes the relation between an external force F and the change in momentum, the product of mass m and velocity u. Newton's second law is defined in an earth fixed reference frame. The impulsive force is defined as a reaction force, it describes the force on the body due to the change in momentum that it caused in the fluid around it. Since there is no external force, the total of the impulsive force and the change in momentum must be zero, Equation 5.3. The rate of change of momentum can be split in two components as shown in Equation 5.4.

$$\vec{F}^{(e)} = \frac{\partial}{\partial t}\left(m \cdot \vec{u}^{(e)}\right) \qquad [N] \tag{5.2}$$

$$\vec{F}^{(e)}_{\text{IMPACT}} + \frac{\partial}{\partial t}\left(m \cdot \vec{u}^{(e)}\right) = 0 \qquad [N] \tag{5.3}$$

$$\vec{F}^{(e)}_{\text{IMPACT}} = -\left(\vec{u}^{(e)}\frac{\partial m}{\partial t} + m\frac{\partial \vec{u}^{(e)}}{\partial t}\right) \qquad [N] \tag{5.4}$$

The rate of change of the mass is zero in most physical systems, but if a body moves in water it generates a flow and a dynamic pressure on the body. The component of the pressure that is in-phase with the (oscillating) motion gives rise to a force which, when divided by the acceleration, results in the so-called added mass. Especially when the body enters the water, the geometry of the submerged part of the body changes rapidly and therefore also the amount of added mass.

Ship motions in waves are usually described by a linearized set of six equations of motion. In these equations, the added mass effect is described by linear coefficients expressing the reaction force in a certain direction due to an acceleration in any of the six directions. In general this is expressed as:

$$F_i^{(e)} = \sum_{j=1:6} a_{ij}\ddot{x}_j \qquad [N] \tag{5.5}$$

The added mass coefficients a_{ij} are also used in the expression of the impulsive force. The first term in Equation 5.4 describes the rate of change of the total mass, the physical mass m and the added mass a. The rate of change of the physical mass is zero, the rate of change of the added mass is expanded using the spatial derivatives of the added mass coefficients a_{ij} and the time derivative of the spatial coordinate, the velocity. The added mass is determined on basis of the actual immersion of the body (including pile-up effects). The relevant spatial coordinate is the coordinate of the intersection point of the body and the free surface. The time derivative of this coordinate is the relative velocity, the velocity in the body reference frame. Introducing the spatial added mass derivatives into Equation 5.4 results in Equation 5.6:

$$F^{(e)}_{X-\text{Imp}} = -\left(\frac{\partial a_{11}(x,z)}{\partial x}u^{(b)} + \frac{\partial a_{11}(x,z)}{\partial z}w^{(b)}\right)u^{(e)} + a_{11}(z)\dot{u}^{(e)} \qquad [N/m]$$

$$F^{(e)}_{Y-\text{Imp}} = -\left(\frac{\partial a_{22}(x,z)}{\partial x}u^{(b)} + \frac{\partial a_{22}(x,z)}{\partial z}w^{(b)}\right)v^{(e)} + a_{22}(z)\dot{v}^{(e)} \qquad [N/m] \tag{5.6}$$

$$F^{(e)}_{Z-\text{Imp}} = -\left(\frac{\partial a_{33}(x,z)}{\partial x}u^{(b)} + \frac{\partial a_{33}(x,z)}{\partial z}w^{(b)}\right)w^{(e)} + a_{33}(z)\dot{w}^{(e)} \qquad [N/m]$$

Rotational accelerations are not included in the expressions 5.6. The expressions are evaluated as line integrals along the actual water line; the coordinates and velocities are

local coordinates and local velocities. The translations due to rotations defined at the CoG are thus included, only the effect of the local rotations is ignored. The evaluation of Equations 5.6 is detailed in Chapter 6.

Damping terms to describe the forces due to wave radiation should not be added to this equation (as was done by Beukelman and Radev [12]). Later on, section 5.7, it will be shown that real slamming starts when the generated surface wave has no time to travel away from the body, so it also cannot radiate energy.

5.4   Added mass derivatives

Usually, the added mass is calculated to calculate ship motions in waves. The calculation is carried out for one draft at a range of frequencies to determine the effect of the radiated waves on the forces. Slamming is considered as a high velocity impact and gravity is usually ignored. This means that the formation of radiating surface waves is also not included. In a later chapter this assumption will be studied in detail.

The calculation of the added mass is based on the conservation of momentum. Following Newman [137], it can be derived, Cointe [34], that the added mass follows from the integral of the potential over the wetted surface S of the impacting body:

$$F_Z = -\rho \frac{d}{dt} \left(\iint\limits_S \phi n_3 dS \right) = \frac{d}{dt} \left(A_{33}.U \right) \qquad [N] \qquad (5.7)$$

in which:

S	Wetted surface of the impacting body.
ϕ	Velocity potential.
n_3	Component of the normal in Z-direction.
A_{33}	Added mass in vertical direction.
U	Impact velocity.

The potential flow problem posed in Equation 5.7 is solved by describing the body geometry by panels and using source potentials to force the boundary condition on the body:

$$\frac{\partial \phi}{\partial \vec{n}} = -U\vec{n} \qquad [m/s] \qquad (5.8)$$

The problem is solved ignoring the free surface; in fact, the double body problem is solved.

For this application we are interested in added mass derivatives. The longitudinal added mass derivative can be derived from the solution of the radiation problem at a single draft, the vertical added mass derivative requires a solution of the radiation problem at at least two different drafts. The procedure how to calculate these parameters is detailed in Section 6.2.

5.5   The pile-up effect

5.5.1   Pile-up and pressure distribution

During the impact of a body, fluid is being displaced and causes a local rise of the surface next to the body. This rise is known as the pile-up. This effect was described analytically by Wagner for wedges [187]; the rise of the contact point of the fluid and the body is quantified by the pile-up factor $(1 + \psi)$, the parameters involved in describing this effect are defined in Figure 5.4. The pile-up gets longer as the deadrise decreases; the angle at the contact point between body and fluid surface gets sharper. Wagner found a pile-up factor of $\psi = \pi/2$ for small deadrise angles; since this refers to a vertical distance as shown in Figure 5.4, the length of the wetted part of the section above the calm water surface is $\pi/(2.sin\beta)$.

For small deadrise angles the length of the jet is much longer as has been determined by Zhao and Faltinsen [205] and shown in Figure 5.3; this result is obtained with a nonlinear BEM. However, the jet is not very interesting for the calculation of the impulsive force, since the pressure is atmospheric. Apart from the shape of the free surface deformation, Zhao and Faltinsen also calculated the pressure distribution over the face of the wedge. According to the asymptotic theory developed by Howison *et al.* [77], the location of the point having maximum pressure is at a distance $(\pi/2-1)z$ above the apex of the wedge, independent of the deadrise angle and so the length of the jet. This result is confirmed by the results of their calculations as shown in the figures. The point of maximum pressure is located at the root of the jet. Similar results are obtained when a flat plate enters a fluid at some pitch angle and at high horizontal velocity as shown by Iafrati [79].

Since we are interested in the impulsive force on a body dropping into a fluid, the point of the maximum pressure is much more relevant than the position of the tip of the jet. Therefore from this point on, the pile-up is defined as the location on the face of the body of the maximum pressure. Schematically the pile-up parameters are given in Figure 5.4.

5.5.2   Importance of the pile-up effect

The pile-up factor $(1 + \psi)$ is defined as the ratio of the height of the point of maximum pressure on the face of the body relative to the vertex of the wedge (z^*) and the immersion of the vertex relative to the undisturbed fluid surface (z). This ratio is immersion independent for a wedge and also independent of the impact velocity - if gravity is ignored. In this thesis, the point (y^*, z^*) is often referred to as the waterline intersection point.

The pile-up has an effect on the added mass derivative and on the relative velocity of the contact point. If we use Wagner's formula for the added mass of a fully submerged
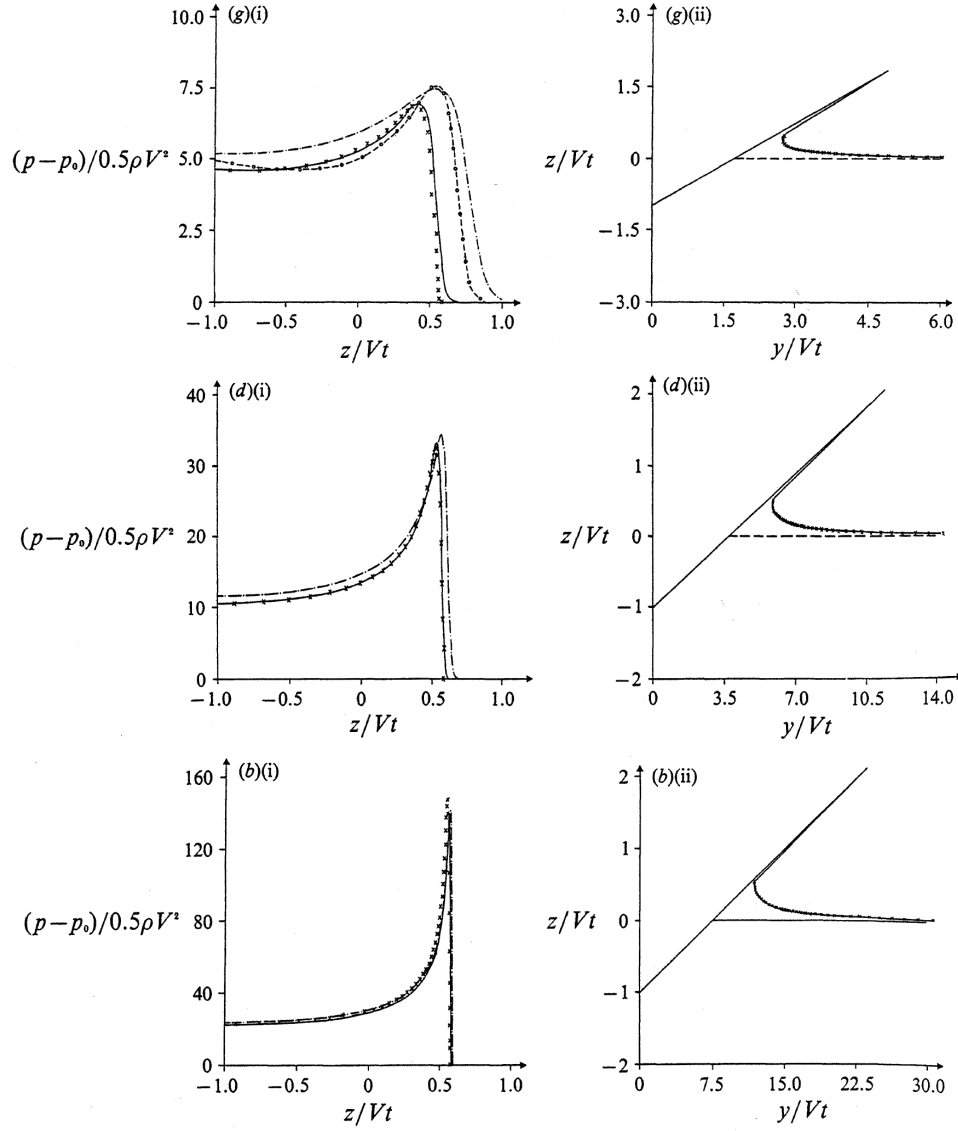
Figure 5.3: Pressure distribution (left) and deformation of the free surface (right) for a series of wedges. From top to bottom: wedge with deadrise angle of resp. 30, 15 and 7.5 deg. Results from Zhao and Faltinsen [205].

flat plate and apply the 'wedge' correction for a finite deadrise angle by Lewis [114], the added mass of a wedge is proportional to the width of the actual wetted part of the wedge squared, Equation 5.9:

$$a_{33} = \rho \frac{\pi}{2} \left(1 - \frac{\beta}{2\pi} \right)^2 y^{*2} \qquad [kg/m] \qquad (5.9)$$

Using this expression and $y/z = \tan\beta$, the vertical added mass derivative is:

$$\frac{\partial a_{33}}{\partial t} = \rho\pi \left(1 - \frac{\beta}{2\pi} \right)^2 \frac{z^*}{\tan^2\beta} \cdot \frac{dz^*}{dt} \qquad [kg/ms] \qquad (5.10)$$
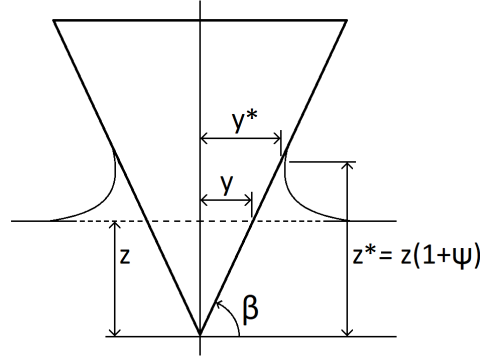
Figure 5.4: Definition of the pile-up for a wedge with large deadrise angle. The point (y*,z*) refers to the point of maximum pressure on the face of the wedge rather than to the intersection point of the rise of water and the wedge.

If we use $z^* = z(1 + \psi)$ and $dz^*/dt = (1 + \psi)\dot{z} = (1 + \psi)w$ as the vertical velocity in the body fixed reference frame, the impulsive force, for a constant velocity impact, is:

$$FZ_{Z-\mathrm{Imp}} = \rho\pi \left(1 - \frac{\beta}{2\pi}\right)^2 \frac{z}{\tan^2\beta} w^2 (1 + \psi)^2 \qquad [N/m] \qquad (5.11)$$

The result of Equation 5.11 illustrates that there is a $(1 + \psi)^2$ effect of the pile-up factor on the impulsive force. Originally Wagner [187] calculated the pile-up factor for a flat plate as $(1 + \psi) = \pi/2$; this was refined by Payne in 1994 [143] by an estimate for wedges. Using the results of experiments by Pierson (1954) [145] and of calculations by Zhao and Faltinsen (1993) [205], he proposes to use:

$$(1 + \psi) = \frac{\pi}{2} - \beta\left(1 - \frac{2}{\pi}\right) \qquad (5.12)$$

This result means that the effect of the pile-up factor on the impact force is a factor $2.47 - 1.14\,\beta + O(\beta^2)$, so well over a factor 2 for low deadrise angles.

5.5.3 Derivation of a new pile-up estimator

The equation given by Payne, Equation 5.12 and graphically shown in Figure 5.5, works well for wedges, but this study concerns ships with ship-like sections that typically have a varying deadrise angle as function of the vertical coordinate. It is assumed that the pile-up is a cumulative effect of the deadrise angle at the waterline intersection point. The rationale behind this assumption is, that the impact velocity is sufficiently high so that no surface waves are radiated. Therefore the pile-up can be considered as a result of the displacement effect of the immersing body. A new pile-up estimator has been derived using the added mass derivative as the independent parameter rather than the deadrise angle. This choice was made because the added mass derivative is dependent on the deadrise angle, Figure 5.6, and it is needed for the impulsive force calculation anyway.
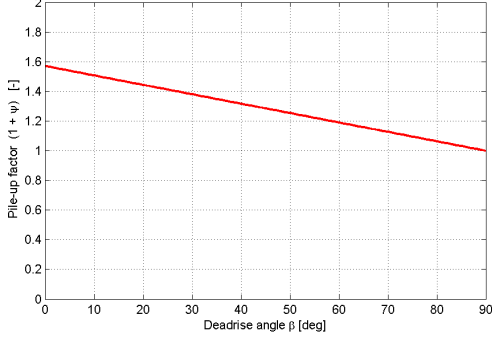
Figure 5.5: Pile-up as a function of the deadrise angle according to Payne [143].
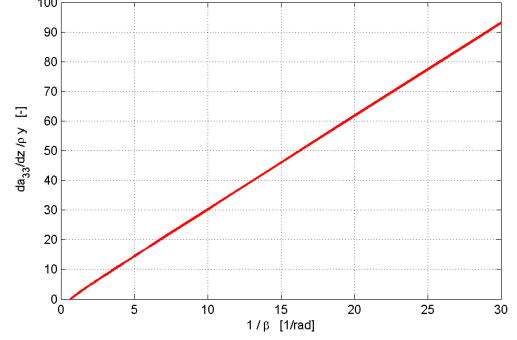
Figure 5.6: Relation added mass derivative of a wedge and the inverse of the deadrise angle.

Table 5.2: Impact force coefficients, $c_{FZ} = FZ/\frac{1}{2}\rho w^2$, for different wedges.

Deadrise angle	PU from pressure pulse	c_{FZvK}	c_{FZW}	$\frac{c_{FZW}}{c_{FZvK}}$	PU from force coefficients
[deg]	[-]	[-]	[-]	[-]	[-]
2	1.606	18734	49061	2.619	1.618
5	1.603	2834	7462	2.633	1.623
7.5	1.598	1204	3168	2.632	1.622
10	1.592	646.5	1700	2.630	1.622
15	1.579	260.8	683.4	2.621	1.619
20	1.563	132.2	344.0	2.603	1.613
30	1.531	46.09	117.7	2.553	1.598
40	1.491	19.14	47.47	2.480	1.575
60	1.380	3.400	7.568	2.226	1.492
80	1.180	0.232	0.375	1.615	1.271

The new estimator was derived using the 2D-BEM program and simulating drop tests with wedges while ignoring pile-up effects, the von Kármán mode, and including pile-up effects, the Wagner mode. The pile-up factor was derived from the square root of the ratio of the impact forces as predicted by the two methods, as derived in Subsection 5.5.2. Calculations were carried out for series of wedges with varying deadrise angle. The choice of the impact velocity is irrelevant in the program because gravity (and so buoyancy) effects are ignored. The velocity is used to non-dimensionalize the impact force. The results are listed in Table 5.2.

Next to calculating the impact force with the 2D-BEM program, also local pressures were calculated. Pile-up effects can also be quantified by considering the moment the pressure pulse arrives at a certain location. The time instant of the pressure pulse has

been monitored on 9 locations distributed over the half beam of the wedge: $2.y/B = 0.1 : 0.1 : 0.9$. Results for a pressure pulse on a 10 deg wedge at different moments in time are shown in Figure 5.7. The characteristics of the pressure pulse of a very steep rise, a constant peak pressure for the different locations and the widening of the pressure response for the larger immersions are illustrated. The time instant of the rise of the pressure pulse at the different locations has been used to derive the relative velocity along the section and hence derive an estimate for the pile-up factor; this result is also listed in Table 5.2. The results are quite similar, but not identical see Figure 5.8. The main reason for the difference is the approximate way the pile-up is calculated by the 2D-BEM program as mentioned in Section 3.1.

The estimator for the pile-up factor has been derived from the square root of the ratio of the force coefficients. The fit is defined in Equation 5.13.

$$(1 + \psi) = 1 + \frac{3}{(1.75 + Fa_3)^3} \tag{5.13}$$

with:

$$Fa_3 = \frac{\rho y}{\partial a_{33}/\partial z} \qquad [-] \tag{5.14}$$

in which:

a_{33}	[kg/m]	Added mass due to vertical motion of the 2D wedge.
$\partial a_{33}/\partial z$	$[kg/m^2]$	Vertical derivative of added mass.

The results of this new estimation formula are compared to experimental results obtained by Tveitnes [182] and to several other prediction methods that are available in the literature; the comparison is made in Figure 5.9. The new estimation formula is well in line with other methods.
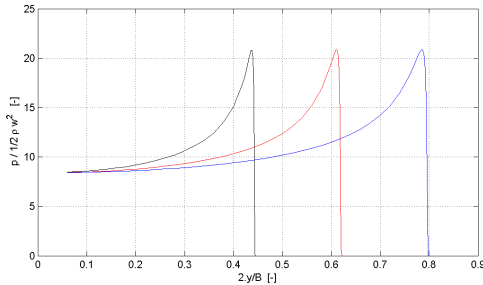
Figure 5.7: Pressure distribution over a 10 deg wedge at different time instants of an impact.
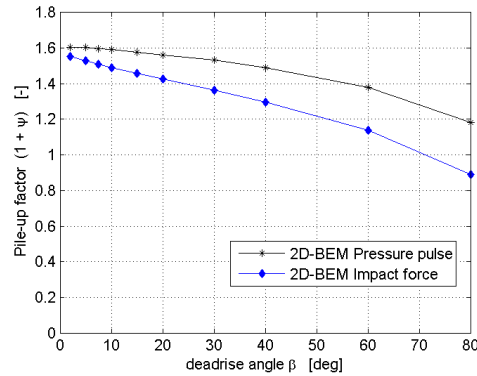
Figure 5.8: Pile up factor for wedges based on forces and pressure pulse.
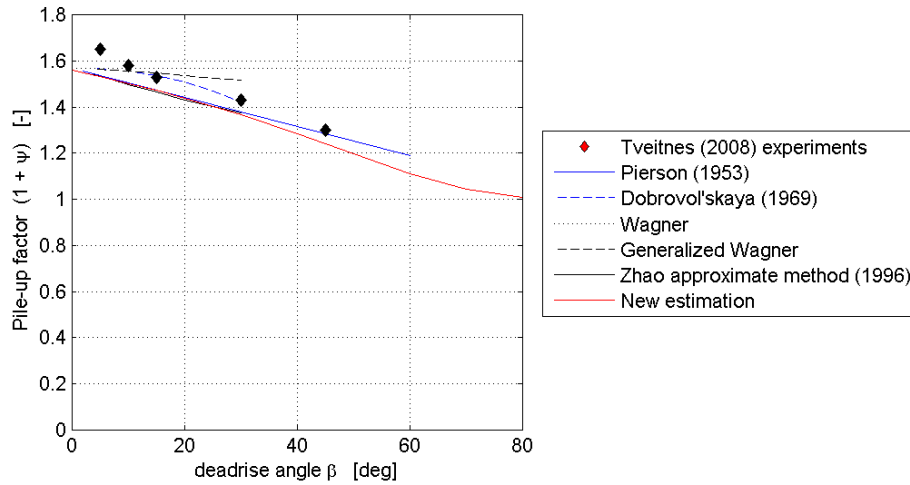
Figure 5.9: Pile-up for wedges with different deadrise angle. Results from experiments by Tveitnes, [182], Pierson [145], the similarity solution published by Dobrovol'skaya [44], Wagner [187], the Generalized Wagner method and Zhao's method [205] and the result of the new prediction formula.

5.6   Asymmetric sections

The inflow conditions on PS and SB of a section are only symmetrical when the ship is sailing in head seas. For all other conditions the problem is asymmetric and this has large consequences for the conditions on the two sides: as well the relative velocity as the pile-up. The analytical and numerical aspects of the problem have been studied by Scolan [161], Semenov and Iafrati [163], Riccardi [153], Judge *et al.* [82] and Xu *et al.* [200], while experiments were reported by Kim *et al.* [96].

Judge *et al.* [82] were especially interested in the comparison of a rotated wedge dropping in calm water and in a symmetric wedge having also a horizontal velocity when dropping in calm water. They followed the division of Type A and Type B impacts made by Xu *et al.* [203]: Type A is a mild asymmetric condition such that there is an attached flow on both sides of the vertex; Type B is a more extreme condition in which there is flow separation on one side. This phenomenon was studied through model experiments on a 37 deg deadrise wedge. They found that a considerable horizontal velocity (75% of the vertical velocity) combined with a rotation angle of 20 deg was necessary to visualise the flow saration eparation at the vertex typical for a type B impact.

Semenov and Iafrati [163] developed a potential flow method that they applied to the problem of asymmetric wedges. They calculated the free surface deformation on both sides of the wedge and the pressure distribution on the wetted parts for a constant velocity drop test. Force coefficients were determined from the pressure distributions. This theory has been used to verify numerical results using an improved Generalized Wagner Model by de Lauzon *et al.* [109]; this comparison is shown in Figure 5.10.

The improved Generalized Wagner Model has been used to generate results for a constant velocity impact for a 10, 20 and 40 deg deadrise angle wedge and each with different rotation angles. The results, the vertical force coefficient for each face of the wedge, has been plotted as a function of the effective deadrise angle, Equation 5.15.

$$\beta_{\text{EFF}} = \beta + \delta_{\text{ROT}} \tag{5.15}$$

The results, presented in Figure 5.11, show that there is quite some interaction between the two faces of the wedge, especially for a low deadrise angle. This effect is not covered by the approximate method; in fact, this method assumes no interaction between the two faces of the wedge. For large deadrise angles this approach is quite acceptable as also shown by Semenov and Iafrati, Figure 5.12. For small deadrise angles there can however be a factor 2 difference in the vertical force.

The lateral force can be derived from the vertical force, even if it is assumed that there is no interaction between the faces. The vertical force on a face is used to determine the force normal to the face and this in its turn determines the horizontal force, see Figure 5.13 and Equation 5.16.

$$\begin{aligned} F_1 &= FZ_1/\cos\beta_1 \\ FY_1 &= F_1 \sin\beta_1 \end{aligned} \tag{5.16}$$

It is assumed that the impact force is mainly generated at the intersection of the water surface and the body. Therefore, the body normals as used in Equation 5.16 are taken at the intersection point for curved sections. A comparison of the lateral force predicted
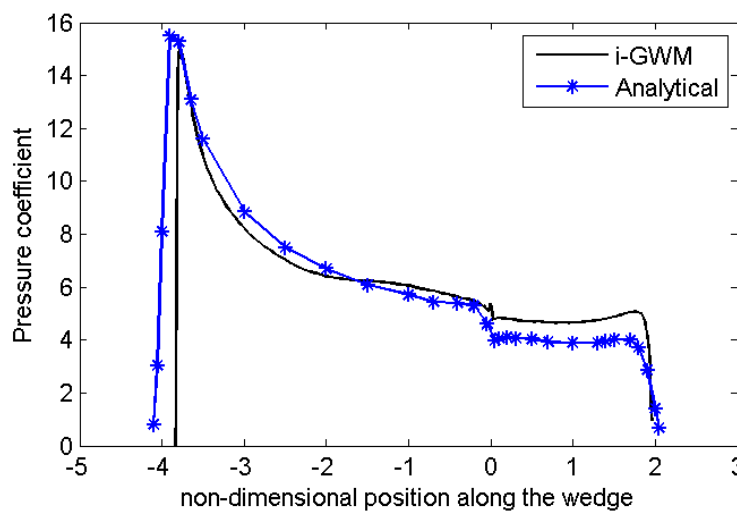
Figure 5.10: Pressure distribution along the wetted part of a wedge during a constant velocity impact. The wedge has a 30 deg deadrise angle and is rotated over 10 deg. Results from the analytical model by Semenov and Iafratie [163] are compared to results by the Generalized Wagner Model by de Lauzon et al. [109].
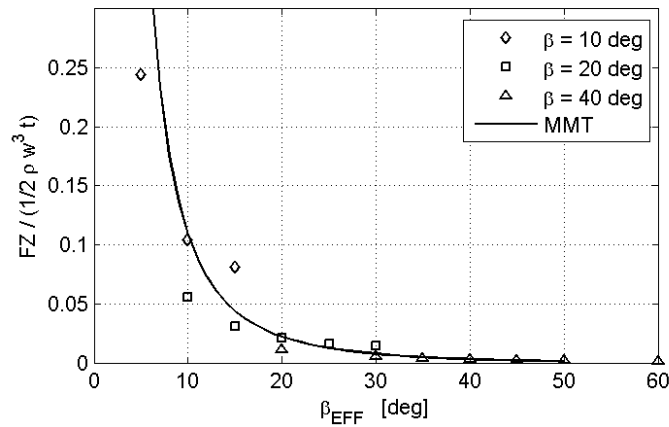
Figure 5.11: Impact forces on a 10, 20 and 40 deg deadrise wedge and various rotation angles. Results from the 2D GWM and from the approximate model MMT.
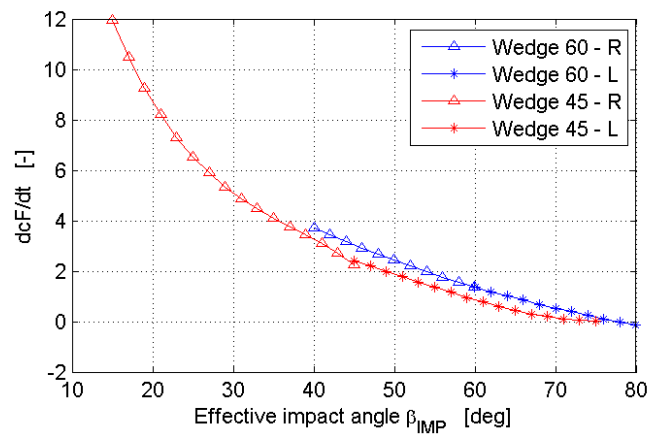
Figure 5.12: Force coefficients for two wedges having a deadrise angle of 45 and 60 deg respectively. These wedges were rotated over angle δ such that the effective impact angle of the faces covered the range 15 - 80 deg. the plot is based on the results of Semenov and Iafrati [163].
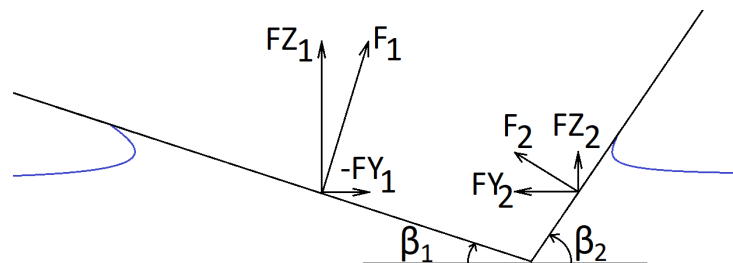
Figure 5.13: Definition sketch of forces on an asymmetric wedge.

by the approximate method to the force predicted by the improved GWM method is shown in Figure 5.14. The figure shows that the lateral force on a rotated 40 deg wedge

is reasonably well predicted, but that the lateral force is quite over-predicted for a wedge
with a low deadrise angle.
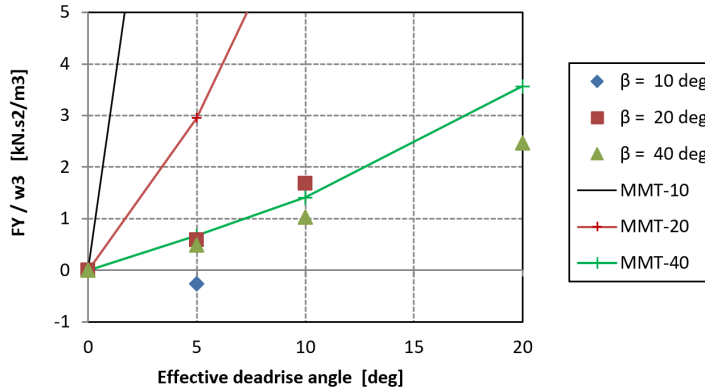
Figure 5.14: *Lateral force on an asymmetric wedge during a constant velocity impact. Results
from the improved GWM and from the approximate method MMT.*

5.7   Gravity effects and a threshold velocity

Theoretical studies usually consider impacts at relatively high velocities and hence gravity
effects are ignored. For a practical method it is however important to consider also impacts
at lower velocities where gravity does play a role. In fact, it is this effect that has led to
a 'threshold velocity' for slamming as introduced by Ochi [139]. Greenhow [58] studied
the effect of gravity on impacting wedges, he concluded that the effect of gravity can be
ignored for the initial phase of the impact, $t \leq w/2g$. Surprising to this time limit is, that
it is independent of the deadrise angle.

    Fairlie-Clarke and Tveitnes [48] carried out calculations with and without gravity
using a commercial CFD package. They showed quite an effect of gravity, especially de-
pending on the deadrise angle of the wedge, see Section 2.3.

    The effect of gravity on the hydrodynamic forces is studied here considering the pro-
blem of a vertically oscillating wedge at the free surface. For low frequencies, this problem
can be solved using linear diffraction theory. Since this study concerns large amplitude
motions with high relative velocities, it is of interest to find the high frequency limit of this
theory. Within this context, the main limitation of diffraction theory lies in the assump-
tion of linearity. The consequence thereof is, that a harmonic motion input of the system
ship-in-waves should result in a harmonic output, so a linear wave should be produced. It
is known that at high velocity impacts this is not physically correct, a pile-up of water is
generated at the intersection of fluid surface and body and, if the velocity is high enough,
a jet is being produced. It is assumed, that the important parameter for the start of the
formation of pile-up and a jet is the ratio of the horizontal velocity of the intersection

point of body and fluid surface and the phase velocity of the wave that is generated by the oscillating body as expressed by the non-dimensional velocity w', Equation 5.17:

$$w' = \frac{\omega x_{3a}/\tan\beta}{g/\omega} \qquad [-] \qquad (5.17)$$

in which:

x_{3a}	[m]	Amplitude of the vertical oscillation.
ω	$[rad/s]$	Oscillation frequency.

The hypothesis is, that the validity of linear diffraction theory is limited to values of $w' < 1$. If $w' > 1$, the body moves into the fluid faster than the wave that is being produced can move away. The effect of the deadrise angle on this limit is clear, for a deadrise of 90 deg there is no limit and for a deadrise angle of 0 deg the limit is always exceeded.

The ratio of horizontal velocity of the contact point and the phase velocity of the wave can be rewritten as the ratio of the amplitude of the horizontal acceleration of the contact point and the acceleration due to gravity, Equation 5.18, stating that the horizontal acceleration of the contact point should be below g to allow the radiated wave to move away from the body.

$$w' = \frac{\ddot{y}_{CP}}{g} \qquad [-] \qquad (5.18)$$

The validity of this hypothesis has been investigated considering the problem of the oscillating wedge at the free surface, this work has been performed by Hu [78]. A variation of the amplitude and frequency of the oscillation and of the deadrise angle of the wedge have been considered. Calculations have been done using two different programs: a linear 2D diffraction theory and a CFD program based on the VoF method. The results of the CFD calculations have been analysed using a FFT analysis and a force component in-phase with the acceleration of the applied motion and a second one in-phase with the velocity has been determined by multiplying the force signal with these parameters respectively. An equivalent linear damping and added mass coefficient can be determined from these parameters, Equation 5.19.

$$a_{33} = \frac{\omega}{\pi \left(x_{3a}\omega^2\right)^2} \int_{t=0}^{T} FZ\ddot{z}dt$$

$$b_{33} = \frac{\omega}{\pi \left(x_{3a}\omega\right)^2} \int_{t=0}^{T} FZ\dot{z}dt \qquad (5.19)$$

The equivalent damping coefficient is compared to the results of the linear diffraction method in Figure 5.15. This quantity is related to the energy dissipation in the radiated wave and, for high frequencies, in the jet. Up to a certain frequency the results agree
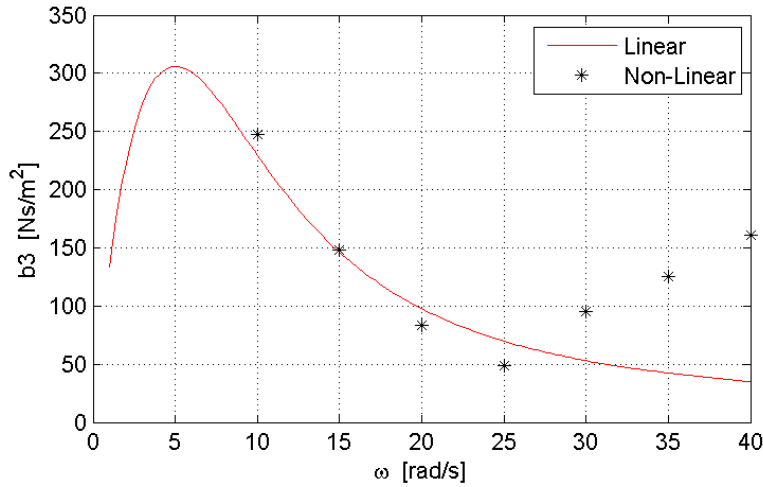
Figure 5.15: Damping coefficient of a 45 deg deadrise angle wedge in oscillating heave motion. Results of linear diffraction theory are compared to CFD results.
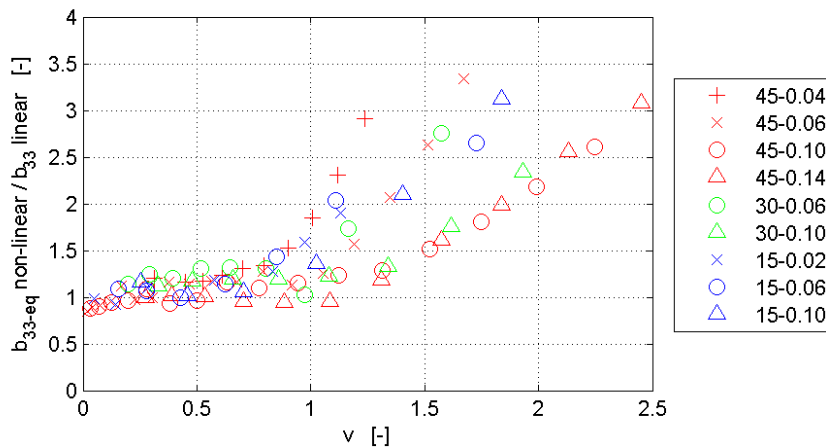
Figure 5.16: Ratio of equivalent damping determined from CFD simulations and linear damping calculated by diffraction theory as function of the non-dimensional velocity of the contact point. The plot shows results for wedges with different deadrise angles and different ampltides. The legend indicates the deadrise angle in degrees and the ratio of the amplitude of the heave motion to the initial draft of the section: x_{3a}/T.

closely and then they deviate. Plotting the results of calculations for wedges with different deadrise angles and different amplitudes of oscillation and replacing the frequency of oscillation by the non-dimensional velocity v', results in Figure 5.16. This figure shows that indeed $v' = 1$ is a reasonable limit of the applicability of linear theory. Based on these results it is concluded that the calculation of pile-up effects should be started at $v' = 1$. A visualisation of the CFD result shows that for this velocity a jet is being generated, indicating also that the limit of linear theory is exceeded.

Time traces of the vertical force on the oscillating wedge have been calculated using the approximate method MMT; the results are compared to results from the CFD pro-

gram. The calculations were carried out for a constant amplitude and an increasing frequency for the different plots. Results are presented in Figure 5.17, 5.18 and 5.19 for values of the velocity parameter ranging from $w' < 1$ to $w' > 10$. These results show that the strong increase of the vertical force amplitude for increasing frequency is well covered by MMT predictions. These predictions do not use a threshold velocity; it is the result of Equation 5.6 augmented with the hydrostatic force. Noted is, that the result in Figure 5.19 represents an extremely violent condition in which the horizontal acceleration of the contact point is larger than 12 times the acceleration due to gravity.
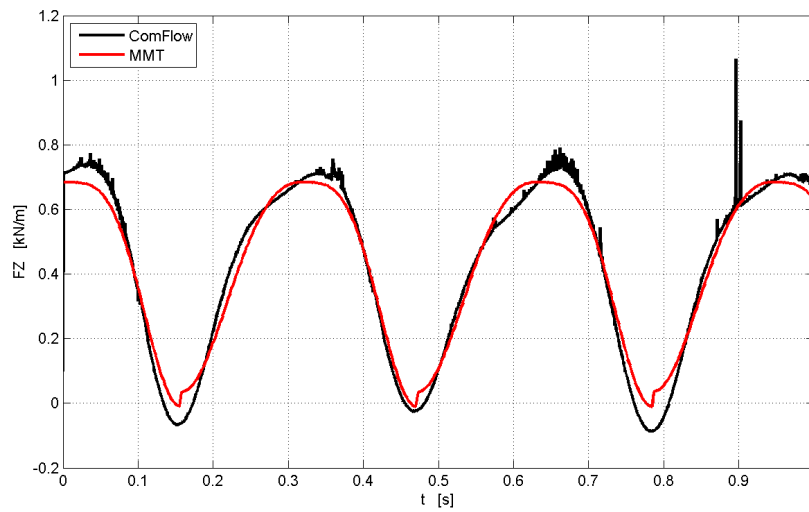
Figure 5.17: Comparison of vertical reaction force of a 45 deg deadrise angle wedge in oscillating heave motion. The figure shows results of COMFLOW *and MMT. Oscillation amplitude* $x3_a/T = 0.10, \omega = 20\ rad/s$. *Non-dimensional velocity* $w' = 0.77$.
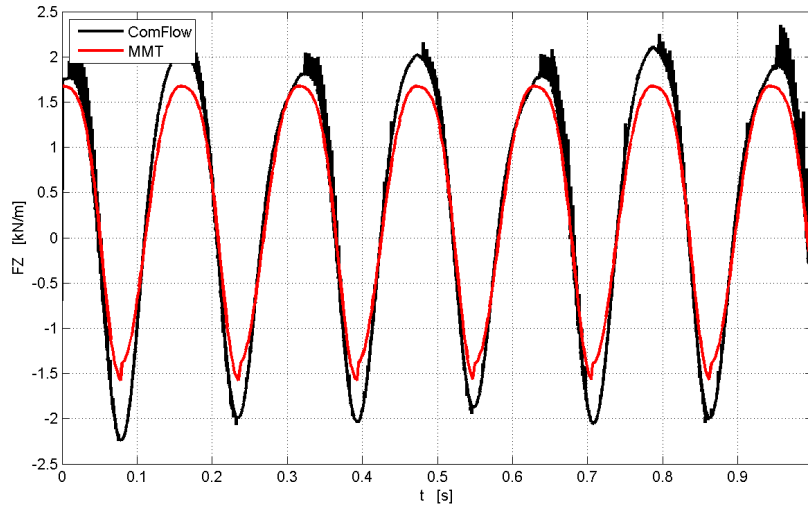
Figure 5.18: Comparison of vertical reaction force of a 45 deg deadrise angle wedge in oscillating heave motion, results of COMFLOW *and MMT. Oscillation amplitude $x3_a/T = 0.10, \omega = 40 \ rad/s$. Non-dimensional velocity $w' = 3.10$.*
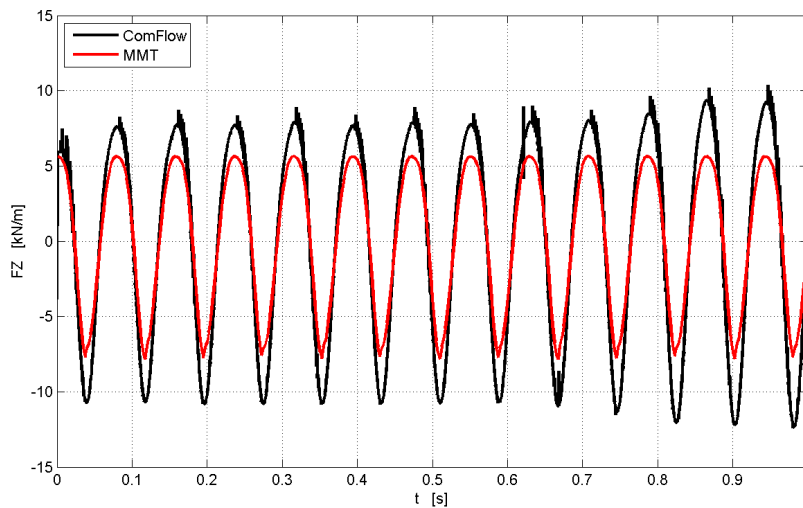
Figure 5.19: Comparison of vertical reaction force of a 45 deg deadrise angle wedge in oscillating heave motion, results of COMFLOW *and MMT. Oscillation amplitude $x3_a/T = 0.10, \omega = 80 \ rad/s$. Non-dimensional velocity $w' = 12.4$.*

5.8   Wave slap loads

A wave impacting against a body is, from a hydrodynamic point of view, a different phenomenon than a body dropping into calm water. The forces on the latter can be estimated by considering the time derivative of the product of added mass and impact velocity as shown in the previous paragraphs. For the wave impacting against a body it is not the change in momentum of the added mass of the body that is relevant, but the change in momentum in the crest of the wave. Although in general this type of impact generates lower forces than the type described before, it is an important area of research for Coastal Engineers as demonstrated in a series of publications on wave impacts against a vertical wall by Bullock, Obhrai, Peregrine and Bredmose [22, 20, 19], for sloshing problems as illustrated by Kaminski and Bogaert [83, 84] and for impact forces on moored objects like FPSO's. In the latter category, the damage inflicted on the bow of the *Schiehallion* FPSO has generated research projects among which the EU project SAFE-FLOW. Results of this project were published by Guedes Soares *et al.* [67] and by de Voogt and Buchner [185]. Overview results of this project were published by Xu, Barltrop and Okan [202, 201]. This project is mentioned here since results of their experiments have been used to validate the force estimation derived in this chapter.

The research mentioned indicates that wave slap loads are not easy to determine. It was demonstrated that repeatability of experiments is rather poor, indicating that details in the impact condition, especially the shape of the impacting wave, are very important. Severe impacts occur when the wave is breaking just before the impact and the run-up against the body meets the jet of the overturning wave. This so-called flip-through condition is studied by many researchers amongst which Lugni *et al.* [118]. It is also apparent that air inclusions play an important role in the physics of the impact problem as shown by Bullock *et al.* [21]. Air inclusions necessitate sub-dividing the impact process in different stages, the Elementary Loading Processes (ELPs), as proposed by Lafeber *et al.* [106]. Each of these ELPs requires a different method to predict full scale values from results obtained by model tests as argued by Bogaert *et al.* [17].

The method to estimate the wave slap load that is developed in the next chapter uses the velocity of the approaching wave. The velocity in the crest of a steep wave has been measured by Skjelbreia [164] using Laser Doppler Velocimetry (LDV) measurements; one of his results is reproduced in Figure 5.20. Grue *et al.* [65] published very similar results from Particle Image Velocimetry (PIV) measurements in a wave flume, Figure 5.21.

In an earlier publication, Grue *et al.* [64], analysed experiments on steep waves in a wave flume. The wave elevation was measured by a single wave probe, the velocities were measured by a PIV system. Grue *et al.* used the trough to trough time (T_{TT}) as the period parameter and they derived from that parameter the local angular velocity $\omega = 2\pi/T_{TT}$. The wave height η_m was determined by the difference of the maximum and minimum value of the wave elevation in the interval between the two troughs. Then they determined the wave number κ and the wave slope parameter ϵ by solving the two Equations 5.20. These equations only give a realistic solution, $\epsilon > 0$, when $\eta_m \omega^2 / g > 1$,
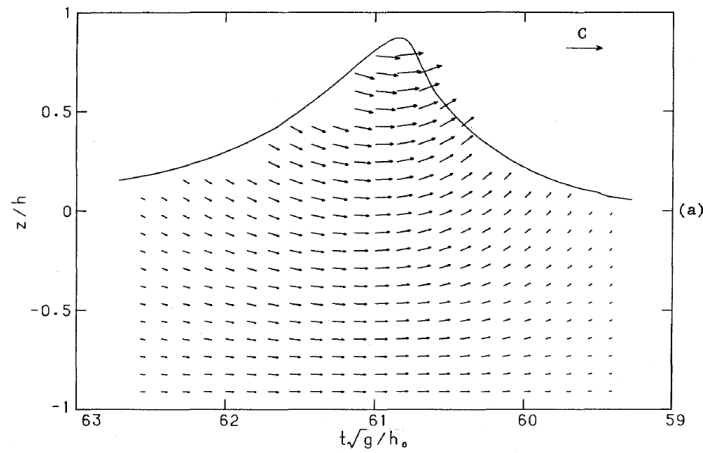
Figure 5.20: Velocity field in the crest of a spilling breaker. Results of LDV measurements by Skjelbreia, [164].
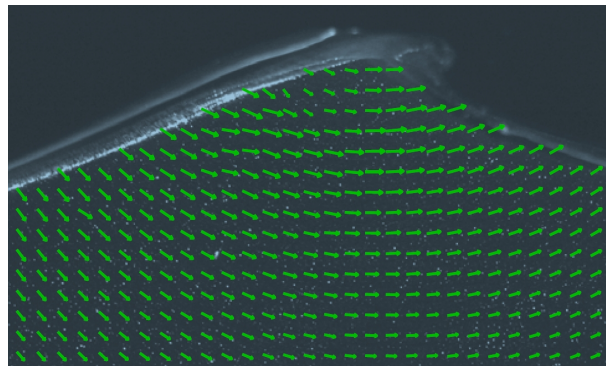
Figure 5.21: Results of PIV measurement of the velocity in a steep wave crest, $\epsilon = 0.34$. Result published by Grue [65].

so sufficiently high waves.

$$\omega^2/(g\kappa) = 1 + \epsilon^2$$
$$\kappa\eta_m = \epsilon + \frac{\epsilon^2}{2} + \frac{\epsilon^3}{2} \tag{5.20}$$

The horizontal velocity in the wave crest could be approximated by an extension of the velocity field below the calm water surface, Equation 5.21. A comparison of this model to the results of the experiments is shown in Figure 5.22.

$$\frac{u}{\epsilon\sqrt{g/\kappa}} = e^{\kappa z} \qquad [-] \tag{5.21}$$
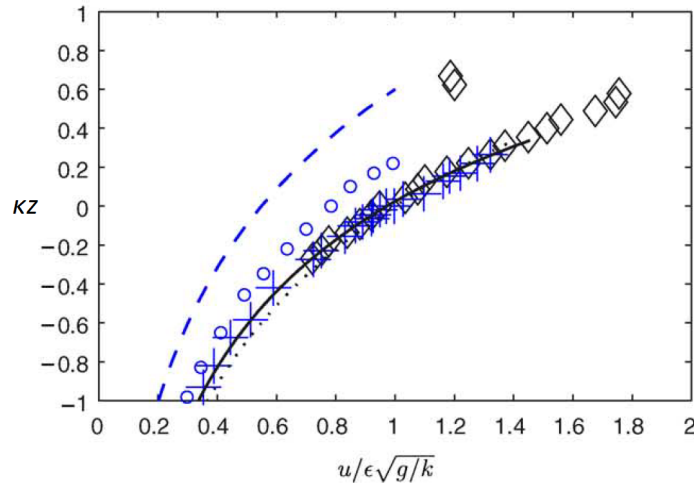
Figure 5.22: Profile of the horizontal velocity in a wave crest. Results of LDV measurements published by Baldock et al. [9] (+), results from PIV measurements by Grue et al. [64] (◇) for waves with $\epsilon = 0.46$, results from 2nd order model by Baldock et al. (1996) [9] (○). Solid line: result of approximation by Grue et al. (2003), dotted line: $e^{\kappa z}$, dashed line: Wheeler stretching [193].

5.8.1 Approximate method for wave slap loads

Modelling the details of the impact of an overturning wave against an object is a bridge too far for this approximate method. Apart from computational problems and time required to find a solution, the wave model used in the simulation must be able to generate the shape and physics of overturning waves; at present it is not capable of doing so. In fact, the wave model is based on linear theory. Therefore the method developed here aims at modelling the impacts due to steep - but not overturning - waves. This restriction excludes air inclusions and its associated problems.

The approximate method is based on a comparable approach as the method to estimate the force due to essentially a drop test. Since, apart from the pile-up, free surface effects are irrelevant during the impact, the impact of a curved water surface (like a wave crest) against a flat body can be considered equivalent to the impact of a curved body on flat water; this is illustrated in Figure 5.23. Essentially there is no rigid body in potential flow theory, the problem can be solved as a BVP with a boundary condition on the body stating that the normal velocity must be zero: $\vec{v}.\vec{n} = 0$. This approach makes the two problems equivalent.

The problem is further simplified by considering the impacting body as a semi-wedge impacting in a fluid. The wedge axis of symmetry is oriented horizontally with the vertex at the z=0 plane at the moment of the impact. The impact velocity is equal to the wave propagation velocity, this is considered an acceptable approximation for non-breaking waves as shown in the previous chapter.

Using the sketch in Figure 5.24, the hull is considered as the fluid and the wave crest as the impacting wedge. The apex of the wedge is at the calm water surface. The wetted
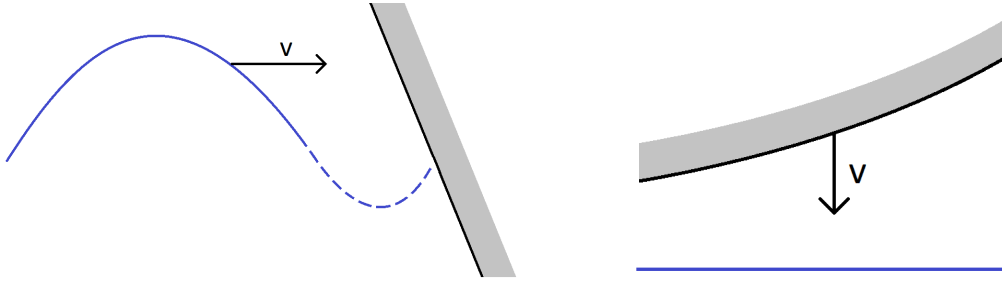
Figure 5.23: Model used to describe wave slap loads. The wave approaching the fixed body (left) is treated as a body dropping in calm water (right). The curved body is treated as a semi-wedge.
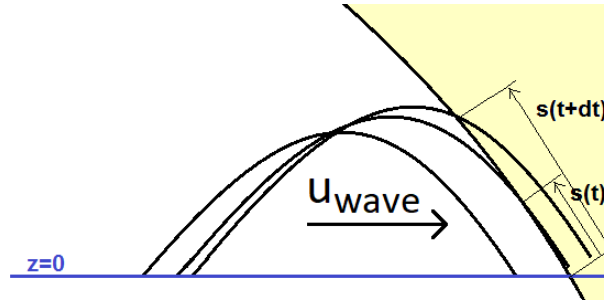
Figure 5.24: Definition sketch of a wave impacting against a ships hull.

length s is the wetted part of the semi-wedge, the time derivative $\dot{s}(t)$ is used as a measure for the rate of change of the added mass.

If we use again Wagner's formula for the added mass of a wedge, Equation 5.9, assume the deadrise angle $\beta = 0$ and replace the actual (including pile-up) wetted width of the wedge y^* by the parameter s along the hull, divide by two since we model the wave slap load as the impact of half a wedge, we have:

$$\frac{\partial a_{33}}{\partial t} = \rho\, \pi/2\, s\, \dot{s} \qquad [kg/ms] \qquad (5.22)$$

This added mass derivative must be multiplied with the component normal to the hull of the velocity of the wave relative to the body, Equation 5.23. It was assumed that horizontal velocity u_{wave} is constant over the height of the wave above $z = 0$; the model used does not allow for a realistic exponential velocity distribution. The approximate wave slap load is determined from the added mass, the rate of change of the added mass and the relative velocity, Equation 5.24.

$$u_N = T_{(e)}^{(b)}\, \vec{u}_{\text{wave}}^{(e)} \cdot \vec{n} \qquad [m/s] \qquad (5.23)$$

$$F_{\text{SLAP}} = \rho\frac{\pi}{2}\left(s\,\dot{s}\,u_N + \frac{s^2}{2}\dot{u_N}\right) \qquad [N/m] \qquad (5.24)$$
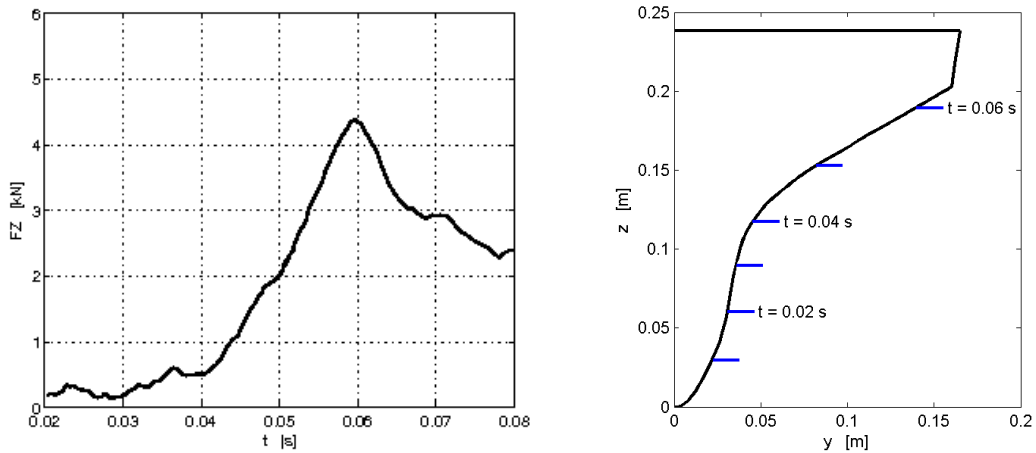
Figure 5.25: Left figure: Measured vertical force during the impact of a ship section, results by Zhao et al. [207]. Right: Indication of water level along the section using the measured velocity and the pile-up estimate presented in this chapter.

This load F_{SLAP} is the load normal to the hull; it must be multiplied with the components of the normal vector on the hull to arrive at the forces in the different directions. The validation of this approach will be shown in Section 5.13.

5.9 The effect of submerging chines

The effect of chines on the impact force is quite pronounced. It is assumed, and confirmed by experiments, that the flow separates at the chine, so the pressure peak at the intersection point disappears as soon as the root of the jet passes the chine. Fairlie-Clark and Tveitnes (2008) [48] used CFD to calculate impacts of wedges and to analyse the results in terms of added mass and pile-up parameters for the chines-dry and the chines-wetted phase of the impact. They found that the added mass continues to increase, up to 10%, after immersion of the chines; they suppose that this is due to dynamic effects at the chine where the jet separates from the section and continues outward. This effect is not apparent at high deadrise angles (30 and 45 deg).

Results of experiments with a ship section with a clear knuckle were presented by Zhao *et al.* [207]. The measured impact force shows a pronounced peak at $t = 0.060\ s$, Figure 5.25. If the measured velocity is integrated, the water level reaches the knuckle at $t = 0.076\ s$, but this is without taking pile-up effects into account. Using the pile-up calculation method presented in this chapter, the water level reaches the knuckle at $t = 0.064\ s$ showing good agreement with the measurements. The calculated water level is indicated along the section profile in Figure 5.25.

Calculation methods impose this phenomenon by assuming a Kutta-condition at the

knuckle point; this approach has been used by, for instance, Zhao and Faltinsen in 1998 [206] and by Iafrati and Battistin in 2003 [80]. This approach has been demonstrated to work well for a clearly defined knuckle. For a rounded section the separation point cannot be easily defined before hand; an empirical trigger to force flow separation in a BEM has been introduced by Sun and Faltinsen [171] when they studied the impact of a horizontal circular cylinder.

The approximate method MMT calculates a sudden drop of the added mass derivative $\partial a_{33}/\partial z$ at the knuckle point. As a consequence, the impact force also drops suddenly which is a reasonable approximation of the flow separation effect. This point will be demonstrated in Section 5.12 where the geometry and the experimental result shown in Figure 5.25 will be used in a validation exercise.

5.10   The water exit problem

There is very little information on the water exit problem due to the simple fact that it is hardly ever experienced as a problem in the sense of high pressures being created. Theoretically, water exit is an identical problem as water entry and it would create similar pressure peaks as has been argued by Moran (1965) [135], Greenhow (1988) [59] and Piro (2012) [146]. In practice, an area on the body and close to the free surface will be ventilated in case of a high negative pressure. Therefore the pressure in such an area reduces no further than the atmospheric pressure. Deeper in the fluid, the pressure can drop to lower values than atmospheric pressure which results in water being pulled up together with the exiting section Figure 5.26. A similar condition exists for water falling from underneath a horizontal deck, after it has been hit by a wave crest and large negative forces have been measured as shown by Scharnke and Hennig (2015) [158] and Scharnke and Lafeber (2016) [159]. The lower limit of the pressure is obviously the vapour pressure of the fluid.

Experiments were carried out by Tveitnes *et al.* [182] using a set-up for forced water
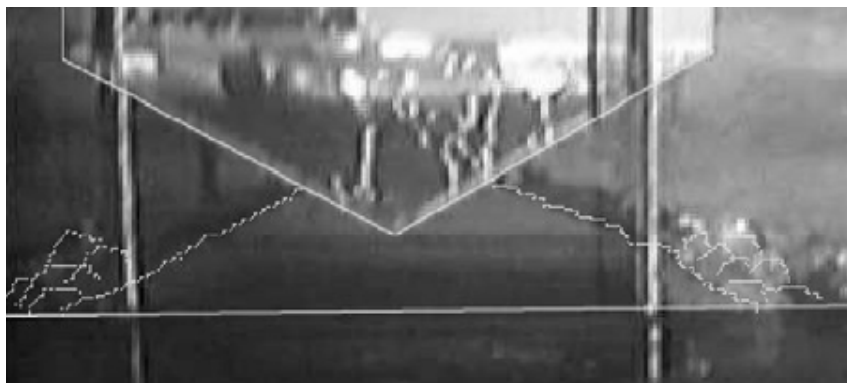
Figure 5.26: Video still from water exit test of a 30 deg deadrise angle wedge,
           Tveitnes et al. [182]

.

entry and exit tests on 2D sections. The set-up allowed experiments at constant velocity; end plates were used to create 2D flow conditions. The models used for the exit tests consisted of wedges with deadrise angles of 10, 15, 30 and 45 deg. Stills from the video taken during the tests showed water being lifted together with the section, Figure 5.26. The measured result showed that the hydrodynamic force consisted of the buoyancy force and an oscillating force component. These oscillations were also present during the water entry tests and were quoted to be caused by flexibility in the test sections. Results for the 10 and 45 deg wedges are shown in Figure 5.27. Similar effects were visualised for the water exit problem of a sphere by Wu *et al.* [197].

From the work presented and discussed in this section, it is concluded that using the only the buoyancy force during the water exit phase is a sufficiently accurate approximation.
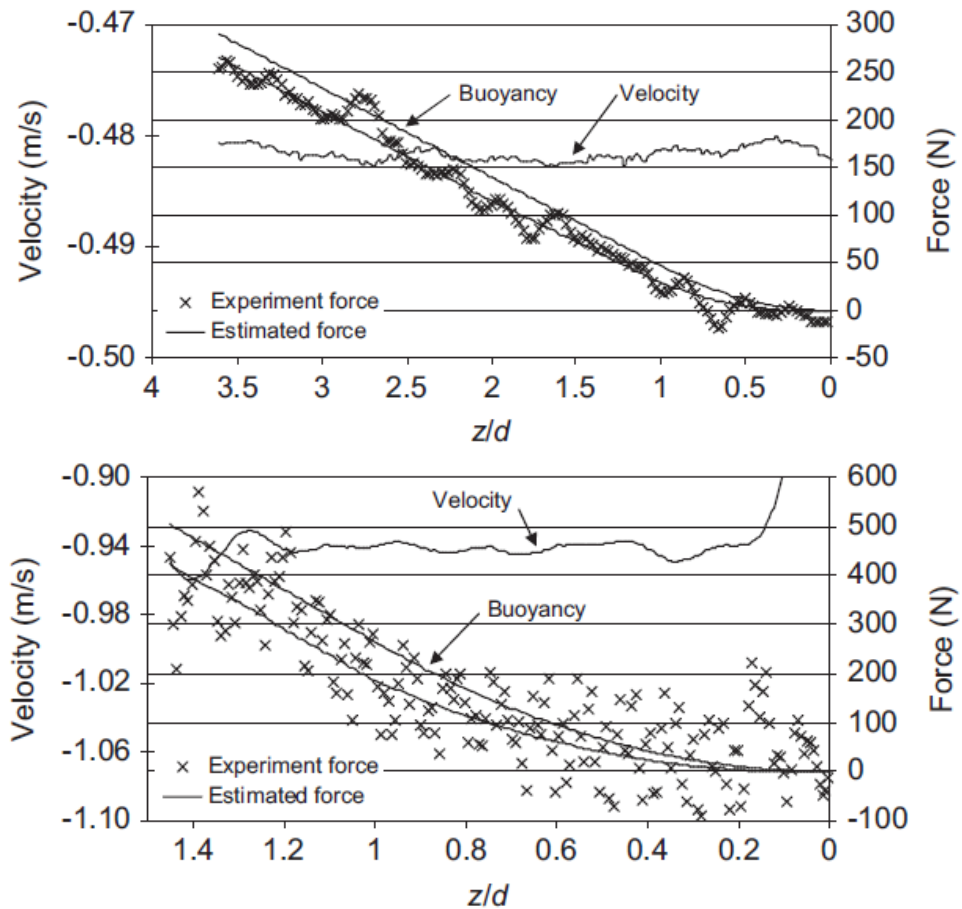
Figure 5.27: Water exit force of a 10 deg deadrise (top) and a 45 deg deadrise wedge (bottom) as measured by Tveitnes et al. [182].

5.11 Verification: Results for a wedge

Since the method presented is based on wedges, this section should be considered as a verification. Use has been made of experiments carried out at MARINTEK in Norway and published by Zhao *et al.* [207]. The set-up of the experiment consisted of a test rig with a fixed guiding system and a large frame dropping down. The test section was fitted via a force sensor to the frame. The test section was essentially a 2D section of a small 'live' part in between two dummy sections. The experiments were carried out as a free drop test, as a consequence the velocity was not constant. The raw data resulting from the experiments were not available; the vertical velocity and force time records have been reproduced from plots in the publication.

The impulsive force calculation makes use of an earth fixed reference frame YZ^E. A number of parameters are defined in this reference frame that are illustrated in Figure 5.28. The force calculation consists of the rate of change of the impulse as defined in Equation 5.4 and added to it the hydrostatic force:

$$F_{\mathrm{MMT}} = \frac{\partial a_{33}}{\partial z}\dot{z}\dot{z}^* + a_{33}\ddot{z} + \rho g z y \qquad [N/m] \tag{5.25}$$

in which:

y	the half-width of the wedge at the undisturbed water surface
y^*	the half-width of the wedge at distance $(z_0 + z^*)$ from the vertex
z	the immersion of the vertex of the wedge relative to the undisturbed water surface
z^*	the rise of the water surface - body intersection point
$\dot{z}$	the vertical velocity in the earth fixed reference frame
$\ddot{z}$	the vertical acceleration of the wedge
$\frac{\partial a_{33}}{\partial z}$	the added mass derivative based on the total immersion $(z_0 + z^*)$. For a wedge it is based on Wagner's analytical expression [187].

$$a_{33} = \rho\frac{\pi}{2}\left(1 - \frac{\beta}{2\pi}\right)^2 \frac{z^2}{\tan^2\beta} \qquad [kg/m] \tag{5.26}$$
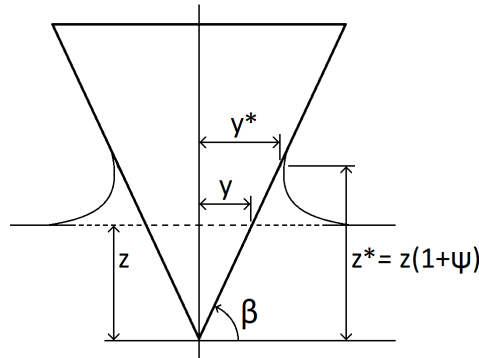
Figure 5.28: Definition of parameters for an impacting wedge
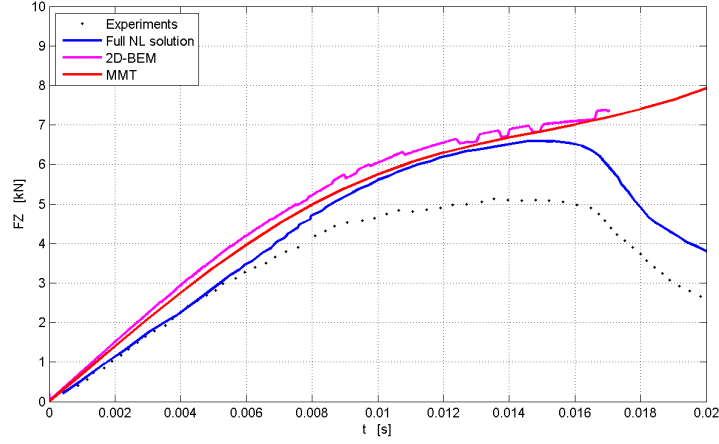
Figure 5.29: Results from drop tests of a 30 deg deadrise wedge. The plot shows experimental results published by Zhao et al. [207], calculations using 2D-BEM, the NL solution published by Zhao [207] and MMT. The calculations use the measured velocity.
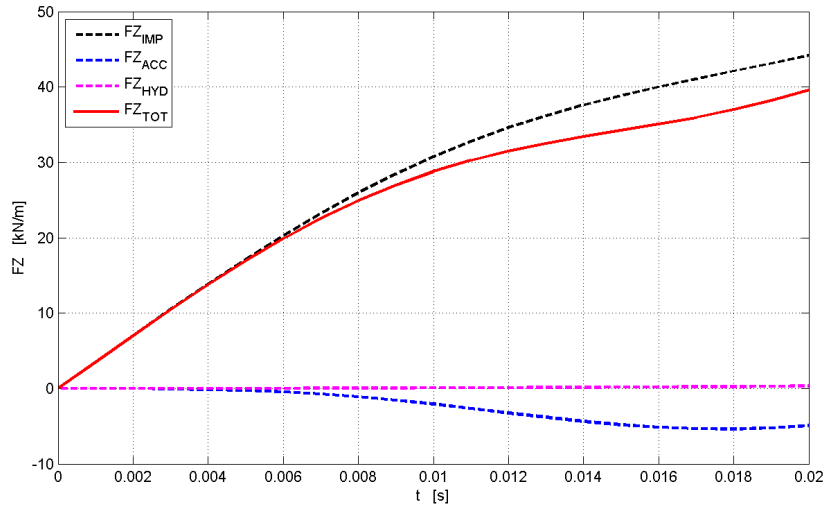
Figure 5.30: Components of the impact force on the 30 deg wedge. The impulsive force (black dashed line) is a little larger than the total force (red line). The hydrostatic force (cyan) is close to zero and the acceleration force (blue dashed line) is slightly negative due to the deceleration of the wedge during the impact.

This expression is used to derive the added mass derivative:

$$\frac{\partial a_{33}}{\partial z} = \rho \pi \left(1 - \frac{\beta}{2\pi} \right)^2 \frac{z}{\tan^2 \beta} \qquad [kg/m^2] \qquad (5.27)$$

The results are shown in Figure 5.29. The results of this approximate method MMT are very close to the result of 2D-BEM and to the full non-linear solution as developed by Zhao *et al.* [207], also shown in Figure 5.29. In their publication, Zhao *et al.* attribute the differences between their solution and the experimental results - the calculated peak

force is about 20% higher - to 3D effects for which they quote Meyerhoff's results, [128]. These 3D effects reduce the peak of the impact force with a factor 0.80.

The different components of the force calculated by MMT, Equation 5.25, are shown in Figure 5.30. The main force component is the impulsive force, there is a negative contribution of the added mass because of the deceleration of the wedge during the impact. The hydrostatic force is very small for this case.

5.12   Validation: Results for a ship like section

The real proof of method - on a 2D level - is the comparison of measured and calculated values for a ship section. Again use has been made of results published by Zhao *et al.* [207]; their second experiment consisted of a ship like section, Figure 5.31, with a considerable flare and a knuckle. The experiment has been carried out in the same manner and using the same test rig as the experiment on the wedge. The test section of this experiment is only half as long as the one for the wedge while the length of the full impacting body was kept the same. In this way the 3D effects are reduced.

The result of the approximate method is compared to the experimental result in Figure 5.32. The calculations show results that are in-line with the approximate method 2D-BEM and over-predicting the maximum experimental load 15%, while the predictions for the wedge were about 20% larger than the experimental result. The components of the vertical force shown in Figure 5.33 again illustrate the very dominant contribution of the component based on the rate of change of the added mass.
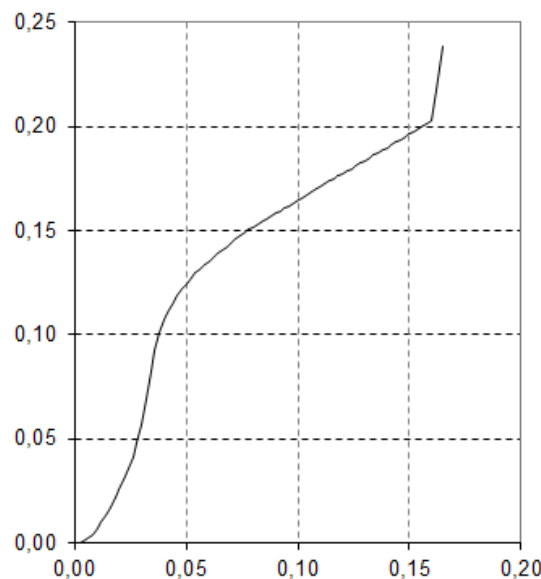
Figure 5.31: Geometry of the ship section used for the impact tests by Zhao et al. [207].
    Dimensions are in [m].
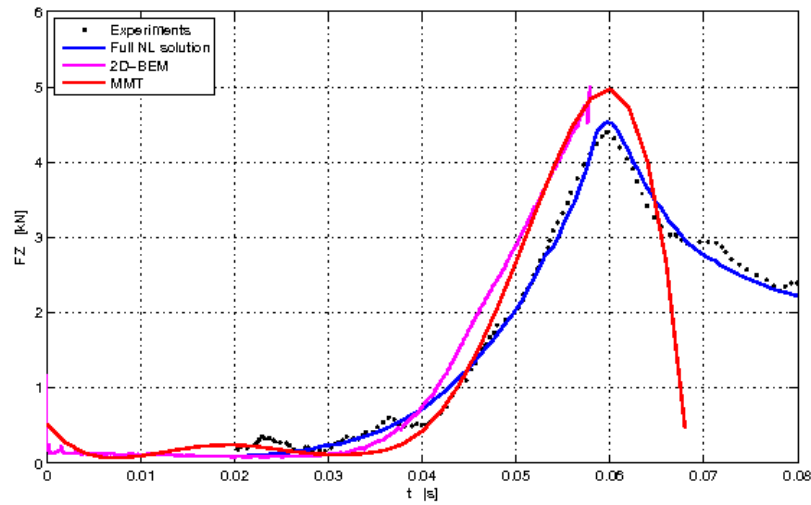
Figure 5.32: Results from drop tests of a ship section. The plot shows experimental results published by Zhao et al. [207], calculations using 2D-BEM, the NL solution published by Zhao [207] and MMT. The calculations use the measured velocity.
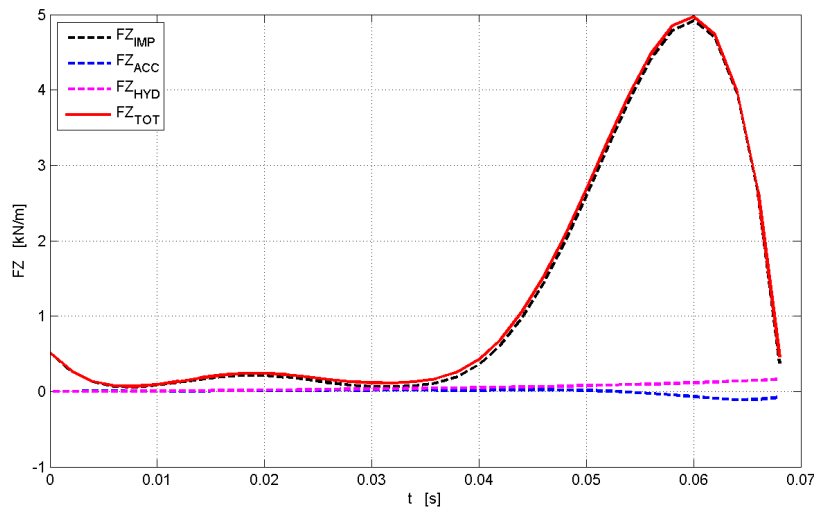
Figure 5.33: Components of the impact force on the ship section. The impulsive force (black dashed line) is very close to the total force (red line). The hydrostatic force (cyan) is slightly positive and the acceleration force (blue dashed line) is slightly negative.

5.13 Validation: Results for wave slap loads

The validation of the model for wave slap loads makes use of the results of the EU - SafeFlow project that was carried out in the period from January 2001 - December 2004. A part of the experimental program consisted of wave impact measurements against a flat plate, tilted by 15 deg in the direction of the incoming wave. The plate was instrumented with 40 pressure gauges in a matrix as indicated in Figure 5.34. The wave was measured by

an array of 6 wave height gauges just in front of the plate. The set-up of the experiments in the MARIN Offshore Basin is shown in a picture in Figure 5.35. Part of the results of these experiments were published by Voogt and Buchner in 2004 [185].

The objective of the experiments was to measure wave slapping loads on a simplified structure in conditions with breaking waves. The background of the experiment was the already mentioned damage inflicted on the bow of the *Schiehallion* FPSO. Long duration measurements were first carried out in an irregular sea state, from these results some critical events were selected and 10 repeat tests were carried out for such an event. The results showed that even repeat tests resulted in quite different wave slap loads as is illustrated in Figure 5.37.

The propagation speed of the wave was determined from the signals of the six wave gauges, the actual wave profile for the calculation of the wave slap load was taken from the measurement of the wave gauge closest to the plate while delaying the wave elevation signal with the time needed for the wave to travel the distance from this wave gauge to the plate. This approach assumes that the shape of the wave does not change in this extrapolation. The force on the plate was not directly measured, it was estimated from the total of all pressure gauges, each with its associated area of $3.0 * 4.5 \ m^2$.

The signals from the pressure gauges indicate that indeed the wave was breaking just before the impact. Figure 5.38 shows that only the pressure gauges on rows 4 and 5 have a high peak pressure. The calculations were carried out using Equation 5.24 augmented with a curling factor ($\lambda = 0.5$) as often is used for impacts due to breaking waves by for
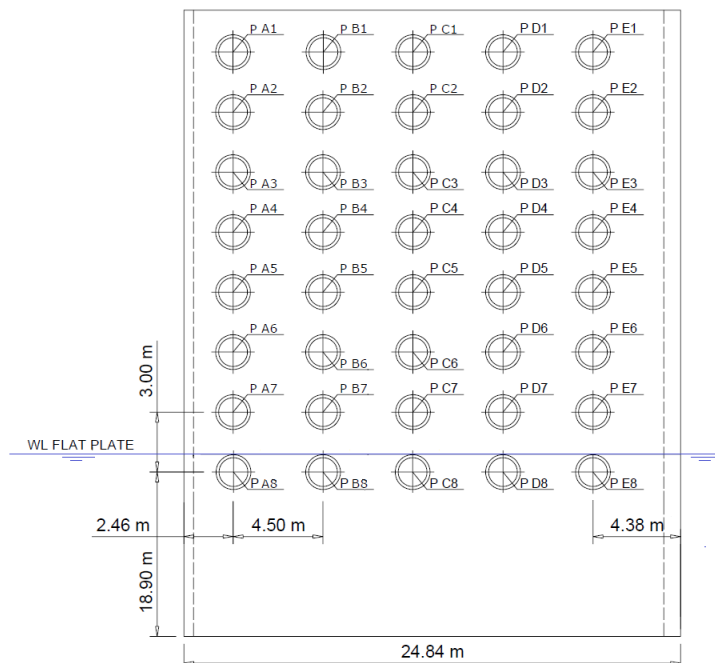
Figure 5.34: Instrumentation of the vertical plate used in the wave impact tests of the SafeFlow project. Dimensions are full-scale values; the experiments were carried out at scale 60.
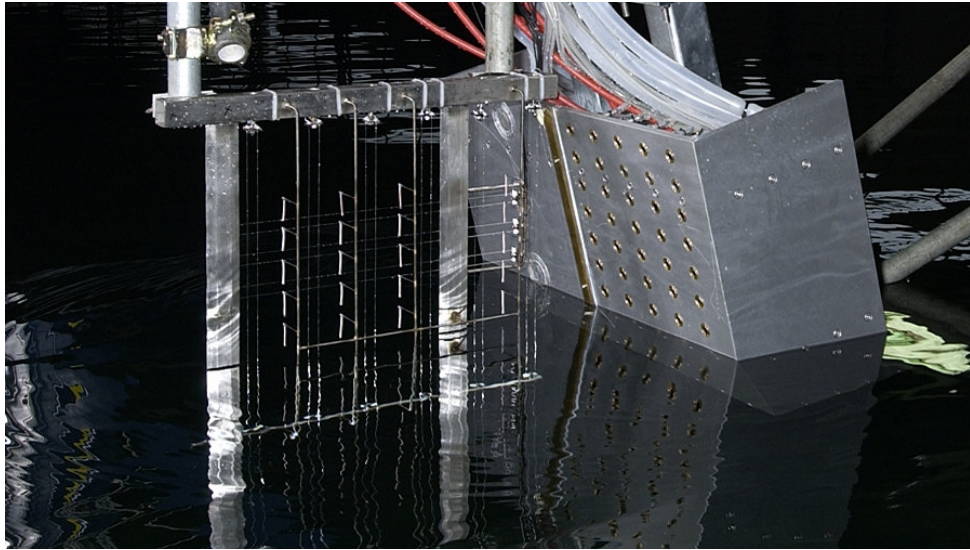
Figure 5.35: Set-up of the wave impact tests for the SafeFlow project in the MARIN Offshore Basin.
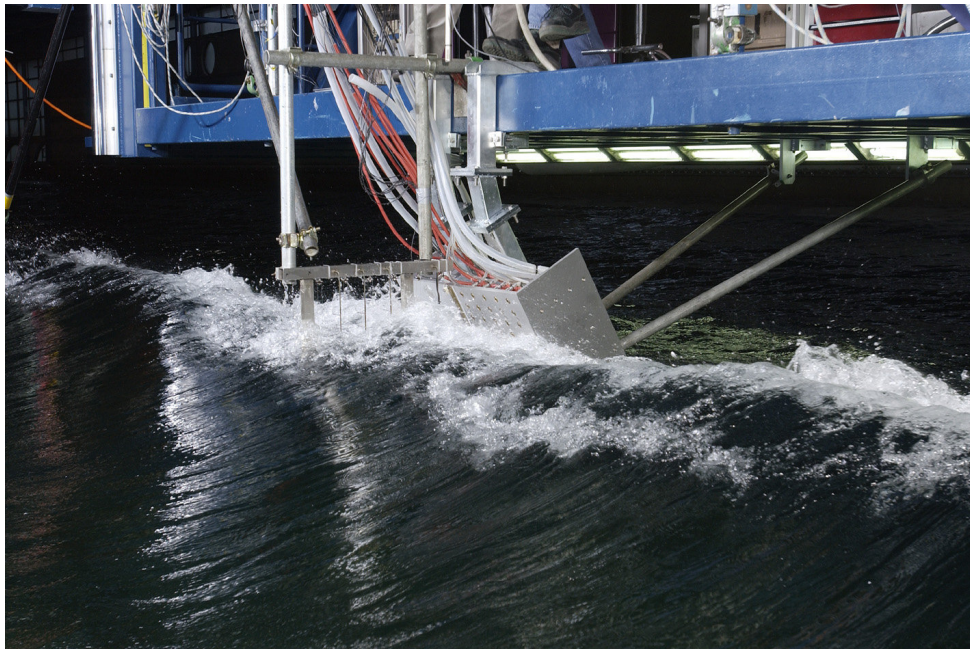
Figure 5.36: Measurement of wave slap load due to a breaking wave. The picture is taken just before the impact.

instance Wienke, Sparboom and Oumeraci [194]. The curling factor is just a multiplier for the impact force, it is used to account for the local effect of the high horizontal velocity in the breaking wave crest. The calculation of the wave slap force is continued until the intersection point of the water surface and the plate reaches the top of the plate; at that time instant the force is set to zero. The result of this approach is far from perfect, but it satisfies the requirement of a reasonable estimate of the magnitude and duration of the impulsive force as illustrated in Figure 5.39.
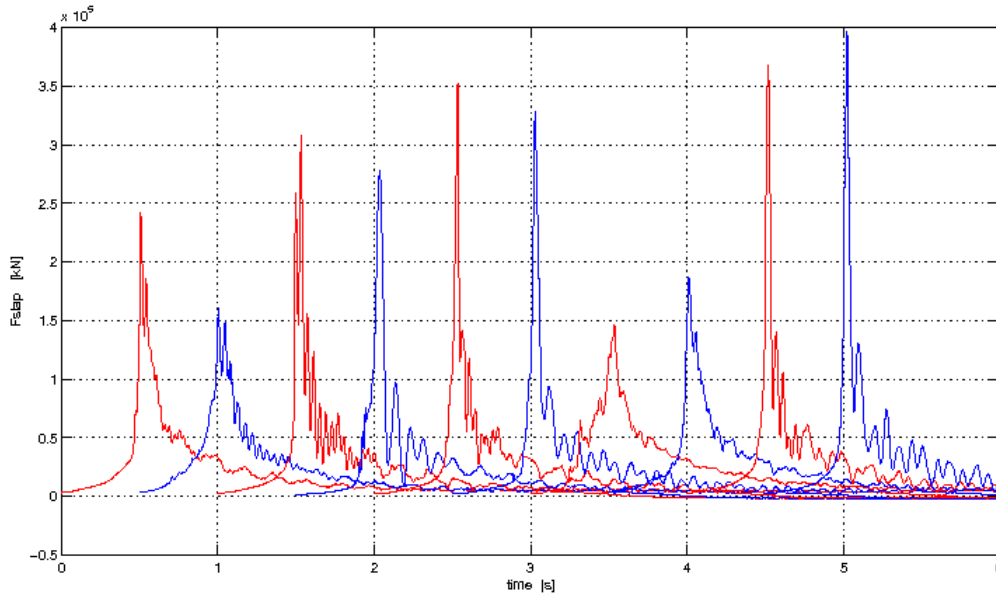
Figure 5.37: Results of wave slap loads of 10 repeat experiments. Each force is plotted with an additional time shift of 0.5 s.

For another experiment within this series, the wave did not break in front of the plate. The pressure signals show then a pressure pulse rising over the plate with a velocity in the order of 30 m/s as can be derived from the time difference of the pressure pulse in subsequent rows in Figure 5.40. Consequently, the force signal shows a much more gradual rise which is well captured by the prediction model, Figure 5.41. Figure 5.40 also shows that the pressure ridge has a high peak value for only rows 4 to 6, the top 3 rows hardly show a pressure peak. MMT predicts a force over the full height of the plate due to the pile-up effect. This explains why the wave slap force is over-predicted and it illustrates the limitations of the approach chosen.
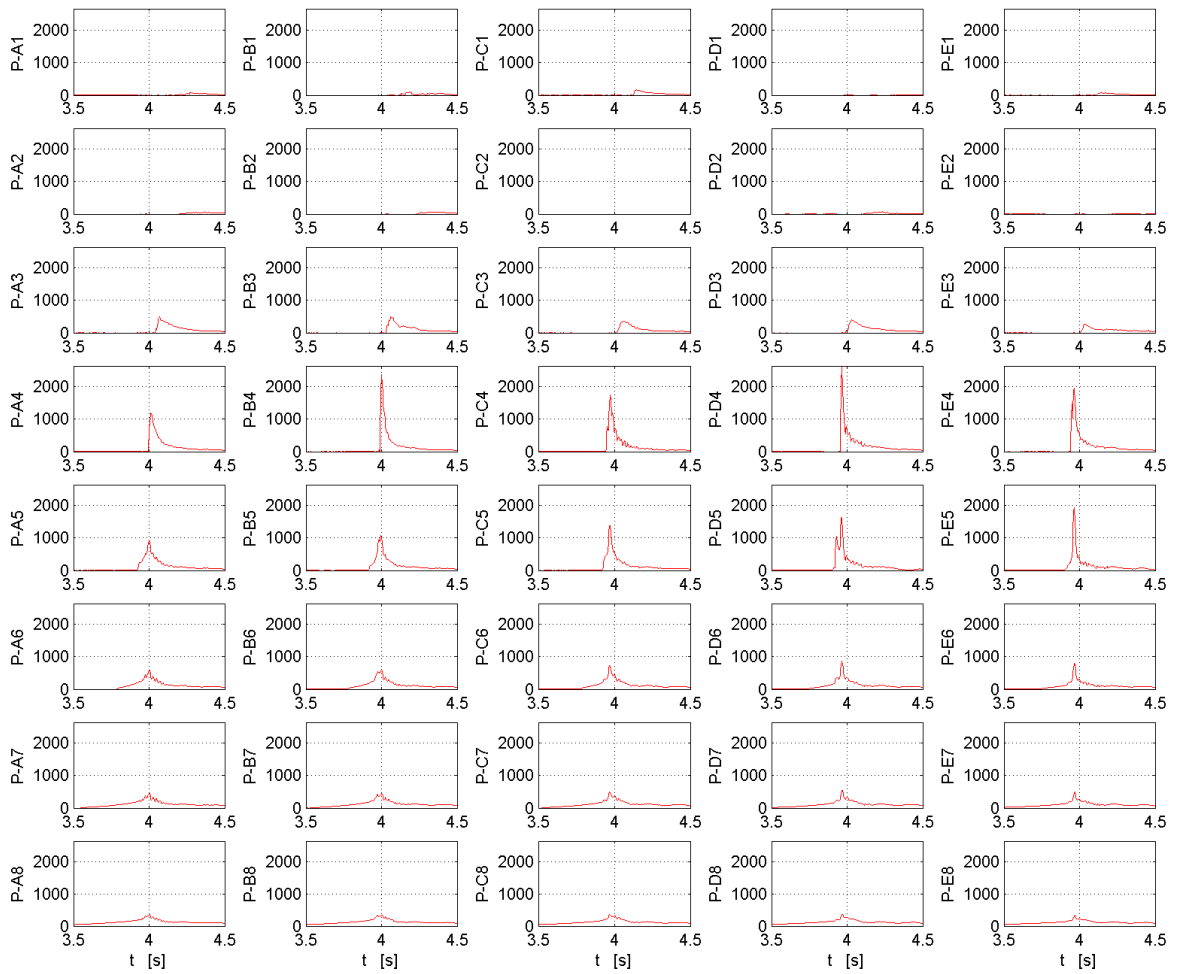
Figure 5.38: Pressures due to a wave impact against a flat plate, tilt angle 15 deg. The wave did break just before the impact. The total force on the plate is shown in Figure 5.39.
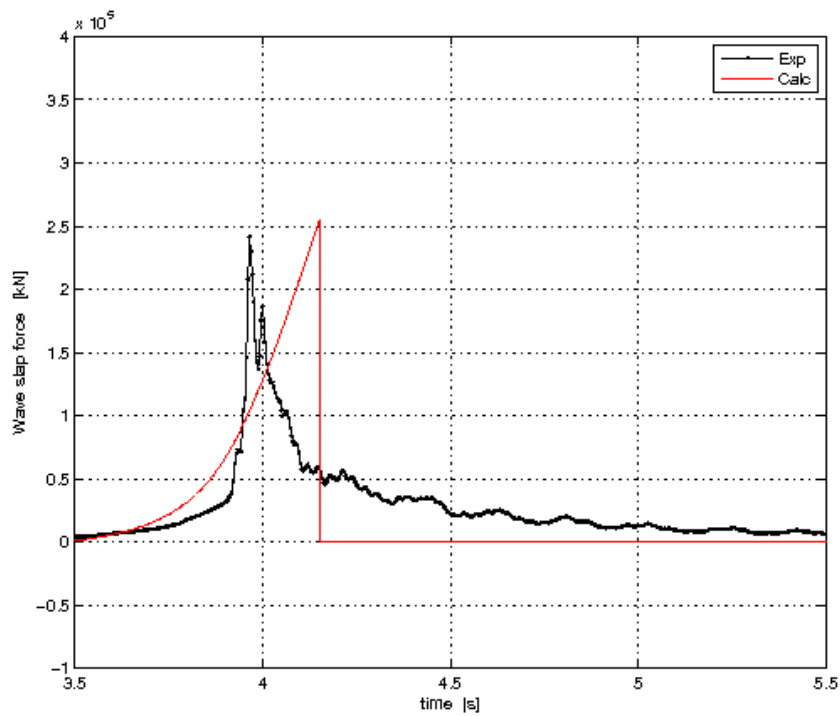
Figure 5.39: Wave slap load due to a wave impact against a flat plate, tilt angle 15 deg. The wave did break just before the impact. Results from the total of the pressure gauges and the approximate model.
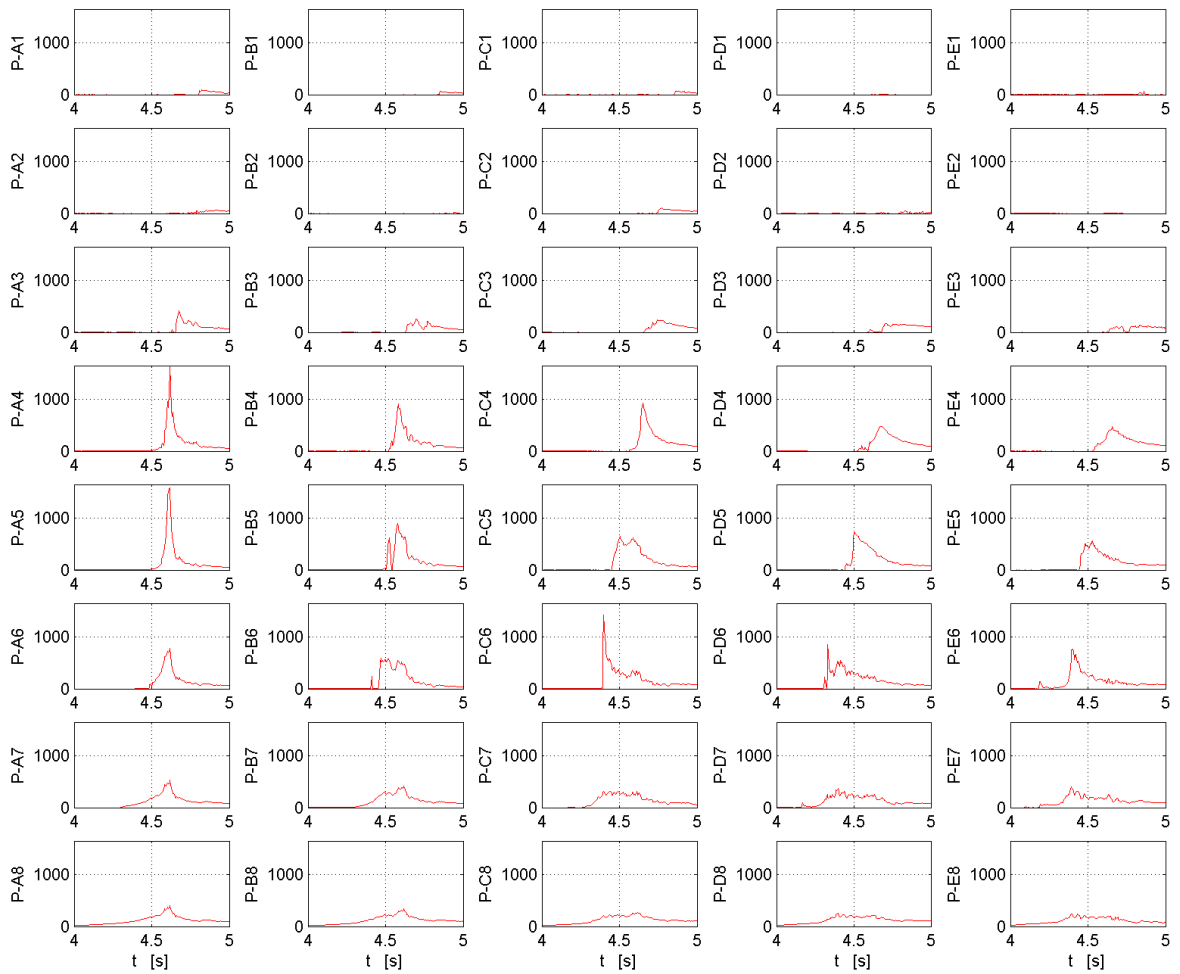
Figure 5.40: Pressures due to a wave impact against a flat plate, tilt angle 15 deg. The wave did not break before the impact. The total force on the plate is shown in Figure 5.41.
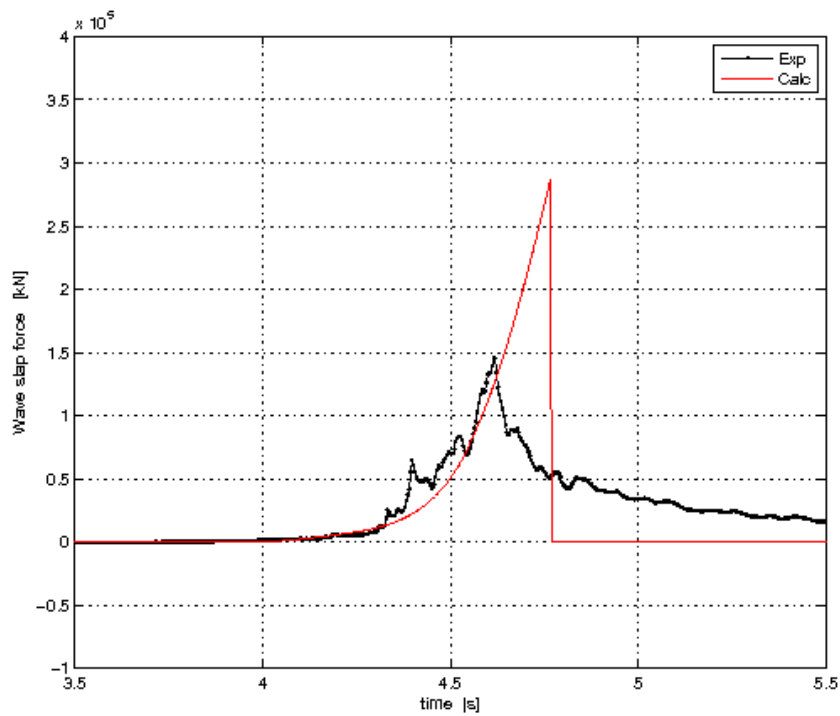
Figure 5.41: Wave slap load due to a wave impact against a flat plate, tilt angle 15 deg. The wave was steep but did not break before the impact. Results from the total of the pressure gauges and the approximate model.

5.14   Conclusions for the approximate model

This chapter discussed the building blocks of the approximate model in detail. Summarized these building blocks are:

- The impact force consists of two distinct cases: one due to the effect of a body having an earth fixed velocity entering a fluid (the impulsive force) and a second one due to a wave hitting a body that does not move in the earth fixed reference frame (the wave slap force).

- The impulsive force is determined by the change in time of the added mass times the earth fixed velocity.

- The wave slap force is determined by the velocity of the wave crest relative to the body.

- The pile-up factor is a very important component that increases significantly the relative velocity, the rate of change of the added mass and hence the change in impulse and the impulsive force.

- For a low relative velocity, the hydrodynamic force can be approximated by linear potential flow theory; at high relative velocity, impact forces are important. The cross-over between these components is, when the local lateral acceleration of the contact point of water surface and body exceeds the acceleration due to gravity.

- Impact forces need to be considered for a positive value of the relative vertical velocity (immersion of the body). For a negative value of the relative vertical velocity (water exit), the hydrodynamic forces are well approximated by the hydrostatic force only.

- If the waterline intersection point reaches the upper limit of the body or a chine, the impulsive force immediately disappears. If the point of flow separation is not clear, like for a convex section shape, no firm conclusion can be drawn.

- The main part of the impulsive force is generated at the waterline intersection point. Therefore this point can be chosen as point of application of the impulsive force to calculate moments.

Chapter 6

Application of momentum theory to ships

6.1 Approach

The problem of slamming on ships sailing in waves

The problem of a body impacting in a fluid at rest was discussed in the previous chapter. For the major part the discussion focussed on impacting 2D sections. When a ship sailing in waves is considered, not all impacts can be modelled as an impacting body in calm water. Such an approach can be used in case the fore body of a ship fully emerges and re-enters, but significant impacts can also occur if the conditions are less extreme and the fore body does not completely emerges. Such conditions could occur in a rising sea with short - relative to the ship length - and steep waves. Ship motions are then small and severe impacts can occur if the relative angle between the hull and the wave surface is small. Such conditions are referred to as wave slapping; the accident with the *Schiehallion* FPSO in 1998 renewed interest in this area.

Using the concepts of linear seakeeping theory, the first type of impact is related to an extreme form of the radiation problem, the second to a non-linear form of wave diffraction. The distinction between these two types of impacts is important in two ways. The first aspect is the physical process involved, the second is in combining the estimation of the impact force with the forces calculated by linear seakeeping theory and avoiding 'double counts'.

The physical processes involved in a body impacting in waves and wave slapping are different. In the first case, an amount of water underneath the complete body is suddenly accelerated; the force required to increase the impulse of this amount of water is the slamming force. In the case of wave slapping, the impulse in the moving mass of fluid in the wave crest is changed in a short period of time. Therefore not only the shape of the section is relevant, but also the shape and velocity of the wave crest as it impacts on the hull.

6.2   Added mass derivatives for a ship

The theory presented in Chapter 5 can be applied to the 3D problem of a ship at speed with some enhancements, the main ones are the effect of the draft dependent bow wave and the (lack of) impulsive loads on the leeward side of the bow in quartering seas conditions. Comparing results of impacts against the bow stem of the vessel showed the need for such an enhancement as will be shown later in this chapter.

Since the Equations 6.1 using the added mass derivatives require the change in total added mass (of the section) rather than the contribution of individual panels, the choice has been made to re-arrange the results of the solution of the BVP over the panels. All results of the BVPs are mapped to a Cartesian grid that is projected on the impact area of interest. This grid consists of nz horizontal rows in the range $z_{\mathrm{LOW}} - z_{\mathrm{UP}}$ and nx vertical columns in the range $x_{\mathrm{LOW}} - x_{\mathrm{UP}}$. These rows and columns are defined in Equation 6.2; an example is given in Figure 6.1.

$$F_{X-\mathrm{Imp}}^{(e)} = -\left(\frac{\partial a_{11}\left(x,z\right)}{\partial x} u^{(b)} + \frac{\partial a_{11}\left(x,z\right)}{\partial z} w^{(b)} \right) u^{(e)} + a_{11}\left(z\right) \dot{u}^{(e)} \qquad [N/m]$$

$$F_{Y-\mathrm{Imp}}^{(e)} = -\left(\frac{\partial a_{22}\left(x,z\right)}{\partial x} u^{(b)} + \frac{\partial a_{22}\left(x,z\right)}{\partial z} w^{(b)} \right) v^{(e)} + a_{22}\left(z\right) \dot{v}^{(e)} \qquad [N/m] \qquad (6.1)$$

$$F_{Z-\mathrm{Imp}}^{(e)} = -\left(\frac{\partial a_{33}\left(x,z\right)}{\partial x} u^{(b)} + \frac{\partial a_{33}\left(x,z\right)}{\partial z} w^{(b)} \right) w^{(e)} + a_{33}\left(z\right) \dot{w}^{(e)} \qquad [N/m]$$

$$x_{ix} = x_{LOW} + (ix - 1)\,\Delta x \qquad [ix = 1 \dots nx]$$
$$z_{iz} = z_{LOW} + (iz - 1)\,\Delta z \qquad [iz = 1 \dots nz] \qquad (6.2)$$

and:

$$\Delta x = (x_{UP} - x_{LOW})/(nx - 1)$$
$$\Delta z = (z_{UP} - z_{LOW})/(nz - 1)$$

A 'normal', non-Cartesian panelization (on top in Figure 6.1) is used to solve the BVP to find the added mass coefficients. This panelization is cut for each horizontal row at $z = z_{iz}$ of the defined grid. The result of the BVP is used to construct a longitudinal distribution of the cumulative added mass $ca_{jj}^{C}(x_{ix}, z_{iz})$ valid for that draft of the vessel. The cumulative added mass is determined by the sum of the contribution of each panel for which at least one corner point satisfies $x_{CP} < x_{ix}$. Panels for which not all corner points satisfy this requirement are proportionally taken into account. This procedure is specified in Equation 6.3. The notation in this equation is chosen to illustrate that the cumulative added mass ca_{jj}^{C} is a parameter of the Cartesian grid while the added mass a_{jj} is a parameter of the 'normal' panelization that is used to solve the BVP. The result for ca_{jj}^{C} is smooth, also the spatial derivative, the longitudinal added mass distribution
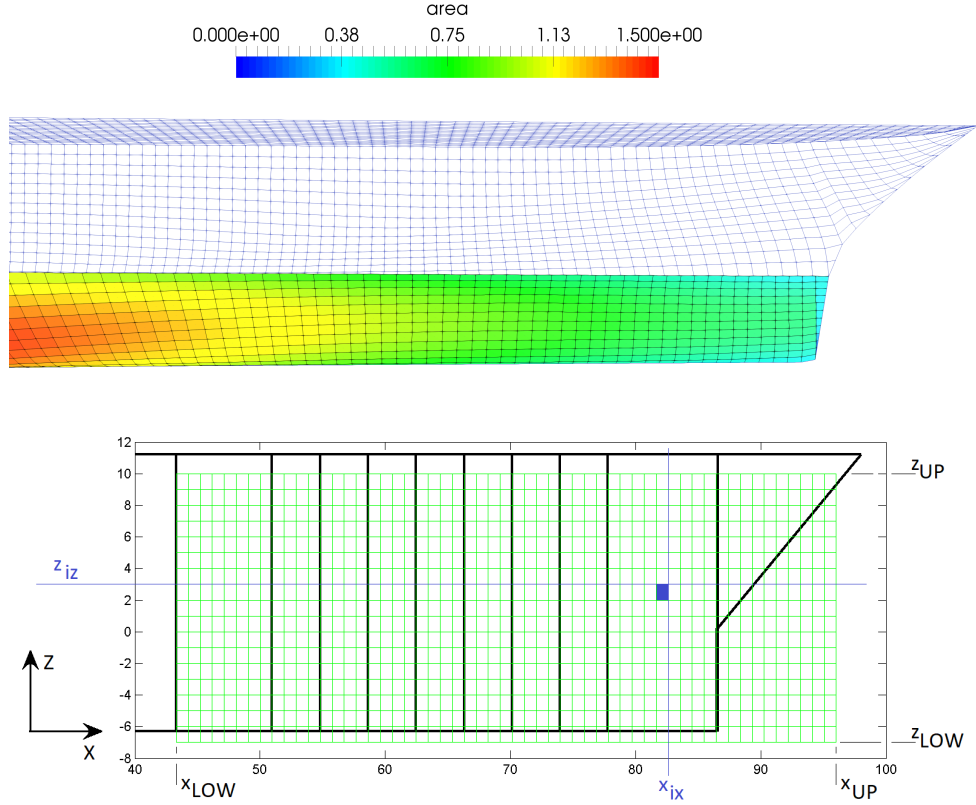
Figure 6.1: *Panelization up to draft z_{iz} to solve the BVP for the added mass coefficients (top). Cartesian grid projected on the bow area of the ship to calculate the added mass derivatives and the impulsive forces (bottom). Grid cell ca(ix,iz) is indicated in blue.*

$a_{jj}^{C}(x_{ix}, z_{iz})$, is quite smooth as shown in Figure 6.2. The added mass and the longitudinal derivative of the added mass can directly be derived from the cumulative added mass distribution using a difference (defined in Equation 6.4) and a central difference stencil as defined in Equation 6.5.

$$ca_{jj\,(ix,iz)}^{C} = \sum_{z_{(k)\,max} < z_{iz}} \left(\sum_{x_{(k)\,max} < x_{ix}} a_{jj\,(k)} + \sum_{x_{(k)\,min} < x_{ix}} \frac{A_{(k)l}}{A_{(k)}} a_{jj\,(k)} \right) \qquad [ix = 1 \dots nx] \qquad [kg]$$

(6.3)

with:

$a_{jj\,(k)}$	Contribution to added mass coefficient a_{jj} of panel k. This panel is defined on the grid used to solve the BVP.
$x_{(k)\,max}$	Maximum value of the x-coordinates of the corner points of panel k.
$x_{(k)\,min}$	Minimum value of the x-coordinates of the corner points of panel k.
$A_{(k)}$	Area of panel (k).
$A_{(k)l}$	Area of the part of the panel k on the left of x_{ix}.
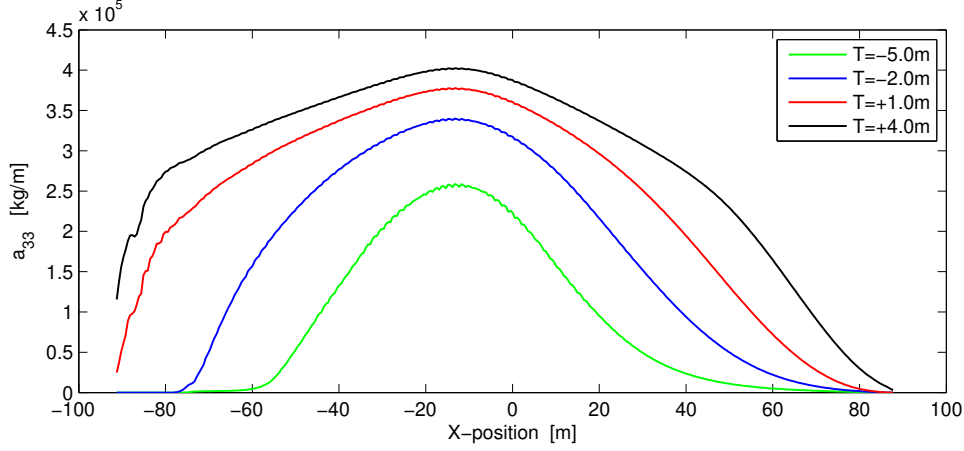
Figure 6.2: Distribution of the added mass coefficient a_{33} over the length of the ship. Results are plotted for calculations at different drafts.

$$
\begin{aligned}
a^C_{jj\,(ix,iz)} &= 0 \qquad [ix = 1] \\
a^C_{jj\,(ix,iz)} &= ca^C_{jj\,(ix,iz)} - ca^C_{jj\,(ix-1,iz)} \qquad [ix = 2\ldots nx] \qquad [kg]
\end{aligned}
\tag{6.4}
$$

$$
\begin{aligned}
\frac{da^C_{jj\,(ix,iz)}}{dx} &= \frac{a^C_{jj\,(ix+1,iz)} - a^C_{jj\,(ix,iz)}}{\Delta x} \qquad\quad [ix = 1] \qquad [kg/m] \\
\frac{da^C_{jj\,(ix,iz)}}{dx} &= \frac{a^C_{jj\,(ix+1,iz)} - a^C_{jj\,(ix-1,iz)}}{2.\Delta x} \qquad [ix = 2\ldots nx-1] \qquad [kg/m] \\
\frac{da^C_{jj\,(ix,iz)}}{dx} &= \frac{a^C_{jj\,(ix,iz)} - a^C_{jj\,(ix-1,iz)}}{\Delta x} \qquad\quad [ix = nx] \qquad [kg/m]
\end{aligned}
\tag{6.5}
$$

The vertical derivative requires calculations at different horizontal levels. The value of the added mass derivative at level z_{iz} is based on the results of calculations at levels z_{iz-1} and z_{iz+1}. This result is allocated to the row of panels having the upper corner points at level z_{iz}; these are the so-called water line panels for that draft. The added mass distribution $a^C_{jj\,(ix,iz)}$ is used to determine the vertical derivative:

$$
\frac{da^C_{jj\,(ix,iz)}}{dz} = \begin{cases}
\left(a^C_{jj\,(ix,iz+1)} - a^C_{jj\,(ix,iz)}\right)/\Delta z & \text{if iz} = 1; \\
\left(a^C_{jj\,(ix,iz)} - a^C_{jj\,(ix,iz-1)}\right)/\Delta z & \text{if iz} = nz; \\
\left(a^C_{jj\,(ix,iz+1)} - a^C_{jj\,(ix,iz-1)}\right)/(2\cdot\Delta z)) & \text{otherwise;}
\end{cases}
\tag{6.6}
$$

The method that is described above has been implemented in the grid program NELSON. The program uses a panelization over the hull up to the upper deck as input. In order to solve the BVP at each draft z_{iz}, a cut is made through the panelization at each level. These calculations result in tables of the added mass derivatives on the Cartesian
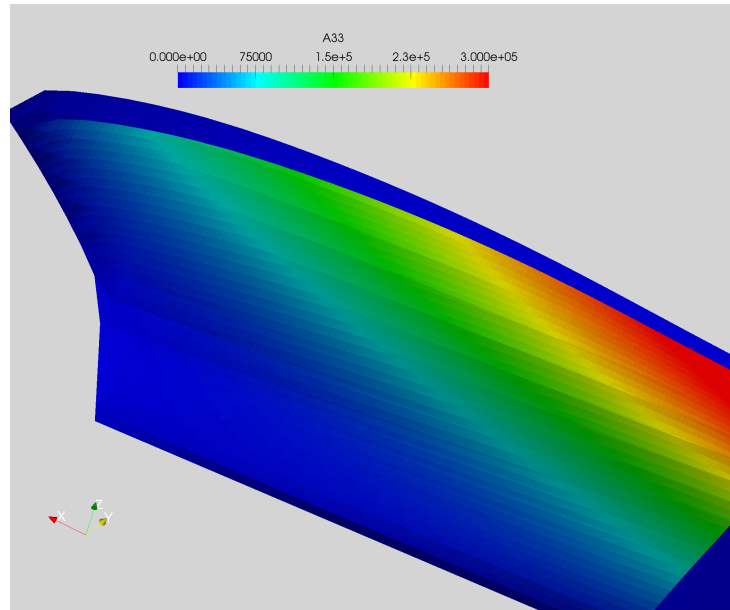
Figure 6.3: Distribution of the added mass coefficient a_{33} over the bow of a vessel.

grid $da_{jj\,(x,z)}/dx$ and $da_{jj\,(x,z)}/dz$ defined above. The program also calls the program Ra-PID to calculate the stationary bow wave at each draft z_{iz}. These calculations result in tables of the stationary bow wave $\zeta_{SBW}(x, z_{iz})$.

Examples of the added mass and added mass derivatives over the forward part of the hull are given in Figure 6.3 and in Figure 6.4.
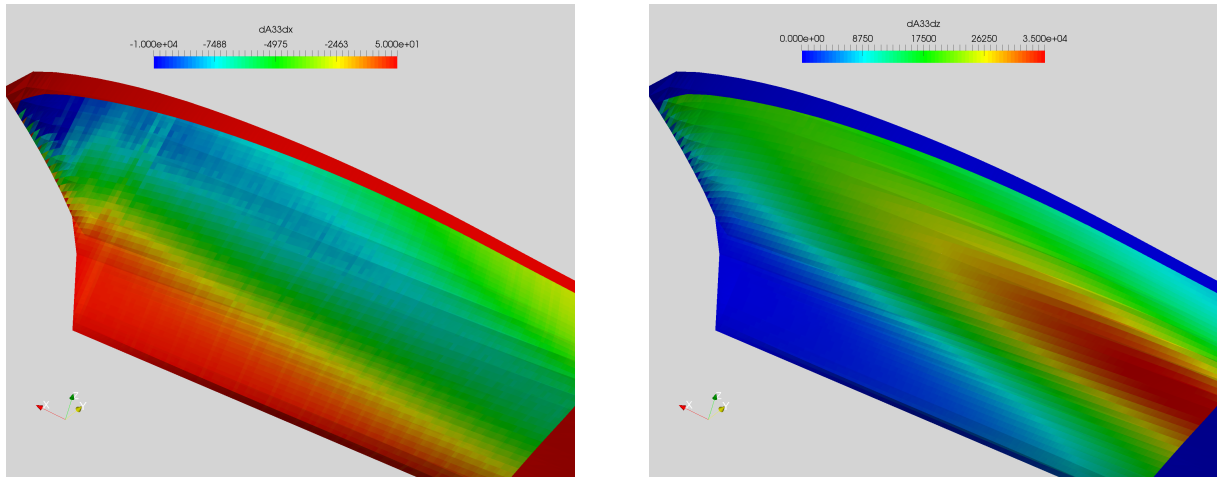
Figure 6.4: Distribution of the longitudinal added mass derivative $\partial a_{33}/\partial x$ (left) and the vertical added mass derivative $\partial a_{33}/\partial z$ (right) over the bow of a vessel.

6.3   Impulsive force calculation for a ship

The force components due to the change in impulse are calculated for the PS and SB side separately. In general, this results in a horizontal and in a vertical component for a normal ship section. The force components on one side are transformed to a normal force on the waterline intersection point and then added, Equation 6.7. This total normal force then determines the resulting impulsive force components, Equation 6.8. In this way, a lateral force component can be generated due to a vertical velocity for a normal V-shaped section; these components on PS and SB cancel for symmetric impact conditions (head seas with no roll).

$$F_N = \frac{FX_{\mathrm{IMP}}}{n_X} + \frac{FY_{\mathrm{IMP}}}{n_Y} + \frac{FZ_{\mathrm{IMP}}}{n_Z} \tag{6.7}$$

$$\begin{aligned} FX_{IMP} &= F_N \cdot n_X \\ FY_{IMP} &= F_N \cdot n_Y \\ FZ_{IMP} &= F_N \cdot n_Z \end{aligned} \tag{6.8}$$

6.4   Pile-Up effects for a ship

The method to determine pile-up effects for ships is based on the method that was developed in Section 5.5. This pile-up effect only considered the vertical added mass derivative since it was developed for 2D sections. Momentum theory calculates the impulsive force by considering the total of the vertical added mass derivative multiplied with the vertical velocity and the longitudinal added mass multiplied with the longitudinal velocity Equation 6.1. Using this logic, the pile-up effect of a ship is considered to have two contributions ψ_x and ψ_z that are defined as:

$$(1 + \psi_x) = 1 + \frac{3}{\left(1.75 + \rho y / \left(\partial a_{33}/\partial x\right)\right)^3} \tag{6.9}$$

$$(1 + \psi_x) = 1 + \frac{3}{\left(1.75 + \rho y / \left(\partial a_{33}/\partial z\right)\right)^3} \tag{6.10}$$

The total pile-up is the sum of the pile-up effect due longitundinal and vertical motions and the bow wave derivative:

$$(1 + \psi_{\mathrm{TOTAL}}) = \sqrt{1 + \psi_X^2 + \psi_Z^2} + \frac{\partial \zeta_{SBW}}{\partial z} \tag{6.11}$$

This method is used for both the PS and SB sides of the ship in head seas and for the windward side of the vessel in quartering seas. It is assumed that the pile-up effect on the leeward side quickly reduces to zero when the wave changes direction from head towards quartering seas. The function used to described this effect is given in Equation 6.12.

$$
\begin{aligned}
c_{PU-LW} &= \cos^{10}\mu \quad [-] \qquad \forall \quad \pi/2 < \mu < 3\pi/2 \quad [rad] \\
c_{PU-LW} &= 0 \qquad\qquad\qquad\qquad otherwise
\end{aligned}
\tag{6.12}
$$

Outside the range indicated, the value of the factor is zero. The c_{PU-LW} factor is used as a multiplier for the pile-up parameter ψ. The effect of this additional multiplier is, that the wave elevation on the leeward side quickly reduces to the sum of the stationary bow wave and 'linear' wave components: the total of incoming, radiated and diffracted waves when the heading of the ship changes from head seas to a quartering direction. The impulsive force calculation changes from a 'Wagner' impact to a 'von Kármán' impact. An example of the distribution of the pile-up factor on the windward side of the bow is given in Figure 6.5.
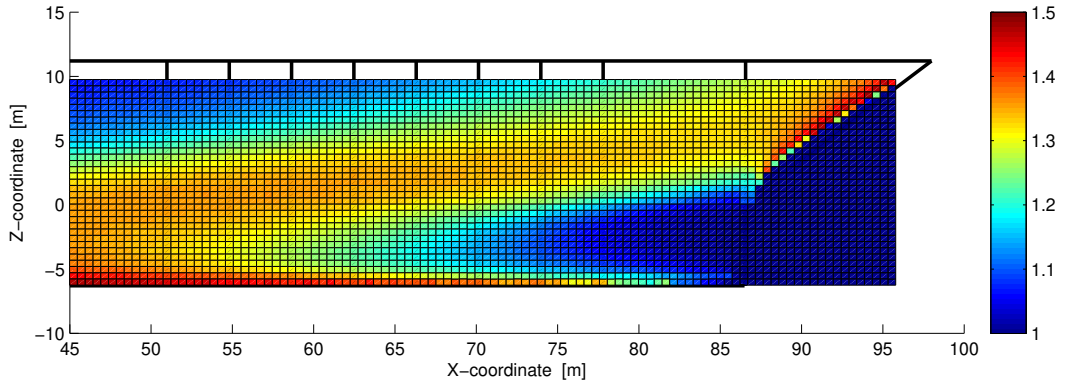
Figure 6.5: *Distribution of the pile-up factor over the bow of the ferry for a simulation in wave heading 150 deg. The windward bow is shown in the figure, the pile-up factor on the leeward side $c_{PU-LW} = 1.0$.*

6.5 Wave slap loads for ships

The method to calculate wave slap loads on the bow of a vessel is based on the approach developed in Section 5.8. The important 3D effect is the angle of the incoming wave relative to the normal on the hull in the waterline intersection point on a given longitudinal position. This angle β_{IMP}, is defined in Figure 6.6; it is an angle in the horizontal plane. The impact angle is taken into account as a deadrise angle for the wedge model that is used to calculate the wave slap load. Equation 5.24 is therefore adapted to include the effect of the deadrise using the approximation of the added mass coefficient for a 2D wedge as published by Lewis [114] and used before in Equation 5.9. The resulting equation is given in Equation 6.13.

$$
F_{\mathrm{SLAP}} = \rho\frac{\pi}{2}\left(1 - \frac{\beta}{2\pi}\right)^2\left(s\,\dot{s}\,u_N + \frac{s^2}{2}\dot{u}_N\right) \qquad [N/m]
\tag{6.13}
$$
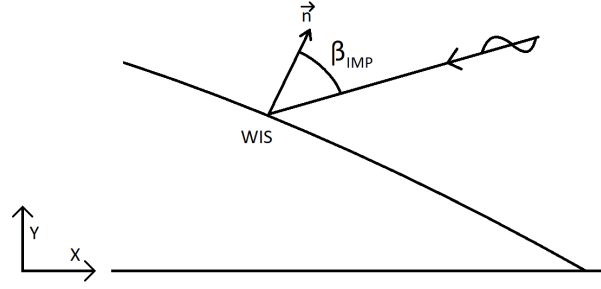
Figure 6.6: Definition of impact angle β_{IMP}. The impact angle is the angle in the horizontal plane between the undisturbed incoming wave and the normal to the hull $\vec{n}$ in the Waterline Inter Section point.

The procedure described above estimates the magnitude of a force due to a wave crest, so above the $z = 0$ plane. This procedure should only be carried out when the earth fixed motions of the body are zero, or very small. A physical criterion to choose whether or not this procedure should be activated has not been found. A rather arbitrary choice of an activation criterion $\dot{z}^{(e)} < 0.5 \ [m/s]$ has been set in the simulation program.

6.6   Including the stationary bow wave

The bow wave increases the relative motion at the bow significantly. This phenomenon has been studied in the past to estimate the probability of green water events. Blok and Huisman [16] already explained this 'swell-up' effect as a draft dependent bow wave; although their analysis did not include radiation and diffraction effects in the calculation of the relative motion, it correlated well with experimental results on a frigate hull form.

This approximate slamming model uses the stationary bow wave as calculated by the program RAPID. Figure 6.7 shows the result of a series of calculations for the ferry hull form, the figure shows the increasing wave elevation at the bow for larger immersions.

The calculation of the bow wave is done for all drafts defined in the Cartesian grid defined in Section 5.4. The results are used in the simulations in a similar way as the pile-up effect; the vertical bow wave derivative is calculated, Equation 6.14, and stored for each point on the computational grid. This derivative is multiplied with the local relative velocity w and the time step dt to arrive at the increase of the local wave elevation at the next time step, Equation 6.15.

$$\frac{\partial \zeta_{bw}}{\partial z}(ix, iz) = \begin{cases} \left(\zeta_{\text{bw}}(ix, iz + 1) - \zeta_{\text{bw}}(ix, iz)\right)/\Delta z & \text{if iz} = 1; \\ \left(\zeta_{\text{bw}}(ix, iz) - \zeta_{\text{bw}}(ix, iz - 1)\right)/\Delta z & \text{if iz} = \text{nz}; \\ \left(\zeta_{\text{bw}}(ix, iz + 1) - \zeta_{\text{bw}}(ix, iz - 1)\right)/(2.\Delta z) & \text{otherwise}; \end{cases} \tag{6.14}$$

$$\zeta_{\text{bw}}(x, t + \Delta t) = \zeta_{\text{bw}}(x, t) + \frac{\partial \zeta_{\text{bw}}(x, z)}{\partial z} \, w^{(b)} \, \Delta t \qquad [m] \tag{6.15}$$
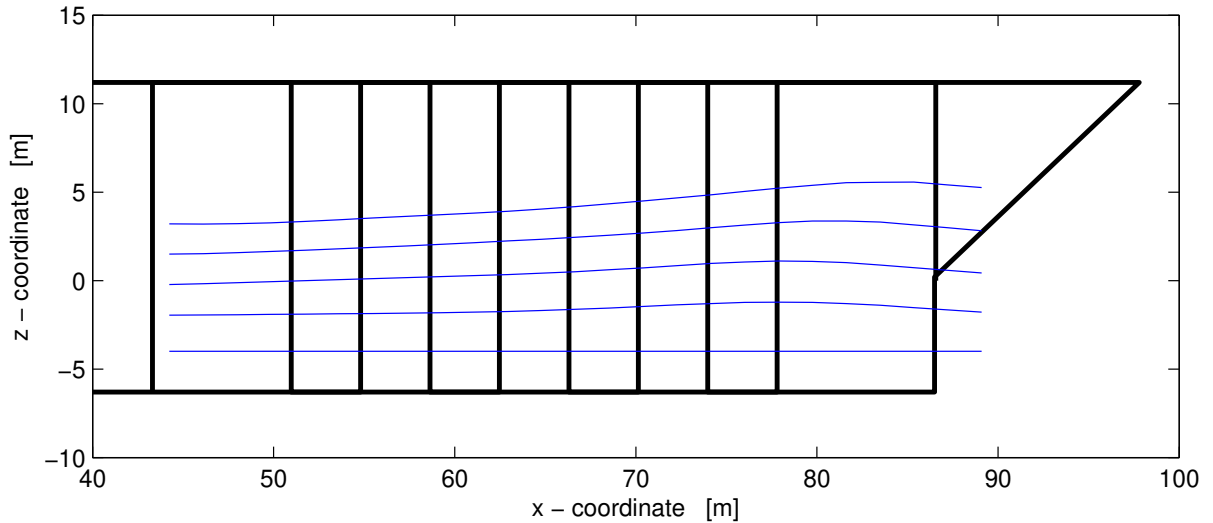
Figure 6.7: Stationary bow wave for different drafts as calculated by the RAPID program. Ferry hull form, Vs = 20 kt

This result is used in the time domain simulation in a special way. For a non-impact condition, when the ship is emerging, the profile of the stationary bow wave along the hull is based on the the waterline intersection at the Forward PerPendicular (FPP). This stationary bow wave elevation is added to the total wave elevation. For an impact condition, when the ship is immersing, the local rise of the water surface is calculated using the local vertical bow wave derivative, defined in Equation 6.14, multiplied with the local relative velocity, to determine the waterline intersection point on the next time step. This procedure is defined in Equation 6.15. To be fully complete, the normal pile-up factor is added to the vertical bow wave derivative before it is multiplied with the local relative velocity.

6.7   Relative motions and velocities

An accurate calculation of the relative velocity $w^{(b)}$ just before and during the impact is crucial for the magnitude of the impact. Next to the direct effect of the relative velocity on the impulsive force, it also determines the rise of the waterline intersection point during the impact and hence which part of the hull is being wetted and which added mass to use for the impulsive load calculation.

The relative motion is defined as :

$$z^{(b)} = \zeta_{\text{inc}} + \zeta_{\text{dif}} + \zeta_{\text{rad}} - x_3 + x \cdot \cos\left(x_5\right) - y \cdot \cos\left(x_4\right) \qquad [m] \qquad (6.16)$$

with $x_j, \quad j = 1\ldots 6$ the rigid body motions of the vessel.

The calculation of the relative velocity is based on the ship motions and on linear wave propagation theory. Each local event for which impulsive forces are being calculated

starts at a zero up-crossing of the relative velocity (immersing). During the event, the calculated relative velocity, Equation 6.16 is augmented with sum of the pile-up effect and the vertical bow wave derivative. The pile-up factor is used as a multiplier for the relative velocity. In order to use the increased relative velocity to calculate the waterline intersection point at the next time step, the velocity in the ship fixed reference frame is transferred to the earth fixed frame as a correction to the velocity of the wave profile:

$$\vec{v}_{abs}^{(e)} = \left(\vec{v}_{rel}^{(b)} + \vec{v}_{ship}^{(b)} \right) \cdot \mathbf{T}_{(b)}^{(e)} \qquad [m/s] \qquad (6.17)$$

in which $\vec{v}_{ship}^{(b)}$ is the local velocity in the waterline intersection point *(x,y,z)* in the body fixed reference frame:

$$\vec{v}_{ship}^{(b)} = \begin{pmatrix} \dot{x}_1 - y \cdot \dot{x}_6 + z \cdot \dot{x}_5 \\ \dot{x}_2 - z \cdot \dot{x}_4 + x \cdot \dot{x}_6 \\ \dot{x}_3 - x \cdot \dot{x}_5 + y \cdot \dot{x}_4 \end{pmatrix} \qquad [m/s] \qquad (6.18)$$

The velocity $\vec{v}_{abs}^{(e)}$ is used to determine the new wave elevation in the earth fixed reference frame; together with the ship motions on the new time level, the new position of the waterline intersection point can easily be determined.

The end of the impact event is determined again by the relative velocity; as soon as there is a zero down-crossing of the relative velocity, the event is ended. The pile-up is set to zero and the computed wave elevation drops instantaneously back to the undisturbed wave height. The routine to calculate the impulsive force is not activated. A result of this procedure is shown in Figure 6.8.
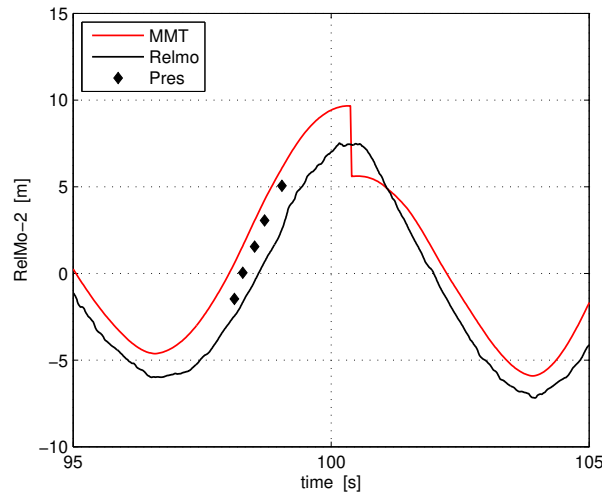
Figure 6.8: Demonstration of the pile-up effect on the relative motion and the discontinuous drop to the undisturbed wave when $w^{(b)} < 0$. The plot shows the measured relative motion as a black line, the time instant of activation of a pressure sensor as a black diamond and the result of MMT as a red line. Simulation in head seas, $v_S = 20$ kt.

6.7.1   The diffracted wave

The incoming wave is defined as a Fast Fourier Transform (FFT), a series of n harmonic components with each an amplitude and a phase angle at an earth fixed reference point (the origin of the XYZw system, Table 5.1). The local undisturbed wave elevation is determined from this FFT by linear wave propagation. The presence of the ship changes the wave elevation around the hull. The difference between this disturbed wave and the incoming wave, the diffracted wave, can be pre-computed in the time domain using the linear frequency domain results. This calculation requires a known speed and heading of the ship. For convenience, the phase difference between undisturbed and diffracted wave is stored. The mentioned pre-computation calculation is carried out by the frequency domain pre-processor, which is either PRECAL (Section 3.3) or FATIMA (Section 3.4), for all waterline panels at the design draft.

The frequency domain result is the complex (indicated by a hat) RAO of the local diffracted wave, normalized by the amplitude of the incoming wave. The real part of this result is used in the time domain as a multiplier for each of the harmonic components of the incoming wave, Equation 6.19.

$$\zeta_{\text{diff}}(x,t) = \sum_{j=1}^{n} \Re \left\{ \frac{\hat{\zeta}_{\text{diff}}(x,\omega_j)}{\zeta_{\text{inc-a}}(\omega_j)} \right\} \zeta_{\text{inc}}(x,\omega_j,\epsilon_j,t) \tag{6.19}$$

with: n the number of frequency components in the FFT.

The basis assumptions related to the forward speed are different in PRECAL than in FATIMA. The result of this difference is illustrated in Figure 6.9 and in Figure 6.10. In general the differences between the two results are quite important, but when focusing on the forward part, $43 < x < 86.5\ m$, the results are rather similar.
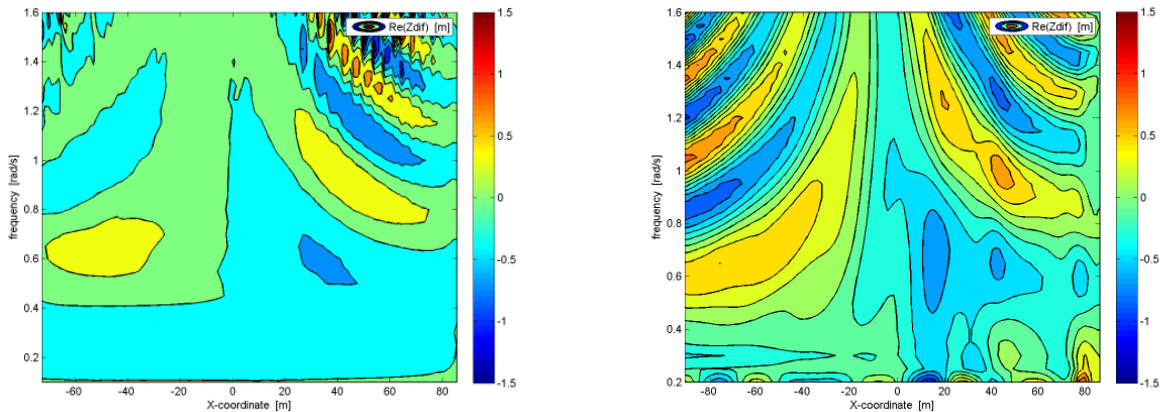
Figure 6.9: Real part of the diffracted wave. Right result from PRECAL, left is the result from FATIMA. The plot shows the longitudinal position along the hull on the horizontal axis, the earth fixed frequency on the vertical axis while the amplitude of the diffracted wave is shown in colors. Speed 20 kt, heading 180 deg.
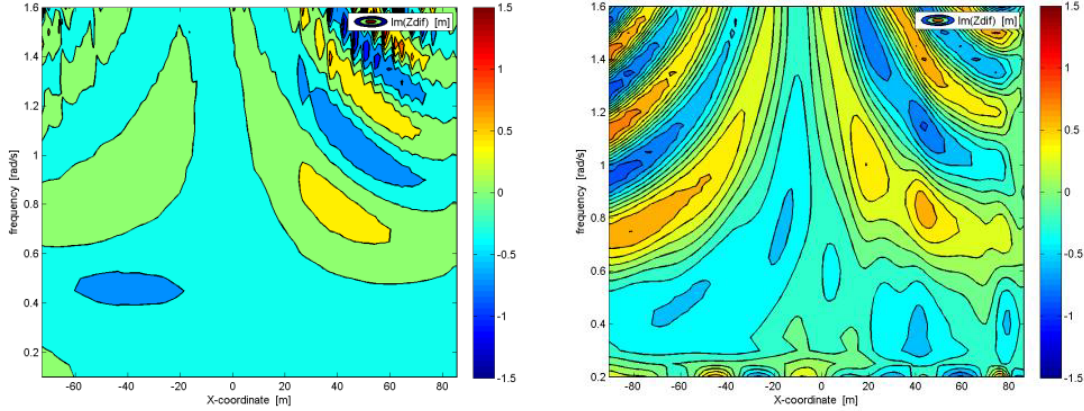
Figure 6.10: Amplitude of the imaginary part of the diffracted wave. Right result from PRECAL*, left is the result from* FATIMA*. The plot shows the longitudinal position along the hull on the horizontal axis and the frequency on the vertical axis. Speed 20 kt, heading 180 deg.*

6.7.2   The radiated wave

The radiated wave is dependent on the ship motions. The motions are a-priori unknown, they are a result of the simulation. The radiated waves are, for a given ship speed, dependent on the frequency and the amplitude of each mode of motion. The RAO's, $\left((\hat{\zeta}_{rad}/x_a)(\omega) \right)_j$ are calculated by the frequency domain pre-processor, either PRECAL or FATIMA.

Transferring frequency dependent parameters to the time domain is done using Linear Time-Invariant (LTI) system theory. By definition, the output of a LTI system due to an input can be described by the convolution integral:

$$y(t) = x(t) * h(t) = \int_{\tau=-\infty}^{\infty} x(t-\tau) \cdot h(\tau) d\tau \tag{6.20}$$

which can be re-written as:

$$y(t) = \int_{\tau=-\infty}^{\infty} x(\tau) \cdot h(t-\tau) d\tau \tag{6.21}$$

The input function $x(\tau)$ can be defined as a Dirac delta function, defined as:

$$x(\tau) = \Re \left\{ \int_{\omega=-\infty}^{\infty} e^{i\omega t} \right\} \tag{6.22}$$

If $x(\tau)$ is a delta function, it is called an Impulse Response Function (IRF). The result of a frequency domain calculation, the transfer function, in naval architecture usually

identified as the Response Amplitude Operator (RAO), is the Laplace transform of the IRF. The RAO for mode j is denoted here as the complex function $\hat{R}_j(\omega)$.

The IRF can be calculated by multiplying the RAO $\hat{R}_j(\omega)$ with the delta function:

$$h_j(\tau) = \frac{1}{2\pi} \int\limits_{\omega=-\infty}^{\infty} \hat{R}_j(\omega)e^{i\omega\tau}d\omega \tag{6.23}$$

The integral converges if the RAO $\hat{R}_j$ is strictly proper, which means that $\lim\limits_{\omega\to\infty} R_j = 0$. If this is not the case, but it there is some finite limit for $\lim\limits_{\omega\to\infty} R_j$, one can subtract this limiting value and thus splitting the RAO in a strictly proper part R' and a frequency independent part. This latter component can directly be used in the time domain; the real part is used by multiplying it with the displacement, the imaginary part, divided by the frequency, is multiplied by the velocity of the relevant mode of motion.

The frequency dependent part is used in the time domain by applying the impulse response function (IRF) Equation 6.23 and the convolution integral.

$$h_j(\tau) = \frac{2}{\pi} \int\limits_{\omega=0}^{\infty} \Re\left\{R_{jk}(\omega)\right\} \cos(\omega\tau)d\omega \tag{6.24}$$

which should (except for $\tau = 0$) be identical to:

$$h_j(\tau) = \frac{2}{\pi} \int\limits_{\omega=0}^{\infty} \Im\left\{R_{jk}(\omega)\right\} \sin(\omega\tau)d\omega \tag{6.25}$$

Combining the above in the equations as used in the time domain results in:

$$\begin{aligned} y(t) &= \lim_{\omega\to\infty}\left(\Re\left\{R_{jk}(\omega)\right\}\right)\cdot x(t) + \lim_{\omega\to\infty}\left(\Im\left\{\frac{R_{jk}(\omega)}{\omega}\right\}\right)\cdot\dot{x}(t) + \\ &+ \int\limits_{\tau=0}^{\infty} x(t-\tau)\cdot h(\tau)d\tau \end{aligned} \tag{6.26}$$

Application

A result of a local radiated wave produced by a forced heave motion of the ferry is shown in Figure 6.11. Normally the radiated wave is normalized by the amplitude of the motion, but the result shows that there is no finite limit for $\omega \to \infty$, so the function is not strictly proper. This problem is solved by considering the radiated wave normalized by the velocity of the motion; this result can be used to determine an IRF as shown in the right-hand side of Figure 6.11.

$$\zeta_{rad}(t) = -\int\limits_{\tau=-\infty}^{t} \mathrm{IRF}_j(\tau)\cdot\dot{x}_j(t-\tau)\,d\tau + G_j^1\dot{x}_j(t) + G_j^2x_j(t) \tag{6.27}$$

and:

$$G_j^1 = \lim_{\omega_e \to \infty} \Re \left\{ \frac{\hat{\zeta}_{rad}(\omega_e)}{i\,\omega_e\,x_j} \right\}$$

$$G_j^2 = \lim_{\omega_e \to \infty} \Re \left\{ \frac{\hat{\zeta}_{rad}(\omega_e)}{x_j} \right\}$$

This approach has been implemented in the time domain program.
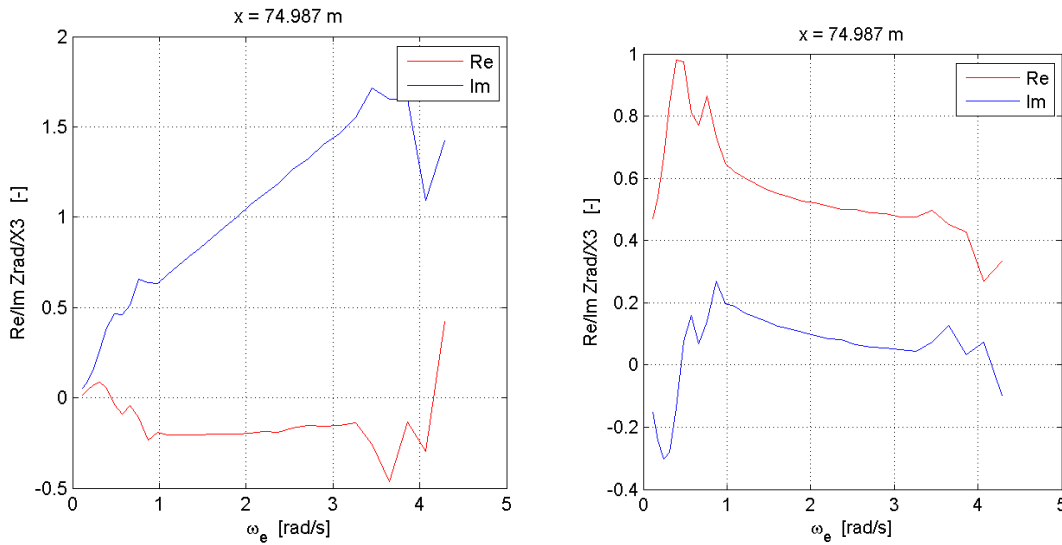
Figure 6.11: *Real and imaginary part of the radiated wave at $x = 75$ m due to a forced heave motion of the ferry. Left: radiated wave amplitude normalized by the amplitude of the motion. Right, the same result but now it is normalized by the velocity of the motion.*

6.8   Effect of pile-up and stationary bow wave

Both the pile-up and the stationary bow wave affect the relative motions at the bow. The pile-up always increase the relative motions, the effect of the stationary bow wave can be to in- or decrease the relative motion, depending on a position in a wave crest or in a wave trough. For impacts against the stem, including the bow wave has always the effect of increasing the relative motions.

The effect has been demonstrated for impacts against the bow segment of the ferry, a result from the first series of experiments. The results of adding the individual components to the base case, the incoming wave only, are shown in Figure 6.12; this figure also shows the results for using all effects that have been described. The figure shows that the effect of the pile-up due to the added mass derivatives is about twice as large as the effect of including the stationary bow wave. Both effects are required to arrive at a good estimation

of the force on the segment as is also shown in this figure when comparing the calculated result is to the result of the experiments.

The contribution of the different pile-up components has also been tested for the impulsive forces against a segment in the bow of the ferry not being the stem. The example shown is a case from the second series of experiments, Figure 6.13. This figure shows that the effect of adding the stationary bow wave to the incoming wave is small and also reduces the impulsive force on Segment 9. If the effect of the stationary bow wave is added to the incoming wave augmented with the effect of the pile-up due to the added mass derivatives, there appears to be an increase of the impulsive forces on this segment. This effect is however quite dependent on the location in the bow as demonstrated by the result in Figure 6.14. On this location the effect of adding the stationary bow wave to the incoming wave including the pile-up is a decrease of the impulsive forces.

The underlying effect of the pile-up components on the relative motion along the hull is shown in Figure 6.15; this is the same condition as used in Figures 6.13 and 6.14. The plot on top in this figure corresponds to Segment 7, while the plot in the bottom corresponds to Segment 9. These figures confirm that on these locations the pile-up effect is dominant and the effect of adding the stationary bow wave is much smaller and can have an increasing or decreasing effect depending on the location.
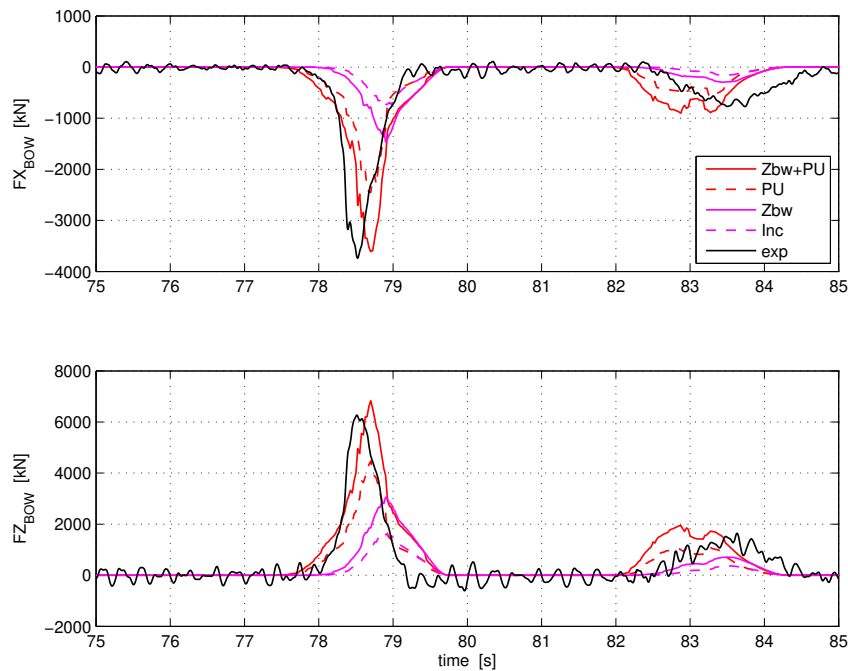
Figure 6.12: Effect of including different components for the pile-up effect on impacts against the bow segment of the ferry, 1st series of experiments. 'Zbw+PU' is the full effect of the stationary bow wave and the pile-up from the added mass derivatives; 'PU' is only the pile-up from the added mass derivatives; 'Zbw' is only the effect of the stationary bow wave and 'Inc' is no pile-up at all, just the incoming wave. Simulation in head seas, extreme wave of 5 m wave height, $v_S = 20$ kt.
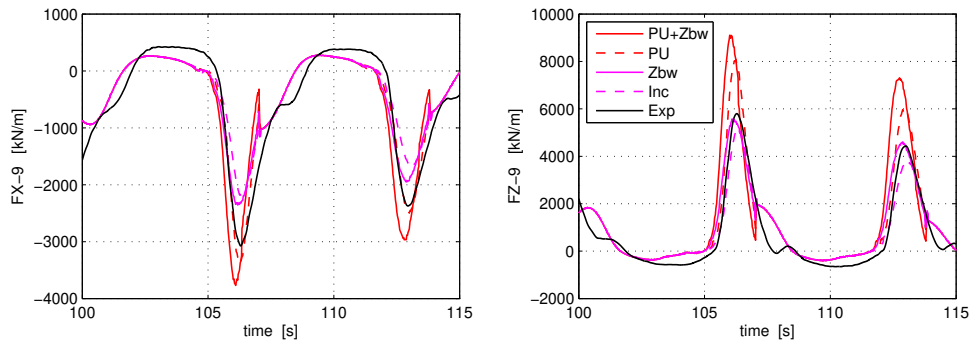
Figure 6.13: Effect of including different components for the pile-up effect on impacts against Segment 9 of the ferry, 2nd series of experiments. 'Zbw+PU' is the full effect of the stationary bow wave and the pile-up from the added mass derivatives; 'PU' is only the pile-up from the added mass derivatives; 'Zbw' is only the effect of the stationary bow wave and 'Inc' is no pile-up at all, just the incoming wave. Simulation in head seas, wave sweep $H_W = 5$ m, $v_S = 20$ kt.
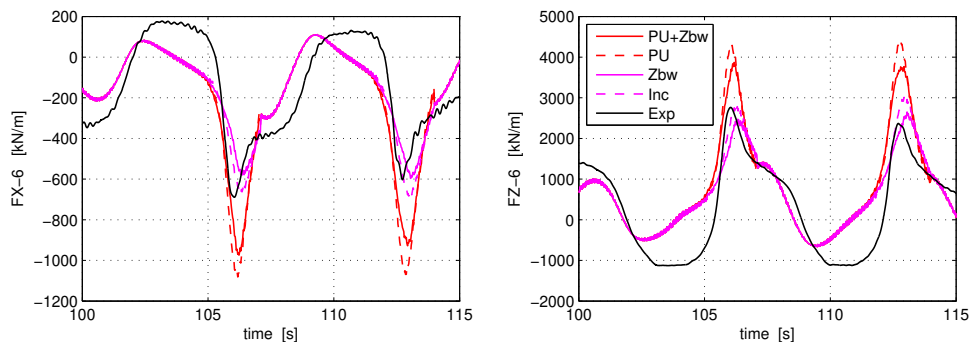
Figure 6.14: Similar plot as shown in Figure 6.13, but now for Segment 6 of the ferry used in the 2nd series of experiments. Simulation in head seas, wave sweep $H_W = 5$ m wave height, $v_S = 20$ kt.
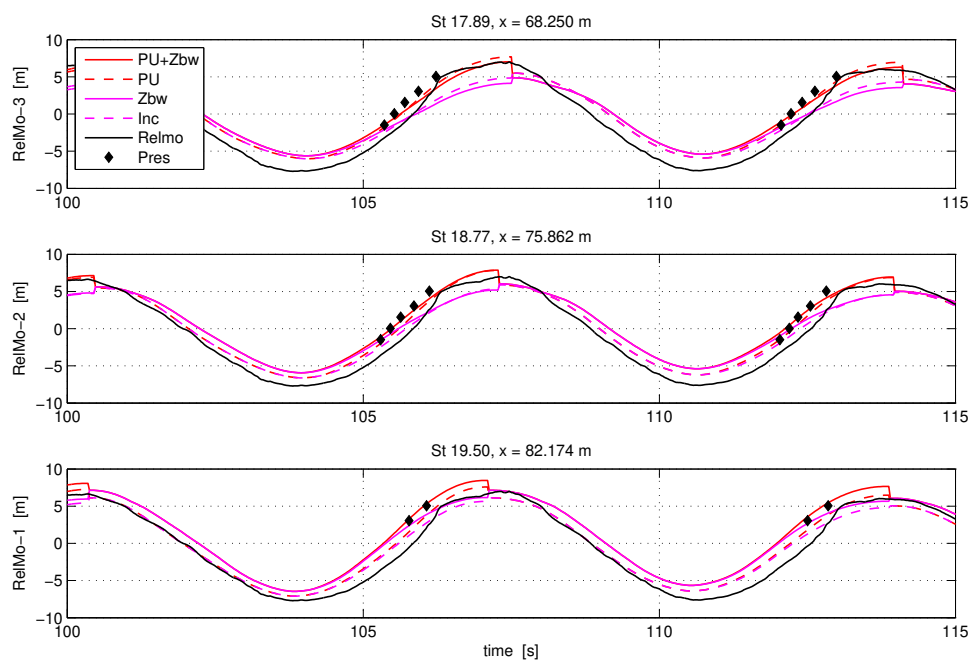
Figure 6.15: Effect of including different components for the pile-up effect on impacts against Segment 9 of the ferry, 2nd series of experiments. 'Zbw+PU' is the full effect of the stationary bow wave and the pile-up from the added mass derivatives; 'PU' is only the pile-up from the added mass derivatives; 'Zbw' is only the effect of the stationary bow wave and 'Inc' is no pile-up at all, just the incoming wave. Simulation in head seas, wave sweep $H_W = 5$ m, $v_S = 20$ kt.

Chapter 7

Time domain model to calculate the slamming force

7.1 Components of the calculation suite

The suite of programs used for a slamming calculation is schematically shown in Figure 7.1.

The main components are:

- AMG, the program that generates a mesh on a hull defined by 2D cross-sections. The program uses linear interpolation in-between the sections, therefore a large number of sections is to be used for an accurate description of the shape of curved parts like the bow. The program generates panels on the wetted part of the hull, on the part from the waterline to the deck and it creates an internal lid at the surface in the hull. This lid is used in the frequency domain program to suppress irregular frequencies; the panels are not used for a pressure integration.

- PRECAL (or FATIMA) is the frequency domain pre-processor. Using the hull defied by its panelization, it calculates the radiated and diffracted waves; if necessary for a hull sub-divided in segments to determine the internal loads. The calculation can be carried out for a range of speeds, headings and frequencies. When the results are used for time domain simulations, care must be taken to have sufficiently high frequencies to determine accurate IRFs - which in their turn require a fine mesh.

- NELSON is a pre-processor program for the slamming calculations in the time domain. It solves the BVP to determine the infinite frequency added mass at a range of drafts. From this result it determines the added mass derivatives on a Cartesian grid different to the panelisation used to solve the BVP for the radiation problem. It also runs the RAPID program for each of the drafts to determine the stationary bow wave along the hull.

- PRETTI-MMT is the time domain program that calculates ship motions including non-linear effects of the Froude-Krilov and restoring forces. For the area defined

by the Cartesian grid in the Nelson program, the pile-up effect on the relative motions is calculated including the effect of the draft-dependent bow wave. When the local relative vertical velocity $w^{(b)} > 0$, impulsive forces or wave slap forces are being calculated.

The relation between these components and the files that are used as interface is illustrated in the diagram in Figure 7.1.
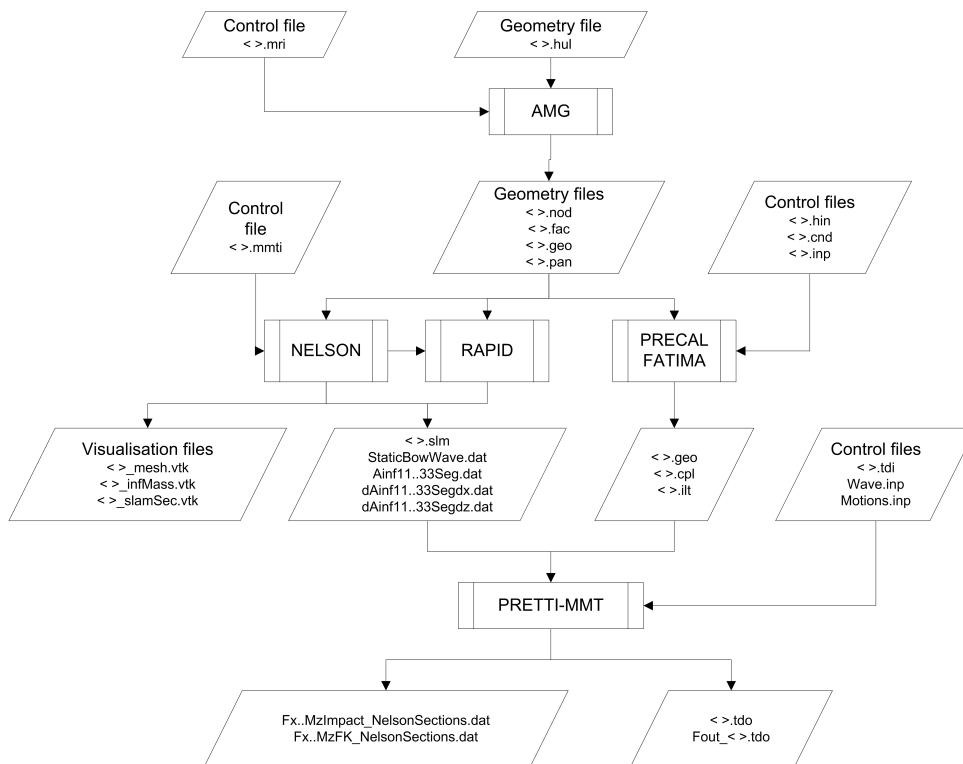
Figure 7.1: Organization of the Nelson - Precal - Pretti-MMT program suite and the flow of data via the various data files.

7.2   Calculation of a slamming event

There is one main routine, CalcFimpact, in the time domain program Pretti-MMT that is the heart of the slamming calculation. The routine checks for each column of the Cartesian grid and for each time step if a slamming condition is present. This condition is defined by the local relative velocity $w^{(b)} > 0$. When this condition is satisfied, the intersection of the water surface and the body is determined and the added mass derivatives and the local stationary bow wave elevation is obtained from interpolation of these results in the column of the Cartesian grid. The local velocity, including pile-up effects and the effect of the stationary bow wave, is determined. The impulsive force is calculated and the result of the relative velocity is used to determine the wave elevation at the next time
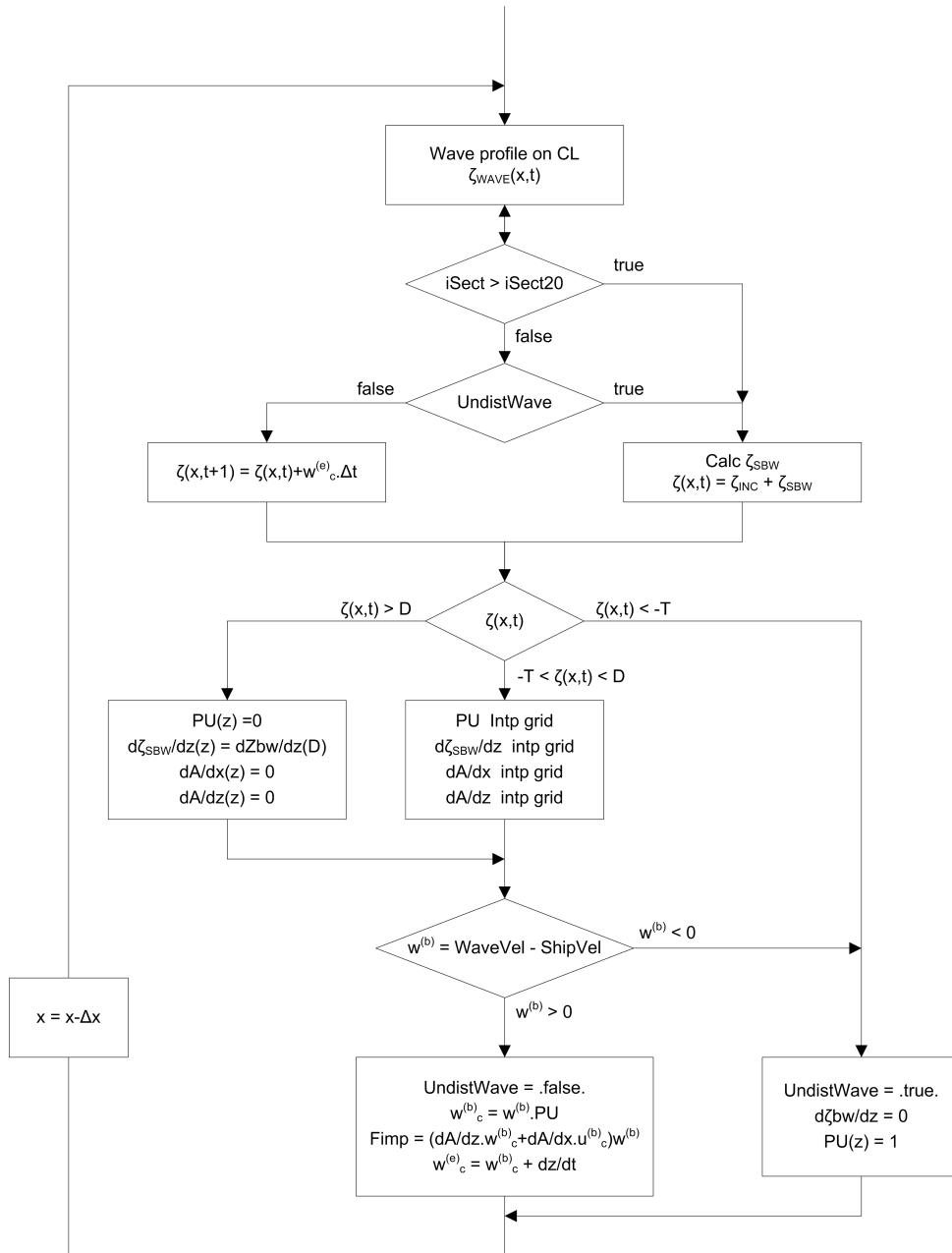
Figure 7.2: Procedure to calculate the relative motion, velocity and the impulsive forces in the F_{IMPACT} routine at one time instant. The main loop is the loop over all x-coordinates of the Cartesian grid.

step. The event is completed when the relative velocity changes sign again. During the exit phase there are no pile-up effects and no impulsive forces calculated. This procedure is schematically given in Figure 7.2.

The main steps in the calculation procedure are:

Wave profile on grid

The relative motion at the FPP is calculated, this determines the wave elevation along the hull of the stationary bow wave for a non-impact condition (logical UndistWave = TRUE).

Local wave elevation

The wave elevation is based on the sum of the undisturbed wave and the bow wave at $t = 0$, for $t > 0 \cap w^{(b)} < 0$ and for $\zeta(x, t) < -T$. If any of these conditions is true, logical UndistWave = TRUE. For $t > 0 \cap w^{(b)} > 0$, UndistWave = FALSE; in that case the wave elevation is based on the elevation at the previous time step and the corrected wave velocity $w_{wave}^{(e)}$ multiplied with the time step.

Pile-up factors

The block 'PU Intp grid' interpolates the local added mass derivatives, the pile-up factors and the bow wave derivative for the waterline intersection point on the Cartesian grid. If the depth of the vessel is exceeded, $\zeta(x, t) > D$, the pile-up and the added mass derivatives are set to zero. This condition is considered as being similar to passing a hard chine that induces flow separation.

Corrected relative velocity

The relative velocity $w_c^{(b)}$ is determined by multiplying the relative velocity calculated from ship motions and the undisturbed wave with the sum of the pile-up factor and the bow wave derivative.

Impulsive and wave slap force

The impulsive force is calculated when $w^{(e)} > 0.5 \ [m/s]$. The force is based on the added mass derivatives, the corrected relative velocity and the earth fixed velocity. If $w^{(e)} < 0.5 \ [m/s]$, the wave slap force is calculated.

Corrected wave velocity

The corrected relative velocity (body fixed reference frame) is transferred to a wave velocity in the earth reference frame, $w^{(e)}$, which is used to determine the local wave elevation in the next time step.

7.3   Tuning factors for the slamming calculation

Because the model developed in this thesis is an approximate model based on 2D theoretical methods, it was considered necessary to include tuning parameters to get a closer agreement to experimental or numerical results. The idea behind this approach is, that the model has sufficient theoretical basis to predict the effect of parameters defining the impact condition and of parameters defining the geometry of the ship - but insufficient accuracy to predict the absolute level of the impact accurately. The choice was made to have tuning factors on the definition of the pile-up effects and in this way affecting the

relative velocity and the maximum height of the water surface - hull intersection point. These parameters in their turn affect the slamming force.

The tuning factors for the normal pile-up effect are applied to Equation 6.11, resulting in Equation 7.1. Next to this general effect, tuning factors are included for the determination of the pile-up effect on the leeward side of the hull, Equation 7.2.

$$(1 + \psi) = \sqrt{1 + (c_1 \psi_X)^2 + (c_2 \psi_Z)^2} + \frac{\partial \zeta_{SBW}}{\partial z} \tag{7.1}$$

$$c_{PU-LW} = c_3 \cos^{c_4} \mu \tag{7.2}$$

The default values for the tuning factors are chosen to be:

$$
\begin{aligned}
c_1 &= 1.0 \\
c_2 &= 1.0 \\
c_3 &= 1.0 \\
c_4 &= 10.0
\end{aligned}
$$

7.4 Verification

The solution methods of the programs used for the slamming calculation are based on a discretization of the flow parameters. Since the methods used are all boundary element methods, it suffices to discretize the wetted surface of the vessel by way of panels. The solution obtained is in general dependent on the number of panels used, the verification procedure is intended to determine the minimum number of panels for which convergence of the required results is obtained.

In order to study the effect of the discretization on the results, several panelizations for the hull of the example ferry were made and several densities of the Cartesian grid. The panelizations and grids used for this verification study are detailed in Table 7.1.

7.4.1 Verification of the calculation of the stationary wave profile

The program RAPID uses a grid on the hull independent of the one used for the determination of the added mass. RAPID calculations were made for each of the rows of the Cartesian grid. Therefore the grid on the hull used for RAPID extends to the upper deck and is cut case-by-case at a convenient height above the actual waterline to allow an intersection between the wave crest and the hull.

The results, Figure 7.3, show that the effect of the panel length is very small for the test cases used. It is recommended by Raven [150], the original developer of RAPID, to use 30 panels in the wave length of the transversal wave, this results in a length of the panel of
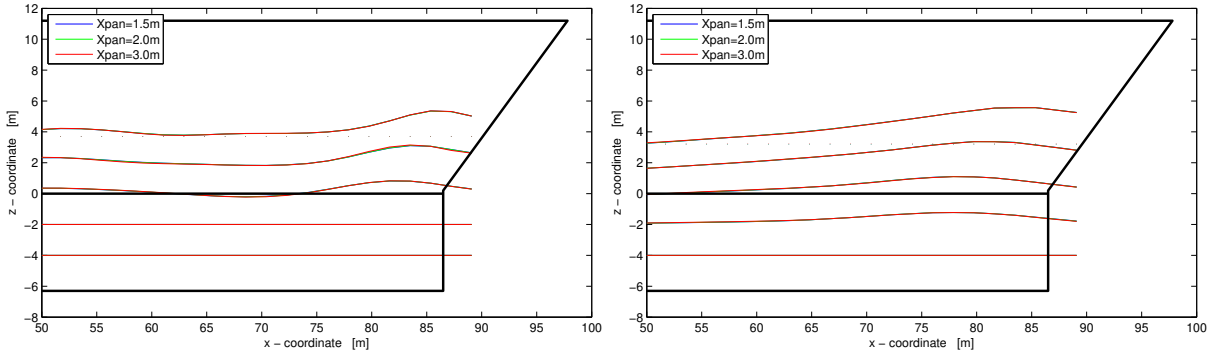
Figure 7.3: Height of the stationary waves generated by the ferry at 15 kts (left) and at 20 kts (right) with 3 different panelizations at 5 different drafts, T = 3.30 (2.00) 11.30 m. The average length of the panels along the waterline is given in the legend.

$X_{\text{PANEL}} = (2\pi/30) Fn^2 L_{PP}$; for the case considered this is $X_{\text{PANEL}} = 2.26\ m$. The length of the panels used in the calculation varied in the range $1.7 < X_{\text{PANEL}} < 2.9\ m$. The results of the profile of the bow wave are almost identical; noted is that the recommended panel length focuses on a converged value of the wave making resistance; this parameter is more sensitive than the wave elevation at the bow.

7.4.2 Verification of the calculation of the added mass derivatives

The added mass derivatives are calculated by the potential flow program included in the program NELSON. The results are in general dependent on the underlying panelization of the hull and on the density of the Cartesian grid that is used for the slamming calculation. The effect of these parameters is studied by performing calculations for 6 cases, detailed

Table 7.1: Parameters of the grid study. NX: Number of panels in X-direction, NZ1: Number of panels in Z-direction below the waterline, NZ2: Number of panels in Z-direction above the waterline, NB: total number of panels below the waterline, NA: total number of panels above the waterline, NXN: number of vertical lines in the Cartesian grid and NZN: number of horizontal lines used in the Cartesian grid. NB and NA refer to the number of panels on the demi-hull.

	Panels hull			Nr of panels		Cartesian grid	
Id	NX	NZ1	NZ2	NB	NA	NXN	NZN
1-1	60	7	8	476	633	55	17
1-2	60	7	8	476	633	110	34
2-1	80	9	10	850	1070	55	17
2-2	80	9	10	850	1070	110	34
3-1	100	11	12	1325	1635	55	17
3-2	100	11	12	1325	1635	110	34
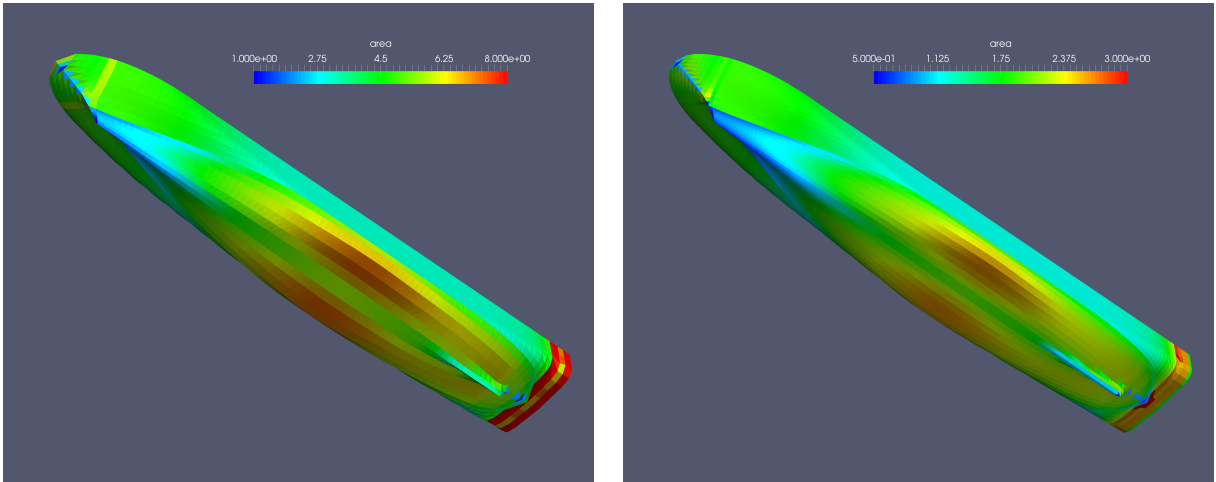
Figure 7.4: Two panelizations for the hull form of the ferry. Grid-1 with 476 panels below and 633 panels above the calm water line (left) and Grid-3 with 1325 panels below and 1635 panels above the calm water line (right). The colorbar gives the area of the panels; note that the scaling is different for the two plots.

in Table 7.1. Two panelizations on the hull are shown in Figure 7.4 and the resulting distribution of the $\partial a_{33}/\partial z$ parameter over the hull in Figure 7.5. The result of this study shows that the effect of the number of panels on the hull is rather low; the effect of the size of the Cartesian grid is however much larger.

The important result is however the accuracy of the impulsive force. As a test case a simulation has been made in a bow quartering test wave condition. The hull form used is the one from the 2nd series of model tests and the force considered is the one on Segment 9 (from St 19 to St 20). The wave is composed of 10 different components with a phase angle such that 10 s after starting the simulation the maximum wave height is encountered. The pitch motion of the vessel is imposed with a sine-squared function such that the maximum nose-down angle of 2.0 deg occurs after 10 s. This procedure creates a significant impact condition, suitable for this verification purpose.

A comparison of calculations for the same panelization but different densities of the Cartesian grids is shown in Figure 7.6; the effect of the changes in the grid is quite small and limited to the peak value of the impulsive force. The effect of the underlying PRECAL panelization is larger as shown in Figure 7.7.

The effect of changing the number of columns of the grid is larger than changing the number of rows as shown in Figure 7.8. Based on these results, a Cartesian grid having 110 vertical subdivisions and 34 horizontal subdivisions is considered to give accurate results.

Considering how little the parameters changed affect the resulting impact force, it can be concluded that even the coarsest grid is converged for this example.
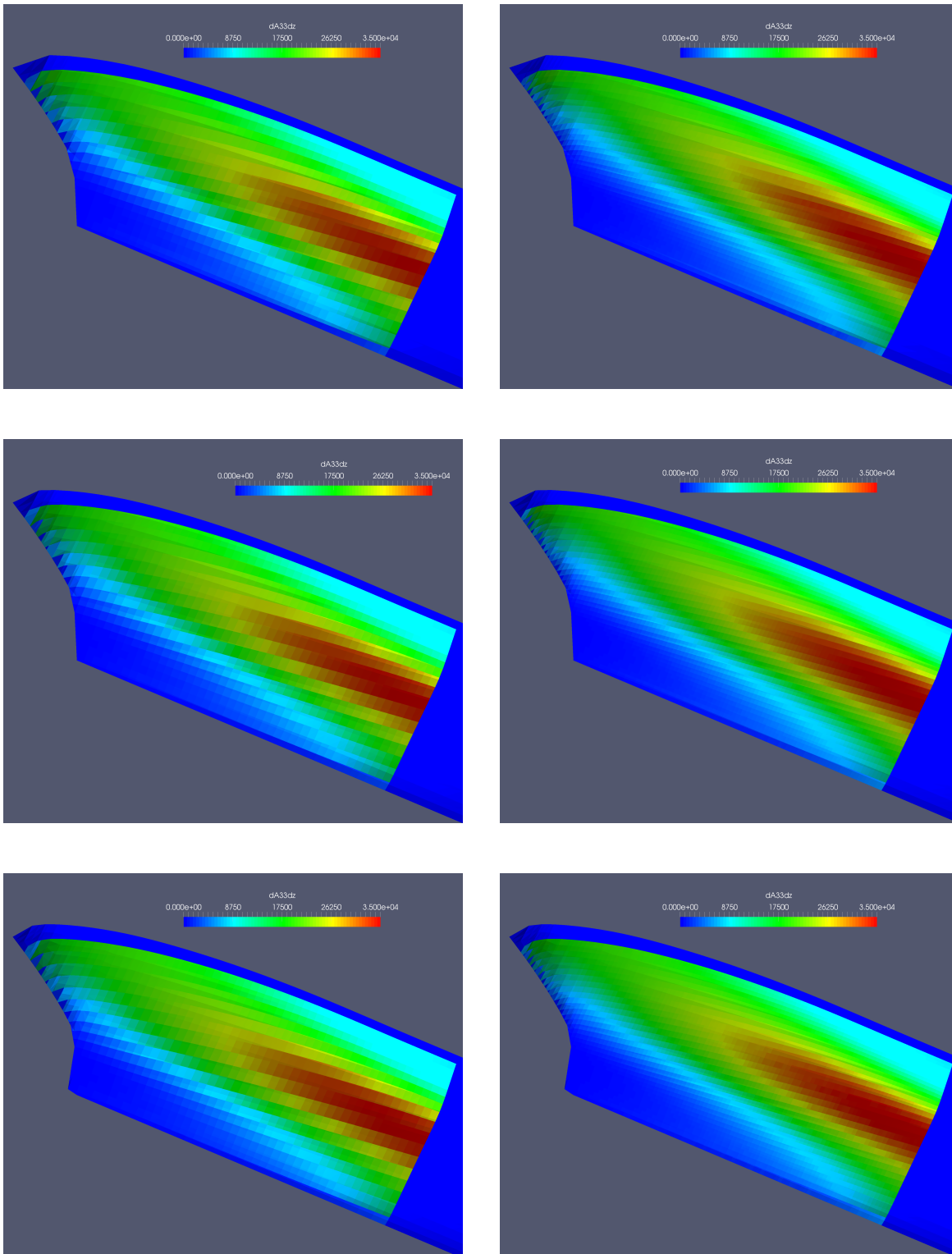
Figure 7.5: Distribution of the vertical added mass derivative $\partial a_{33}/\partial z$ over the bow of the ferry. Top left: results for grid 1-1; top right: grid 1-2. Middle left: grid 2-1, middle right grid 2-2. Bottom left: grid 3-1, bottom right grid 3-2.
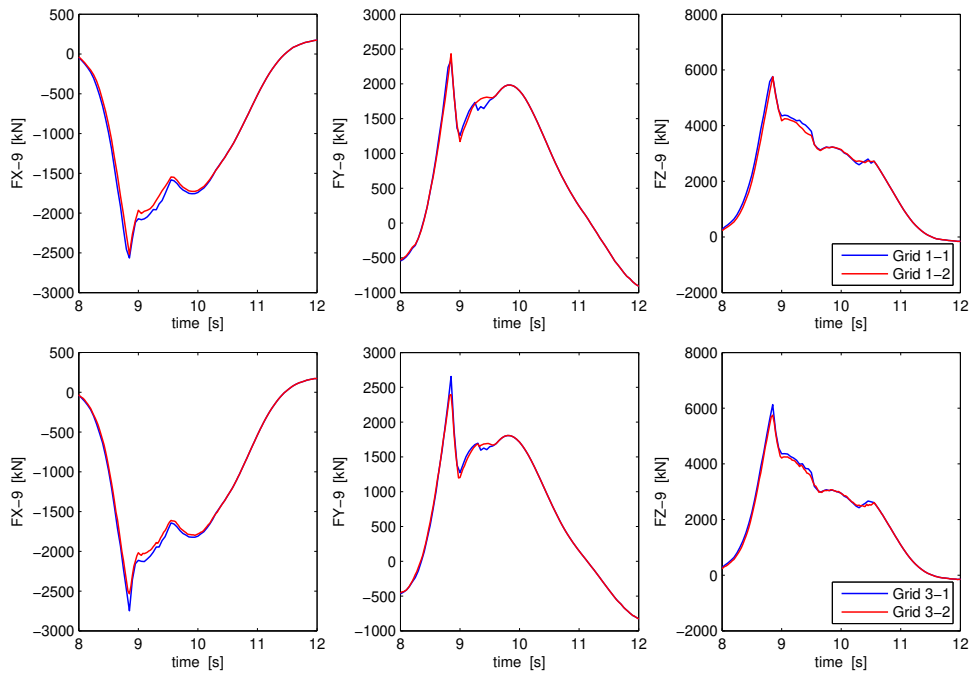
Figure 7.6: *Results of impulsive forces for 2 different Cartesian grids. Top figure shows the comparison for the coarsest PRECAL panelization, while the bottom figure shows the same result for the finest panelization.*
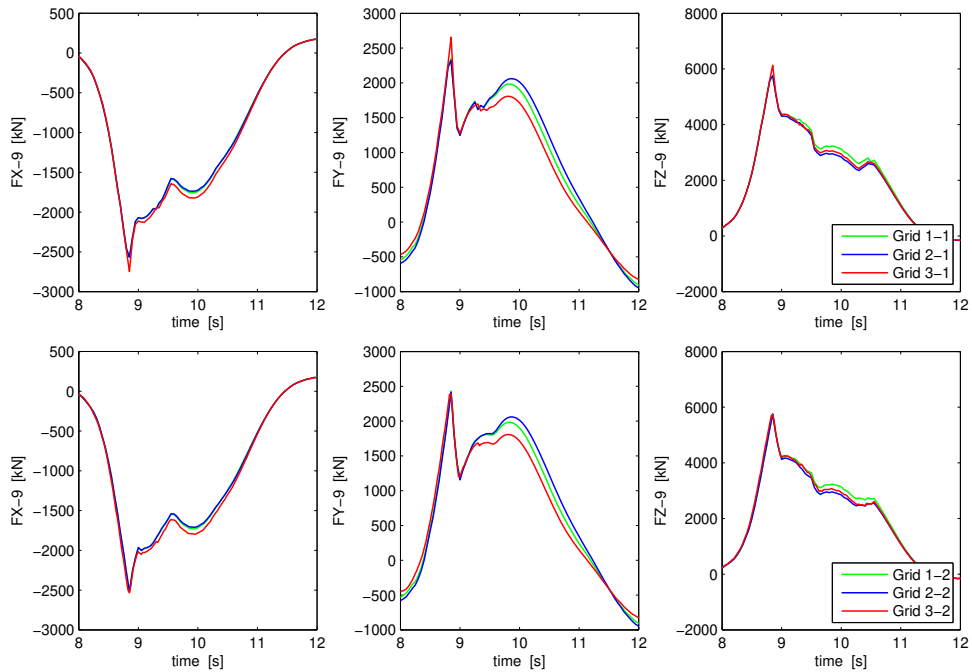
Figure 7.7: *Results of impulsive forces for 3 different PRECAL panelizations on the hull and the coarse (55*17) Cartesian grid (top) and the same but for the fine (110*34) Cartesian grid (bottom).*
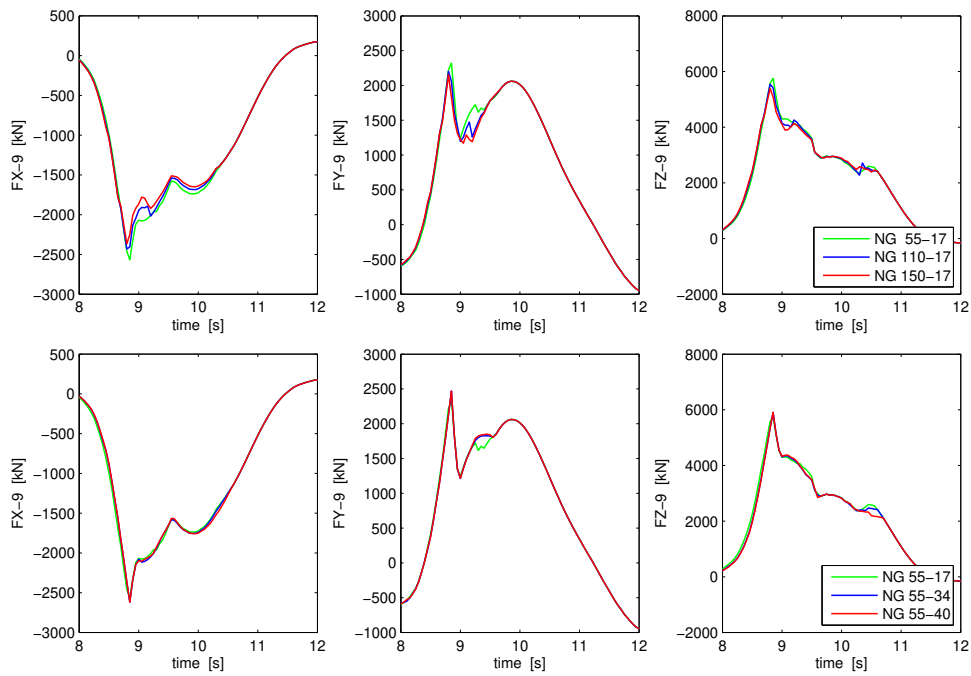
Figure 7.8: Results of impulsive forces for 3 different vertical divisions of the Cartesian grid (top) and 3 different horizontal divisions (bottom).

The longitudinal derivative of the surge added mass

The results for the added mass derivative $\partial a_{11}/\partial x$ appeared to be giving problems. The most forward panels have the largest component of their normal vector in the forward direction of all panels in the bow. These panels have a tendency to contribute a lot to the surge added mass coefficient a_{11}. The longitudinal derivative of this parameter is even more sensitive to the orientation of the last panel; the effect has a tendency to diverge for an increasing number of panels as shown in Figure 7.9. Since the impulsive force calculated with this parameter appeared to be very small, it was chosen not to use this component in the calculation of the impulsive forces.
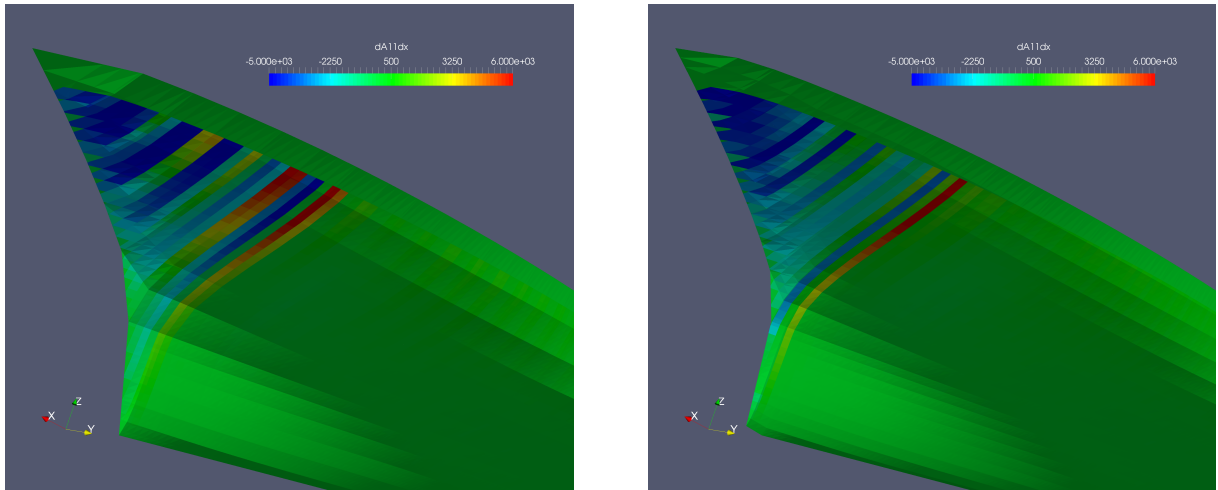
Figure 7.9: Added mass derivative $\partial a_{11}/\partial x$ on a coarse panelization of the hull (left) and on a fine panelization (right). The Cartesian grid is 110*34 in both cases.

7.4.3   Verification of the time step in the simulation

The time step has been varied for the Grid 3-2 case. This parameter again has the main effect on the peak value of the impulsive force. Based on the results shown in Figure 7.10 a maximum time step of $dt = 0.025$ s is chosen for the simulations.

7.4.4   Verification of the number of frequency components in the wave input

The wave input is defined as the sum of a finite number of frequency components at an earth fixed position. This position is chosen as the centre of gravity of the ship at $t = 0$. Using this information, the undisturbed wave can be calculated on any place and time using linear wave theory. This input FFT of the wave is derived from the wave
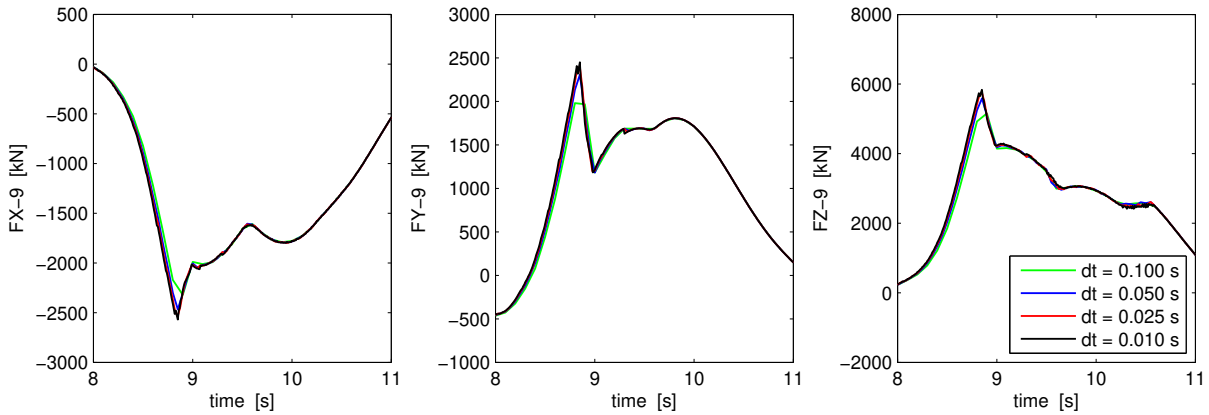
Figure 7.10: Variation of the time step for the test condition, Grid 3-2.

measured close to the bow of the model during the experiment. The frequency range and step of the FFT is defined by the length T $[s]$ of the measurement (low frequency limit $\omega_{LOW} = 2\pi/T$ $[rad/s]$) and by the sample rate f $[s^{-1}]$ of the wave measurement which determines the frequency step $\Delta\omega = \pi/f$ (Nyquist frequency). Since the wave elevation has to be calculated at every time step, at every longitudinal position of the Cartesian grid, both sides of the model, it is efficient to use a minimum number of frequency components.

The number of frequency components can be reduced by limiting the FFT to a maximum frequency. It seems logical that waves with a frequency above a certain value, do not contribute to the magnitude of the impulsive forces. Testing this method, Figure 7.11, shows that the maximum frequency can be reduced to $\omega_{MAX} = 2.0$ $[rad/s]$ without losing accuracy of the peak value of the impulsive force.
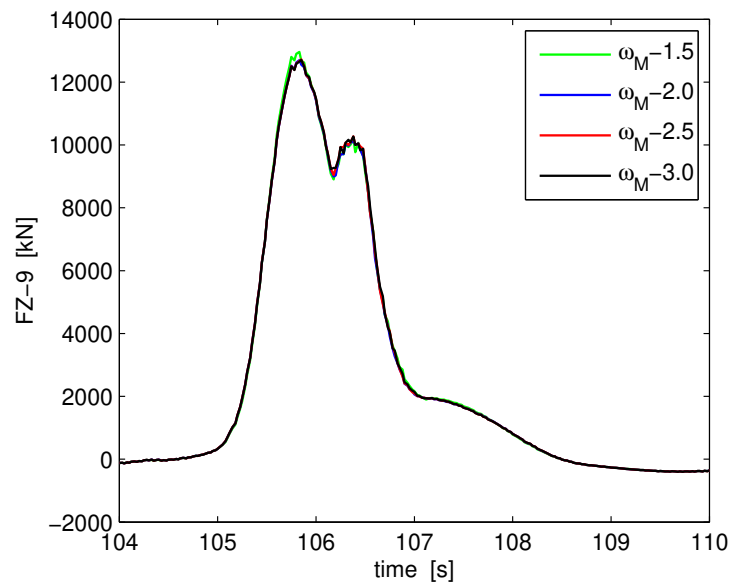
Figure 7.11: Effect of a limiting maximum frequency in FFT of the wave input. The legend indicates the maximum frequency in [rad/s]; the number of frequency components is 170, 273, 401 and 554 respectively.

Chapter 8

Simulation and Validation

8.1   Introduction

The validation of this slamming model was done in two phases; the first phase focusing on the forces on a small part of the bow, forward of St 19.5 and above the calm water line, a second phase focusing on the loads of a much larger part of the bow, forward of St 15. In fact, the development started with a very ambitious test campaign using a flexible free running model for which also the loads on a bow segment were being measured. Although this campaign was quite successful, it appeared to have too many degrees of freedom for validation purposes. In other words, the slamming phenomenon was too complicated to solve everything in one go. Therefore the 'first phase' experiments were designed: experiments were done with a captive model and also with a model in a forced (pitch) motion. Much attention was paid to measuring the shape of the wave just before the impact by a specially designed array of wave probes. The results of these tests compared quite well to the version of the slamming model at that time. Considering this, it was decided that it would be very valuable to extend the measurements over a larger part of the hull. The hull form used had a relatively large deadrise angle at the level of the waterline in the range St 15 - St 18, therefore it was expected that important slamming forces would also be generated by this part of the hull. In quartering waves it was also expected that the main forces would be in this forward area of the hull and it was realized that quartering conditions might very well be the more demanding ones.

The experiments were mainly done in an artificial wave train, meaning that no attempt was made to realize a certain wave spectrum. The main focus of the experiments was to generate useful data to develop insight in the slamming phenomenon and to generate data for validation of the developed models. Some experiments in a normal wave spectrum with many wave components having randomly selected phase angles were carried out to generate statistics of slamming loads.

Because it was already known that wave steepness is a very important parameter for slamming, a wave train was developed in which the waves have a constant wave height and a decreasing wave length. This wave train was identified as a wave sweep. Details of

the generation and use of such waves are given in subsection 4.5.1.

8.2 Presentation of the results

The results of the simulations are in general time traces of the forces on the vertical sections on the calculation grid, separate on port and starboard side. These forces are added (PS and SB) and integrated over the length of the physical segments of the model to allow a comparison to measured values. Presenting these results as such, forces in 3 directions, in the case of the 2nd series of experiments on 10 different segments, for each condition (speed, heading, type of wave condition) requires a lot of space and the overview is completely lost. Results have to be condensed in some way without losing too much detail. A statistical approach is not useful; the length of the measurement in the basin is too short so there are not enough events to have meaningful results. Also measurements were done in special wave trains, so these statistics are meaningless for a normal sea state.

Transferring the forces to the impulse using a characteristic time interval like 1/4 of the period of the 2-node vertical bending mode of the ships hull does not reduce the amount of information. Essentially it only means that the results are processed by a low-pass filter. Another approach was to present plots of peak values, measured values on the horizontal and calculated values on the vertical axis. These plots were made using a threshold value for each force component and finding peak values in-between zero up-crossings. Peak values are separately determined for measured and calculated signals and then pairs are selected that occur on the same time instant (with a margin of 2 s).

This procedure is demonstrated using the results shown in Figure 8.1. This figure shows the measured and calculated time traces for an example run in head waves. Figure 8.2 illustrates the peaks found in the measured signal using a threshold values $FX_{TRSH} = -100\ kN$ and $FZ_{TRSH} = 200\ kN$. The bottom plot shows the final comparison of corresponding peak values.
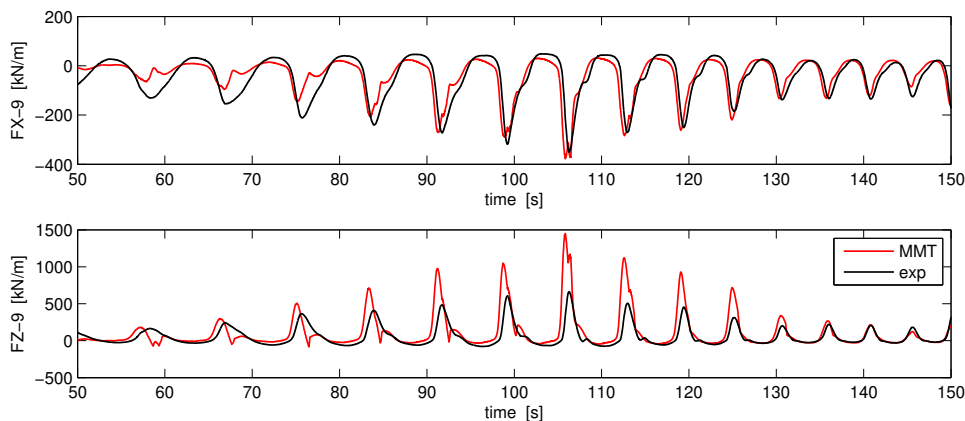
Figure 8.1: Example of time traces of measured and calculated forces on Segment 9. Second series of experiments, free running model in head waves, wave sweep, $v_S = 20$ kt.
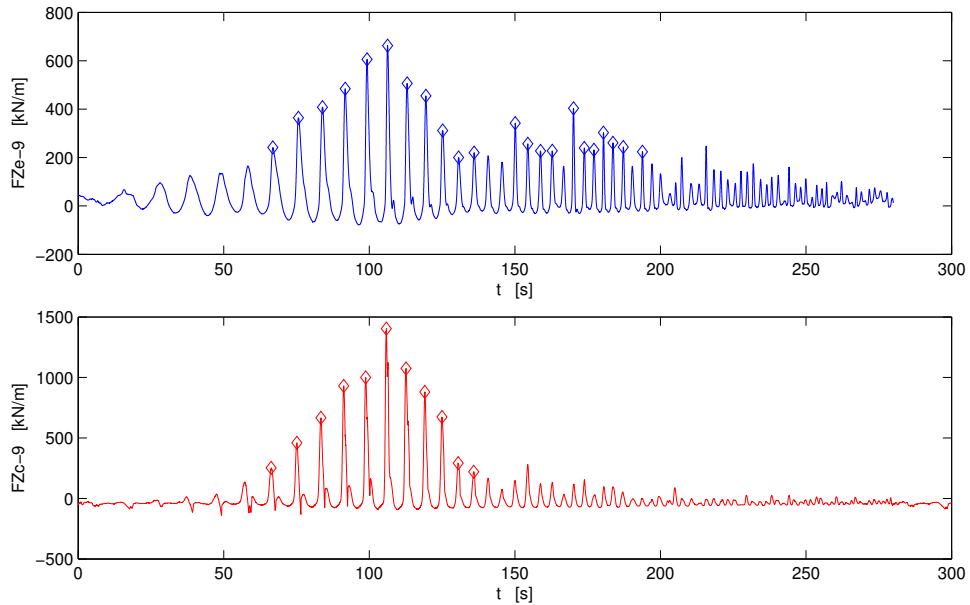
Figure 8.2: Example of procedure to find peaks in the experimental (top) and the calculated (bottom) force signal.
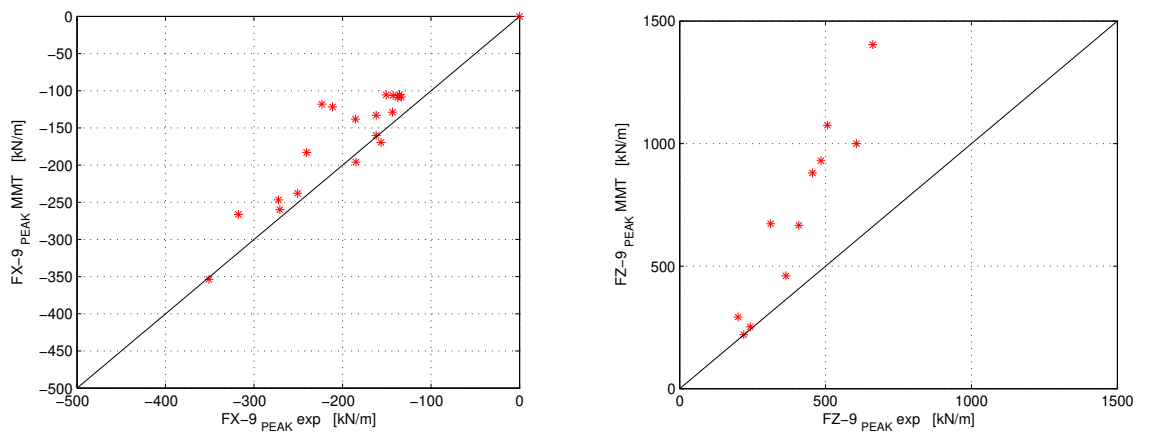
Figure 8.3: Plots of the comparison measured - calculated of the peak values of the longitudinal and vertical forces on Segment 9. These plots represent the same data as shown in Figure 8.1.

One disadvantage is, that peaks detected in one, but not in the other method, are not shown in the diagram. A second disadvantage is, that the comparison focusses on the peak value, while this is very often not the most important parameter. Also the relation between the peak values and the wave is lost in this way of presentation. Finally, the original objective is not achieved: the number of plots is not reduced.

Finally it was decided to reduce the number of plots by mapping the forces measured and calculated on the segments to the mode shape for the 2-node vertical and horizontal bending, this method is detailed in section 8.3.

8.3   Modal excitation

A way to quantify the flexural behaviour of a structure is by using mode shapes. Mode shapes are solutions of the structural Equations of Motion (EoM) for the natural frequencies. The mode shape is the unit deformation shape for that natural frequency; the amplitude is determined by the solution of the EoM. The deformation of the structure by a general excitation is explained by the sum of the deformations of mode shapes belonging to individual resonance frequencies. When determining the mode shapes, a choice can be made to use the 'wet' or the 'dry' mode shapes; taking the added mass of the fluid into account or not. This has consequences for both the natural frequencies and the mode shapes. Essentially both methods can be used, Loukogeorgaki *et al.* [117] found better results (in comparison to experiments) using the wet mode shapes when studying a very large floating structure and a thin large floating plate. It can be argued that for relatively low natural frequencies it is better to include the added mass and for high natural frequencies, like local vibration of a plate in-between stiffeners, it is better to use the dry mode shapes. The main argument for this choice is the effect of cavitation when a body vibrates with high frequency in a fluid. Cavitation has been observed by Faltinsen when studying impact tests of a flat plate [49].

Describing the rigid body motions and the flexural modes in one set of equations is usually done by the so-called Generalized Modes. This concept was introduced by Newman in 1994 [138] and used for time domain applications by Farstad [51] and Tuitman *et al.* [180].

The results of the measurement of the forces on the segments can be condensed to the modal excitation for the 2-node vertical and horizontal bending modes. Since the model was designed as a rigid model, simplified mode shapes (parabolas) of these bending modes were used. These simplified shapes are defined in Equation 8.1.

$$
\begin{aligned}
y(x) &= -\tfrac{1}{3} + 4 \left(\tfrac{x}{L}\right)^2 \qquad \forall\, -0.5 < \tfrac{x}{L} < 0.5 \\
z(x) &= -\tfrac{1}{3} + 4 \left(\tfrac{x}{L}\right)^2
\end{aligned}
\tag{8.1}
$$

The measured forces are mapped onto the simplified mode shapes for the interval for which the forces have been measured, $0.25 < x/L < 0.50$. The resulting modal excitation for the horizontal and vertical 2-node bending mode is, Equation 8.2:

$$
\begin{aligned}
F_{2H}(t) &= \sum_{x=L/4}^{L/2} FY(x,t)\, y(x) \\
F_{2V}(t) &= \sum_{x=L/4}^{L/2} FZ(x,t)\, z(x)
\end{aligned}
\tag{8.2}
$$

Applying this to the measured and calculated data, a figure like Figure 8.4 is obtained. This figure condenses 10 different plots of the forces on the 10 segments into one plot. It is stressed that the input for this plot is just the vertical force; the longitudinal one is not included. A problem is, that the centre of effort of this force component - and hence the

moment arm - is unknown. Therefore its contribution cannot be taken into account, but, it is expected that its influence is small.

8.4   Force components

The calculated hydrodynamic forces contain several components:

- The hydrostatic force due to the undisturbed incoming wave (Froude-Krilov force). The pressure is integrated up to the actual free surface using the actual wetted geometry. The pressure in the fluid is defined for $z < 0$; for $z > 0$ Wheeler stretching has been used [193, 64]. This component includes the restoring forces, therefore it is often referred to as Froude-Krilov-Restoring force (FKR) force.

- The diffraction force, this is the effect of the presence of the body on the incoming wave. It is computed by linear theory by imposing a zero normal velocity as boundary condition on the body. This calculation is essentially done for zero speed in PRECAL; it is done at the correct forward speed in FATIMA.

- The radiation force is the force induced by the moving body. It also results from linear theory, again essentially for zero speed in PRECAL and correctly at speed in FATIMA. Since the radiation forces are proportional to the a-priori unknown motions, impulse response functions are convoluted with the history of the motions in the time domain simulations. The effect of the high frequency limit of the radiated wave is added separately.

- The impulsive force and the wave slap load; these components are calculated by the approximate method developed in this thesis.

Normally there are more components of the forces, like the force produced by appendages and the inertia force. Appendages were not present on that part of the model where slamming was measured. The inertia force is not mentioned since this component was removed from the experimental results to which the results of the calculations have been compared. The different components of the hydrodynamic forces in a large slamming event are shown in Figure 8.5. These plots show that the impulsive force is indeed a very
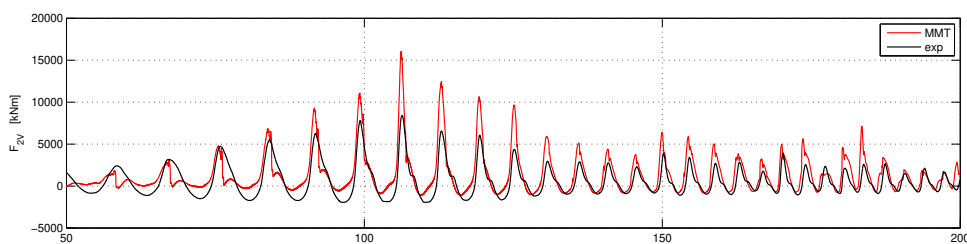
Figure 8.4: Modal excitation (2-node vertical bending) based on the measured and calculated forces forward of St 15. Experiment in head seas, $v_S = 20$ kt.
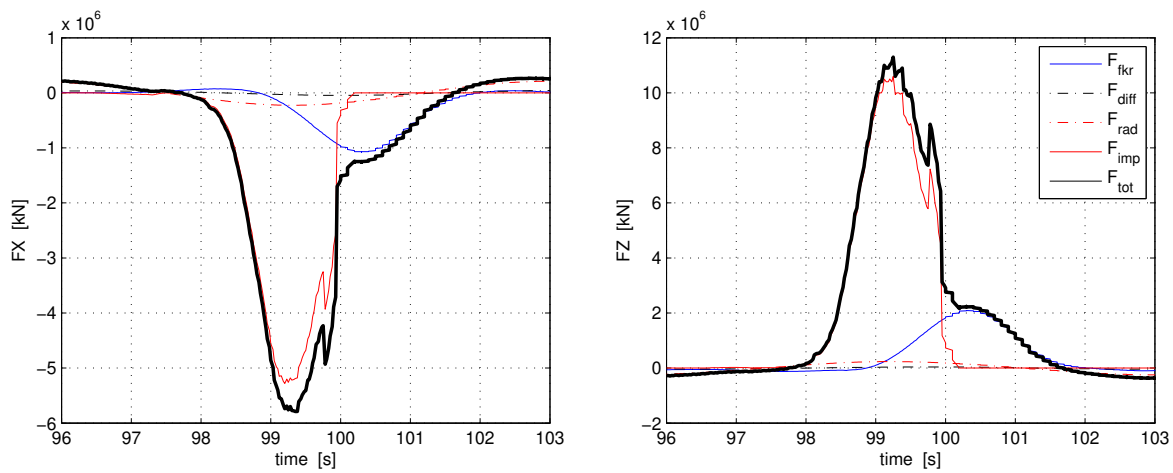
Figure 8.5: Components of the longitudinal and vertical force for a peak event in head seas,
        $v_S = 20 \ kt.$

important component in the first part of the event; later on the major part is due to
the FKR component. Linear diffraction and radiation effects are very small and can be
ignored.

8.5   Relative motions and velocities

Accurate calculations of relative motions and relative velocities are of paramount importance in slamming calculations. At the start of this research project this was not fully realized, measuring the wave profile just in front of the model was considered sufficient. More emphasis was put on measuring the relative motions in the impact area in the second series of model experiments. These results proved to be of great value in understanding the force levels measured.

8.5.1   Relative motions at the bow

Relative motions just in front of the bow were measured in the first series of experiments. The ship speed is large enough not to radiate waves in front of the model ($\tau = u\omega_{\mathrm{ENC}}/g > 0.25$) therefore diffracted and radiated wave should have no effect. The stationary bow wave however is important for the relative motions at the bow. The height of the bow wave has a tendency to increase, for a large part due to the increasing bluntness of the waterlines.

A result of this measurement and the result from the simulation is shown in Figure 8.6 for an extreme wave case in head seas. The measured steepness and height of the first wave in the plot is not matched by the MMT program, the second less steep wave is better matched. The difference in the first case is partly due to the use of a linear wave model in the simulation program, but most likely for the larger part due to the spray generated at the bow. This spray is not relevant for the impulsive force since the pressure in the spray is atmospheric, so it is not included in MMT. It is however measured by the twin wire system used to measure the relative motion in the experiments.

8.5.2   Relative motions measured with rows of pressure sensors

For the second series of experiments, the relative motions were measured on three locations on the leeward side by traditional twin-wire sensors. Pressure sensors were fitted on the weather side on the same longitudinal positions in three vertical rows; the idea was to use the start of the pressure pulse as a measurement of the relative motion and the time
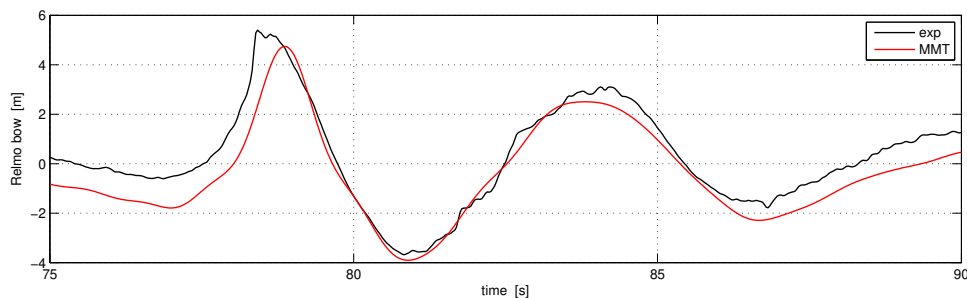
Figure 8.6: Comparison of measured and calculated relative motion at the bow. Captive model at $v_S = 20$ kt in head seas. Extreme wave case.
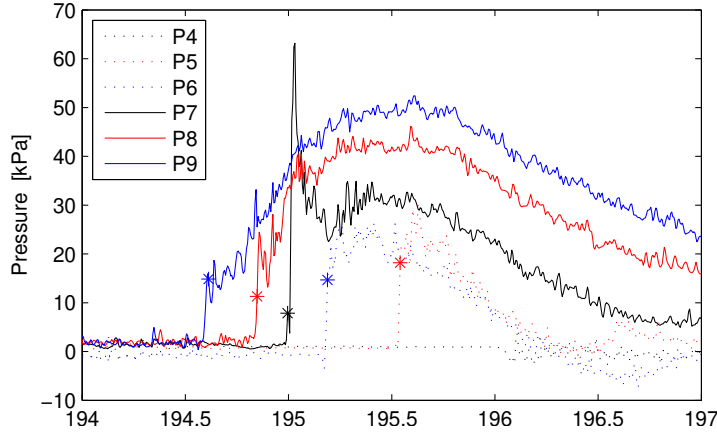
Figure 8.7: Example of series of pressure pulses measured by the vertical row P4..P9 pressure sensors on the segmented ferry model. The start time of the pressure pulses, defined by the conditions given in Equation 8.3 is indicated by an asterix.

difference of the start of the pulse on different sensors for the relative velocity. This system appeared to be working well; the pressure pulses could clearly be detected and by adopting a set of conditions, Equation 8.3, the start time $t_{start}(k)$ of event k could be determined. The parameters used in this equation are time averaged over 20 samples (sampling frequency 196 Hz full scale, 1 kHz model scale) to avoid a large effect of noise.

An example of a series of pressure pulses is shown in Figure 8.7. An asterix in this figure indicates the start time according to the criterion defined in Equation 8.3.

$$
\begin{cases}
p_{t-1} < 10 \quad \wedge \; p_t > 10 & [kPa] \\
t_{start}(k) - t_{start}(k-1) > 3 & [s]
\end{cases}
\tag{8.3}
$$

The choice of the parameters in Equation 8.3 is not very critical. The rise of the pressure is very steep, so a different value for the first criterion will result in only a small change in the time instant. The choice is determined such that it is above the noise level of the pressure sensor and below the peak value of the pressure pulse that should still be taken into account. The interval of 3 s for subsequent pressure peaks is used to avoid two peaks in the same event. The value should be chosen as a minimum wave encounter period.

8.5.3   Relative motions along the side - head waves

Relative motions along the side are affected by radiated and diffracted waves in the linear regime and by pile-up effects in the non-linear regime. The profile of the stationary wave system along the hull also has an effect; the profile changes as the bow changes draft. It was already noted in 1983 by Blok and Huisman [16] that this draft dependent bow wave was the main component of what was then called 'swell-up'. The effect of changes in draft are largest for the primary bow wave at St 19 - St 19.5 as shown in Figure 7.3.
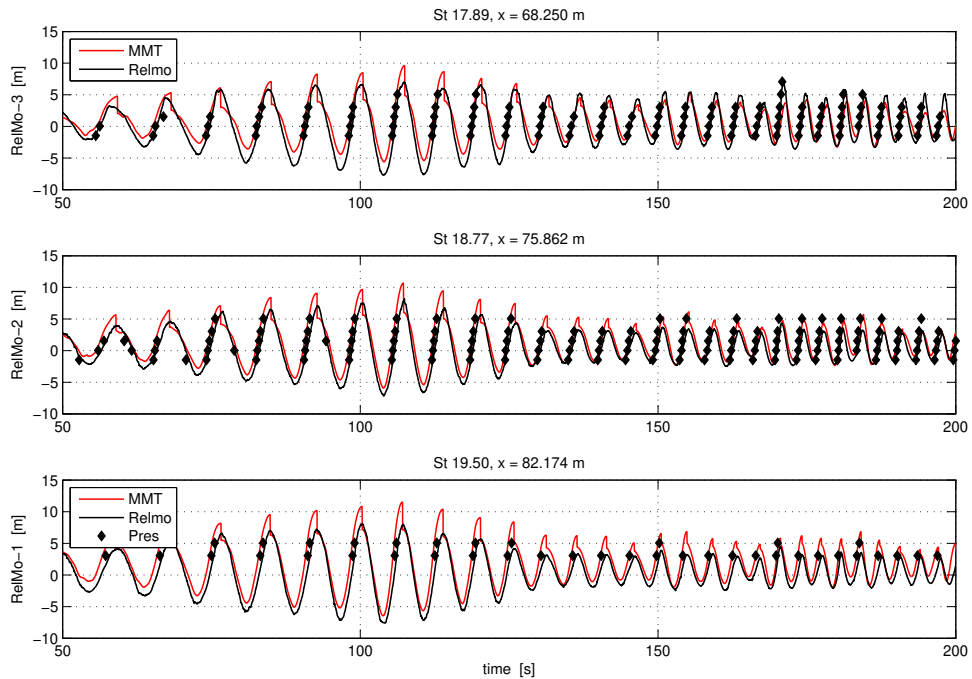
Figure 8.8: Relative motions on 3 locations along the side of the ferry model in head seas. The result of the relative motion sensors on PS are shown as black lines; the result of the analysis of the start time of the pressure pulse measured by the pressure sensors is shown as dots. Predictions by MMT are shown as a red line. Wave sweep, $v_S = 20\ kt$.

A result of measured and calculated relative motions in head waves is shown in Figure 8.8. The figure shows some differences between the results from the wire sensors at a distance from the hull (about 0.40 m full scale) and the results from the pressure sensors. These differences occur mainly in short steep waves where the pile-up effects are very local, so the pressure sensors indicate larger relative motions than the wire sensors. The pressure sensors on the highest position, at 7.05 m above the still water line, were only activated once in this test. The calculations show large pile-up effects for the first half of the plot as illustrated by the instantaneous drop of the relative motions as soon as the relative velocity becomes negative.

The relative velocity derived from these results is shown in Figure 8.9. The results are noisy due to the numerical differentiation although a moving average filter has been used over 5 samples. The results from the pressure sensors consistently show that the relative velocity close to the waterline is largest and that it reduces as the relative motion increases. The results from the calculations are consistent with the results from the relative motion sensors and lower than those from the pressure sensors.

Stills from the video taken during the experiments show the impact at $t = 101\ s$, Figure 8.10. The vessel motions are large, the fore body emerges totally. The impact pressure is sufficiently high to create a large amount of spray that is thrown to a conside-

rable distance from the bow of the model.
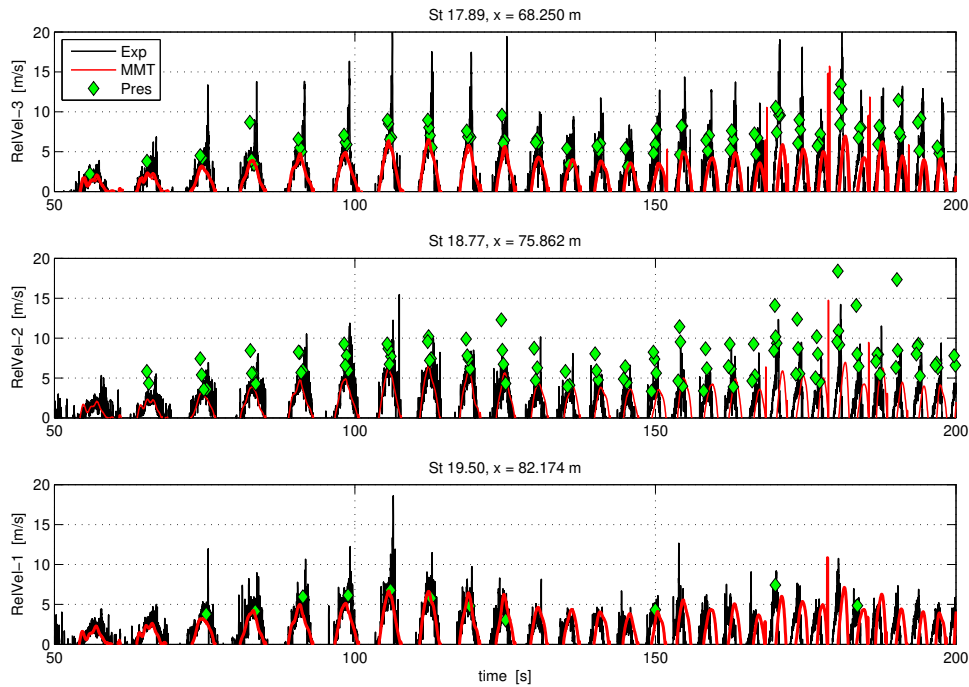
Figure 8.9: Relative velocity on 3 locations along the side of the ferry model. The result derived from the relative motion sensors on PS are shown as black lines; the result of the analysis of the start time of the pressure pulse measured by the pressure sensors is shown as dots. Wave sweep, Head seas, v_S = 20 kt.

Figure 8.10: Stills from the video of the experiments, the start of the impact at t = 101 s, the maximum immersion of the model and the moment the spray drops back in the water.

8.5.4   Relative motions along the side - quartering waves

In bow quartering seas there can be significant differences in the relative motions and velocities between the windward and the leeward sides. Results of relative motion measurements on both sides of the ship, resulting from a run in a heading of 120 deg, are shown in Figure 8.11. The differences are quite small in the first part of the run, where the vertical ship motions are large and the roll motion low. As the waves get shorter and steeper in the second part of the run the differences get more important; the pressure sensors on the highest level are activated while the wire sensors indicate much lower relative motions. The ship motions are very low for this part of the run, it is the regime of the wave slap forces. The figure shows however a significant difference in the relative velocity, this is further illustrated in a direct comparison, Figure 8.12. In the shortest waves the vertical velocity can be twice as high on windward as it is on the leeward side.

The simulation program uses a reduction of the pile-up factor on the leeward side; this results in a reduction of the relative motion. A comparison of predictions on the windward and on the leeward side are shown in Figure 8.13 for the leeward side and in Figure 8.14 for the windward side. The predictions are considered to be quite accurate although no definite comparison can be made on the peaks of the relative motion on the windward side. Plots of the relative velocity as derived from the measured relative motions and as calculated are shown in Figure 8.15 for the leeward side and in Figure 8.16 for the windward side. These plots show differences that were not so apparent from a comparison of the motions.

A plot of the signals recorded by the vertical row of pressure sensors mounted in Segment 8 is shown in Figure 8.17. The plot shows the pressure signals for the steeper
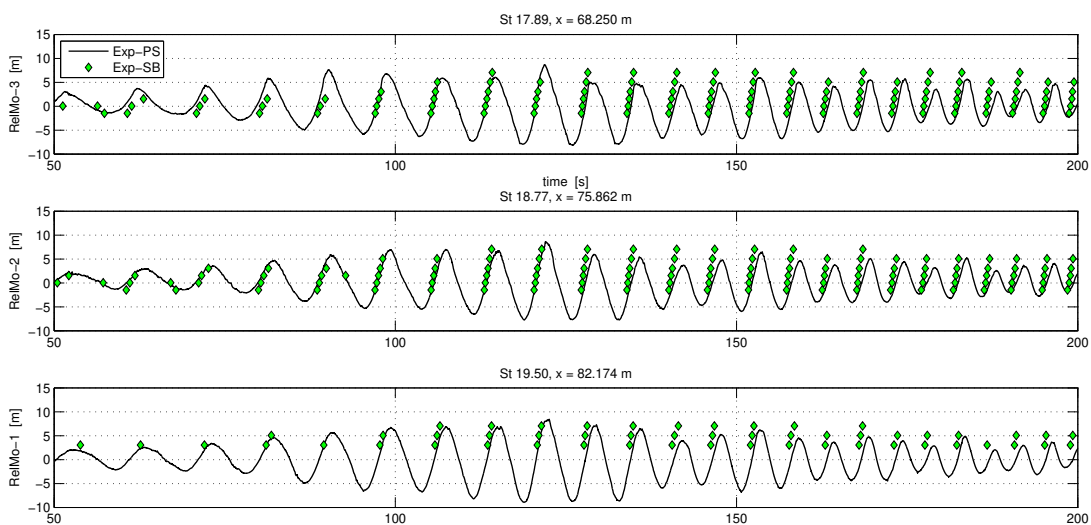
Figure 8.11: Comparison of relative motion measurements on windward and leeward in quartering waves. The full line is the measurement on the leeward side and the dots are results from the pressure sensors on the windward side. Heading 120 deg, $v_S = 20$ kt.
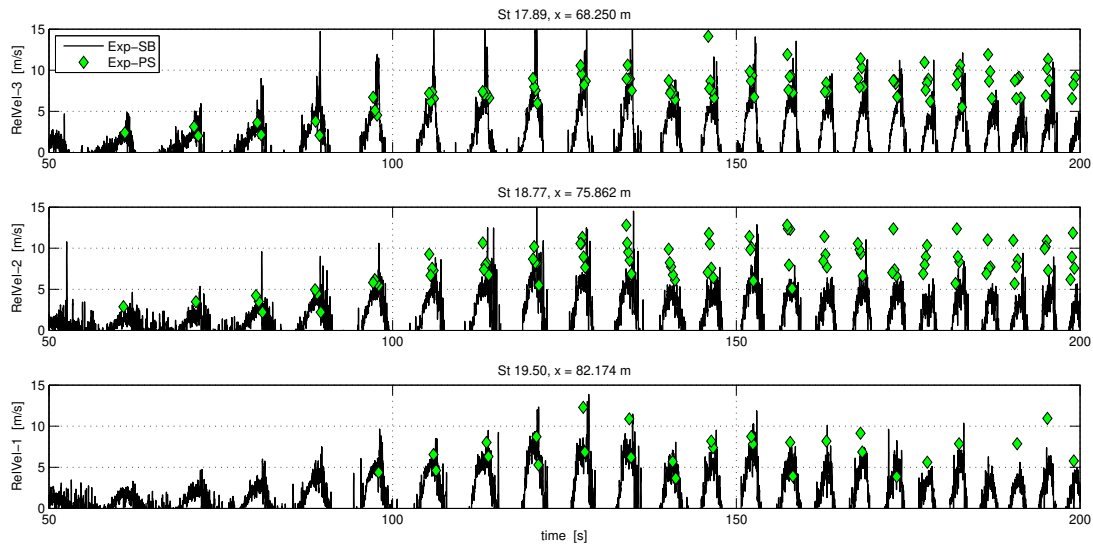
Figure 8.12: Comparison of relative velocity measurements on windward and leeward in quartering waves. The full line is the measurement on the leeward side and the dots are velocities derived from the pressure sensors on the windward side. Heading 120 deg, $v_S = 20$ kt.
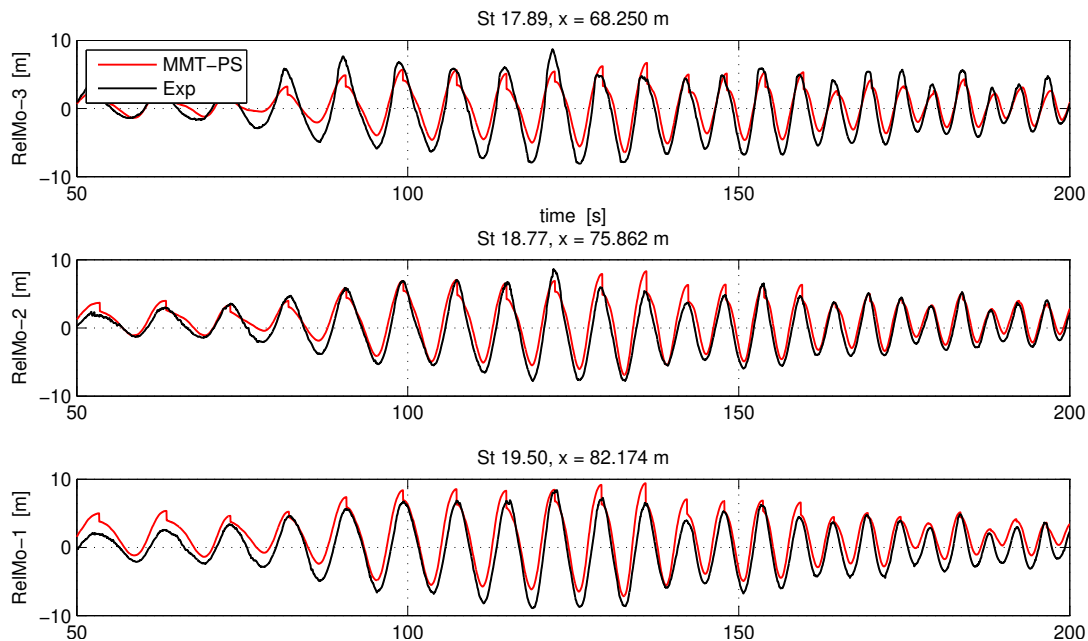
Figure 8.13: Relative motion on 3 locations along the PS bow (leeward) of the ferry model. The experimental results from the relative motion sensors are shown as black lines. Wave sweep, heading 120 deg, $v_S = 20$ kt.

waves in the second half of the run. The pressure sensors are activated from the bottom to the top in all cases, a picture of the installation in the model was shown in Figure 4.9. The peak pressure is mostly recorded by sensor P7, the sensor just above the waterline.
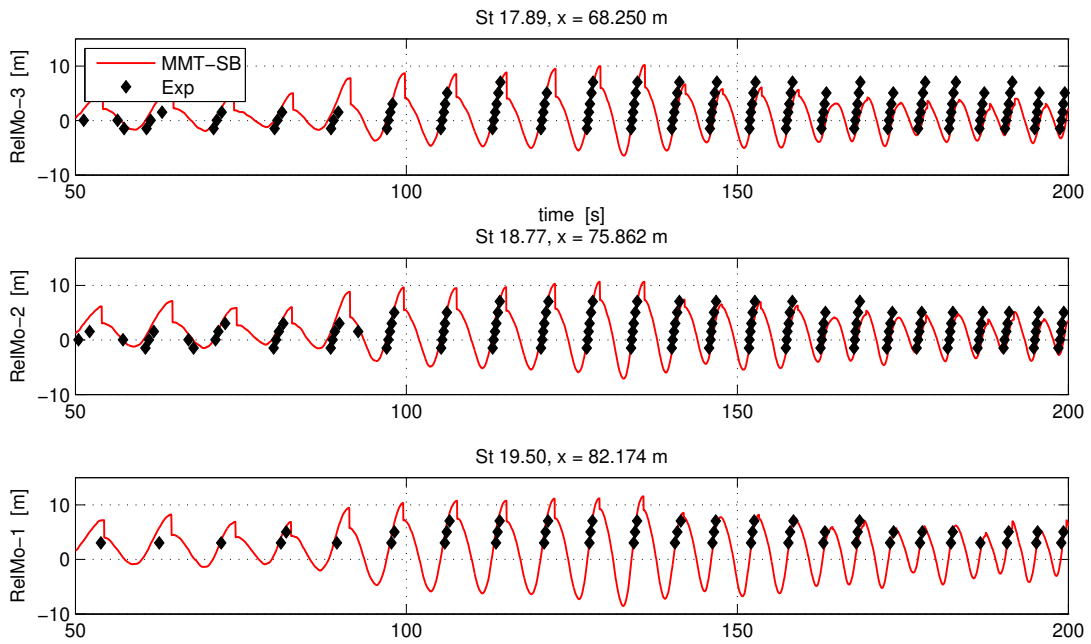
Figure 8.14: Relative motion on 3 locations along the SB bow (windward) of the ferry model. The experimental results from the pressure sensors are shown as black diamonds. Wave sweep, heading 120 deg, $v_S = 20$ kt.
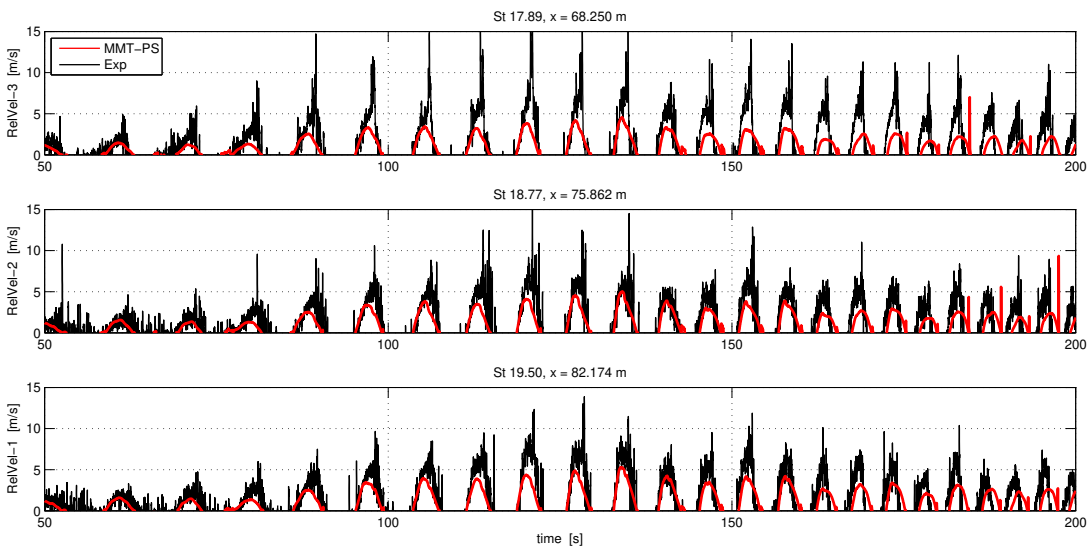
Figure 8.15: Results for the relative velocity on the leeward side on 3 longitudinal locations. Results derived from traditional wire sensors and results from the simulations. Heading 120 deg, $v_S = 20$ kt.
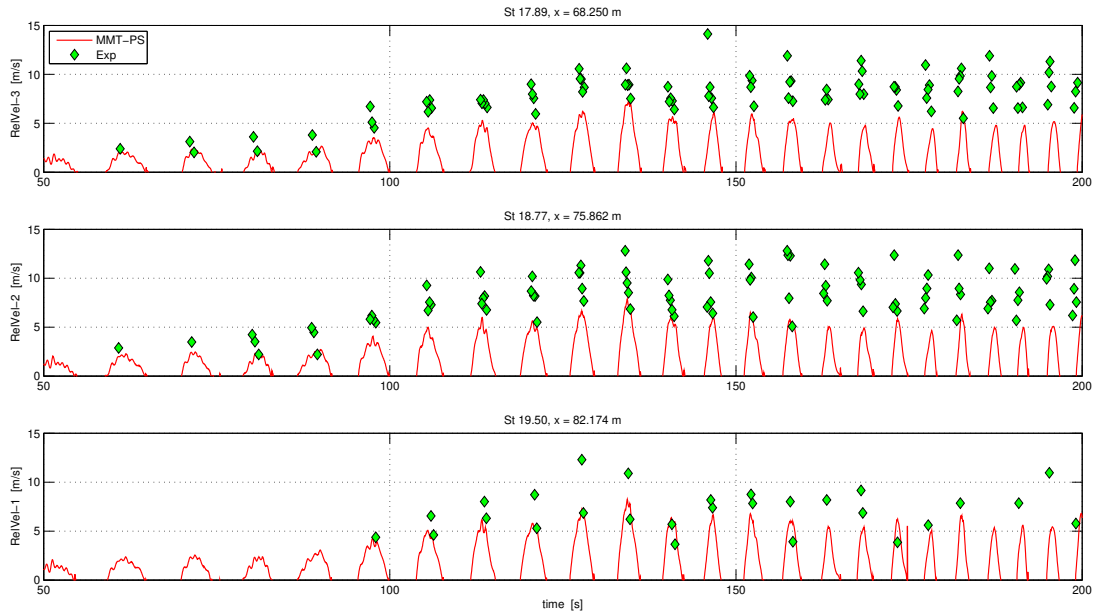
Figure 8.16: Results for the relative velocity on the windward side on 3 longitudinal locations. Results derived from the time difference in the start of the pressure pulse on subsequent pressure sensors in the column compared to results from simulations. Heading 120 deg, $v_S = 20$ kt.
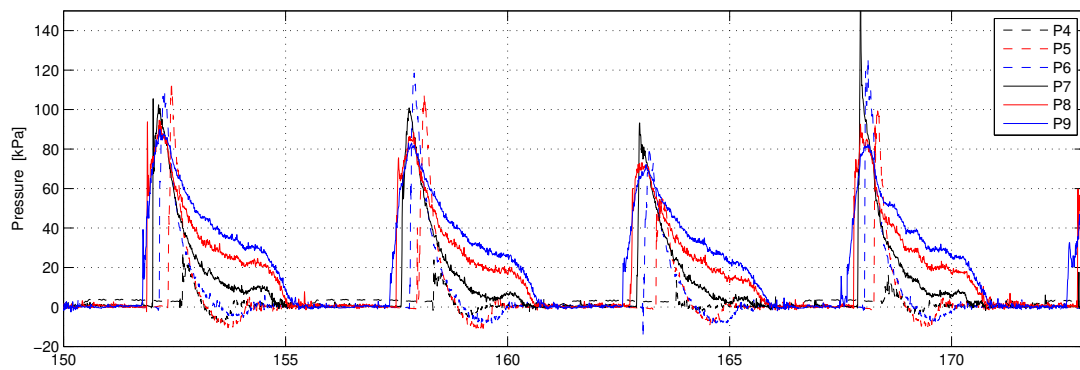
Figure 8.17: Results for the vertical column of pressure sensors at St 18.77. The plot shows that the sensors are activated from the bottom to the top, but the peak at P7 at $t = 168$ s is much steeper than the others. This indicates an overturning wave crest. Wave sweep, heading 120 deg, $v_S = 20$ kt.

8.6   Forces on a bow segment

The first series of experiments to measure forces on a bow segment were carried out with two set-ups: the first with a captive model, the second with the model fitted to a mechanical (pitch) oscillation mechanism. Experiments were done at high speed in high waves to have sufficient impulsive loads on the bow segment. The wave conditions for the experiments consisted of wave sweeps, focused waves and of a normal wave train representing an irregular sea (Jonswap spectrum, $\gamma = 3.3$). The experiments in which the model is forced in a pitch motion were carried out in regular waves. The frequency of the forced motion was chosen slightly different to the wave encounter frequency; in this way each successive wave encounter had a slightly different impact condition (relative velocity) to the previous encounter. The frequency difference $\omega_{OSC} - \omega_{ENC}$ was chosen such that results for two low frequency periods were obtained in one run.

Some results of experiments in the focused wave are shown in Figure 8.18 for a run in head seas. The measured relative motion at the bow is higher than predicted for the first wave encounter due to the effect of spray as explained before in Section 8.5.1. The prediction of the impulsive force appears to be quite good.

A result of an experiment in a wave sweep, also in head seas, is shown in Figure 8.19. If this result is compared to Figure 8.18, it is clear that the latter experiment contains
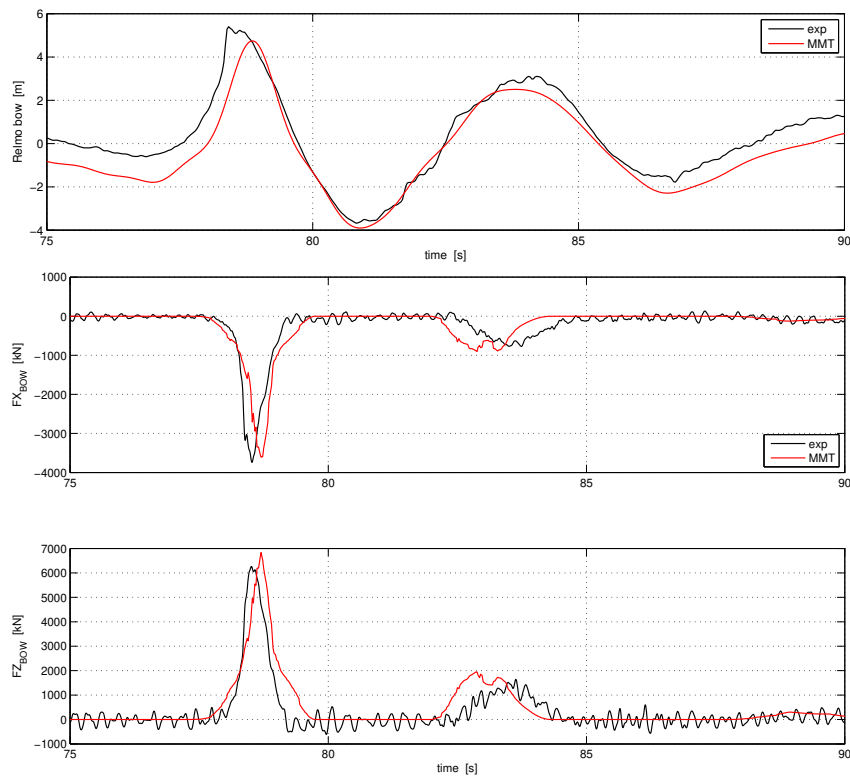
Figure 8.18: *Comparison of measured and calculated relative motion at the bow (top) and longitudinal and vertical force on the bow segment of the ferry. Captive model at $v_S = 20$ kt in head seas. Extreme wave case.*

much more information. Comparing the force levels between the two experiments, the focused wave is not an event as extreme as the largest impact in the wave sweep. The focused wave has a wave height and a force level of the waves in the wave sweep in the interval $155 < t < 175\ s$. The large peak in the wave sweep is the result of an extreme wave, about 2 m higher than the other waves. It was concluded that the focused wave contained as much information as a single extreme event from the wave sweep; this last technique is much more informative and therefore preferred for validation purposes.

Results of the forced oscillation experiments are shown in Figure 8.20 through Figure 8.21 for different cases in quartering seas, heading 150 deg. The figures show the changing impact conditions over about 30 wave encounters; the differences that are created by the changing phasing between the wave and the forced pitch motion. The predicted forces are based on the change in impulse in the vertical direction. Due to the differences in the pile-up between the windward and the leeward side of the bow, there are diffe-
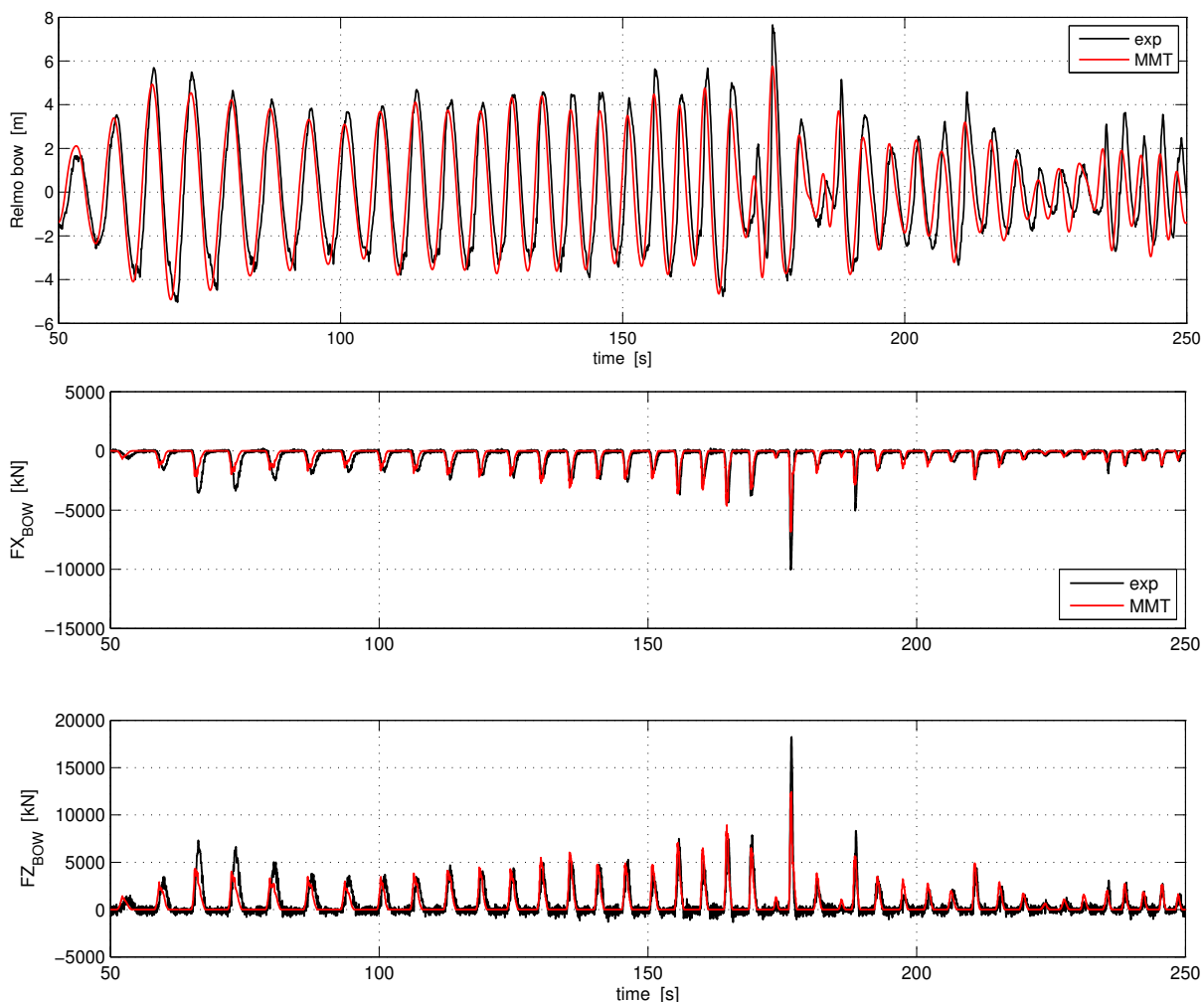
Figure 8.19: Comparison of measured and calculated relative motion at the bow (top) and longitudinal and vertical force on the bow segment of the ferry. Captive model at $v_S = 20\ kt$ in head seas. Wave sweep.

rent force levels on both sides, these differences are responsible for the calculated lateral force. The lateral forces are relatively low: even the longitudinal force is higher and the vertical force is a factor 4 higher. The over-prediction of the lateral force in the interval $110 < t < 130\ s$ indicates that the force level on the windward (SB) side is too large while in a later stage $150 < t < 220\ s$ the force on the PS is too large. These peaks are however of short duration, the prediction of the main part of the run appears to be good.

The difference between Figure 8.20 and Figure 8.21 is a difference in oscillation frequency. In the first figure the oscillation frequency is slightly lower than the wave encounter frequency, while in the second figure it is slightly higher. The comparison between calculation and measurement is similar.
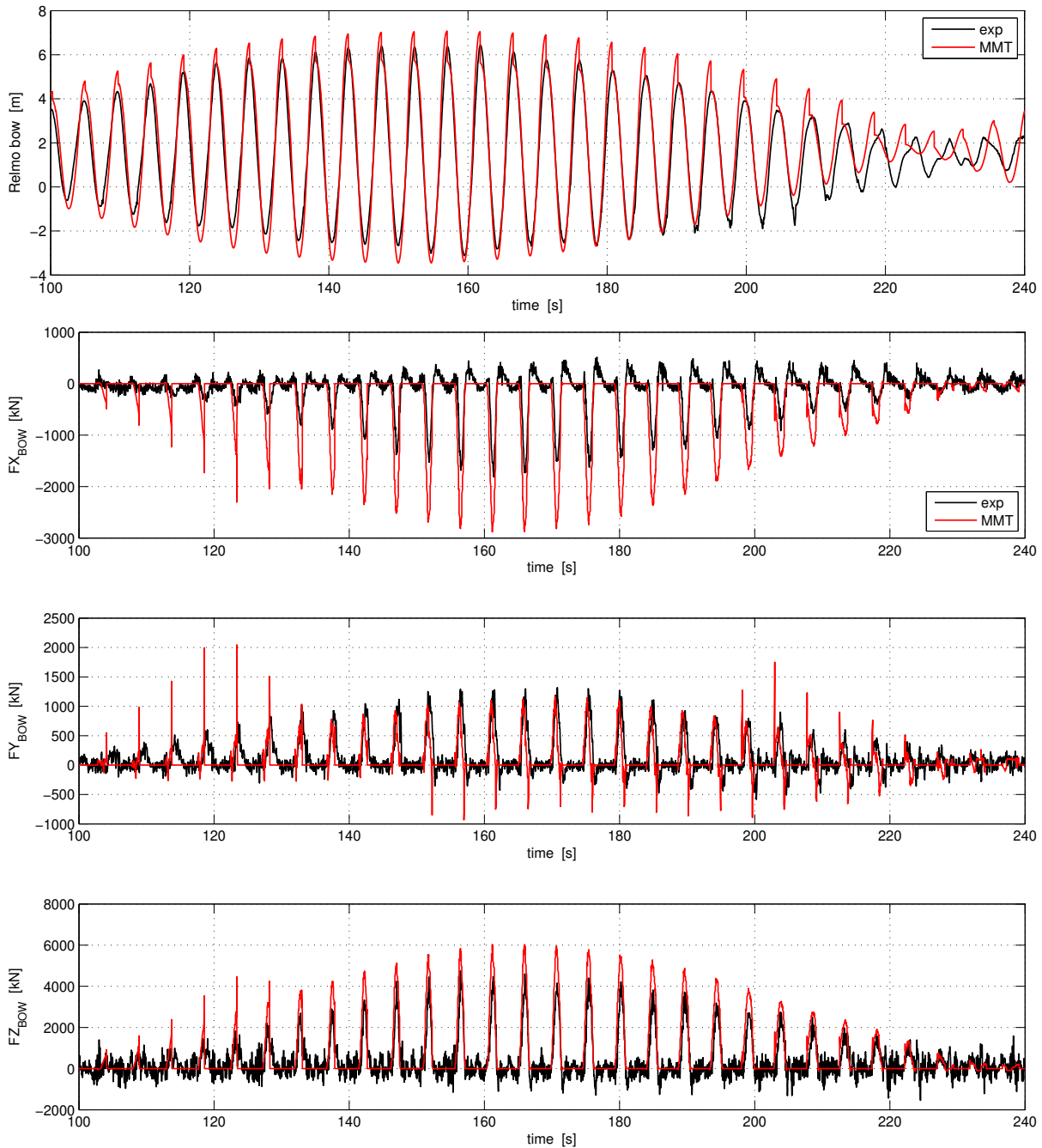
Figure 8.20: Comparison of measured and calculated relative motion at the bow (top) and longitudinal and vertical force on the bow segment of the ferry. Forced pitch oscillation tests at $v_S = 20$ kt, heading 150 deg. Regular wave, $T = 7.9$ s, $T_{ENC} = 4.59$ s. Oscillation period $T_{OSC} = 4.83$ s.
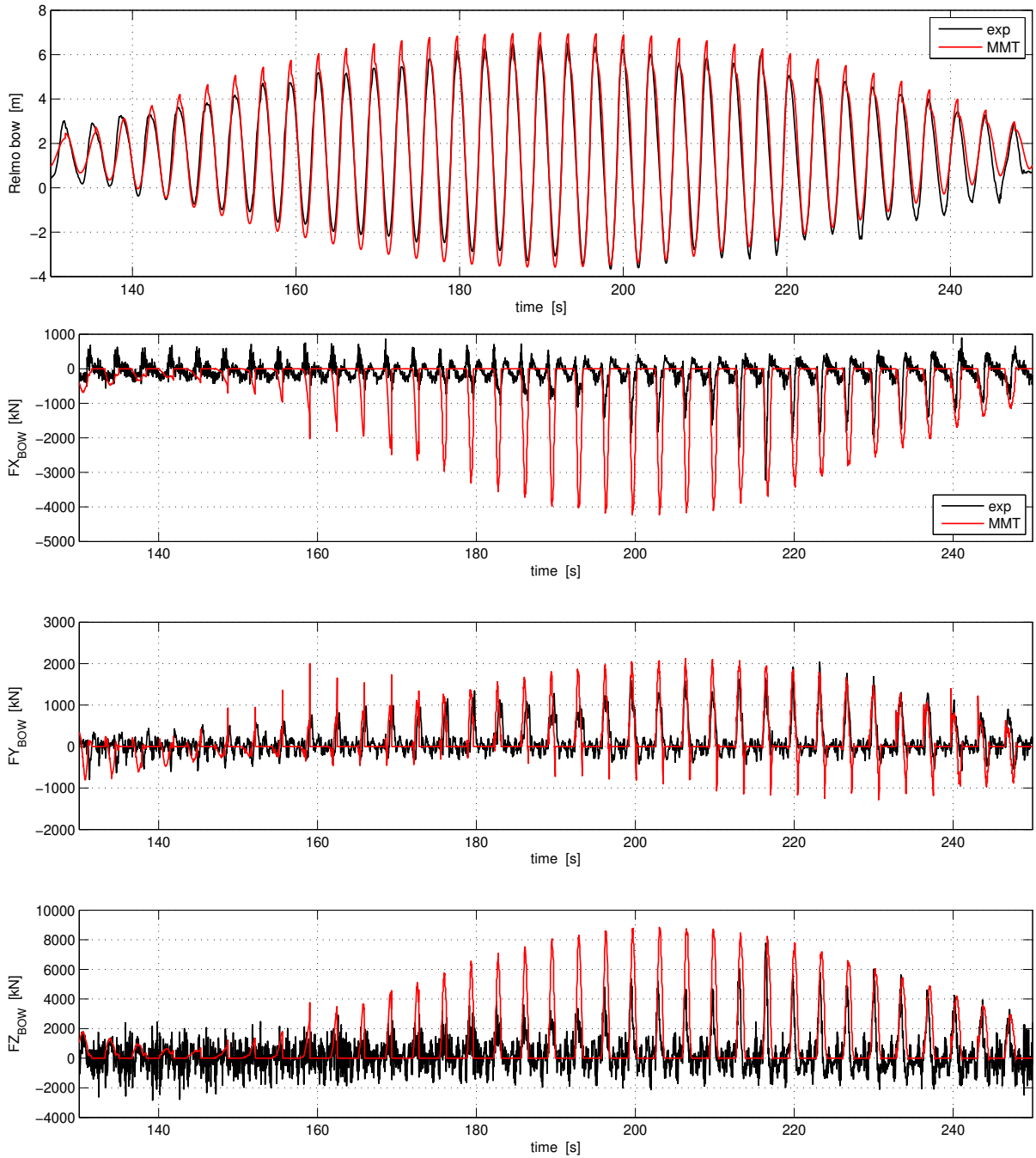
Figure 8.21: Comparison of measured and calculated relative motion at the bow (top) and longitudinal and vertical force on the bow segment of the ferry. Forced pitch oscillation tests at $v_S = 20$ kt, heading 150 deg. Regular wave, $T = 7.9$ s, $T_{ENC} = 4.59$ s. Oscillation period $T_{OSC} = 3.43$ s.

The forced oscillation test in 120 deg bow quartering waves shows a near perfect prediction of the vertical force, Figure 8.22. The longitudinal force is slightly over-predicted and the lateral forces are slightly under-predicted. The lateral force is much larger relative to the other forces than was the case for the 150 deg wave direction.
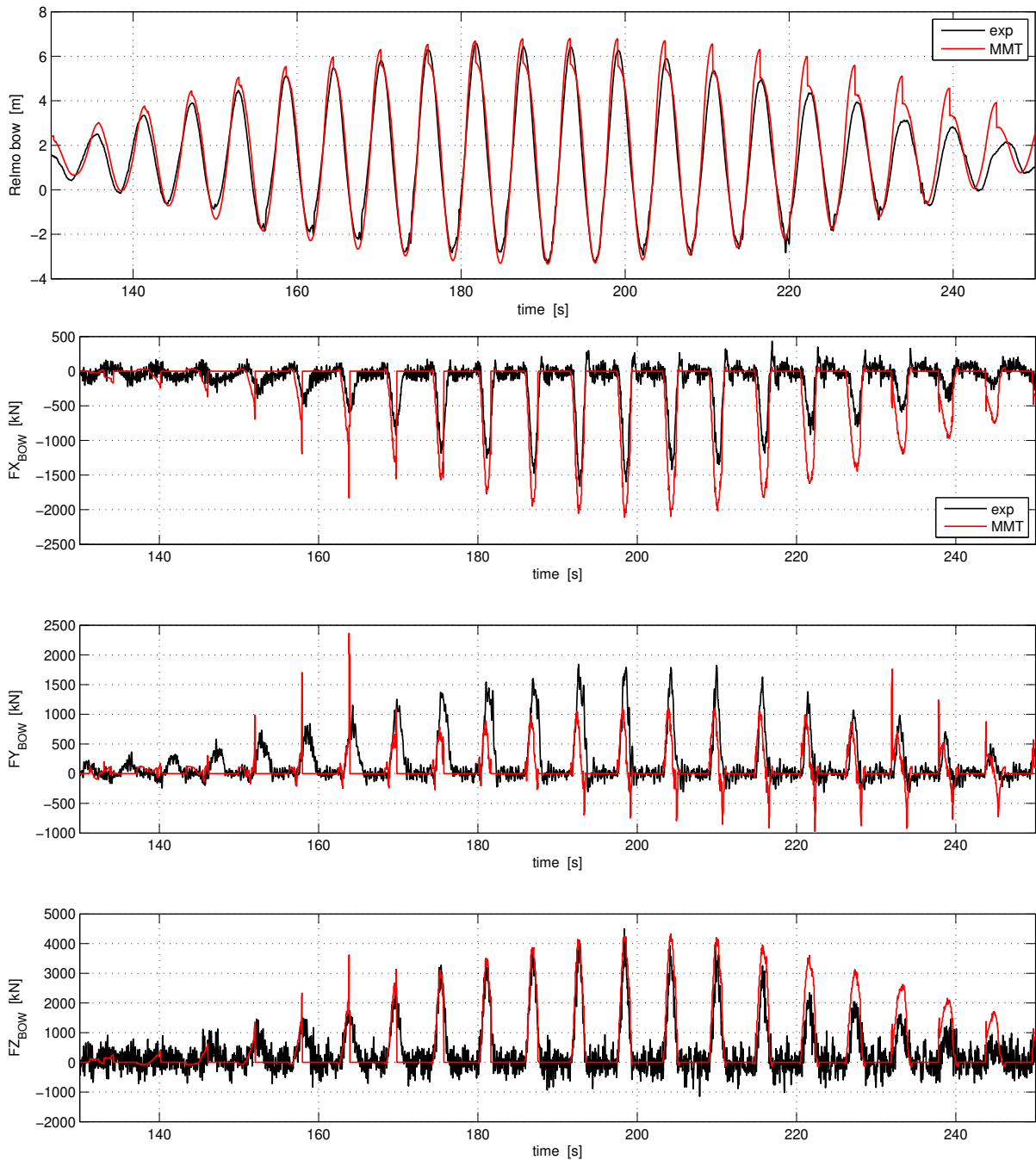
Figure 8.22: Comparison of measured and calculated relative motion at the bow (top) and longitudinal and vertical force on the bow segment of the ferry. Forced pitch oscillation tests at $v_S = 20\ kt$, heading 120 deg. Regular wave, $T = 7.9\ s$, $T_{ENC} = 5.57\ s$. Oscillation period $T_{OSC} = 5.98\ s$.

As an illustration of the impact conditions for these forced pitch oscillation tests two sets of stills from the video recordings are shown. Figure 8.23 shows an experiment in a wave direction of 150 deg. Figure 8.24 shows an experiment in a wave direction of 120 deg.

Figure 8.23: Stills from the video of the forced pitch oscillations, bow quartering waves, heading 150 deg, v_S = 20 kt. The phasing of the forced motion and the incoming regular wave is such that it results in a maximum force on the bow segment.
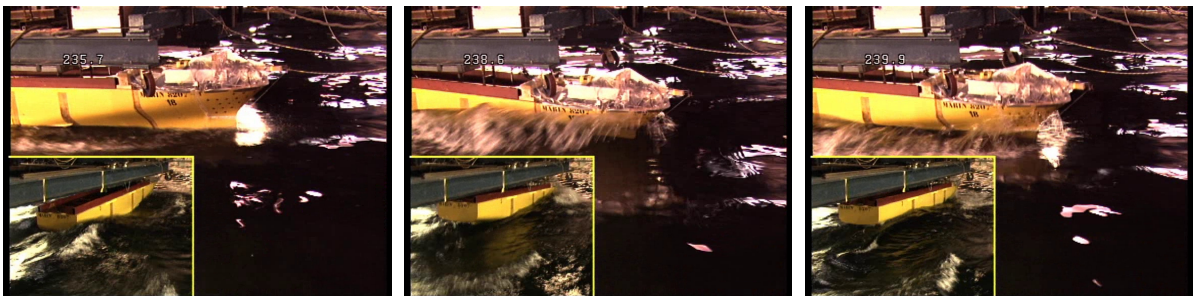
Figure 8.24: Stills from the video of the forced pitch oscillations, bow quartering waves, heading 120 deg, v_S = 20 kt. The phasing of the forced motion and the incoming regular wave is such that it results in a maximum force on the bow segment.

8.7   Forces on the forward part of the hull

The second series of experiments was carried out using a hull with 10 segments in the bow area, forward of St 15. The model is described in detail in Section 4.2. The main purpose of these experiments was to quantify loads on the hull in quartering waves as it was assumed that then the main impact forces would be in the area St 17 - St 20 rather than on the part of the bow forward of St 20.

8.7.1   Impulsive loads in head seas

Runs in head seas were made in wave sweeps as described in Subsection 4.5.1. The ship motions are large for the first part of the run and reduce to very low values in the short waves in the second part of the run. An example of measured motions at the Centre of Gravity (CoG) is given in Figure 8.25. The hydrodynamic forces for the first part of run are dominated by the impulsive forces calculated from the added mass derivatives, the wave slap forces are dominant in the second part of the run. The excitation of the 2-node vertical bending mode, calculated from the measured vertical forces on the 10 segments of the model for the full test, is shown in Figure 8.27. This plot shows an important over-prediction of the excitation for the period $90 < t < 130$ s.

   The forces on the individual segments are shown in Figure 8.26. This results shows that the prediction of the forces is in general quite good. The excitation force for the 2-node VB mode appears to be very sensitive to an accurate prediction of the vertical force on the foremost segment. This segment has the largest weight factor in the determination of the modal excitation.
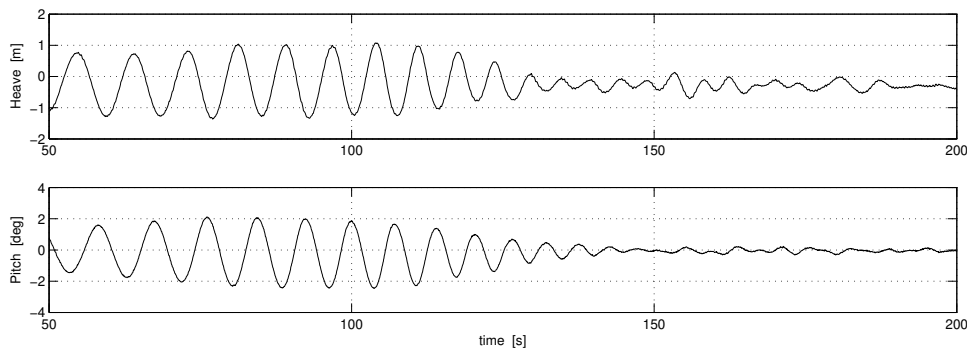
Figure 8.25: Measured heave and pitch motions for the wave sweep $H_W = 5.0$ m, heading 180 deg, $v_S = 20$ kt.
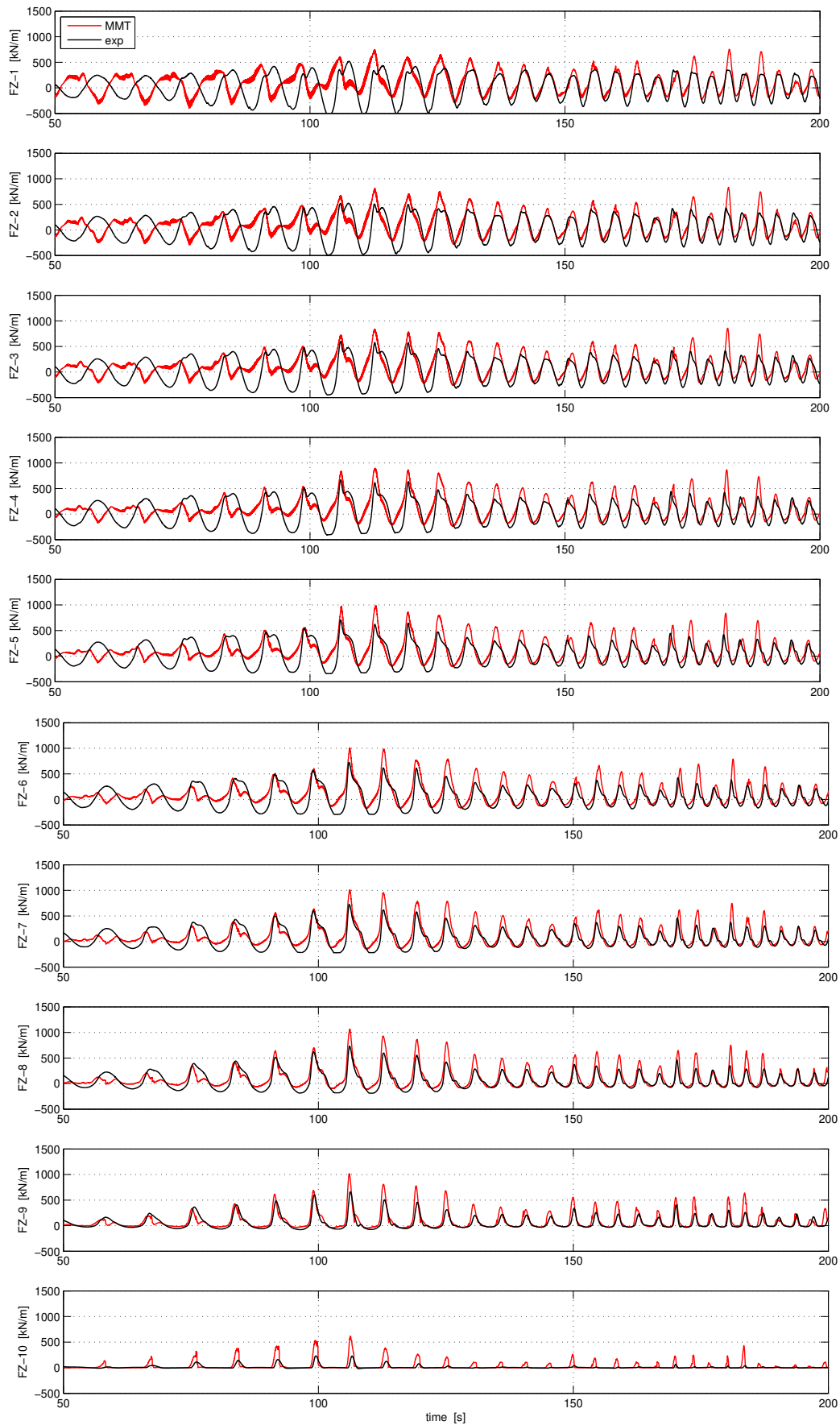
Figure 8.26: Vertical force on the 10 segments of the ferry model. Wave sweep $H_W = 5.0$ m, heading 180 deg, $v_S = 20$ kt.
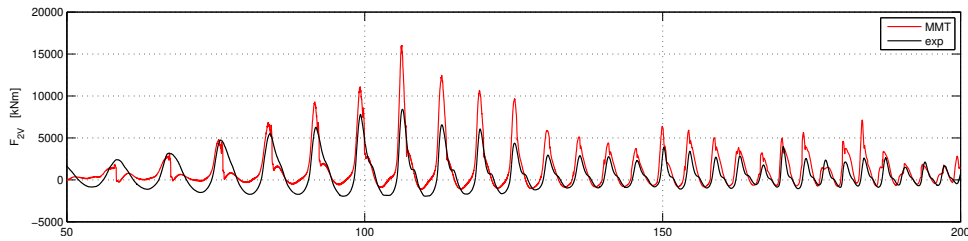
Figure 8.27: Excitation for the 2-node VB mode. Wave sweep $H_W = 5.0$ m, heading 180 deg, $v_S = 20$ kt.

The measured and calculated maximum vertical force on the segments for the largest value of the 2-node VB excitation force at $t = 106$ s are compared in Figure 8.28. This figure compares the measured and calculated force on each segment; the forces are normalized by the length of the segment to make them comparable in case the length of the segment is different. The plot is made for a case where the forces are at maximum; this appears to be when also the absolute motions are at maximum. The bow of the vessel emerges completely before the event; the calculation of the forces is completely based on the added mass derivatives; the wave slap loads module is not activated. The figure shows a good degree of agreement for the longitudinal force and an over-prediction of the vertical force.
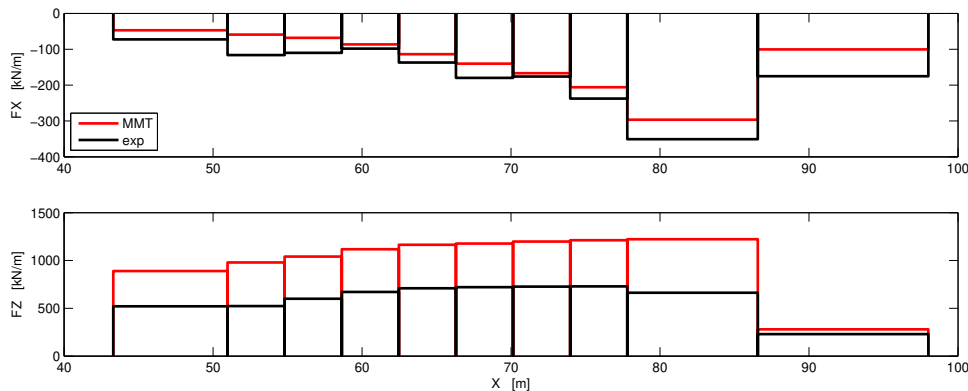
Figure 8.28: Distribution of the maximum force over the length of the bow of the ferry for one impact at $t = 106$ s. Wave sweep $H_W = 5.0$ m, heading 180 deg, $v_S = 20$ kt.

8.7.2   Impulsive loads in bow quartering seas, heading 150 deg

Similar experiments as in head seas were carried out in bow quartering seas, heading 150 deg. The measured motions are shown in Figure 8.29 and the excitation of the 2-node vertical VB and Horizontal Bending HB modes in Figure 8.30. The prediction of the VB mode is accurate, for the HB mode it is less good. The level of excitation in the horizontal plane is much lower, about a factor 5, than for the vertical plane. The distribution of the forces for the maximum value of the 2-node VB excitation at $t = 113$ s is shown in Figure 8.31.

Comparing these results to the ones in head waves in a comparable wave train, shows that the force level in longitudinal and vertical directions did not change a lot. However, locally the differences will be quite big. The forces in head seas are equally generated by the PS and SB side of the ship, while in quartering waves the major part is generated by the windward side only. The excitation level in horizontal direction for this test is about
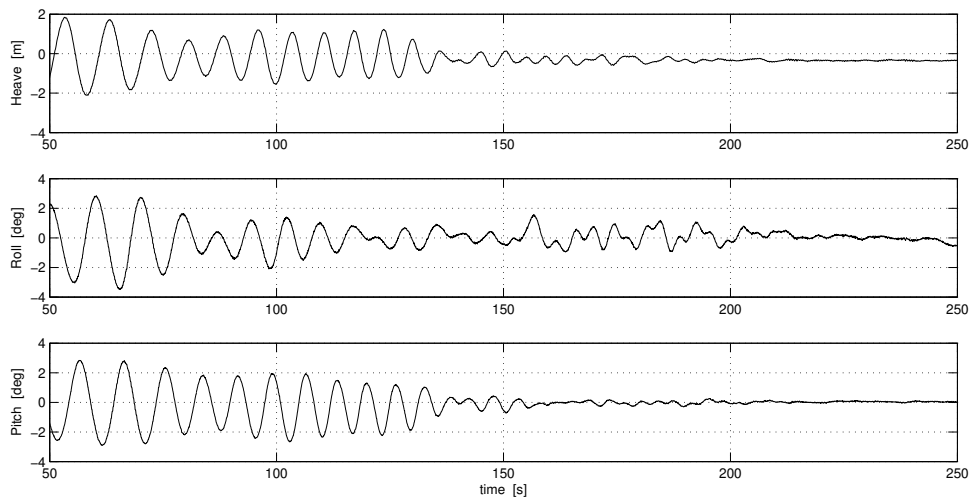
Figure 8.29: Measured heave, roll and pitch motions for the wave sweep $H_W = 5.0$ m, heading 150 deg, $v_S = 20$ kt.
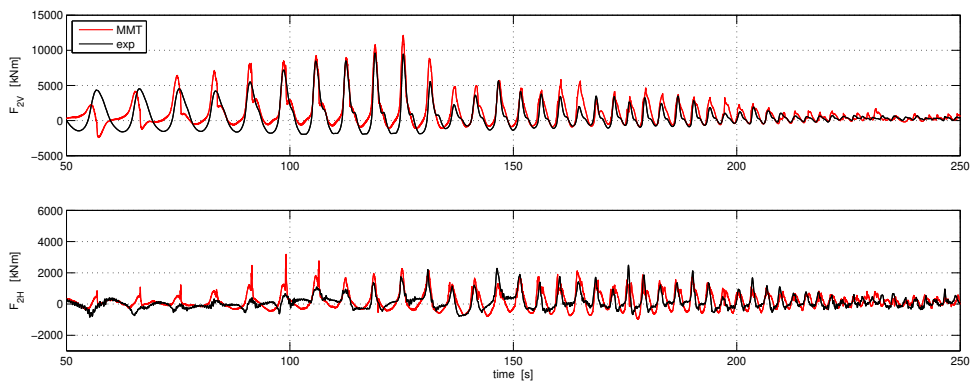
Figure 8.30: 2-node VB and HB modal excitation. Wave sweep $H_W = 5.0$ m, heading 150 deg, $v_S = 20$ kt.

a factor 5 lower than for the vertical direction. The relative error between measurement and prediction is larger, but in absolute terms these differences are not significant.

The distribution of the peak force of this experiment over the different segments is shown in Figure 8.31. The predicted vertical force agrees quite well to the measured values, the longitudinal force is under-predicted as is the lateral force for all but the two foremost segments.
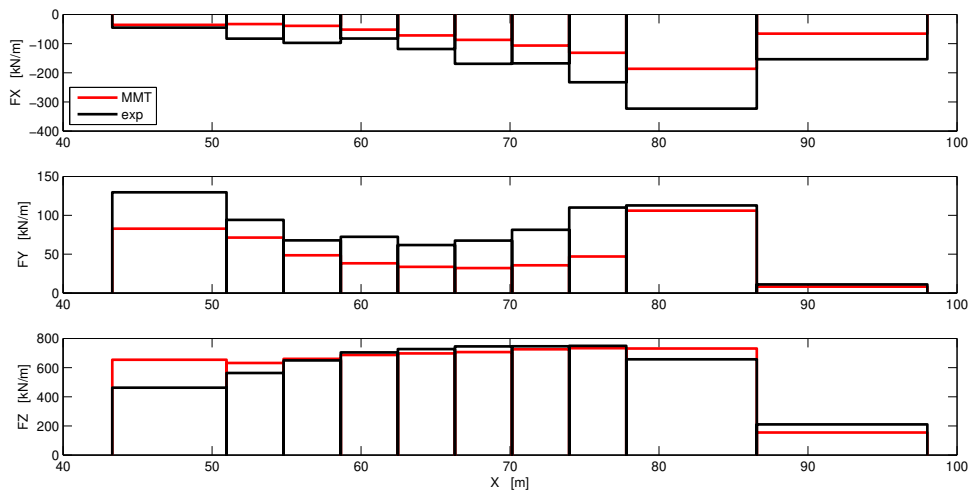
Figure 8.31: Distribution of the maximum forces over the length of the bow of the ferry for one impact at t = 113 s. Wave sweep, heading 150 deg, $v_S = 20$ kt.

8.7.3   Impulsive loads in bow quartering seas, heading 120 deg

The motions measured in a run at a heading of 120 deg are shown in Figure 8.32; the excitation of the 2-node vertical and Horizontal Bending modes is shown in Figure 8.33. The results for the excitation of the VB mode is again more accurate than the one for the HB mode. The ratio between the two levels is changed; there was about a factor 5 difference at a heading of 150 deg, while now there is just a factor 2 difference.

The distribution of the forces for the maximum impact at $t = 128\ s$ is shown in Figure 8.34.

Comparing the results in head waves to the ones in the two quartering directions, it appears that the excitation of the 2-node VB mode increases a little when going from head to quartering waves. The force level for the HB mode increases significantly; at 120 deg heading the force level is more than twice the level at 150 deg.

The approximate model assumes that the impulsive load is essentially generated on
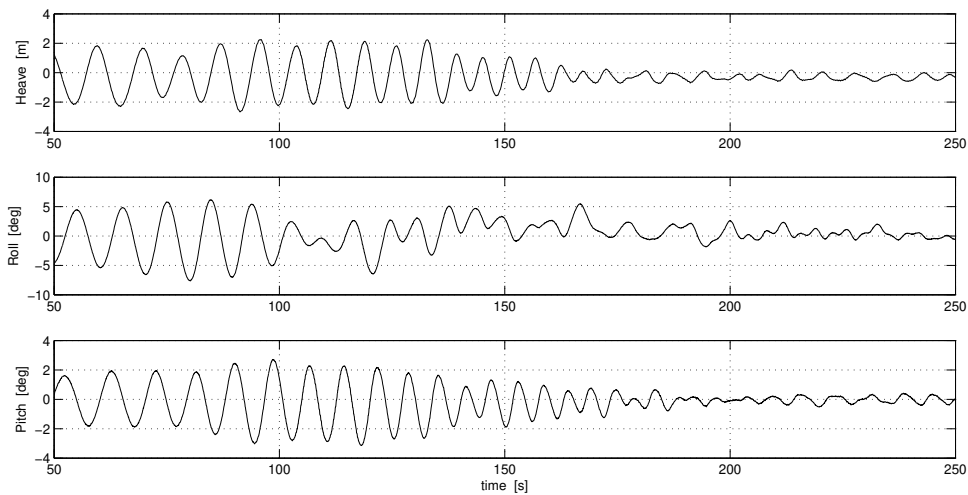
Figure 8.32: Measured heave, roll and pitch motions for the wave sweep $H_W = 5.0\ m$, heading 120 deg, $v_S = 20\ kt$.
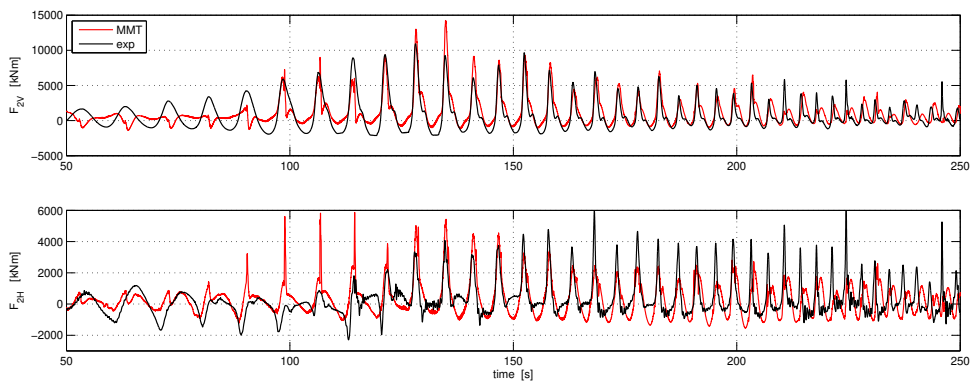
Figure 8.33: 2-node VB and HB modal excitation. Wave sweep $H_W = 5.0\ m$, heading 120 deg, $v_S = 20\ kt$.
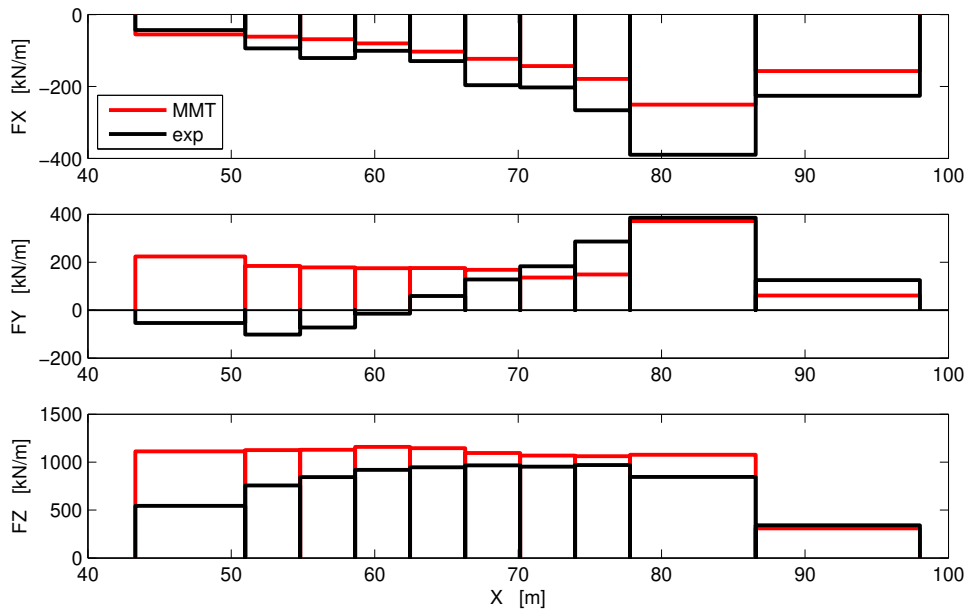
Figure 8.34: Distribution of the maximum forces over the length of the bow of the ferry for one impact at t = 128 s. Wave sweep, heading 120 deg, $v_S = 20$ kt.

the windward side of the hull only. It was therefore expected that the pressures on that side would increase significantly. This appears not to be the case as shown in Figure 8.35.
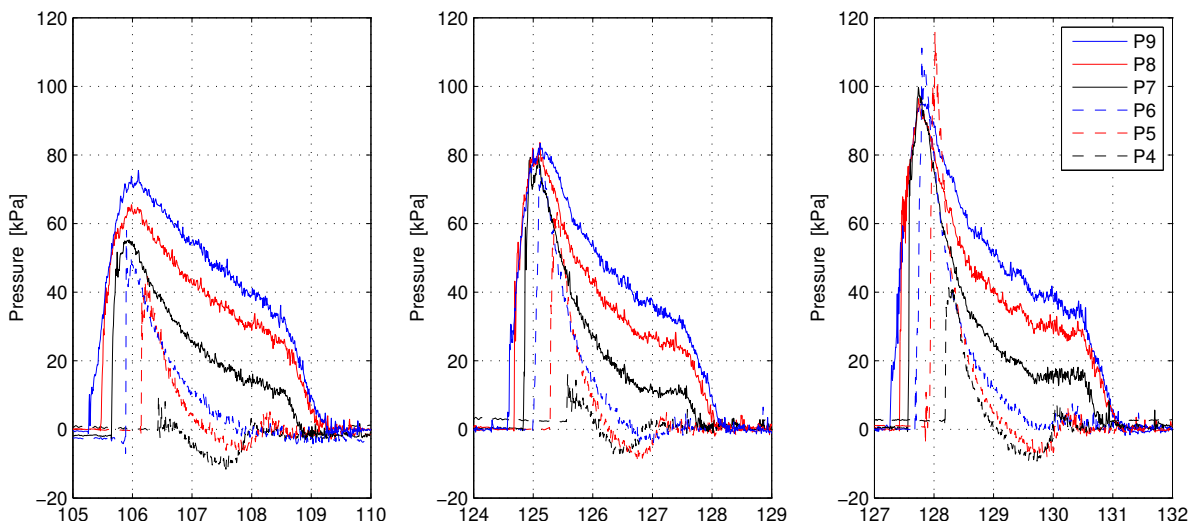
Figure 8.35: Results of one column of pressure sensors at St 18.8. Results in head seas: heading 180 deg (left) are compared to those in quartering seas: heading 150 deg (middle) and heading 120 deg (right). The results are shown for the event generating the maximum force in a wave sweep, $H_W = 5.0$ m, $v_S = 20$ kt.

8.8   Tuning

Since MMT is an approximate method, an option to tune the calculated results has been built-in from the beginning. The choice has been made to do the tuning on the pile-up factor and to keep the relation between relative motions, relative velocity and impulsive force as it is according to the theory. The pile-up factor is considered to be the most uncertain parameter because it is based on a 2D method, while it is applied for a ship at speed. The tuning factors are multipliers for the effect of the local changing impulse in vertical and longitudinal direction expressed by the added mass derivatives. There are separate tuning factors for the reduction of the pile-up on the leeward side in case of quartering waves. The tuning factors are defined in Section 7.3.

The effect on the relative motion of a change in the tuning factor is shown in Figure 8.36. The maximum pile-up in the simulation can be estimated from the vertical drop of the relative motion at the time instant that the relative motion is at maximum and the relative velocity is zero. The pile-up is discontinuously set to zero at the time of the zero down-crossing of the relative velocity.

The tuning factor c_1 is a multiplier for pile-up effect due to vertical motions (in the earth reference frame), see the definition in Equation 7.1. If both c_1 and c_2 are set to zero, the effect of the change of the bow wave for drafts different than the design draft remains.

The effect on the vertical force on Segment 9 in shown in Figure 8.37; the effect on the force is much more pronounced than on the relative motion; there is the direct effect of the reduced relative velocity and the immersion of the hull is lower. For a wedge this would result in a quadratic effect, for a concave sections the effect is even stronger.
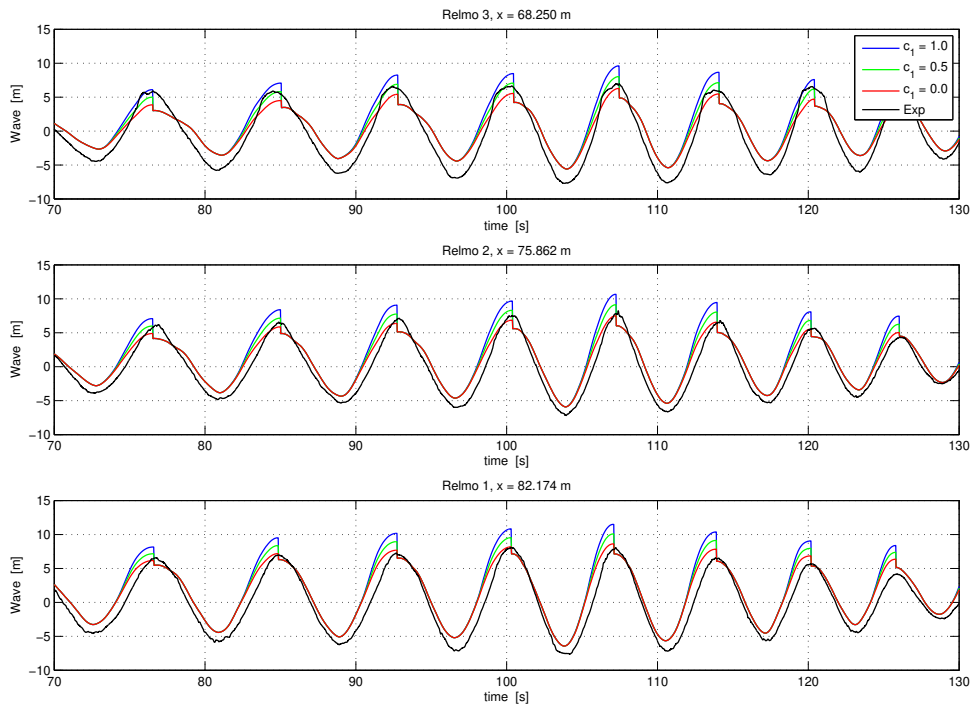
Figure 8.36: Effect of the tuning parameter c_1 on the relative motions on 3 locations. Wave sweep, heading 180 deg, $v_S = 20$ kt.
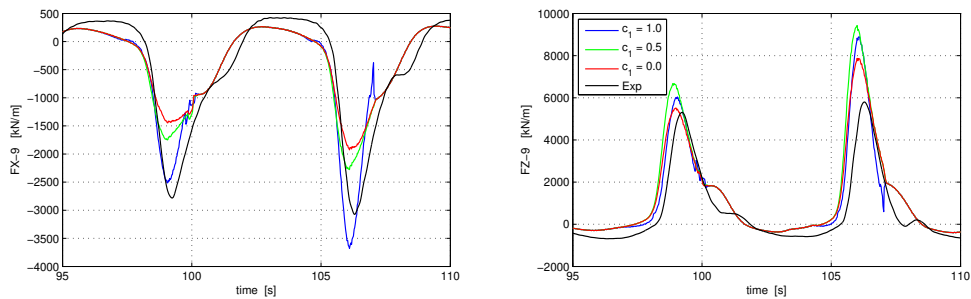
Figure 8.37: Effect of the tuning parameter c_1 on the vertical force on Segment 9. Wave sweep, heading 180 deg, $v_S = 20$ kt.

8.9 Extreme slamming events

Although the impulsive forces as they are presented up to now are very large, they cannot be regarded as extreme slamming events. The extreme event has a very short duration and usually excites several global flexural modes of the ship and it can also excite local flexural modes. When carrying out experiments in the wave basin, extreme events can be identified by the banging sound they make. This sound is assumed to be produced by an air inclusion that has been compressed and from which the air escapes in an explosive manner. If the model is not infinitely stiff and properly instrumented, the whipping effect of such events can be recorded; for instance by an accelerometer in the bow.

An example of such a recording is shown in Figure 8.38. This example results from the second series of experiments. The model used in this series was intended as a stiff model with very high resonance frequencies, therefore the segments were connected through a large size steel beam. The 'whipping' response measured in the hull segment is due to the flexibility in the 6-component strain gauge system that connects the segment to the steel beam; the resonance frequency of this flexible mode is 9.3 Hz (full scale value).

The motions of the model are recorded by an optical system amidships. From this measurement local accelerations are calculated in the fore body of the model (in Segment 8) and compared to the actual measured values. The acceleration corresponds closely for the main part of the duration of the measurement as shown in the left plot of Figure 8.38. A zoom-in is made for the impact at $t = 195\ s$, right plot of Figure 8.38. There is a strong local vibratory acceleration that is not measured by the motion system at the CoG of the model, proof of the short duration impact.

The event is visualized by a few stills taken from the video, Figure 8.39. The wave crest was overturning just before the impact. It is surprising that even in head seas a wave can create such an impact against the bow.

The program MMT predicts this large force surprisingly well; Figure 8.40 shows the longitudinal and vertical forces on the 5 fore most segments. The prominent peak at $t = 195\ s$ is well captured. This is however not always the case. A similar large impact in a short wave occurred during the experiments in bow quartering waves, at the end of the wave sweep. The forces are shown in Figures 8.41, 8.42 and 8.43. The extreme event that occurred at t = 246 s is not captured by MMT at all.
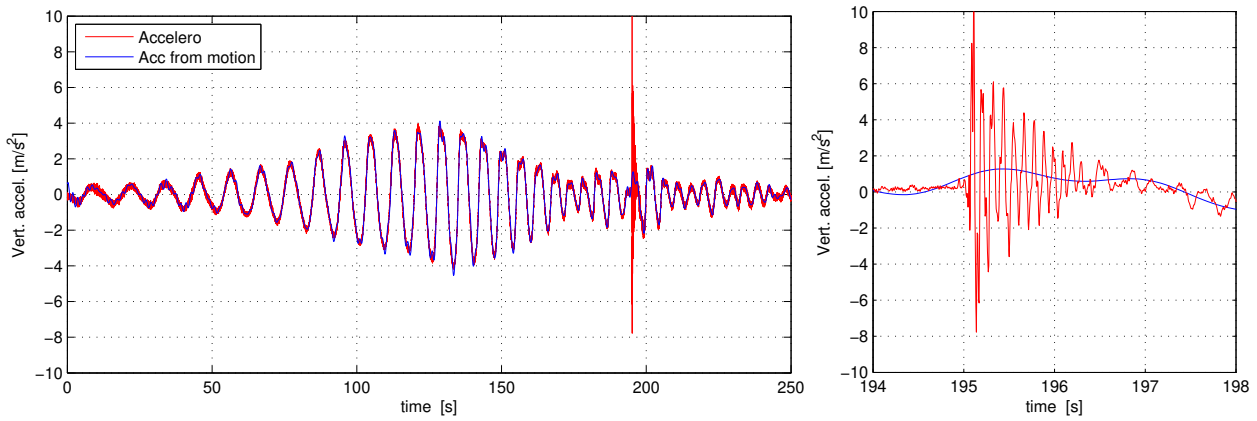
Figure 8.38: Vertical acceleration in the bow of a model. The rigid body acceleration is calculated from the measured motions amidships (blue) and measured by a local accelerometer (red). The response due to the extreme impact at $t = 195$ s is shown in detail on the right.

Figure 8.39: Stills from the video of the experiments, a severe impact resulting in a whipping response in the structure of the model. Head seas, $H_W = 6$ $m, v_S = 15$ kt.
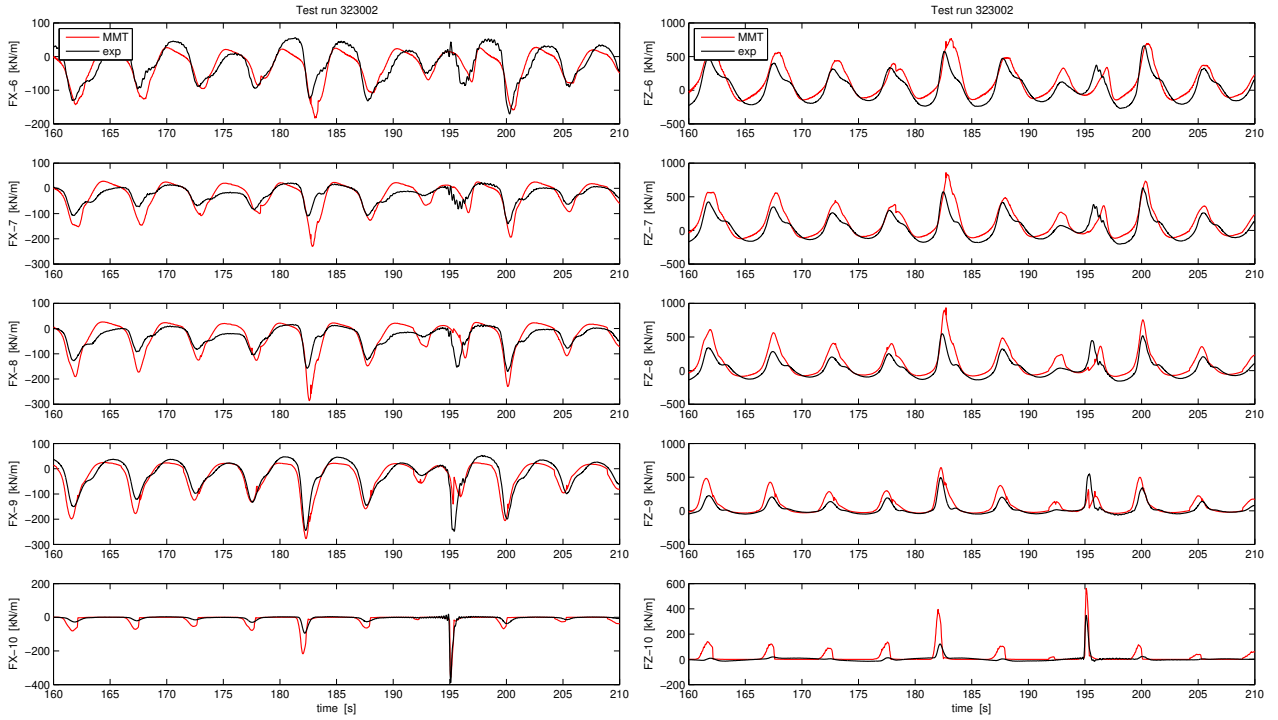
Figure 8.40: *Longitudinal (left) and vertical (right) forces on the foremost 5 segments during an extreme slamming event at t = 195 s. Wave sweep, heading 180 deg, $H_W = 6$ m, $v_S = 15$ kt*
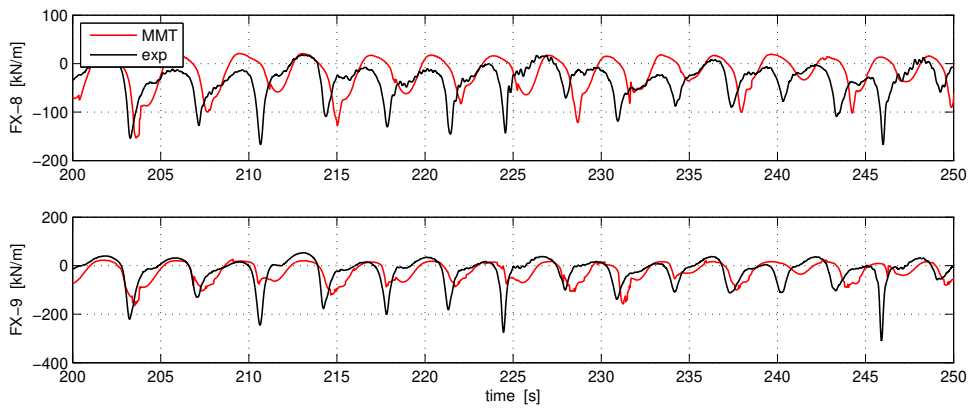
Figure 8.41: *Distribution of the maximum forces over the length of the bow of the ferry for one impact at t = 246 s. Wave sweep, heading 120 deg, $v_S = 20$ kt.*
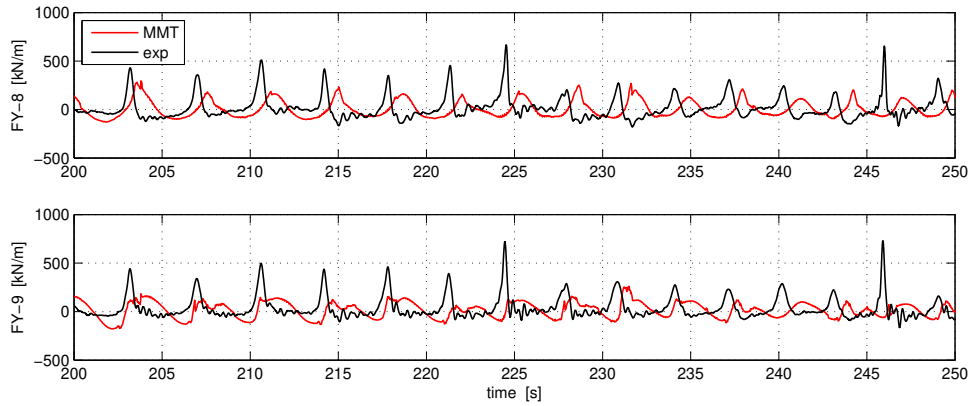
Figure 8.42: Distribution of the maximum forces over the length of the bow of the ferry for one impact at t = 246 s. Wave sweep, heading 120 deg, $v_S = 20$ kt.
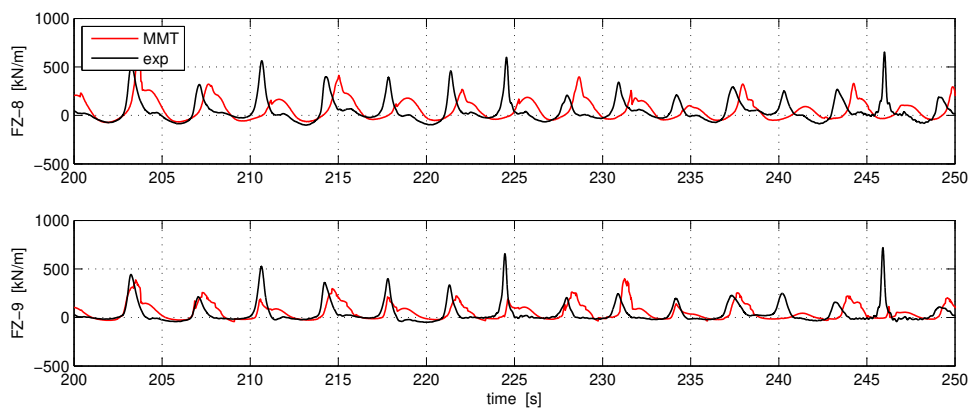
Figure 8.43: Distribution of the maximum forces over the length of the bow of the ferry for one impact at t = 246 s. Wave sweep, heading 120 deg, $v_S = 20$ kt.

Chapter 9

Trends in impulsive forces

9.1   Introduction

The previous chapter compared in detail the calculated impulsive forces for a variety of combinations of speed and heading. Results of the calculations were compared to experiments, but it is not possible to compare the various conditions; although the wave trains were similar, they were not identical. In order to determine the effect of these important parameters on the impulsive forces, new simulations were made. The earth fixed wave train is the same for all simulations, but the encountered wave train depends on speed and heading. The motions of the ship are determined by the EoM, so in general they will be different for each speed - heading combination.

The study presented in this chapter is very limited. It is intended to show the possibilities of the developed approximate method and to show the main trends. More extensive and detailed studies should be carried out in the future.

9.2   Distribution of the forces

The distribution of the forces over the forward 25% of the length as measured in the experiments are presented on basis of the results of the experiments in wave sweeps. The 5 largest peaks are used in the plots; results of the experiments and of the calculations are plotted in separate graphs. The forces plotted are normalized by the length of the segment it refers to.

A comparison of calculated and measured maximum forces in head seas is given in Figure 9.1 and in Figure 9.2.

The longitudinal force FX is largest for Segment 9 (St 19 - St 20) and reduces quickly going aft. Differences in the magnitude of the individual impacts on the aft segments are proportional to the difference in magnitude on Segment 9. The impulsive longitudinal force on the segments aft of St 18 is rather small.

The vertical force FZ is much larger than the longitudinal force. This force component gives rise to vertical vibrations in the ships hull. The peak forces are much more evenly
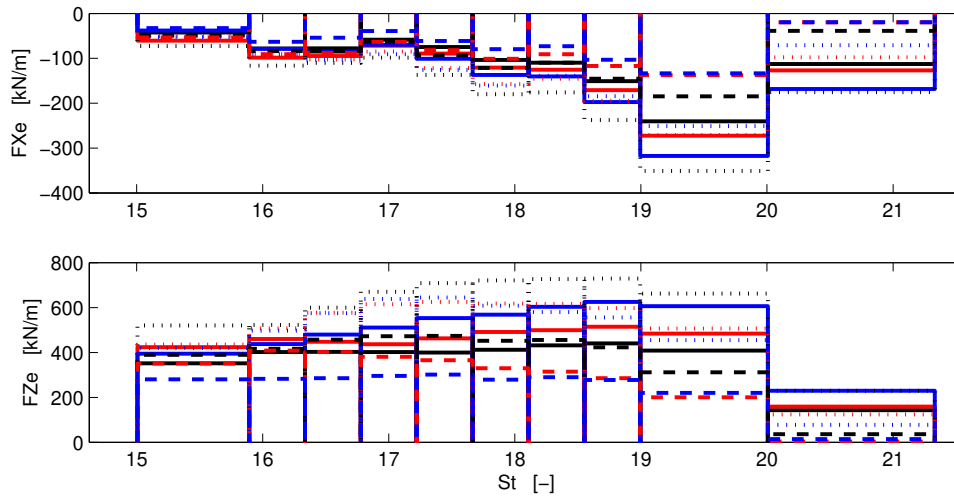
Figure 9.1: Measured distribution of the peak forces over the length of the hull forward of St 15. The force is divided by the length of the segment. Wave sweep in head waves, $v_S = 20$ kt.
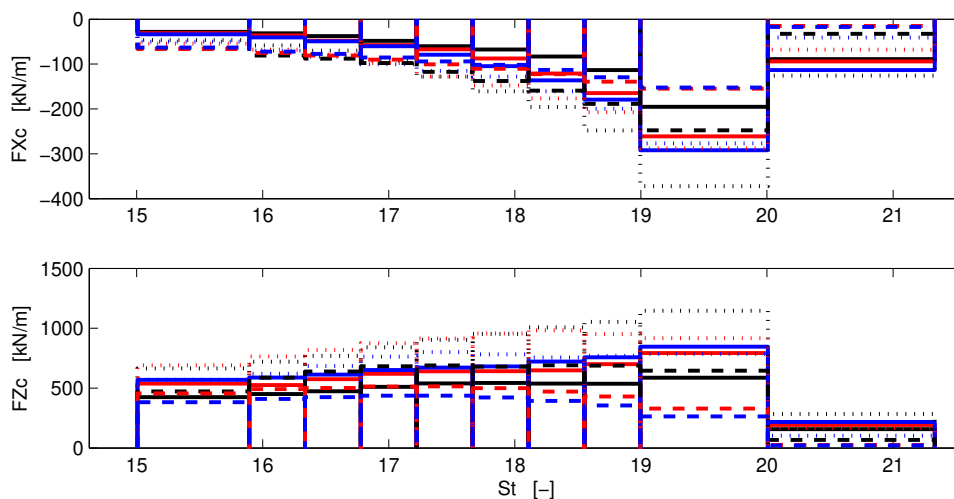
Figure 9.2: Calculated distribution of the peak forces over the length of the hull forward of St 15. The force is divided by the length of the segment. Wave sweep in head waves, $v_S = 20$ kt.

distributed over the forward 15% than is the case for the longitudinal force.

Figure 9.3 and Figure 9.4 give similar results for experiments in quartering waves (headings 150 and 120 deg respectively). With respect to the longitudinal forces, there is not much effect of the wave direction. The magnitude of the vertical force is also remarkably constant. The vertical force at 150 deg wave direction appears to be somewhat lower than in head seas or at 120 deg wave direction, but the effect is too small to be significant considering the limitations of this comparison.

The lateral force increases significantly when the wave direction is changed from 150 to 120 deg. Similar as for the vertical force, the lateral force appears to be quite evenly
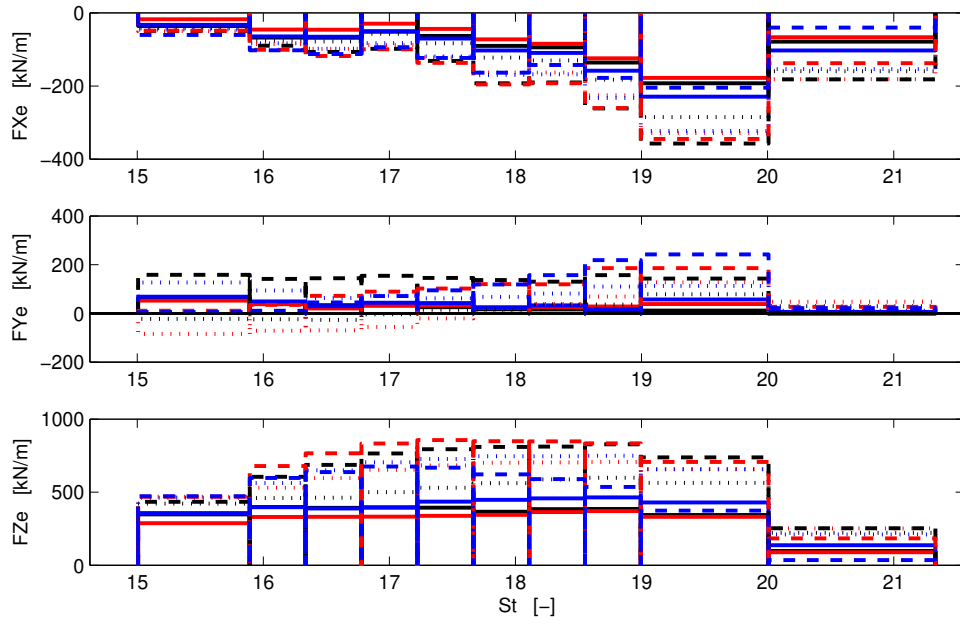
Figure 9.3: Measured distribution of the peak forces over the length of the hull forward of St 15. The force is divided by the length of the segment. Wave sweep, heading 150 deg, v_S = 20 kt.
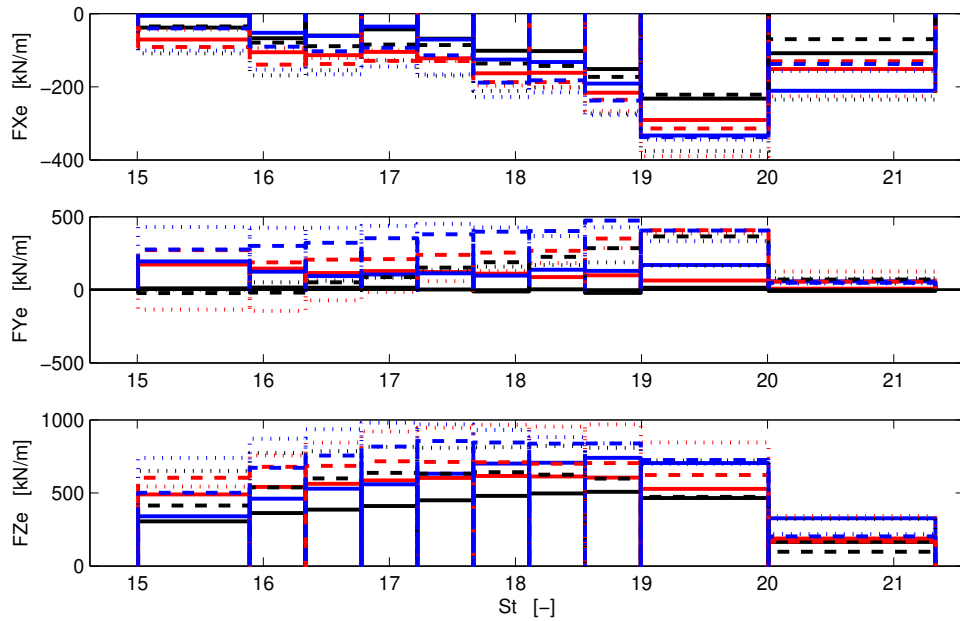
Figure 9.4: Measured distribution of the peak forces over the length of the hull forward of St 15. The force is divided by the length of the segment. Wave sweep, heading 120 deg, v_S = 20 kt.

distributed over the forward 15 % of the length of the ship.

9.3   Effect of forward speed

The effect of forward speed is demonstrated by simulations in an identical wave train (wave sweep). The wave train is defined as a FFT of the earth fixed wave. The number of wave encounters is not sufficiently large to derive reliable statistics, but, since the wave train is identical, the peak values can be compared in a probability of exceedance plot. The parameter used is the excitation of the the 2-node vertical bending mode as introduced in Section 8.3.

The distributions for the three speeds, Figure 9.5, show different basic shapes. The distribution for $v_S = 15$ kt shows the typical concave shape of a linear system, the one for $v_S = 20$ kt shows a straight shape typical of an exponential distribution and the one for the highest speed, $v_S = 25$ kt, has a very convex shape. This latter characteristic has the unpleasant consequence that the magnitude of extreme impacts can be very different. It is believed by this author, that it is the knowledge of this characteristic makes seafarers rightly afraid of slamming and induce them to reduce speed.

Apart from the different shapes of the distribution, Figure 9.5 shows that the effect of forward speed on the extreme values is very large: reducing the speed from 25 to 20 kt reduces the peak excitation 19%, while a further reduction of the speed to 15 kt reduces the peak more than 30%.
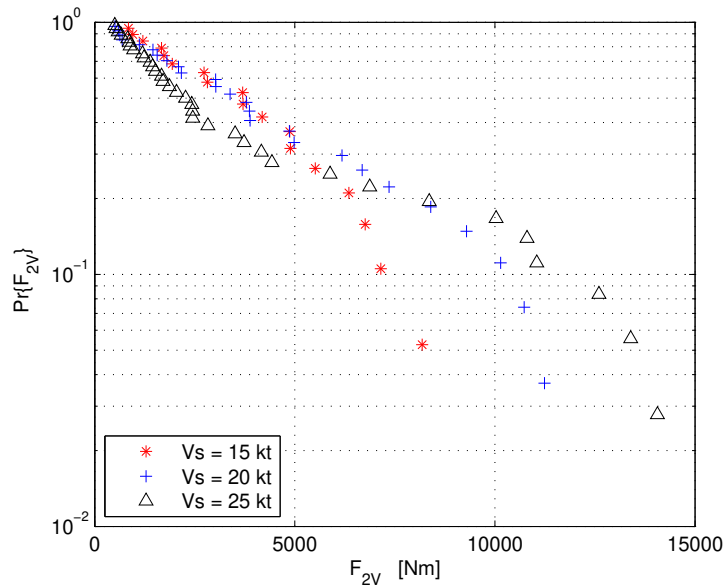
Figure 9.5: *Probability of exceedance plot of the peak excitation of the the 2-node VB. Results of simulations in head seas in an identical wave train at $v_S = 15$, 20 and 25 kt.*

9.4   Effect of wave direction

The effect of the wave direction is illustrated on a similar basis as was done for the effect of forward speed. Due to the reduction of the wave encounter frequency as the waves are in a more quartering direction, the simulation time was chosen to be longer to encounter all the waves in the wave train. The comparison has been made for a speed of 20 kt.

The result of the simulations is shown in Figure 9.6. The shape of the distributions for the various wave directions is again very remarkable. It appears from this plot that the excitation for the 2-node VB deformation mode is much lower for a heading of 150 deg than it is for headings of either 180 or 120 deg. It can be possible, and, if true, it is important information for ship operators. However, it is definitely a point that needs further research before final conclusions can be drawn.
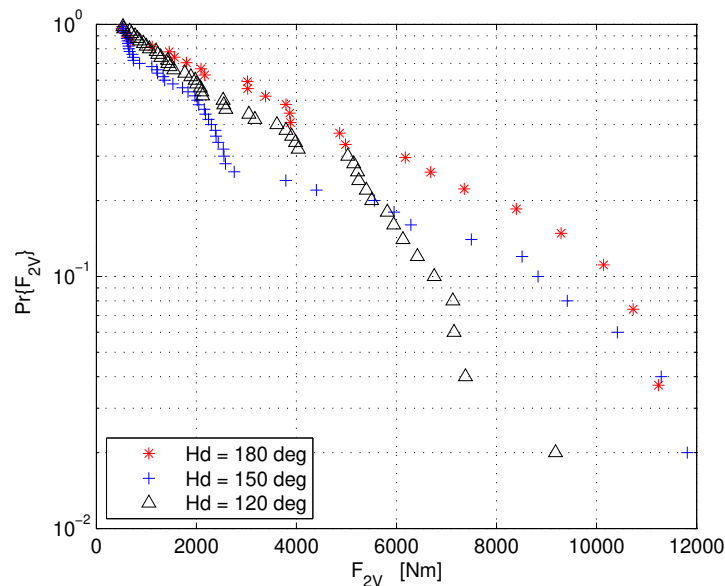
Figure 9.6: Probability of exceedance plot of the peak excitation of the the 2-node VB. Results of simulations at $v_S = 20$ kt in an identical wave train at a heading of 120, 150 and 180 deg.

Chapter 10

Finish up

10.1   Lessons learned

Wave sensors

It seems to this author that wave measurements are the weak link in the chain of measuring impact forces on the model of a ship in a wave basin. The classical method of a twin wire system in between which the resistance or the capacity is being measured works reasonably fine at zero speed, but it is less accurate at speed. At speed there is run-up on the front of the wires and ventilation at the aft end. Also the wave formation of the supporting strut of the sensor needs to be taken into account. This is a factor of concern in quartering wave directions where the supporting strut is normally aligned in the longitudinal axis of the basin since the forward speed is the dominant velocity component. In all cases there is the problem of pollution of the wires after prolonged use. The pollution changes the calibration of the system.

The effect of forward speed appears to be quite acceptable in head waves as shown in the 1999 ITTC report [148]; results of side-by-side experiments of a classical twin-wire sensor and a servo-controlled wave probe are shown in Figure 10.1. The plot was made
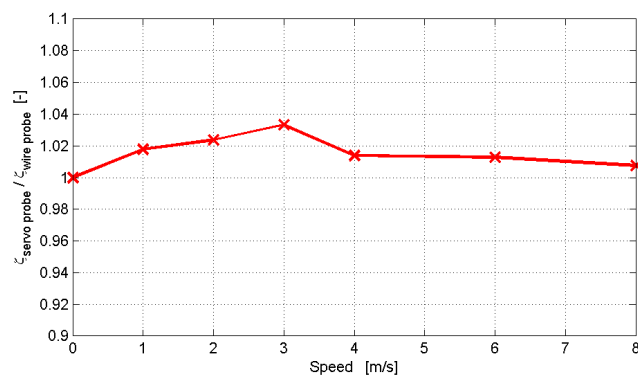
Figure 10.1: *Result of a side-by-side experiment with a servo-controlled wave probe and a classical twin-wire probe.*

for a vertical twin-wire sensor. If the sensor is tilted, as is often done to measure the relative motion along the stem, there can be a much larger effect of forward speed.

Acoustical sensors are non-intrusive, so wave formation is not an issue. The main draw-back of the system is, that the exact location on the water surface that reflects the sound pulse is unknown. It is at some location within the cone in which the transmitter transmits the sound pulse. This position varies over the wave period which is a serious draw-back of this type of sensor when measuring a deterministic wave train.

Segmented model tests

When performing experiments on a segmented model with the aim to measure the loads on individual segments, it is considered good practice to close the gap between the segments with a flexible seal. Having fluid in-between the segments will create a sizeable force due to dynamic pressures in the gap. Since it cannot be assumed that the pressure distribution is uniform in-between the segments, it produces not only a longitudinal force, bt moments around the lateral and vertical axes as well. It can be expected that this effect is more relevant for experiments at-speed than for zero-speed tests, but it is present in both conditions.

The important thing to worry about is 'cross-talk' of the segments due to forces transferred by the seals. Therefore the segments need to be fixed to the backbone in an as rigid as possible manner. Strain sensors have a certain deformation when they are loaded by nature, so some flexibility cannot be avoided. A large size force frame minimizes rotations due to moments. For a case like the one studied in the second series of experiments, the most important mode of deformation of the segment is a rotation around the longitudinal axis due to a transverse load. The shear force in the bottom part of the seal is then responsible for transferring part of the transverse load to the neighbouring segments.

10.2   Conclusions

A method has been developed to predict impulsive forces due to large amplitude motions and due to impacts of steep waves. The method is able to predict impulsive forces on the forward part of the bow of a vessel sailing at speed in head or bow quartering waves. The method has been validated by model experiments.

Based on the results presented in this thesis it is concluded that:

- Large impulsive forces can be created due to large amplitude motions of the vessel and by very steep waves that are close to the breaking limit. There is reason to believe that the latter type is the more dangerous one because the duration of the impact is shorter, so more vibration modes will be excited.

- Although the basics of the slamming phenomenon, the sudden change in momentum in the fluid, are similar for both types of impact, the approach to build a model for

the prediction of impulsive forces is different. The change in momentum in the fluid underneath the full wetted part of the body is relevant for the impulsive force due to large amplitude motions. This type of impact can be approximated by a drop test of the body in calm water. The change in momentum in the wave crest is an important parameter for the second type of impact. A crucial aspect is the angle between the face of the wave and the hull of the vessel just before the impact. This is the same type of impact that is being studied in sloshing studies.

- Impacts due to large amplitude motions require a good estimate of especially the relative vertical velocity of the contact line of water surface and body. From the analysis it appears that the incoming wave, the pile-up effect and the effect of the draft dependent bow wave are important components for this relative velocity. The effects of radiation and diffraction are only minor.

- It appeared from a study on 2D wedge sections, that there is no such thing as a threshold velocity for slamming. It appeared that the important parameter for the generation of an impulsive force is the lateral acceleration of the contact point of fluid surface and body. An impulsive force starts to be generated when this lateral acceleration is larger than the acceleration due to gravity. In physical terms it means that the radiated wave has no time to move away from the body.

- There are no important dynamic effects during water exit of the hull. The forces on segments of the hull can be determined by the hydrostatic force only.

- Although much work in the area of validation is still needed, the developed method is essentially suitable for design studies of vessels. The method is incorporated in a time-domain simulation program and can perform simulations in the order of magnitude of real time on a normal desktop PC. The performance of the program is for a large part determined by the number of frequency components that is used to describe the wave elevation in space and time.

- A second area of application of the program is using it as a screening method to find critical wave events for large impulsive forces. These critical events can then be studied in detail by CFD or experimental methods.

10.3 Recommendations

The main effort of the project has been the work on the model for impulsive forces due to large amplitude motions. Only at a relatively late stage in the project it was realized that this approach could not predict all impacts, the wave slap load is a different phenomenon. Because of the limited effort spent in this area, it is the weak link in the overall method. It is therefore recommended to study this type of impact in more detail. An important aspect is the velocity distribution in the wave crest, very useful experiments have been

made and reviewed in this thesis, but a suitable model must be derived and implemented in this slamming method.

A point that needs some attention is to define the conditions for which the wave slap load module should be activated in the simulation program. At present this is done in a very crude way that has no physical background at all. This problem does not exist for the impulsive force due to large amplitude motions. The magnitude of the impulsive force is related to the earth fixed velocity, so when this parameter reduces to zero, so does the impulsive force.

More attention should also be paid to carrying out experiments in the type of conditions in which wave slap loads can be expected. A few severe impacts have been recorded in the experiments that have been discussed, but the focus in the design of the wave train was on the impacts due to large amplitude motions. If the wave is breaking just before it hits the body, a very large impact can be expected; this is a condition that is comparable to the 'flip-through' that is being studied in sloshing problems. Creating this type of impact requires an exact tuning of wave and model.

Another parameter worthy of detailed investigation is the effect of the wave direction on the wave slap load. If the wave hits a large part of the vessel in the same moment in time, a very large slap load can be expected.

Since wave steepness and wave breaking are important parameters for wave slap loads, it can be concluded that a linear wave model will no longer suffice for the purpose of predicting these loads. A non-linear model is expected to give a more accurate description of the wave elevation in space and time; this information is needed for both types of impulsive forces. This need for a non-linear wave model does not necessarily mean that the present method of calculating the vessel motions using linear hydrodynamic coefficients and non-linear Froude-Krilov and restoring forces is inadequate. It might well be true that this approach is sufficiently accurate and does not constitutes the weak link in the total force estimation.

Wave probes have already been identified as the weak link in experiments. There is not a direct outlook on a new type of sensor, but non-intrusive options like acoustical or optical systems are the preferred solution. An interesting idea is to use the technique of medical acoustical imaging to visualise the wave surface. However, initial discussions revealed that measuring the wave surface from above is a handicap for this technique.

10.4   Epilogue

At the end of a thesis it needs to be evaluated if the objective is reached or not. It cannot be claimed that slamming is now fully understood, but it has been explained in some length in the introduction that this was not possible. In fact, the increased understanding showed even more how complex this phenomenon is.

Limiting the study to slamming phenomena created at model scale in a seakeeping basin appeared to be a sufficiently large challenge. The initial idea was, that a simulation

of a drop test in calm water would be a valid and sufficient approximation of a slamming impact; in fact, this is done by several other approximate methods. This idea was proven to be wrong. In fact, very severe slamming occurred in very short and steep waves in which the ship hardly moves. The approximation of a drop test in calm water could work for the bow forward of FPP; the sections in this part of the hull are normally fully above the water. For sections aft of FPP this approximation will not work, neither in head nor in quartering seas.

One more aspect that is relevant for this type of research needs mentioning. The scientist is supposed to 'understand' his problem and to have built a picture of the relevant physics in his mind. This picture is leading in developing a theoretical model and in designing a series of experiments. It also determines the choice of sensors and the location were to put them to measure physical quantities during the experiments. The fundamental problem is, that there might be shortcomings in the mental model, the picture in his/her mind, which results in having not enough or the wrong type of sensors. If the measurements fit our model, suspicion is not raised and the scientist is not pushed into unknown territory to improve his mental model. We are unaware of the 'unknown unknowns' and we proceed until proven wrong.

The aim of this project was to develop an approximate method to determine slamming loads. Significant steps forward have been made in calculating non-linear hydrodynamic forces and a reasonable agreement to experimental results has been obtained. However, it was not always possible to model extreme slamming events. Extreme events are being caused by very steep waves on the edge of breaking. As has been stated in the first chapter of this thesis, breaking waves is a bridge too far for this project. These waves require a more advanced (than just a linear) wave model. Research into non-linear wave models has been carried out by Düz et al. [46] in 2016. He compared a number of available non-linear potential flow wave models to CFD calculations and to model experiments. Even for non-linear wave models breaking is very challenging. At most the codes studied contain tricks such that they do not crash when breaking occurs. There are some very fast non-linear models like the one developed by van Groesen *et al.* [61, 63], but they do not describe the wave surface just before breaking.

At present it seems that volumetric methods are required, but then two-phase models must be included. Also particle methods are promising for this purpose; impressive results have been obtained with SPH codes as for instance shown by Guilcher *et al.* [68] and by Veen and Gourlat [183].

References

[1] Aalbers, A., Cooper, C., Nowak, S., Lloyd, J., Leenaars, C., and Vollen, F., 2001. "Safetrans: A new software system for safer rig moves". In RINA Jack-Up Conf.

[2] Aalbers, A., Dallinga, R., and Nienhuis, U., 1987. "Computer prediction methods for the workability of a dynamically positioned vessel". In 3rd Int. Symp. on Pract. Design of Ships and other Floating Structures (PRADS), June.

[3] Aalberts, P., and Nieuwenhuijs, M., 2006. "Full scale wave and whipping induced hull girder loads". In Int. Conf. on Hydroelasticity in Marine Techn. (ICHE), September.

[4] Aertssen, G., 1966. "Service-performance and seakeeping trials on MV. Jordaens". In Trans. RINA, Vol. 108, pp. 305 – 343.

[5] Aertssen, G., 1968. "Laboring of ships in rough seas - with special emphasis on the fast ship". In SNAME Diamond Jubilee Int. Meeting, pp. 10.1–10.16.

[6] Aertssen, G., 1969. "Service performance and seakeeping trials on a large ore carrier". In Trans. RINA, Vol. 111, pp. 217–236.

[7] Arai, M., Cheng, L., and Inoue, Y., 1994. "A computing method for the analysis of water impact of arbitrary shaped bodies (1st report)". *J. of Soc. of Naval Arch. of Japan,* **176**, pp. 233–240.

[8] Arai, M., Cheng, L., and Inoue, Y., 1995. "A computing method for the analysis of water impact of arbitrary shaped bodies (2nd report)". *J. of Soc. of Naval Arch. of Japan,* **177**, pp. 91–99.

[9] Baldock, T., Swan, C., and Taylor, P., 1996. "A laboratory study of nonlinear surface water waves". *Phil. Trans. R. Soc. Lond. A,* **354**(1707), pp. 649 – 676.

[10] Betts, C., Bishop, R., and Price, W., 1977. "A survey of hull damping". *Trans. R. Inst. of Naval Arch.,* **117**, pp. 125–142.

[11] Beukelman, W., 1991. Slamming on forced oscillating wedges at forward speed. Part 1: Test results. Tech. Rep. Report 888, Delft Un. of Techn., Delft, the Netherlands, May.

[12] Beukelman, W., and Radev, D., 1991. "Slamming simulation on penetrating wedges at forward speed". In Symp. on Hydro- and Aerodyn. in Marine Eng. (HADMAR), Oct.

[13] Bigot, F., Derbanne, Q., Sireta, F., and Malenica, S., 2011. "Global hydroelastic ship response: Comparison of numerical model and wils model tests". In 21st Int. Offshore and Polar Eng. Conf. (ISOPE), June.

[14] Bisplinghoff, R., and Doherty, C., 1952. "Some studies of the impact of Vee wedges on a water surface". *J. of the Franklin Inst.,* **253**, pp. 547–561.

[15] Bledsoe, M., Bussemaker, O., and Cummins, W. E., 1961. Seakeeping trails on three Dutch destroyers. Tech. Rep. 1559, David Taylor Model Basin, Bethesda, USA, Nov.

[16] Blok, J., and Huisman, J., 1983. "Relative motions and swell-up for a frigate bow". In RINA Spring Meeting, Apr.

[17] Bogaert, H., Leonard, S., Brosset, L., and Kaminski, M., 2010. "Sloshing and scaling: results from the Sloshel project". In 20th Int. Offshore and Polar Eng. Conf. (ISOPE), June.

[18] Bouvy, A., 2013. "Dynamically verifying the calibration of pressure transducers". In Adv, Model Meas. Techn. for EU Mar. Ind. (AMT'13).

[19] Bredmose, H., Bullock, G., and Hogg, A., 2015. "Violent breaking wave impacts. Part 3: Effects of scale and aeration". *J. of Fluid Mech.,* **765**, pp. 82 – 113.

[20] Bredmose, H., Peregrine, D., and Bullock, G., 2009. "Violent breaking wave impacts. Part 2: Modelling the effect of air". *J. of Fluid Mech.,* **641**, pp. 389–430.

[21] Bullock, G., Crawford, A., Hewson, P., Walkden, M., and Bird, P., 2001. "The influence of air and scale on wave impact pressures". *Coastal Eng.,* **42**, pp. 291 – 312.

[22] Bullock, G., Obhrai, C., Peregrine, D., and Bredmose, H., 2007. "Violent breaking wave impacts. Part 1: Results from large-scale regular wave tests on vertical and sloping walls". *Coastal Eng.,* **54**, pp. 602–617.

[23] Bunnik, T., 1999. "Seakeeping calculations for ships, taking into account the non-linear steady waves". PhD thesis, Delft Un. of Techn. Faculty of Information Techn. and Systems, Nov.

[24] Bunnik, T., Daalen, E. v., Kapsenberg, G., Shin, Y.-S., Huijsmans, R., Deng, G., Delhommeau, D., Kashiwagi, M., and Beck, R., 2010. "A comparative study on state-of-the-art prediction tools for seakeeping". In 28th Symp. on Naval Hydrodynamics, Sept.

[25] Bunt van de, E., and Bouvy, A., 2011. "Dynamic calibration of pressure transducer". In Adv, Model Meas. Techn. for EU Mar. Ind. (AMT'11), 4 - 6 Apr, pp. 301 – 312.

[26] Bunt van de, E., and Lafeber, W., 2011. "Optical measurement techniques in model testing". In Adv, Model Meas. Techn. for EU Mar. Ind. (AMT'11), 4 - 6 Apr.

[27] Chuang, S.-L., 1967. "Experiments on slamming of wedge shaped bodies". *J. of Ship Res.*, Sept., pp. 190–198.

[28] Ciappi, E., Dessi, D., and Mariani, R., 2003. "Slamming and whipping response analysis of a fast monohull via a segmented model test". In Hydroelasticity in Marine Eng., Hydroelasticity'03, Sept.

[29] Clauss, G., 2001. "Synthesis of deterministic rogue waves in extreme seas". In RINA Symposium 'Abnormal wave conditions II', November.

[30] Clauss, G., and Kühnlein, W., 1994. "Seakeeping tests of marine structures with deterministic wave groups and tank side wall wave absorbers". In Int Conf. on the behaviour of Offshore Structures (BOSS'94), July.

[31] Clauss, G., and Kühnlein, W., 1996. "Nonlinear transient wave excitation as a new tool in model testing". In Int. Conf. on Offshore Mech. and Arctic Eng. (OMAE), June.

[32] Clauss, G., Schmittner, C., and Hennig, J., 2003. "Simulation of rogue waves and their impact on marine structures". In Final MAXWAVE meeting, October.

[33] Cointe, R., and Armand, J., 1987. "Hydrodynamic impact analysis of a cylinder.". *J. of Offshore Mech. and Arctic Eng.,* ***109***, pp. 237 – 243.

[34] Cointe, R., Fontaine, E., Molin, B., and Scolan, Y., 2004. "On energy arguments applied to the hydrodynamic impact force". *J. of Eng. Math.,* ***48***, pp. 305 – 319.

[35] Colagrossi, A., and Landrini, M., 2003. "Numerical simulation of interfacial flows by Smoothed Particle Hydrodynamics". *J. of Comp. Physics,* ***191***, pp. 448–475.

[36] Cummins, W., 1962. "The impulse response function and ship motions". *Schiff-stechnik,* ***Bd 9***(Heft 47), pp. 101–109.

[37] Daalen van, E., Luth, H., Kleefsman, K., and Veldman, A., 2000. "Anti Roll Tank simulations with a Volume of Fluid (VOF) based Navier-Stokes solver". In 23rd Symp. on Naval Hydrodynamics, 17-22 Sep.

[38] Dallinga, R., 1999. "The new Seakeeping and Manoeuvring Basin of MARIN". In Int. Workshop on Natural Disaster by Storm Waves and their Reproduction in Experimental Basin, 29 Nov-1 Dec.

[39] Dallinga, R., 2006. "Bow flare slamming of container ships and its impact on operational reliability". In RINA Conf. 'Design and operation of container ships', Nov.

[40] Dallinga, R., and Huijsmans, R., 2010. "Froudes Law of Similitude Contemporary and future seakeeping testing". In The William Froude Conf., Nov.

[41] Derbanne, Q., Malenica, S., Tuitman, J., Bigot, F., and Chen, X.-B., 2010. "Validation of the global hydroelastic model for springing and whipping of ships". In 11th Int. Symp. on Pract. Design of Ships and other Floating Structures (PRADS).

[42] Dessi, D., and Mariani, R., 2006. "Slamming load analysis of a fast vessel in regular waves: a combined numerical/experimental approach". In 26th Symp. on Naval Hydrodynamics, Sept.

[43] Dessi, D., Mariani, R., La Gala, F., and Benedetti, L., 2003. "Experimental analysis of the wave induced response of a fast monohull via segmented-hull model". In 7th Int. Conf. on Fast Sea Transp. (FAST), Oct.

[44] Dobrovol'skaya, Z., 1969. "On some problems of similarity flow of fluid with a free surface". *J. of Fluid Mech.,* **36**(Part 4), pp. 805 – 829.

[45] Drummen, I., 2008. "Experimental and numerical investigation of nonlinear wave induced load effects in containerships considering hydroelasticity". PhD thesis, Norwegian Un. of Sc. and Techn., Department of Marine Techn., Trondheim, Norway.

[46] Düz, B., Bunnik, T., Kapsenberg, G., and Vaz, G., 2016. "Numerical simulation of nonlinear free surface water waves - coupling of a potential flow solver to a URANS/VoF code". In 35th Int. Conf. on Offshore Mech. and Arctic Eng. (OMAE), June.

[47] Eça, L., and Hoekstra, M., 2014. "A procedure for the estimation of the numerical uncertainty of CFD calculations based on grid refinement studies.". *J. of Comp. Physics,* **262**, pp. 104 –130.

[48] Fairlie-Clarke, A., and Tveitnes, T., 2008. "Momentum and gravity effects during constant velocity water entry of wedge-shaped sections". *Ocean Eng.,* **35**(Issue 7), May, pp. 706 – 716.

[49] Faltinsen, O, M., 1996. "Slamming". In Coll. for Ship and Offshore Hydrodynamics.

[50] Faltinsen, O., Ge, C., and Moan, T., 2002. "Water entry of a wedge with finite deadrise angle". *J. of Ship Res.,* **46**(1), Mar., pp. 39–51.

[51] Farstad, T., 1997. "Transient seakeeping analysis using generalized modes". PhD thesis, Massachusetts Inst. of Techn., Dept of Ocean Eng., Cambridge (MA), USA, February.

[52] Fekken, G., 2004. "Numerical simulation of free surface flow with moving rigid bodies.". PhD thesis, Un. of Groningen, Groningen, the Netherlands.

[53] Gagarina, E., Ambati, V. R., van der Vegt, J. J. W., and Bokhove, O., 2014. "Variational space-time (dis)continuous galerkin model for nonlinear free-surface water waves". *J. of Comp. Physics,* **275**, pp. 459 – 483.

[54] Gerrits, J., Loots, G., Fekken, G., and Veldman, A., 1999. "Liquid sloshing on earth and in space.". In Moving Boundaries V: Comp. modelling of free and moving boundary problems, B. Sarler, B. C.A., and H. Power, eds., WIT Press, Southampton, pp. 111–120.

[55] Gerrits, J., and Veldman, A., 2003. "Dynamics of liquid-filled spacecraft". *J. of Eng. Math.,* **45**, pp. 21–38.

[56] Gidel, F., Bokhove, O., and Kelmanson, M., 2017. "Driven nonlinear potential flow with wave breaking at shallow-water beaches". In 36th Int. Conf. on Offshore Mech. and Arctic Eng. (OMAE), 25 - 30 June.

[57] Gourmel, X., 2009. The prediction of slamming loads with ComFlow. Tech. rep., MARIN.

[58] Greenhow, M., 1987. "Wedge entry into initially calm water". *Appl. Ocean Research,* **9**, pp. 214 – 223.

[59] Greenhow, M., 1988. "Water-entry and -exit of a horizontal circular cylinder". *Appl. Ocean Research,* **10**(4), pp. 191–198.

[60] Grin, R., and Fernandez Ruano, S., 2015. "On the prediction of radii of inertia and their effect on seakeeping". In 12th Int. Marine Design Conf. (IMDC), May.

[61] Groesen, E. v., and Andonowati, 2007. "Variational derivation of KdV-type models for surface water waves". *Physics Letters A,* **366**, pp. 195–201.

[62] Groesen, E. v., Andonowati, and Soewono, E., 1999. "Nonlinear effects in bichromatioc surface waves". In Proc. Estonian Acad. Sci. Phys. Math., Vol. 48, pp. 206 – 229.

[63] Groesen, E. v., Bunnik, T., and Andonowati, 2011. "Surface wave modeling and simulation for wave tanks and coastal waters". In Developments in Marine CFD, Nov.

[64] Grue, J., Clamond, D., Huseby, M., and A., J., 2003. "Kinematics of extreme waves in deep water". *Appl. Ocean Research,* **25**, pp. 355 – 366.

[65] Grue, J., and Jensen, A., 2012. "Orbital velocity and breaking in steep random gravity waves". *J. of Geophysical Res.,* **117, C07013**(C7), pp. 1 – 16.

[66] Gu, X.-K., Shen, J., and Moan, T., 2003. "Efficient and simplified time domain simulation of nonlinear responses of ships in waves". *J. of Ship Res.,* ***47***(3), pp. 262–273.

[67] Guedes Soares, C., Pascoal, R., Antão, E., Voogt, A., and Buchner, B., 2004. "An approach to calculate the probability of wave impact on an FPSO bow". In 23rd Int. Conf. on Offshore Mech. and Arctic Eng. (OMAE), OMAE2004-51575, June.

[68] Guilcher, P., Brosset, L., Couty, N., and le Touzé, D., 2012. "Simulations of breaking wave impacts on a rigid wall at two different scales with a two phase fluid compressible SPH model". In 22nd Int. Offshore and Polar Eng. Conf. (ISOPE), June.

[69] Hay, B., Bourne, J., Engle, A., and Rubel, R., 1994. "Characteristics of hydrodynamic loads data for a naval combatant". In 1st Int. Conf. on Hydroelasticity in Marine Techn. (ICHE).

[70] Hermundstad, O., Aarsnes, J., and Moan, T., 1995. "Hydroelastic analysis of a flexible catamaran and comparison with experiments". In 3rd Int. Conf. on Fast Sea Transp. (FAST), Sept.

[71] Hermundstad, O., and Moan, T., 2004. "Numerical and experimental analysis of bow flare slamming on a Ro-Ro vessel in oblique waves". In 25th Symp. on Naval Hydrodynamics, Aug.

[72] Hermundstad, O., and Moan, T., 2005. "Numerical and experimental analysis of bow flare slamming on a Ro-Ro vessel in regular oblique waves". *J. of Mar. Sc. and Techn.,* ***10***(3), pp. 105–122.

[73] Hermundstad, O., and Moan, T., 2009. "Practical calculation of slamming pressures in irregular oblique seas". In 10th Int. Conf. on Fast Sea Transp. (FAST), Oct.

[74] Hermundstad, O., Moan, T., and Mørch, H., 2004. "Motions and slamming loads on a Ro-Ro ship". In 9th Int. Symp. on Pract. Design of Ships and other Floating Structures (PRADS), Sep.

[75] Hirt, C., and Nichols, B., 1981. "Volume of fluid (VOF) method for the dynamics of free boundaries". *J. of Comp. Physics,* ***39***, pp. 201–225.

[76] Hong, S., and Kim, B., 2014. "Experimental investigations of higher-order springing and whipping - WILS project". *Int. J. Nav. Archit. Ocean Eng.,* ***6***(4), pp. 1160 – 1181.

[77] Howison, S., Ockendon, J., and Wilson, S., 1991. "Incompressible water entry problems at small deadrise angles". *J. of Fluid Mech.,* ***222***, pp. 215–230.

[78] Hu, W., 2015. "Effect of gravity on the vertical force of an oscillating wedge at free surface". Master's thesis, Deft Un. of Techn., Delft, the Netherlands, Nov.

[79] Iafrati, A., 2016. "Experimental investigation of the water entry of a rectangular plate at high horizontal velocity". *J. of Fluid Mech.,* **799**, pp. 637 – 672.

[80] Iafrati, A., and Battistin, D., 2003. "Hydrodynamics of water entry in presence of flow separation from chines". In 8th Int. Conf. on Num. Ship Hydrodynamics (NSH), September.

[81] Iijima, K., Hermundstad, O., Zhub, S., and Moan, T., 2009. "Symmetric and antisymmetric vibrations of a hydroelastically scaled model". In 5th Int. Conf. on Hydroelasticity in Marine Techn. (ICHE).

[82] Judge, C., Troesch, A., and Perlin, M., 2004. "Initial water impact of a wedge at vertical and oblique angles". *J. of Eng. Math.,* **48**, pp. 279 – 303.

[83] Kaminski, M., and Bogaert, H., 2010. "Full scale sloshing impact tests - Part 1". *Int. J. of Offshore and Polar Eng.,* **20**(1), March, pp. 24 – 33.

[84] Kaminski, M., and Bogaert, H., 2010. "Full scale sloshing impact tests - Part 2". In 20th Int. Offshore and Polar Eng. Conf. (ISOPE), June.

[85] Kapsenberg, G., 2011. "Slamming of ships: Where are we now? A review.". *Phil. Trans. Royal Soc. A,* **369**, pp. 2892–2919.

[86] Kapsenberg, G., and Brizzolara, S., 1999. "Hydroelastic effects of bow flare slamming on a fast monohull". In 5th Int. Conf. on Fast Sea Transp. (FAST), Aug.

[87] Kapsenberg, G., and Brouwer, R., 1998. "Hydrodynamic development for a frigate for the 21 century". In Int. Symp. on Pract. Design of Ships and other Floating Structures (PRADS).

[88] Kapsenberg, G., and Kat de, J., 2000. "Effects of freeboard and bow height on green water loads for a general purpose cargo ship". In 4th Osaka Colloquium (OC-2000).

[89] Kapsenberg, G., and Thornhill, E., 2010. "A practical approach to ship slamming in waves". In 28th Symp. on Naval Hydrodynamics, Sept.

[90] Kapsenberg, G., Veer, A. v. t., Hackett, J., and Levadou, M., 2002. "Whipping loads due to aft body slamming". In 24th Symp. on Naval Hydrodynamics, July.

[91] Kármán, T. v., 1929. The impact on seaplane floats during landing. Tech. Rep. Techn. Note 321, NACA, Washington, Oct.

[92] Kasper, E., Karppinen, T., Nedrelid, T., and Lundgren, J., 1987. *Assessment of ship performance in a seaway.* NORDFORSK, Nordic Co-operative Organization for Applied Research, Copenhagen, Denmark. ISBN 87-982637-1-4.

[93] Kat, J. d., 1994. "Irregular waves and their influence on extreme ship motions". In 20th Symp. on Naval Hydrodynamics, National Research Council Washington (DC).

[94] Keuning, J., 1994. "The nonlinear behaviour of fast monohulls in head waves". PhD thesis, Delft Un. of Techn., Ship Hydromechanics Laboratory.

[95] Kim, B., Kim, K., Kim, Y., and Hong, S., 2014. "Torsion moment conversion methods in model test with U-shape backbone". In 24th Int. Offshore and Polar Eng. Conf. (ISOPE), 15 - 20 June.

[96] Kim, K., Lee, D., Hong, S., Kim, B., and Kim, Y., 2014. "Experimental study on the water impact load on symmetric and asymmetric wedges". In 24th Int. Offshore and Polar Eng. Conf. (ISOPE).

[97] Kim, S., Novak, D., Weems, K., and Chen, H., 2008. "Slamming impact design loads on large high speed naval craft". In Int. Conf. on Superfast Marine Vehicles, Moving Above, Under and in Water Surface (SuperFAST2008), 2 - 4 July.

[98] Kleefsman, K., 2005. "Water impact loading on offshore structures - A numerical study". PhD thesis, Un. of Groningen (RUG), Groningen, Netherlands.

[99] Kleefsman, K., Fekken, G., Veldman, A., Iwanowski, W., and Buchner, B., 2005. "A Volume-of-Fluid based simulation method for wave impact problems". *J. of Comp. Physics,* **206**(Issue 1), pp. 363–393.

[100] Koning, J., and Kapsenberg, G., 2012. "Full scale container ship cross section loads - first results". In 6th Int. Conf. on Hydroelasticity in Marine Techn. (ICHE), September.

[101] Koning, J., and Schiere, M., 2014. "Measuring hull girder deformations on a 9300 teu containership". *Int. J. Nav. Archit. Ocean Eng.,* **6**, pp. 1 – 19.

[102] Korobkin, A., 2004. "Analytical models of water impact". *Euro. J. of Appl. Math.,* **15**, pp. 821–838.

[103] Korobkin, A., and Scolan, Y.-M., 2006. "Three-dimensional theory of water impact. Part 2. Linearized Wagner problem". *J. of Fluid Mech.,* **549**, pp. 343–373.

[104] Koshizuka, S., and Oka, T., 1996. "Moving-particle semi-implicit method for fragmentation of incompressible fluids". *Nuclear Sci. and Eng.,* **123**(3), pp. 421–434.

[105] Kvålsvold, J., Svenson, T., and Hovem, L., 1996. "Bow impact loads on Ro-Ro vessels". In RINA Spring Meeting, Apr.

[106] Lafeber, W., Brosset, L., and Bogaert, H., 2012. "Elementary Loading Processes (ELP) involved in breaking wave impacts: findings from the Sloshel project". In 22nd Int. Offshore and Polar Eng. Conf. (ISOPE), June, pp. 285 – 299.

[107] Laur, U., Jaakula, H., Metsaveer, J., Lehtola, K., Iivonen, H., Karppinen, T., Eksborg, A.-L., Rosengren, H., and Noord, O., 1997. Final report on the capsizing on 28 September 1994 in the Baltic Sea of the Ro-ro passenger vessel MV Estonia. Tech. rep., The Joint Accident Investigation Commission of Estonia, Finland and Sweden.

[108] Lauzon de, J., Benhamou, A., and Malenica, S., 2015. "Numerical simulations of WILS experiments". In 25th Int. Offshore and Polar Eng. Conf. (ISOPE), June 21-26.

[109] Lauzon de, J., Grgic, M., Derbanne, Q., and Malenica, S., 2015. "Improved Generalized Wagner Model for slamming". In 7th Int. Conf. on Hydroelasticity in Marine Techn. (ICHE), September.

[110] Lavroff, J., Davis, M., Holloway, D., and Thomas, G., 2007. "The whipping vibratory response of a hydroelastic segmented catamaran model". In 9th Int. Conf. on Fast Sea Transp. (FAST), Sept.

[111] Lee, Y., White, N., Southall, N., and Johnson, M., 2015. "Impact loads and whipping responses on a Large Container Ship". In 25th Int. Offshore and Polar Eng. Conf. (ISOPE), June 21-26.

[112] Leibowitz, R., 1962. Comparison of theory and experiment for slamming of a Dutch destroyer. Tech. Rep. Report 1511, DTMB, Jun.

[113] Leibowitz, R., 1963. A method for predicting slamming forces and response of a ship hull. Tech. Rep. Report 1691, DTMB, Sep.

[114] Lewis, F., 1929. "The inertia of water surrounding a vibrating ship". In SNAME Trans., Vol. 37, pp. 1 – 20.

[115] Lockwood Taylor, J., 1930. "Some hydrodynamical inertia coefficients". *Phil. Mag.,* **9**(55), pp. 161–183.

[116] Loots, E., 2003. "Fluid-structure interaction in hydrodynamics". PhD thesis, Un. of Groningen (RUG), Groningen, Netherlands.

[117] Loukogeorgaki, E., Michailides, C., and Angelides, D. C., 2014. "dry and wet mode superposition approaches for the hydroelastic analysis of floating structures". In 9th Int. Conf. on Structural Dynamics, EURODYN 2014, 30 June - 2 July.

[118] Lugni, C., Brocchini, M., and Faltinsen, O., 2006. "Wave impact loads: The role of the flip-through". *Ph. of Fluids,* **18**, pp. 122101–122101–17.

[119] Luppes, R., Heiden, H. v. d., Plas, P. v. d., Veldman, A., and Duz, B., 2013. "Simulations of wave impact and two-phase flow with ComFLOW: Past and recent

developments". In 23rd Int. Offshore and Polar Eng. Conf. (ISOPE), 2013-TPC-0241, June - July.

[120] MAIB, 2008. Report on the investigation of the structural failure of MSC Napoli, English Channel on 18 January 2007. Tech. Rep. MAIB Report 9/2008, Marine Accident Investigation Branch, Carlton House, Southampton, UK, Apr.

[121] Malenica, S., Molin, B., Remy, F., and Senjanovic, I., 2003. "Hydroelastic response of a barge to impulsive and non-impulsive wave loads". In Hydroelasticity in Marine Techn. 2003, 15 - 17 Sep.

[122] Malenica, S., Orozco, J., and Chen, X., 2005. "Some aspects of multibody interactions in seakeeping". In 15th Int. Offshore and Polar Eng. Conf. (ISOPE), Jun.

[123] Malenica, S., Tuitman, J., Bigot, F., and Sireta, F., 2008. "Some aspects of 3d linear hydroelastic models of springing". In 8th Int. Conf. on Hydrodynamics (ICHD), Sep - Oct.

[124] Maron, A., and Kapsenberg, G., 2014. "Design of a ship model for hydro-elastic experiments in waves". *Int. J. of Naval Arch. and Ocean Eng.,* **6**(4), pp. 1130 – 1147.

[125] Marrone, S., Antuono, M., Colagrossi, A., Colicchio, G., Touzé, D. l., and Graziani, G., 2010. "Violent fluid-structure impacts solved through a d-SPH model". In 5th SPHERIC workshop, June, pp. 122–129.

[126] Mayo, W., 1945. Analysis and modification of theory for impact of seaplanes on water. Tech. Rep. 1008, NACA, Langley Field VA, USA, Dec.

[127] McTaggart, K., Datta, I., Stirling, A., Gibson, S., and Glen, I., 1997. "Motions and loads of a hydroelastic frigate model in severe seas". In SNAME Annual meeting, Oct.

[128] Meyerhof, W., 1970. "Added masses of thin rectangular plates calculated from potential theory". *J. of Ship Res.*, June, pp. 100–111.

[129] Moctar el, O., Schellin, T., and Priebe, T., 2006. "Cfd and fe methods to predict wave loads and ship structural response". In 26th Symp. on Naval Hydrodynamics, Sept.

[130] Molteni, D., Colagrossi, A., and Colicchio, G., 2007. "On the use of an alternative water state equation in SPH". In 2nd SPHERIC workshop, May.

[131] Monaghan, J., 1988. "An introduction to SPH". *Comp. Physics Comm.,* **48**, pp. 89–96.

[132] Monaghan, J., 2005. "Smoothed Particle Hydrodynamics (review)". *Rep. Prog. Phys.,* **68**, pp. 1703–1759.

[133] Monaghan, J. J., 1992. "Smoothed Particle Hydrodynamics". *Ann. Rev. Astron. Astrophys.,* **30**, pp. 543–574.

[134] Monroy, C., Seng, S., Diebold, L., Benhamou, A., and Malenica, S., 2016. "Comparative study of different methods for water impact computation". In 26th Int. Offshore and Polar Eng. Conf. (ISOPE), June 26-July 1.

[135] Moran, J., 1965. On the hydrodynamic theory of water-exit and -entry. Tech. Rep. Report TAR-TR 6501, Therm Adv. Research Inc., Thaca, New York, USA, Mar.

[136] Muzaferija, S., Peric, M., Sames, P., and Schellin, T., 1998. "A two-fluid Navier-Stokes solver to simulate water entry". In 22nd Symp. on Naval Hydrodynamics, 9-14 August, pp. 638 – 649.

[137] Newman, J., 1977. *Marine Hydrodynamics.* No. ISBN 0262140268. MIT Press.

[138] Newman, J., 1994. "Wave effects on deformable bodies". *Appl. Ocean Research,* **16**, pp. 47 – 59.

[139] Ochi, M., 1964. "Extreme behavior of a ship in rough seas - Slamming and shipping of green water". In SNAME Annual meeting, Nov.

[140] O'Dea, J., Powers, E., and Zselecsky, J., 1992. "Experimental determination of nonlinearities in vertical plane ship motions". In 19th Symp. on Naval Hydrodynamics, Aug, pp. 73 – 88.

[141] Onorato, M., Proment, D., Clauss, G., and Klein, M., 2013. "Rogue waves: From nonlinear schrdinger breather solutions to sea-keeping test". *PLoS ONE,* **8**(2). e54629.

[142] Pabst, W., 1930. Theory of landig impact of seaplanes. Tech. Rep. TM-580, NACA, Aug.

[143] Payne, P., 1994. "The water rise in front of a model planing hull". *Exp. in Fluids,* **17**, pp. 96–104.

[144] Petersen, J., 1992. "Non-linear strip theories for ship response in waves". PhD thesis, Techn. Un. of Denmark, Dept. Naval Arch. and Offsh. Eng., Copenhagen, Denmark.

[145] Pierson, J., Dingee, D., and Neidinger, J., 1954. A hydrodynamic study of the chines-dry planing body. Tech. Rep. 492, Stevens Inst. of Techn., Davidson Lab., May.

[146] Piro, D. J., and Maki, K. J., 2012. "Water exit of a wedge-shaped body". In Int. Workshop on Water Waves and Floating Bodies (WWWFB), 22-25 Apr.

[147] Plas, P. v. d., and Veldman, A., 2016. "Cfd simulation of wave impact on a semi-submersible: a numerical case study". In 12th Int. Conf. Hydrodyn. (ICHD2016).

[148] Ranocchia, D., Molland, A. F., Abrahamsson, S., Ikeda, Y., Kapsenberg, G. K., Shin, M.-S., Steen, S., and Zseleczky, J. J., 1999. "The specialist committee on model test of high speed marine vehicles". In Int. Towing Tank Conf.

[149] Raven, H., 1996. "A solution method for the nonlinear ship wave resistance problem". PhD thesis, Delft Un. of Techn., Delft, the Netherlands, Jun.

[150] Raven, H., 2010. "Validation of an approach to analyse and understand ship wave making". *J. of Mar. Sc. and Techn.,* **15**(4), pp. 331 – 344.

[151] Raven, H., Ploeg van der, A., and Starke, B., 2004. "Computation of free-surface viscous flows at model and full scale by a steady iterative approach". In 25th Symp. on Naval Hydrodynamics, August.

[152] Ren, D., Park, J.-C., Yun, S.-M., Shin, H.-S., and Hwang, S.-C., 2016. "Particle simulation on a free fall slamming problem for 2-d wedge and ship section". In 26th Int. Offshore and Polar Eng. Conf. (ISOPE), June 26 - July 1.

[153] Riccardi, G., and Iafrati, A., 2004. "Water impact of an asymmetric floating wedge". *J. of Eng. Math.,* **49**, pp. 19–39.

[154] Sames, P., Kapsenberg, G., and Corrignan, P., 2001. "Prediction of bow door loads in extreme wave conditions". In RINA Conf. 'Design and Operation for Abnormal Conditions II', Nov.

[155] Sames, P., Schellin, T., Muzaferija, S., and Peric, M., 1998. "Application of a two-fluid finite volume method to ship slamming". In 17th Int. Conf. on Offshore Mech. and Arctic Eng. (OMAE).

[156] Sasson, M., Chai, S., Beck, G., Jin, Y., and Rafieshahraki, J., 2016. "A comparison between Smoothed-Particle Hydrodynamics and RANS Volume of Fluid method in modelling slamming". *J. of Ocean Eng. and Sc.,* **1**, pp. 119– 128.

[157] Sawada, H., Watanabe, I., Yamamoto, T., Tanizawa, K., Ishida, S., Ueno, M., and Miyamoto, T., 1987. On an elastic model to simulate elastic hull responses of ships. Tech. rep., Ship Res. Inst.

[158] Scharnke, J., and Hennig, J., 2015. "Vertical wave impact loading on a fixed platform deck". In 34th Int. Conf. on Offshore Mech. and Arctic Eng. (OMAE), 41131, May - June.

[159] Scharnke, J., and Lafeber, W., 2016. "A study on simplified loading models for vertical wave-in-deck loading". In 26th Int. Offshore and Polar Eng. Conf. (ISOPE), June.

[160] Scolan, Y.-M., 2004. "Hydroelastic behaviour of a conical shell impacting on a quiescent free surface of an incompressible liquid". *J. of Sound and Vibr.*, **277**, pp. 163–203.

[161] Scolan, Y.-M., Coche, E., Coudrat, T., and Fontaine, E., 1999. "Analytical and numerical study of hydrodynamic impact of asymmetric bodies". In 7th Journées de l'Hydrodynamique, March.

[162] Scolan, Y.-M., and Korobkin, A., 2001. "Three dimensional theory of water impact. Part 1. Inverse Wagner problem". *J. of Fluid Mech.*, **440**, pp. 293–326.

[163] Semenov, Y., and Iafrati, A., 2003. "Asymmetric water entry of a wedge". In 7th Int. Conf. on Fast Sea Transp. (FAST), October.

[164] Skjelbreia, J., 1987. "Observations of breaking waves on sloping bottoms by use of laser doppler velocimetry". PhD thesis, Cal. Inst. of Techn., Division of Eng. and Appl. Science, Pasadena, California, May.

[165] Southall, N., Choi, S., Lee, Y., Hong, C., Hirdaris, S., and White, N., 2015. "Impact analysis using CFD A comparative study". In 25th Int. Offshore and Polar Eng. Conf. (ISOPE), June 21-26.

[166] Southall, N., Lee, Y., Johnson, M., Hirdaris, S., and White, N., 2014. "Towards a pragmatic method for prediction of whipping: Wedge impact simulations using OpenFOAM". In 24th Int. Offshore and Polar Eng. Conf. (ISOPE).

[167] Starke, B., 2004. "The prediction of scale effects on ship wave systems using a steady iterative rans method". In 7th Num. Towing Tank Symp., Oct.

[168] Stern, F., Wang, Z., Yang, J., Sadat-Hosseini, H., Mousaviraad, M., Bhushan, S., Diez, M., S-H., Y., P-C., W., Yeon, S., Dogan, T., D-H., K., Volpi, S., Conger, M., Michael, T., Xing, T., Thodal, R., and Grenestedt, J., 2015. "Recent progress in cfd for naval architecture and ocean engineering". *J. of Hydrodyn.*, **27**(1), pp. 1–23.

[169] Storhaug, G., 2009. "The 4400 TEU container vessel MSC Napoli broke its back, but did whipping contribute?". In 5th Int. Conf. on Hydroelasticity in Marine Techn. (ICHE), Sept.

[170] Sumi, Y., Fujikubo, M., Fujiya, H., Iwano, J., Kawagoe, Y., Kobayashi, K., Nakano, T., Takahira, T., and Ueda, N., 2014. Investigation report on structural safety of large container ships. Tech. rep., ClassNK.

[171] Sun, H., and Faltinsen, O., 2006. "Water impact of horizontal circular cylinders and cylindrical shells". *Appl. Ocean Research,* **28**, pp. 299–311.

[172] Sun, H., and Faltinsen, O., 2011. "Dynamic motions of planing vessels in head seas". *J. of Mar. Sc. and Techn.,* **16**, pp. 168–180.

[173] Szebehely, V., 1952. Hydrodynamics of slamming of ships. Tech. Rep. Report 823, NS 715-084, David Taylor Model Basin, July.

[174] Takewaki, H., Nishiguchi, A., and Yabe, T., 1985. "Cubic interpolated pseudo-particle method (cip) for solving hyperbolic-type equations". *J. of Comp. Physics,* **61**, pp. 261–268.

[175] Tan, S., 1992. Wave load measurements on a model of a large container ship. Tech. Rep. 173S, Neth. Ship Res. Cent., Delft, the Netherlands.

[176] Thomas, G., Davis, M., Holloway, D., and Roberts, T., 2008. "The vibratory damping of large high-speed catamarans". *Marine Struct.,* **21**, pp. 1 – 22.

[177] Thomas, G., Davis, M., Holloway, D., Watson, N., and Roberts, T., 2003. "Slamming response of a large high speed wave-piercer catamaran". *Marine Techn.,* **40**(2), Apr., pp. 126–140.

[178] Tuitman, J., 2010. "Hydro-elastic response of ship structures to slamming induced loads". PhD thesis, Delft Un. of Techn., Ship Hydromechanics Laboratory, Delft, the Netherlands, Feb.

[179] Tuitman, J., and Aanhold, W., 2007. "Using generalized modes for time domain seakeeping calculations". In 22nd Int. Workshop on Water Waves and Floating Bodies (WWWFB), Apr.

[180] Tuitman, J., Malenica, S., and Veer, A. v. t., 2012. "Generalized modes in time-domain seakeeping calculations". *J. of Ship Res.,* **56**, pp. 228 – 251.

[181] Tulin, M., and Wu, M., 1996. "Divergent bow waves". In 21st Symp. on Naval Hydrodynamics, pp. 661 – 679.

[182] Tveitnes, T., Fairlie-Clarke, A., and Varyani, K., 2008. "An experimental investigation into the constant velocity water entry of wedge-shaped sections". *Ocean Eng.,* **35**(14-15), Oct., pp. 1463–1478.

[183] Veen, D., and Gourlay, T., 2011. "A 2d smoothed particle hydrodynamics theory for calculating slamming loads on ship hull sections". In Symp. on High Speed Marine Vehicles (HSMV), Mar.

[184] Veldman, A., Fekken, G., and Kleefsman, K., 2005. "Numerical simulation of hydrodynamic wave impact". In Flow induced unsteady loads and the impact on military applications, B. Oskam, ed., RTO-AVT 123.

[185] Voogt, A., and Buchner, B., 2004. "Prediction of wave impact loads on ship-type offshore structures in steep fronted waves". In 14th Int. Offshore and Polar Eng. Conf. (ISOPE), May.

[186] Vorus, W., 1996. "A flat cylinder theory for vessel impact and steady planing resistance". *J. of Ship Res.*(40), pp. 89 – 106.

[187] Wagner, H., 1932. "Über Stoß- und Gleitvorgänge an der Oberfläche von Flüssigkeiten". *Zeitschrift für Angewandte Mathematik und Mechanik,* **Band 12**(Heft 4), Aug., pp. 193–215.

[188] Wagner, H., 1936. Phenomena associated with impacts and sliding on liquid surfaces. Tech. Rep. Report N-23507, NACA.

[189] Wang, Z.-H., 2000. "Hydroelastic analysis of high speed ships". PhD thesis, Techn. Un. of Denmark, Department of Naval Architecture and Offshore Eng.

[190] Watanabe, I., Ueno, M., and Sawada, H., 1989. "Effects of bow flare shape to the wave loads of a containership". *J. of the Soc. of Naval Arch. of Japan,* **166**, pp. 259–266.

[191] Wemmenhove, R., Luppes, R., Veldman, A., and Bunnik, T., 2015. "Numerical simulation of hydrodynamic wave loading by a compressible two-phase flow method". *Comp. and Fluids,* **114**, pp. 218 – 231.

[192] Wen, P., and Qiu, W., 2016. "Numerical prediction of forces and pressures on wedge and ship sections based on a CIP method". In 26th Int. Offshore and Polar Eng. Conf. (ISOPE), June 26-July 1.

[193] Wheeler, J., 1970. "Method for calculating forces produced by irregular waves". *J. Petroleum Techn.,* **22**(3), pp. 359 – 367.

[194] Wienke, J., Sparboom, U., and Oumeraci, H., 2000. "Breaking wave impact on a slender cylinder". In Int. Conf. on Coastal Eng. (ICCE), July.

[195] Wilson, R., Ji, L., Karman, S., Hyams, D., Sreenivas, K., Taylor, L., and Whitfield, D., 2008. "Simulation of large amplitude ship motions for prediction of fluid-structure interaction". In 27th Symp. on Naval Hydrodynamics, Oct.

[196] Wu, M., and Moan, T., 1996. "Linear and non-linear hydroelastic analysis of high speed vessels". *J. of Ship Res.,* **40**(2), June, pp. 149–163.

[197] Wu, Q., Ni, B., Bai, X., Cui, B., and Sun, S., 2017. "Experimental study on large deformation of free surface during water exit of a sphere". *Ocean Eng.,* **140**, p. 369376.

[198] Xia, J., and Wang, Z., 1997. "Time domain hydro-elasticity theory of ships responding to waves". *J. of Ship Res.,* **41**(4), Dec., pp. 286–300.

[199] Xia, J., Wang, Z., and Jensen, J., 1998. "Non-linear wave loads and ship responses by a time domain strip theory". *Mar. Struct.,* **11**(3), pp. 101–123.

[200] Xu, G., Duan, W., and Wu, G., 2008. "Numerical simulations of oblique water entry of an asymmetrical wedge". *Ocean Eng.,* **35**, pp. 1597–1603.

[201] Xu, L., and Barltrop, N., 2008. "Bow impact loading on FPSO's 2 - Theoretical investigation". *Ocean Eng.,* **35**, pp. 1158–1165.

[202] Xu, L., Barltrop, N., and Okan, B., 2008. "Bow impact loading on FPSO's 1 - Experimental investigation". *Ocean Eng.,* **35**, pp. 1148–1157.

[203] Xu, L., Troesch, A., and Peterson, R., 1998. "Asymmetric hydrodynamic impact and dynamic response of vessels". In 17th Int. Conf. on Offshore Mech. and Arctic Eng. (OMAE).

[204] Yamamoto, Y., Iida, K., Fukasawa, T. Murakami, T., Arai, M., and Ando, A., 1985. "Structural damage analysis of a fast ship due to bow flare slamming". *Int. Shipb. Progress,* **32**(369), pp. 124–136.

[205] Zhao, R., and Faltinsen, O., 1993. "Water entry of two-dimensional bodies". *J. of Fluid Mech.,* **246**, pp. 593–612.

[206] Zhao, R., and Faltinsen, O., 1998. "Water entry of arbitrary axisymmetric bodies with and without flow separation". In 22nd Symp. on Naval Hydrodynamics, Aug., pp. 652–664.

[207] Zhao, R., Faltinsen, O., and Aarsnes, J., 1996. "Water entry of arbitrary 2-dimensional sections with and without flow separation". In 21th Symp. on Naval Hydrodynamics, June, pp. 408–423.

Acknowledgements

Curriculum Vitae

Geert Kapsenberg was born on 20 March 1955 in Sluis, the Netherlands. After finishing high school he went to Delft University of Technology to study Maritime Engineering. After graduation he fulfilled military service by studying hydrodynamics of SWATH vessels by numerical and experimental methods. He started his professional life at TNO-IWECO in 1981. At TNO he worked mainly on models to determine manoeuvring characteristics of submarines. In 1986 he changed to MARIN in Wageningen where he worked in several departments, focussing on the seakeeping behaviour of high speed vessels. This work created an interest in the most important limiting factor of the operability in waves of theses vessels: slamming.

Appendices

Appendix A

Propagation of steep waves

It is well known that steep waves do not propagate as linear waves; nonlinear wave models are required. This is an area of active research by for instance van Groesen *et al.* [62] who use an analytical model. Gagarina *et al.* [53] and Gidel *et al.* [56] use a model based on the variational principle. This last model has the effect of breaking waves, wave damping, at the beach, but does not model the physics of breaking. Duz *et al.* [46] worked on a coupling of a nonlinear flow solver to a CFD code to provide the correct velocities at the inflow boundary. All codes mentioned should give a better solution for the propagation of waves from the measurement in front of the model to the various locations on the ship. However, the simulation program used contains just a linear wave model.

Steep waves have been used in the experiments because these give rise to high impact forces. The propagation of these steep waves using a linear wave model could give rise to inaccuracies. In order to minimize the errors made, waves were measured on several locations close to the model, Table A.1. The analysis was made using the time trace measured by Wave-4 as input; the Fourier transform of this signal was calculated and used to transfer the wave to another position using linear theory. The input for the simulation is the FFT of the wave at the position of the CoG of the model at $t = 0$.

The accuracy of this approach is demonstrated in Figure A.1 . The FFT of Wave-4 has components up to an earth-fixed wave frequency $\omega = 3.0 \ rad/s$ (full scale value), the reconstructed wave is shown in the bottom plot of the figure. The other plots show the results of the linear wave propagation on the locations of Wave-1 and Wave-2 compared to the measured signals. The comparison is not perfect, especially the positive peak values are too low in the linear reconstruction. The reason to chose Wave-4 as a basis signal, and the reason to chose the location of the probe, is that this wave probe is on nearly the same X-coordinate as the FPP of the model, but a bit on the side to avoid contact in quartering waves.

Table A.1: Position of wave probes for the second series of experiments. The data is at model scale; reference point is St 10 of the model and the model centre line. The length of the model is 6.65 m.

	X-pos [m]	Y-pos [m]
Wave 1	6.35	0.0
Wave 2	0.0	-4.82
Wave 4	3.30	-3.15
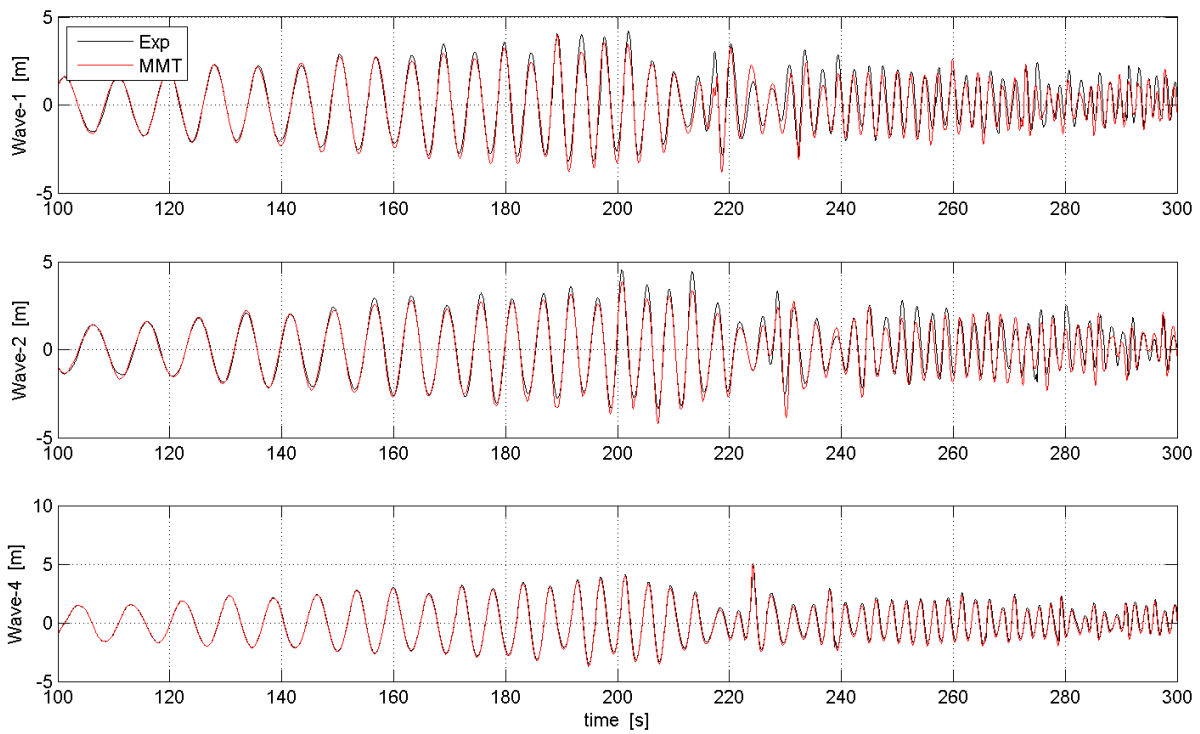
Figure A.1: Comparison of waves measured in the basin and waves calculated on basis of linear theory using the FFT of Wave-4 as input.